DESIGN AND SYNTHESES OF HOLE AND ELECTRON TRANSPORT DONOR-ACCEPTOR POLYMERIC SEMICONDUCTORS AND THEIR APPLICATIONS TO ORGANIC FIELD-EFFECT TRANSISTORS

A Dissertation

Presented to

The Academic Faculty

By

Boyi Fu

In Partial Fulfillment

of the Requirements for the Degree

Doctor of Philosophy in the

School of Chemical & Biomolecular Engineering

Georgia Institute of Technology

May 2015

DESIGN AND SYNTHESES OF HOLE AND ELECTRON TRANSPORT DONOR-ACCEPTOR POLYMERIC SEMICONDUCTORS AND THEIR APPLICATIONS TO ORGANIC FIELD-EFFECT TRANSISTORS

Approved by

Dr. Elsa Reichmanis, *Advisor*
School of Chemical & Biomolecular Engineering
Georgia Institute of Technology

Dr. David M. Collard
School of Chemistry & Biochemistry
Georgia Institute of Technology

Dr. Dennis W. Hess
School of Chemical & Biomolecular Engineering
Georgia Institute of Technology

Dr. Jean-Luc Bredas
Solar and Photovoltaics Engineering Research Center
King Abdullah University of Science and Technology

Dr. William J. Koros
School of Chemical & Biomolecular Engineering
Georgia Institute of Technology

Date Approved: February 27th, 2015

ACKNOWLEDGEMENTS

The Ph.D. training at Georgia Institute of Technology for the past 5 years is a truly valuable, memorable, and pleasant journey for me. This experience improved my insight, capability, confidence, and courage of discovering, thinking and resolving challenges not only in scientific research and development, but also in my entire life.

Herein, I would like to firstly appreciate my advisor, Prof. Elsa Reichmanis. I would not be able to complete this training without her guidance, support, and help crossing my entire Ph.D. study. Prof. Reichmanis is not only an innovative, knowledgeable, and insightful scholar, but also a kind, friendly, and helpful person whom people should work with. I feel quite fortunate being her student in the past five years.

I would like to also express my serious thanks to Prof. David Collard and Prof. Jean-Luc Bredas in my studies of organic and polymeric syntheses, molecular simulations, as well as journal publication writings. I had a really enjoyable time of working with them and their research groups; and gained significant guidance and help from them.

Besides, I would like to thank Prof. Dennis Hess and Prof. William Koros for their great guidance, help, and comments on my Ph.D. thesis proposal, six-months' reviews and this dissertation as my Ph.D. thesis committee.

I would like to truly appreciate our group members and lab-mates, especially Dr. Zhaokang Hu, Dr. Avishek Aiyar, Dr. Mincheol Chang, Ji-Hwan Kang, Nabil Kleinhenz,

Ping-Hsun Chu, Gang Wang, Zhibo Yuan, and Yundi Jiang. It was a wonderful time of working with them during past years in our lab.

I also would like to gratefully acknowledge all our collaborators and people who provided us help and guidance in our research, especially Dr. Jose Baltazar, Prof. Bernard Kippelen and his group members Cheng-Yin Wang and Dr. Canek Fuentes-Hernandez, Dr. Bradley Rose in Prof. Jean-Luc Bredas' group, Siyuan Zhang, Professor Alejandro Briseno and Ben Cherniawski of the Department of Polymer Science and Engineering at the University of Massachusetts Amherst and Professor John R. Reynolds and Kin Lo of the School of Chemistry and Biochemistry in Georgia Tech. Professor Richard Jordan, Ge Feng, and Nate Contrella of the Department of Chemistry at the University of Chicago. It was a great experience for me to work with these innovative and helpful scholars.

My Ph.D. research was funded in part by the National Science Foundation (DMR-1207284), the Georgia Institute of Technology, and the Center for Organic Photonics and Electronics (COPE) Fellowship at Georgia Tech, as well as by the King Abdullah University of Science and Technology. 2D-GIXS measurements were carried out by Linda Sauer at the Characterization Facility, University of Minnesota, which receives partial support from NSF through the MRSEC program.

Eventually, I would reserve my deepest gratitude to my parents. I appreciate all their contributions and sacrifices to my entire life. I always naturally miss them whenever I enjoy the happiness or encounter difficulties. I dedicate my Ph.D. dissertation to my dearest parents.

TABLE OF CONTENTS

LIST OF TABLES

LIST OF FIGURES

SUMMARY

The π-conjugated organic and polymeric semiconducting materials have attracted much attention in the past years due to their electronic and optoelectronic properties and thus their significant potential in applications to electronic and optoelectronic devices including organic field-effect transistors (OFETs), organic photovoltaics (OPVs), and organic light-emitting diodes (OLEDs), etc. Yet, organic and polymeric semiconductors still have challenges associated with their relatively low charge carrier (hole and electron) transport mobilities and ambient stability in OFET applications. This dissertation discusses the molecular engineering of π-conjugated semiconducting polymers to enhance the hole and electron field-effect mobilities via advancing polymer chain intra- and inter-molecular interactions and the ambient stability via decreasing the energy levels of frontier molecular orbitals.

Three donor-acceptor copolymers, poly(hexathiophene-co-benzothiazole) (PBT6), poly(thiophenes-benzothiadiazole-thiophenes-diketopyrrolopyrrole) (pTBTD), and poly(dithieno-diketopyrrolopyrrole-bithiazole) (PDBTz) have been developed, as shown in Chapter 3, 4, and 5, respectively. By tuning the frontier molecular orbital energy levels, PBT6 and pTBTD with relatively higher highest occupied molecular orbitals (HOMOs) and lowest unoccupied molecular orbitals (LUMOs) expressed hole transport behaviors, while PDBTz with lower LUMO and HOMO exhibited an electron transport

characteristics. Besides, the effect of polymer side chains on polymer solution-processability and charge carrier transport properties was systematically investigated, as shown in Chapter 4: a side chain 5-decylheptadecyl (5-DH) having the branching position remote from the polymer backbone merges the advantages of the improved solubility from traditional branched side chains in which the branch chains are close to polymer backbone and the effective π-π intermolecular interactions commonly associated with linear side chains. This indicates the potential of side chain engineering to facilitate the charge carrier transport performance of organic and polymeric semiconductors. Additionally, PDBTz was solution-processed to OFETs based on non-halogenated solvents in Chapter 5. The resultant thin-film OFET devices based on non-halogenated solvents exhibited similar film morphology and field-effect electron mobilities as the counterparts based on halogenated solvents, indicative of the feasibility of developing high mobility OFET devices through more environmentally-benign processing.

LIST OF ABBREVIATIONS

μ	Charge carrier transport mobility, $cm^2V^{-1}s^{-1}$
μ_h	Hole mobility, $cm^2V^{-1}s^{-1}$
μ_e	Electron mobility, $cm^2V^{-1}s^{-1}$
HOMO	Highest occupied molecular orbital, eV
LUMO	Lowest unoccupied molecular orbital, eV
MO	Molecular orbitals, eV
IP	Ionization potential, eV
EA	Electron affinity, eV
$I_{ON/OFF}$	Current on and off ratio
V_T	Threshold voltage, V
V_G	Gate voltage, V
V_{SD}	Source-drain voltage, V
I_{SD}	Source-drain current, A
E_g	Bandgap, eV
E_g^{opt}	Optical bandgap, eV
E_g^{elec}	Electronic bandgap, eV
λ	Wavelength, nm
λ_{max}	Wavelength at highest intensity, nm

CV	Cyclic voltammetry
DPV	Differential pulse voltammetry
UPS	Ultraviolet photoelectron spectroscopy
AFM	Atomic force microscopy
GIWAXS	Grazing incidence wide angle X-ray scattering
κ_{ET}	Electron transfer rate
DFT	Density functional theory
t	Transfer integral
λ_E	Reorganization energy

CHAPTER 1

INTRODUCTION TO ORGANIC SEMICONDUCTORS

Organic semiconductors have attracted much attention within the last few decades, after the groundbreaking discovery and development of conductive polymers pioneered by Alan J. Heeger, Alan MacDiarmid and Hideki Shirakawa.[1] Organic semiconductors can exhibit electronic and optoelectronic properties similar to their inorganic counterparts; meanwhile, they possess a relatively low density and have flexibility typically associated with common organic and polymeric materials.[2] Thus, organic semiconductors have great potential for the development of high-performance, light-weight, flexible, large area and low-cost organic electronic devices for applications in electronic signal switching and amplification such as occurs in organic field-effect transistors (OFETs), organic CMOS (complementary metal-oxide-semiconductor)-like logic, and organic sensors; displays such as organic light-emitting diodes (OLEDs); solar and thermal energy harvesting such as organic photovoltaics (OPVs) and organic thermoelectrics (Figure 1).[3]

As the fundamental building block for electronic circuits, the field-effect transistor unitizes an electric field to drive and manipulate the charge carrier conductivity of semiconducting materials in the transistor channel, and thus the signal can be switched and amplified.[3a, 4] Transistors are generally classified as p- or n-channel, which refer to

transistors having hole or electron transport within the transistor channel, respectively. A transistor that exhibits both hole and electron mobility simultaneously is called an ambipolar transistor, and the corresponding semiconducting material is an ambipolar semiconductor.[5]

In OFETs, p-type (hole transport) or n-type (electron transport) organic semiconductors replace the inorganic semiconductors within the transistor channel, e.g. silicon and zinc oxide, to afford p-channel and n-channel OFETs. Please see the detailed charge carrier transport and OFET device mechanism in Chapter 2. The coupling of p- and n-channel transistors allows for fabrication of CMOS-like logic devices, which are widely used in digital integrated circuits including microprocessors, microcontrollers, and static random access memory devices.[6] Recently OFETs have been incorporated into artificial electronic skin, which has significant potential in robotics, wearable electronics, and biomedical devices.[7]

In OLEDs, organic semiconductors as the optoelectronic active layer convert the electronic current to photons in the visible wavelength region, such as blue, red, and green.[8] It is worthy to mention that OLED technologies have been commercialized and are used in display products such as LG TV sets (based on white light) and the display in Samsung Galaxy smart phones (based on red, green and blue lights).[9] The expected

flexible OLED market size is *ca*. 17.6 billion dollars on 2020 with an approximate 60 % compound annual growth rate.[10]

In contrast to OLEDs, organic semiconductors in OPVs work as photoactive layers to absorb sunlight and convert photons into electric power.[11] The power conversion efficiency (a ratio of electric density gain to the solar energy absorbed) of OPVs up-to-date has reached *ca.* 10 % in lab scale devices, a value that is comparable to that of amorphous silicon PVs.[11a, 12] In organic thermoelectric devices, organic semiconductor p-n junctions carry heat away from the active areas (temperature manipulation) and recover the waste heat to generate electric energy.[13] The detailed mechanism is described in Chapter 6.

The unique electronic and optoelectronic properties of organic semiconductors correlate with their molecular structures. **Figure 1.1** shows a few examples of organic semiconductors including small molecules and polymers.[14] Based largely on the difference in molecular weight (MW), organic π-conjugated semiconductors are typically categorized as small molecule semiconductors which have a MW less than 1 kDa, oligomers possessing MWs in a range of 1 k – 3 kDa with the number of repeating units in a range of 2-10, and polymers with MWs greater than 3 kDa and more than 10 repeat units. Small molecule and oligomeric π-conjugated materials are typically called organic

semiconductors, and the polymeric counterparts are referred to as polymeric semiconductors.

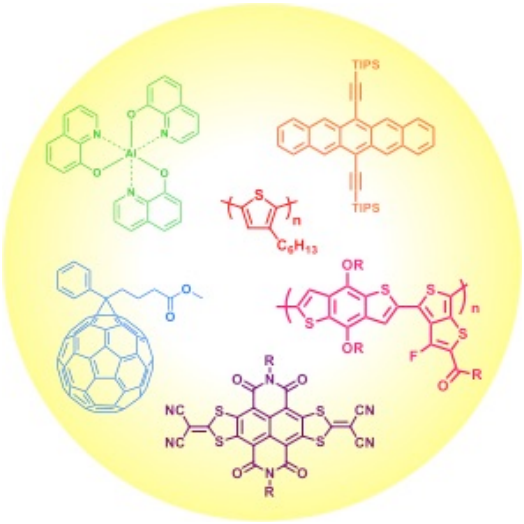

Figure 1.1. Representative examples of organic and polymeric semiconductors (more examples are shown in Chapter 2)

Compared with traditional organic materials and polymers that are electronic insulators, organic and polymeric semiconductor typically have conjugated backbones consisting of unsaturated units such as aromatic units, vinylene bonds, acetylene bonds, etc., in which the π electrons can be delocalized, leading to the formation of intra-molecular π-conjugation (intramolecular electronic coupling),[1a, 15] as shown in Figure 1.2. Typically, aliphatic side chains such as alkyl chains are incorporated onto the unsaturated structure (Figure 1.3) in order to enhance solubility, which enables solution processing into organic electronic devices and can change the molecular packing within the solid state.[16] Within solid films, organic compounds or polymer chains self-assemble to afford a π-π stacked super-molecular packed structure leading to the formation of π-π

intermolecular or inter-chain interactions (intermolecular electronic coupling), through which π-electrons are able to delocalize among molecules or polymeric chains.[16c] Both these intramolecular and intermolecular interactions pave the pathway for long-range charge carrier transport within organic and polymeric semiconducting films, as shown in Figure 1.4. Due to the isolating nature of alkyl side chains, no charge transfer takes place along the side chain direction.

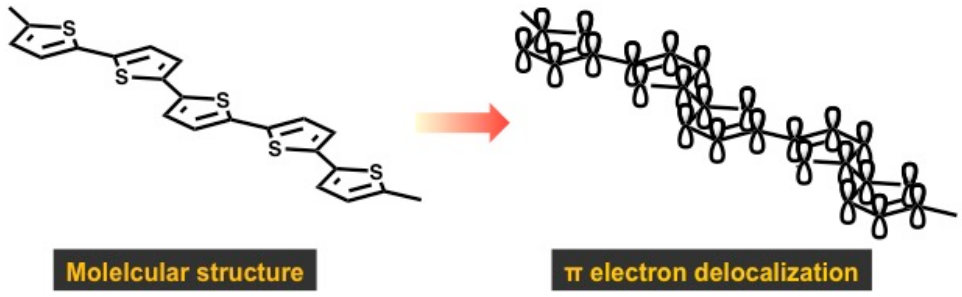

Figure 1.2. The molecular structure of polythiophene and the corresponding π electron delocalization along polythiophene chains.

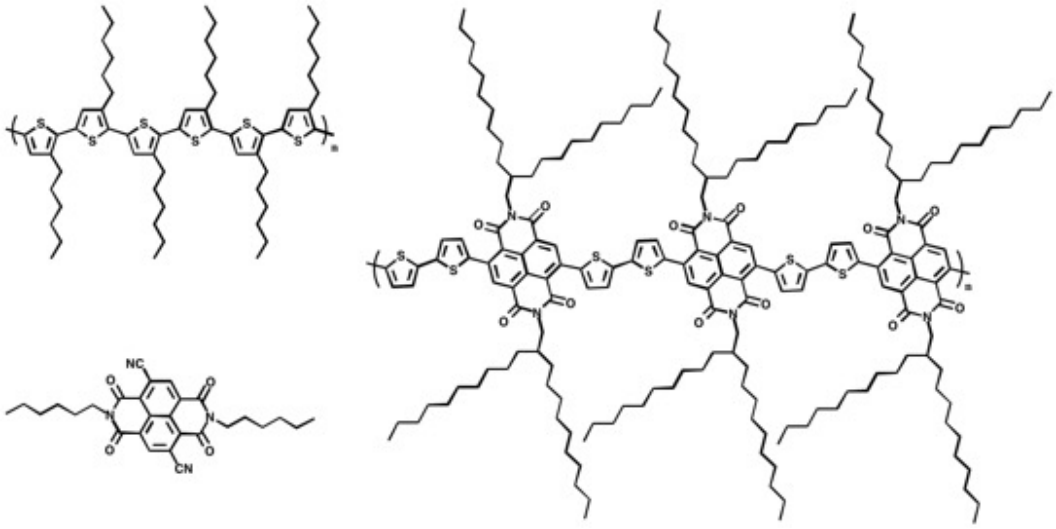

Figure 1.3. Representative examples of alkyl side chains incorporated into organic and polymeric semiconductors.[16b, 17]

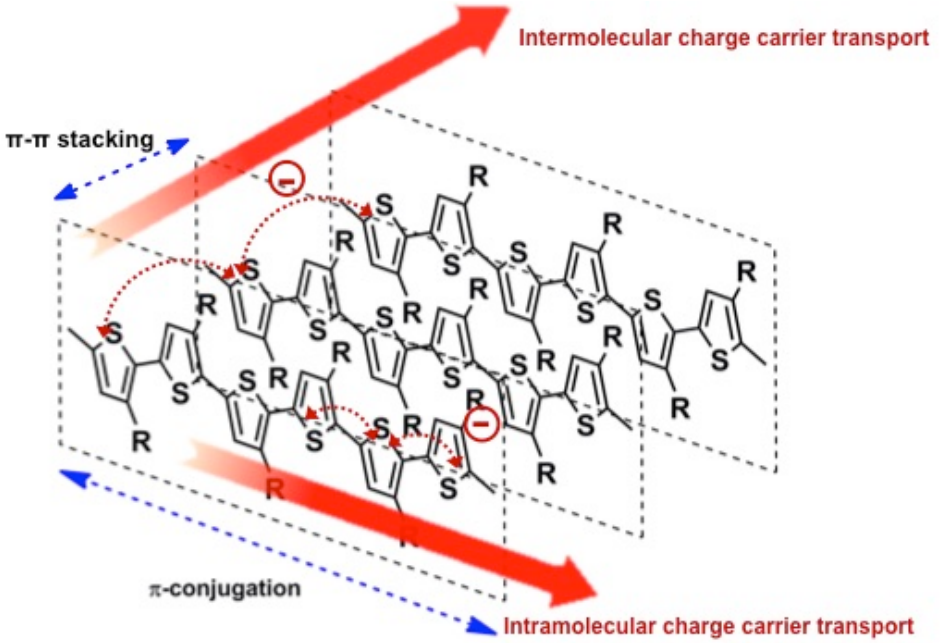

Figure 1.4. Schematic representation of π electron intramolecular delocalization and intermolecular hopping, and the resulting intra- and inter-molecular charge carrier transport pathways

Consistent with inorganic semiconductors, the charge carrier mobility (μ, with the unit of $cm^2V^{-1}s^{-1}$) is the primary parameter used to evaluate the semiconducting properties of organic and polymeric semiconductors. The mobility, μ, describes the rate of charge carriers moving through semiconductors under the influence of an electric field (E, with the unit of V/cm)[1a] [18]:

$$\mu = \frac{v_d}{E} \qquad \text{Eq. 1.1}$$

where v_d is the flow velocity of charge carriers, with the unit of $cm.s^{-1}$. The electric current (I, with the unit of A) through a semiconductor is described as:[3a]

$$I = nev_dA \qquad \text{Eq. 1.2}$$

where n refers to the charge carrier density (number of charge carriers within a unit volume, with the unit of per cm^3); e is the charge per charge carrier (hole or electron) with a constant value of 1.602 $x10^{-19}$ C; and A denotes the cross-sectional area of semiconductor. Through combining Eq. 1.1 and 1.2, the current equals:

$$I = ne\mu(\frac{V}{L})A \qquad \text{Eq. 1.3}$$

The conductivity σ (with the unit of $S.m^{-1}$) equals:

$$\sigma = ne\mu \qquad \text{Eq. 1.4}$$

The corresponding electric current density (J, with the unit of $A.cm^{-2}$) hence equals:

$$J = \sigma(\frac{V}{L}) \qquad \text{Eq. 1.3}$$

One essential difference in organic semiconductors as opposed to inorganic counterparts is that there should be no free charge carrier in pure organic or polymeric semiconductors, that is, organic and polymeric semiconductors are not doped.[19] In reality, however, trace amounts of charge carriers originating from impurities resident in organic semiconductors after synthesis and purification, do exist.[3a, 20] The free charge carriers hence should be injected into organic semiconductors during device operation. In OFETs for instance, holes and electrons are injected from electrodes to the ionization potential (IP), which is theoretically corresponding to the absolute value of highest occupied molecular orbital (HOMO), and electron affinity (EA) relating to the lowest unoccupied molecular orbital (LUMO), during device characterization.[3, 21]

In organic and polymeric semiconductors, both intra- and inter-molecular π-electronic coupling leads to hybridization of the molecular orbitals and thus formation of the valence and conduction bands. The top level of the valence band is the IP or -HOMO, while the bottom level of the conduction band is the EA, or LUMO.[1a, 19b] The difference between the IP and EA is the bandgap (E_g), as shown in Figure 1.5. Holes are injected into the IP in p-channel OFETs, while electrons are injected into the EA in n-channel devices (Figure 1.5).[3a] In ambipolar transistors and p-n junction systems including OPVs, OLEDs and organic thermoelectric devices, both holes and electrons are diffusing through the materials simultaneously.[22] It is worthy to mention that the doping of π-conjugated materials induces the narrowing of E_g. Under certain doping conditions, E_g becomes vanishing small to convert the materials into conductors, such as PEDOT/PSS or doped polypyrrole.[23]

Efforts related to the design and development of high performance organic and polymeric semiconductors have grown rapidly within the last decade. Compared with inorganic materials, such as amorphous and polycrystalline silicon,[24] zinc oxide,[25] and IGZO [26] which have field-effect hole and electron mobilities in a range of 1-100 $cm^2V^{-1}s^{-1}$, typical organic and polymeric semiconductors, still have relatively low charge carrier mobilities (field-effect hole mobility is in the range of 10^{-2} – 1 $cm^2V^{-1}s^{-1}$ though a few very recent examples show hole mobilities of up to 10 $cm^2V^{-1}s^{-1}$;[27] and field-effect

electron mobility is in the range of 10^{-3} – 1 $cm^2V^{-1}s^{-1}$ [28]), and low ambient operation stability (sensitivity to oxidation), especially for n-channel electron transport semiconductor remains a problem.[29] Further, it remains challenging to solution-process polymeric semiconductors in a facile, environmentally benign manner.[30]

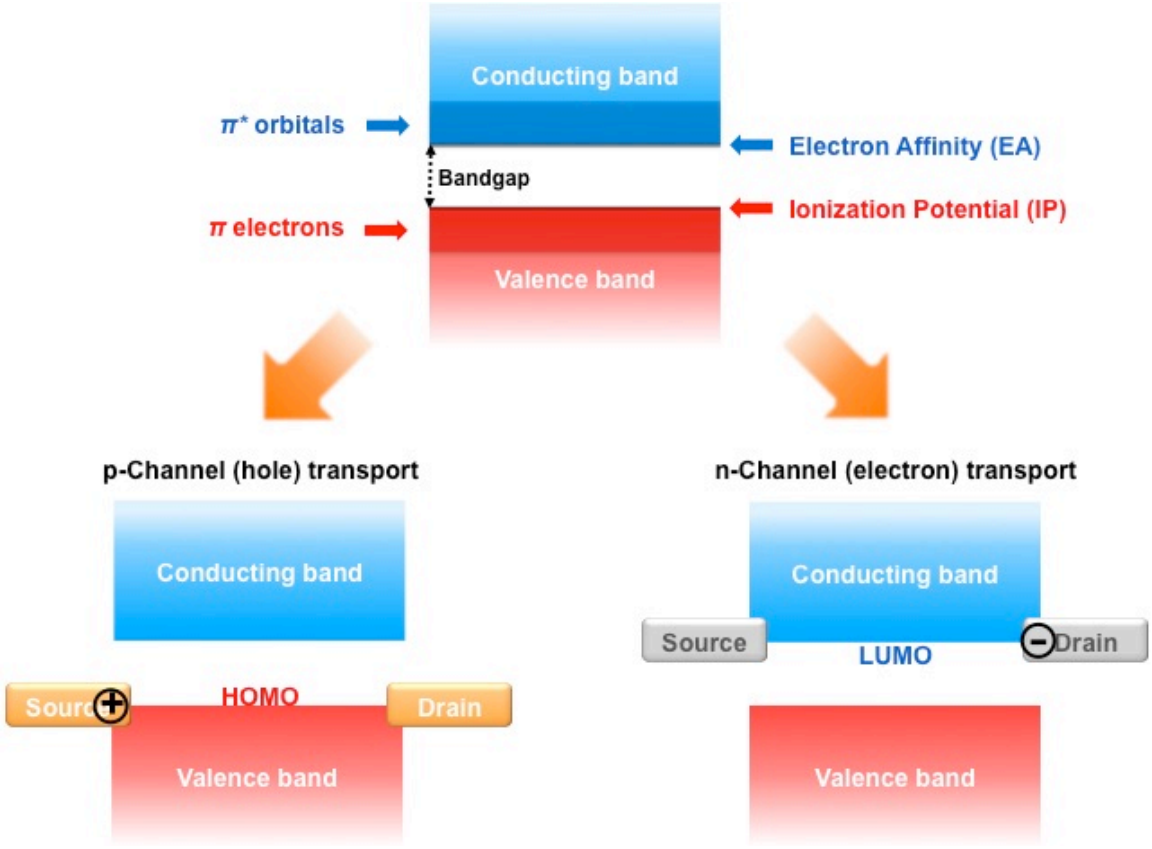

Figure 1.5. A generic scheme of the HOMO, LUMO and bandgap (E_g) of organic and polymeric semiconductors. Hole is injected from the source electrode to the HOMO in p-channel OFETs and electron injection is from the source to the LUMO in n-channel OFETs.

As discussed above, enhancement of intra- and inter-molecular electronic coupling should improve charge carrier transport efficiency; while side chain engineering is expected to address issues associated with solubility and solution processability of

organic and polymeric semiconductors.[31] The ambient stability of organic and polymeric semiconductors correlates with their HOMO and LUMO energy levels. The lower the HOMO and LUMO energy levels, the better ambient stabilities in hole and electron transport materials.[14d, 19a, 29a, 32] Thus, a systematic molecular engineering approach in the design of organic and polymeric semiconductors is highly desirable.

This Ph.D. dissertation focuses on investigations in the molecular design and synthesis of p- and n-channel polymeric semiconductors and investigation of their OFET performance. Chapter 2 introduces typical organic and polymeric semiconductor properties and characterization methods, along with recent progress in organic and polymeric semiconductor synthesis, charge transfer mechanism, OFET fabrication, processing, and optimization. Chapter 3 introduces the incorporation of an electron deficient benzothiadiazole unit into a homopolymer, polythiophene, to afford a family of electron donor-acceptor benzothiadiazole-*co*-oligothiophene based polymers, in which poly(benzothiadiazole-*co*-hexathiophene) (PBT6) showed improvements in field-effect hole mobility and ambient stability.[33] Chapter 4 introduces the incorporation of a second electron acceptor, diketopyrrolopyrrole, into PBT6, to afford a donor–acceptor(1)-donor–acceptor(2) polymer, pTBTD.[34] Three side chains including the branched 5-decylheptadecyl (5-DH), 2-tetradecyl (2-DT), and linear n-octadecyl (OD) chains are substituted onto pTBTD, to systematically explore the effect of side chain structure on π-

conjugated polymer solubility and charge carrier transport properties. This demonstrates that the incorporation of branched side chains in which the branching position is remote from the polymer backbone merges the advantages of improved solubility from branched units with effective π–π intermolecular interactions normally associated with linear side chains on conjugated polymers. In Chapter 5, a novel high-performance n-channel polymer semiconductor, poly(dithieno-diketopyrrolopyrrole-bithiazole), PDBTz, was introduced.[35] With incorporation of 5-decylheptacyl side chains, PDBTz exhibits good solubility in non-halogenated, more environmentally compatible solvents. PDBTz based OFETs were fabricated using several solvent systems. A systematic study of solvent on semiconducting polymer thin-film ordering, texture, and charge carrier transport performance was conducted to explore the practicality of developing high mobility n-channel OFET devices via more environmentally-benign processing. Chapter 6 describes future plans aimed at developing electron transport polymeric semiconductors with improved electron mobility and ambient stability; and their possible applications in CMOS-like logic and organic thermoelectric devices.

CHAPTER 2

ADVANCES OF ORGANIC & POLYMERIC SEMICONDUCTOR SYNTHESIS, CHARACTERIZATIONS, AND OFET APPLICATIONS

2.1. Organic & Polymeric Semiconductor Properties

As discussed in Chapter 1, according to the difference in molecular weight (MW), organic π-conjugated semiconductors typically could be categorized as small molecular semiconductors with MW less than 1 kDa, oligomers with MW in a range of 1 k – 3 kDa and the number of repeating units in a arrange of 2-10, and polymers with MW greater than 3 kDa and the number of repeating units greater than 10. The π-conjugated small molecular and oligomeric ones are typically termed organic semiconductors, and polymeric counterparts are termed polymeric semiconductors.

2.1.1. Organic & Polymeric Semiconductor Properties

Figure 2.1 and 2.2 shows several examples of p-channel (hole transport) and n-channel (electron transport) small molecule and oligomeric semiconductors. Small molecule semiconductors with high purity (> 99%) in general can be realized through various

purification approaches, such as silica or anti-silica gel column chromatography and sublimation or solution recrystallization. The removal of impurities significantly reduces both shallow and deep electron traps remaining in the semiconductors, leading to an increase in charge carrier transport performance. Small molecule semiconductors often form highly crystalline structures after crystallization. The high degree of crystallinity is expected to benefit charge transfer between molecules, thus enhancing charge carrier mobility. For instance, single crystal structures of rubrene,[36] pentacene,[37] TIPS-tetraazapentacene[38] (compound 10 in Figure 2.1), and BTBT-C8[39] have been shown to exhibit hole mobilities beyond 1 $cm^2V^{-1}s^{-1}$ when used as the active layer in OFET devices. The single crystal device performance results are much higher than those obtained from low crystallinity films of the same materials. Poly-crystalline semiconductor films often show much lower mobilities than single-crystal devices of same material due to the presence of grain boundaries between crystalline domains that severely limit effective charge carrier transport.

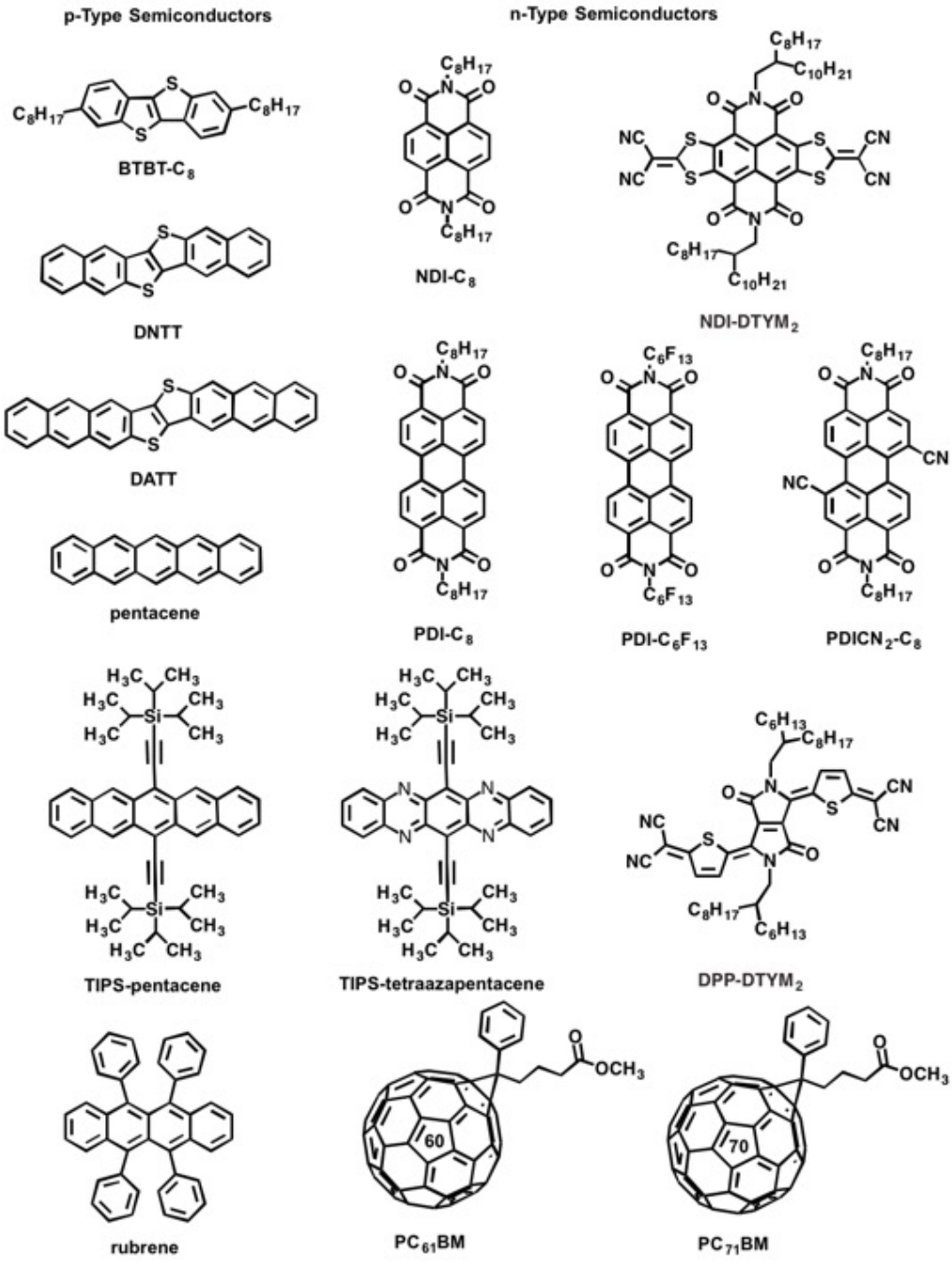

Figure 2.1. Typical p- (left column) and n-type (right two columns) organic small molecular semiconductors.[36, 38, 40]

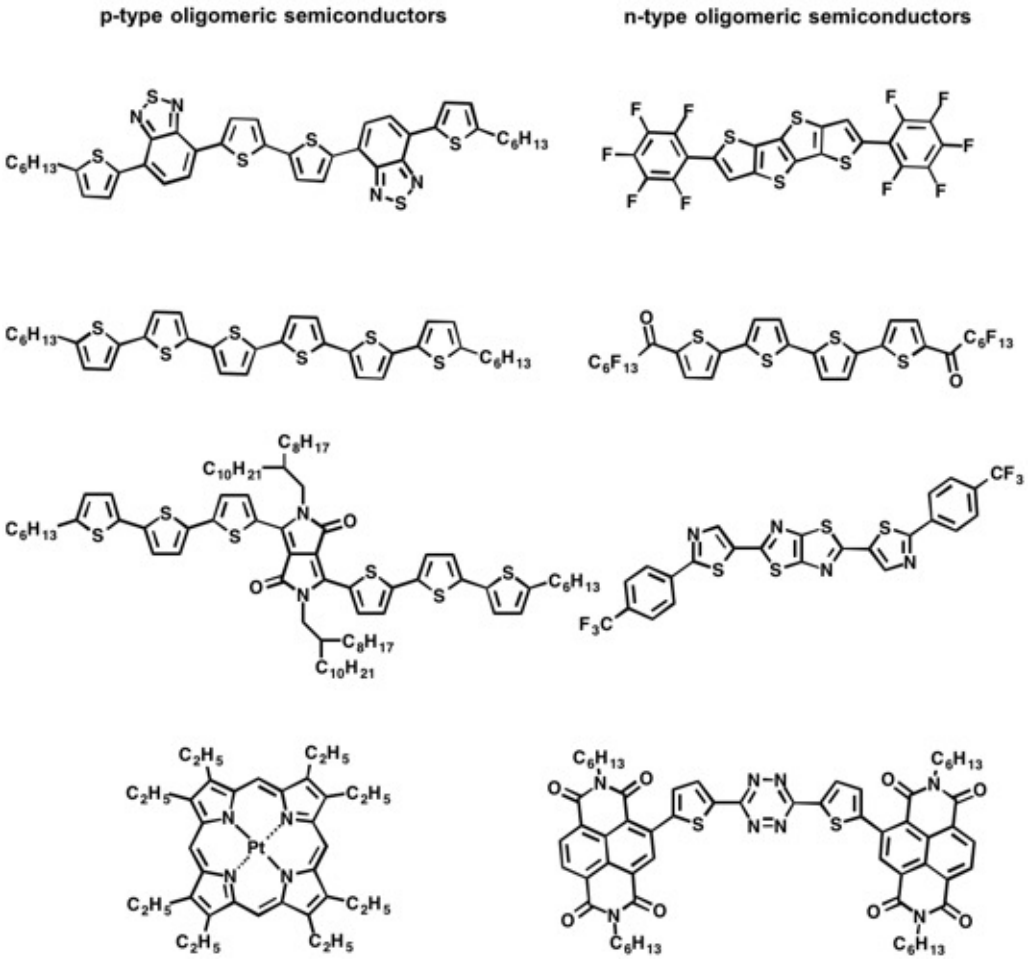

Figure 2.2. Typical p- (left column) and n-type (right column) organic oligomeric semiconductors.[41]

Thin-film small molecular and oligomeric semiconductors can be incorporated into OFET devices through either vapor deposition or solution-processing.[1a] Single crystal small molecular semiconductors, for instance, pentacene,[14b, 40o] α-hexathiophene,[41b] DATT,[40d-f, 42] BTBT,[40b] buckminsterfullerene (C_{60}),[40g, 43] and naphthalene biscarboximide (NDI) derivatives,[40j] can be fabricated into devices through vapor deposition under optimized conditions. As discussed above, single crystal semiconductor FETs typically possess charge carrier mobilities that are 1-3 orders of magnitude greater

than polycrystalline solution-processed devices.[19c, 38, 44] Solution-processing commonly induces the formation of multi-crystalline and amorphous regions within thin-films that restricts the effective charge transfer pathway. Recent discoveries, however, indicate the practicality of achieving single crystals of small molecule semiconductors through solution processing: Minemawari, et al., Diao, et al, and Li, et al. reported the development of single crystal BTBT-C8,[39] TIPS-pentacene,[45] and C60[43] thin-film p-channel and n-channel OFET devices using a solution-based process. The corresponding field-effect hole and electron mobilities were up to 16.5 $cm^2V^{-1}s^{-1}$[39] and 11 $cm^2V^{-1}s^{-1}$,[43] respectively. More interestingly, Yuan et al. recently reported thin films of mixtures of BTBT-C8 and polystyrene (PS) formed via a novel off-center spin-coating process, that possess a highly oriented, meta stable the crystalline lattices that is different from the molecular packing in single-crystals. The resultant field-effect mobility reached as high as 43 $cm^2V^{-1}s^{-1}$ (with an average of 23 $cm^2V^{-1}s^{-1}$), which is significantly higher than that based on single-crystal counterparts of the same material.[46] This result indicates the potential of exploring novel molecular arrangements to improve charge carrier transport performance.

The synthetic approaches to these organic small molecules and oligomers vary depending on their unique structure. Figure 2.14-24 list several examples for well-known semiconducting molecules. It is worthy to point out that the high degree of crystallinity

allows small molecules to reach the high charge carrier mobility, this also leads to fragile materials that lose the flexibility and stretchability that are required for flexible electronic device applications. The decrease in crystallinity of organic semiconductors by solution-processing allows for fabrication of small-molecular based flexible OFETs; the resultant mobility, however, is significantly lower than the single crystal samples.[47] The potential solution involves the blending of small molecules and isolating polymers such as PS[48] or semiconducting polymers such as poly(triarylamine) and poly(fluorine-*co*-triarylamine). There are intense studies focusing on TIPS-pentacene and TIPS-difluoroanthradithiophene (TIPS-diF-TESADT).[49] The synthetic pathway of TIPS-diF-TESADT is shown in Figure 2.14.

2.1.2. Polymeric semiconductors

The polymerization of appropriately functionalized small π-conjugated molecules provides a path to polymeric semiconductors, in which π-electrons are delocalized within a certain region of the polymeric backbone. For instance, the coupling of NDI dibromide with bistrimethyltin-bithiophene units generates the polymer, p(NDI2OD-T2)[17c]; poly(thiophene) can be considered as the extension of thiophene small molecules, as shown in Figure 2.3. The synthetic details of the polymerization are described in the synthesis section (*vide infra*). According to the building blocks incorporated into polymer

backbones, π-conjugated polymers can be categorized as homopolymers or copolymers. Homopolymers refer to polymers consisting of only one type of monomer, such as the poly(3-alkylthiophene)s[17b, 50] (P3ATs), poly(alkylthiazole)s,[51] and poly(diketopyrrolopyrrole)s.[52] On the other hand, copolymers are comprised of more than one type of monomer moiety, such as P(NDI2O2-T2) and P(DPP2T-TT-OD).[27a, 53] A polymer composed of both electron rich (donor) and electron deficient (acceptor) monomers is referred to as a donor-acceptor (D-A) copolymer. For example, the D-A copolymer poly(benzothiadiazole-sexithiophene) (PBT6)[33] has both electron donating (D) sexithiophene and electron deficient (A) benzothiadiazole units; and the D-A polymer, P(NDI2OD-T2), contains bithiophene as a donor with NDI moieties as acceptor. The classifications of π-semiconducting polymers together with several examples are shown in Figure 2.4.

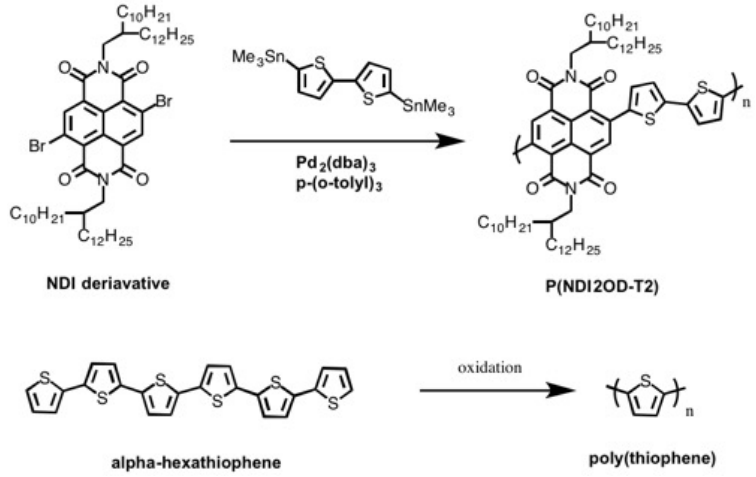

Figure 2.3. The extension of organic small molecules and oligomers to polymers.

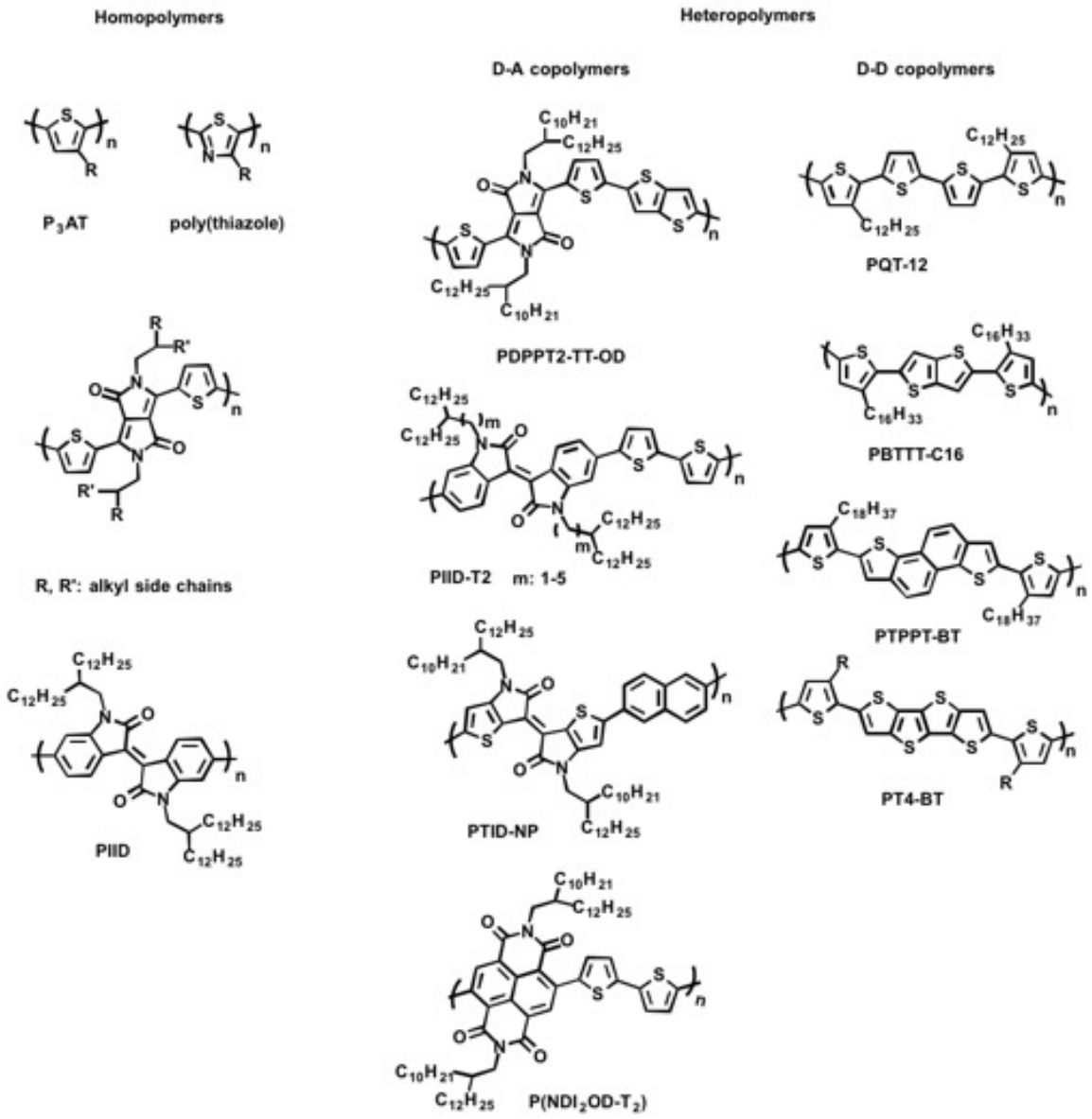

Figure 2.4. Examples of π-conjugated homopolymers, D-A copolymers, and D-D copolymers. [11a, 16c, 17b, 27d, 50-52, 54]

In light of electron push/pull properties and HOMO/LUMO energy levels of donors and acceptors, the resultant polymers can display hole transport or n-channel, electron transport behavior. That is, D-A copolymers consisting of strong donors with weak acceptors are more likely to display hole transport characteristics, with weak or even no

electron transport behavior. Examples of such D-A copolymers include PBT6,[33] poly(bithiophene-*co*-thiazolothiazole),[55] and n-alkylthieno[3,4-c]pyrrole-4,6-dione (TPD) benzodithiophene or bithiophene based polymers (pTPDBDT, pTPDBT),[56] as shown in Figure 2.5. D-A copolymers consisting of strong acceptor and weak donor units are more likely to be effective electron transport materials, with weak or no hole transport properties. For instance, P(NDI2OD-T2),[57] benzodifurandione based poly(p-phenylene vinylene) (BDPPV),[28c] fluorine substituted BDPPV, [28d] and poly(tetraazabenzodifluoranthene diimide *oligo*thiophenes)s (PBFI-T and PBFI-BT), [28e, 58]are representatives of this class of polymer semiconductor, as shown in Figure 2.5. Hence, the modulation of donors and acceptors allows polymers to exhibit both hole and electron transport characteristics, a property termed ambipolarity. For example, poly(benzobisthiazole-*co*-diketopyrrolopyrrole), [59] poly(bisbenzothiadiazole-*co*-diketo-pyrrolopyrrole),[52a] poly(thieno-[3,2-*b*]thiophene-diketopyrrolopyrrole),[27a] and poly-(NDI-cyclopentadithiophene),[60] are considered ambipolar (Figure 2.5). Polymeric materials showing hole, electron, and ambipolarity are classified as p-channel, n-channel, and ambipolar polymeric semiconductors, respectively.

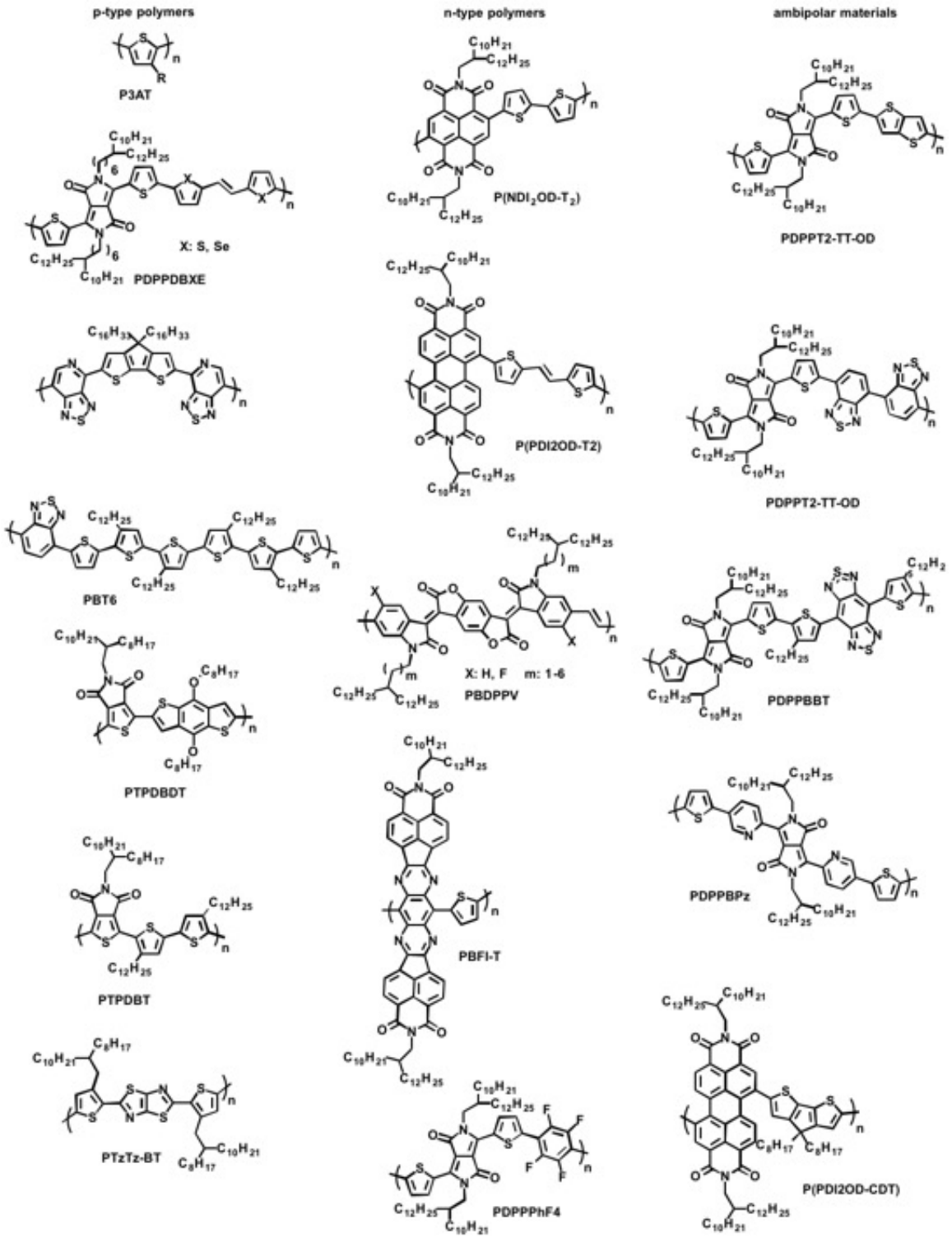

Figure 2.5. Examples of p-type, n-type, and ambipolar polymeric semiconductors.[27c, 29a, 61]

Unlike their small molecule or oligomeric counterparts, polymers with high MWs cannot not be deposited by vacuum deposition. Thin-films are typically cast onto device substrates through solution processing, during which a given polymer is first dissolved in a solvent to afford the polymer solution; a subsequent casting or printing step is then used to apply the semiconductor onto the device substrate.[2a, 62] Solvent evaporation effects polymer thin-film formation. Therefore, the semiconductor film morphology and electronic performance significantly depend on the solution processing.[63] The solubility of π-conjugated polymer depends on both the structure of the polymer backbone and side chains incorporated into the structure.[2, 16a]

Linear and branched alkyl groups have been widely incorporated into π-conjugated polymers with the aim of improving polymer solubility in common organic solvents such as chloroform and chlorobenzene (solvent selection is systematically discussed on Session 2.4.7).[64] Since conjugated polymers are generally insoluble in aqueous solutions, to minimize the number of electronic traps, no ionic functional groups are generally introduced into either aromatic cores or side chains.[3a] Typically, increasing the density of side chains will leads to increased solubility. For instance, un-substituted polythiophene accessed through electrochemical oxidation of thiophene is insoluble in organic solvents; while P3ATs, which have alkyl side chains, show good solubility in many common solvents.[17b, 65] Similarly, in the case of pentacene compared with TIPS-

pentacene, the unsubstituted parent is insoluble, while the triisopropylsilylethynyl (TIPS) side chains impart solubility to the substituted analog.[14b, 37a] The incorporation of side chains, however, might induce steric hindrance within the polymer backbone, resulting in a reduction of π-conjugation along in the polymer backbone and thus lowered charge carrier transport properties.[66] For instance, within one repeating unit of PQT-12, there are two unsubstituted thiophene units and thus steric hindrance is reduced compared with the alkyl moieties in the P3ATs, as shown in Figure 2.4. As a result, PQT-12 is less soluble than its P3AT counterpart, but exhibits relatively higher hole mobility.[67]

A certain degree of solubility is necessary to achieve high MW materials, and to obtain uniform thin films with no macro scale defects. For example, the relative solubility of P3ATs follows the sequence, poly(3-dodecylthiophene) (P3DDT) > poly(3-decylthiophene) (P3DT) > poly(3-octylthiophene) (P3OT) > poly(3-hexylthiophene) (P3HT) > poly(3-butylthiophene) (P3BT).[17b] Due to its low solubility, P3BT is difficult to synthesize with high MW, typically having a much lower MW (<7 $kg.mol^{-1}$) compared with the other P3ATs (20 – 60 $kg.mol^{-1}$). As a result, the field-effect mobility of P3BT is approximately one order of magnitude lower than that of its longer side-chain analogs.[17b] However, above a certain solubility threshold, further increases in solubility do not necessarily facilitate enhanced mobility. P3HT typically exhibits a mobility

similar to, or greater than, P3OT, P3DT, and P3DDT even though there is a positive correlation between side chain length and polymer solubility.[68]

In addition, π-conjugated polymers having branched side chains, such as 2-hexyldecyl,[69] 2-octyldodecyl,[70] and 2-decyltetradecyl,[57] often provide better solubilities compared with linear chain alternatives. These branched side chains have been widely applied into π-conjugated oligomers and polymers via coupling into a variety of moieties such as dithienobenzothiadiazole,[71] benzotriazole,[72] diketopyrrolopyrrole,[73] isoindigo,[74] thienoisoindigo,[75] as well as NDI [17c, 61d, 76] and PDI[57, 61g] (Figure 2.6). However, the branching points within these 2-hexyldecyl, 2-octyldodecyl, and 2-decyltetradecyl groups is close to polymer backbone, which induces steric hindrance between adjacent side chains and thus can negatively affect the efficient inter chain charge carrier transport.[31f, 34, 77] Therefore, movement of the branch point away from polymer backbone is highly desirable to benefit both polymer solubility and effective inter-chain interactions. The linear alkyl groups from methylene to hexylene have been used as the spacer between branching points and the polymer backbone. The details associated with branch position are discussed in Chapter 3. Very recently, several systematic studies relating to the effect of spacer (alkyl) length on charge carrier transport have been reported.[31b, e, f, 34, 64, 78]

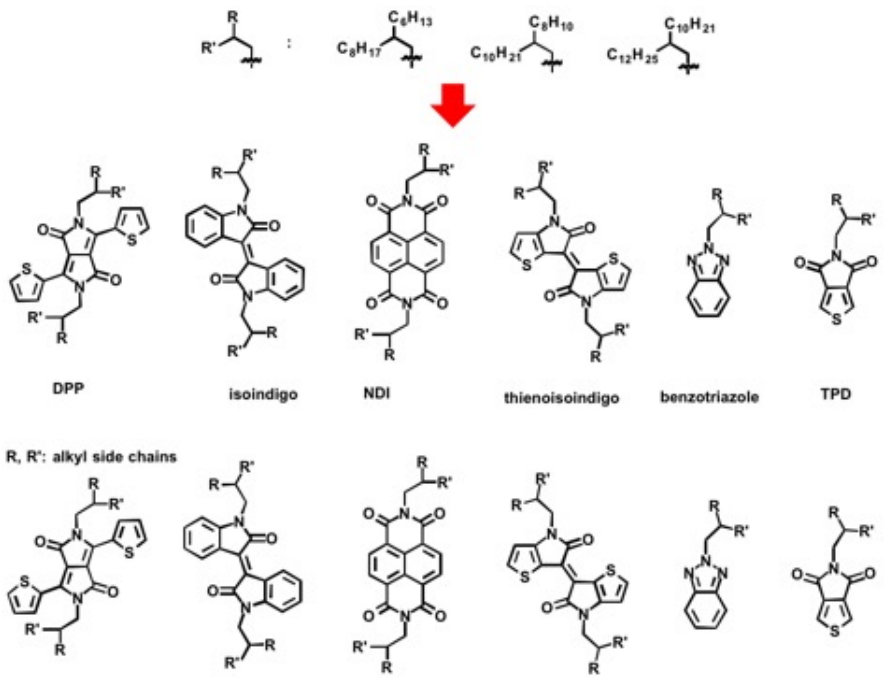

Figure 2.6. The incorporation of branched side chains into heterogeneous aromatic fused units.

Besides modulating the solubility, modification of side chain structures may also able be used to tune the electronic and optoelectronic characteristics of organic and polymeric semiconductors. Fluorinated alkyl side chains and carbonyl substituted side chains having high electron deficiency have been employed in order to lower molecular frontier orbitals and control the bandgap.[40j, k] The studies on polymer PTB7 indicated a 0.1 eV decrease in HOMO/LUMO energy levels and an average 1.5% enhancement in power conversion efficiency of OPVs through replacement of carboxyl side chains by ketone substituted side chains having higher electron deficiency.[14d] These substitutions, however, might induce steric hindrance along the backbone resulting in a reduction in charge transfer mobility. The mobility (or charge transfer rate) is of significance in OFET applications;

while the current density (rather than charge carrier mobility) is important for OPV applications. Hence, an organic or polymeric semiconductor showing good performance in OFET devices will not necessarily be suitable for OPV technologies. Structure-property relationships will be specific to a given application and must be effectively utilized in the molecular design.

In principal, polymers having backbones with a lower degree of cinformational flexibility exhibit lower solubility. The incorporation of fused units into the polymer backbone, e.g., the incorporation of fused thieno[3,2-*b*]thiophene,[79] thiazolothiazole,[80] benzothiadiazole,[81] diketopyrrolopyrrole,[82] and isoindigo [83] moieties provide polymers with improved charge carrier mobility, but at the expense of solubility. Additionally, the incorporation of atoms with high atomic number, and electron deficient functional groups commonly limit polymer solubility.[84] For instance, the replacement of sulfur within PTB7 by selenium lowered polymer solubility and the photovoltaic performance.[84] CN-PPV having cyano- substituents exhibits a relatively lower solubility compared with PPV.[32a] These phenomena might be explained by the "like dissolves like" rule that polymers having atoms with high atomic number or electron deficient groups would more likely to interact with themselves rather than with solvents. On the other hand, it is possible to tune the solvation of solvents towards polymers: poly(pyrazine) with fluorinated alkyl side chains shows poor solubility in chloroform or

hexane, but excellent solubility in fluorinated solvents, such as perfluorooctane, perfluoro(methylcyclohexane), and perfluorodecalin.[85]

The solvents used in π-conjugated polymer inks have great impact on final microstructure of solution-processed polymer films and thereby charge carrier transport performance. Halogenated solvents, such as chloroform, chlorobenzene (CB), *o*-dichlorobenzene (DCB), and trichlorobenzene (TCB), have been widely used in developing π-conjugated polymer inks for solution-processed OFETs and OPVs, due to their superior solvation to π-conjugated polymers; the resulting good polymer solubility facilitates the formation of dense, continuous films and thus avoids macro-scale thin-film structural defects preventing efficient charge carrier transport. Compared with chloroform, aromatic halogenated solvents including CB, DCB, and TCB, which have relatively high boiling points benefit polymer chain self-assembly to enhance the morphology within polymer films.[86] These halogenated solvents, however, have high toxicity to the environment and health.[30a, 87] Hence, the use of non-halogenated solvents is highly desirable. However, studies related to solution-processed organic electronic devices based on non-halogenated solvents are very limited.[17c, 88] In Chapter 5, a solution-process of fabricating n-channel OFETs based on non-halogenated xylenes and tetralin, as well as the effect of solvents on the thin-film morphology and charge carrier transport behavior of polymeric semiconductors, will be discussed.

In general, solutions of polymers exhibit better rheology and wettability in comparison to solutions of small molecules.[16c] This facilitates coating polymeric thin-films through a variety of approaches, including spin-coating,[89] blade-coating,[90] slot-die coating,[91] gravure printing,[17c] roll-to-roll printing,[92] flow-coating,[93] as well as inkjet printing.[94] Except for spin-coating, these casting approaches allow the formation of anisotropic orientation or texture within polymeric thin films, and thus lead to the anisotropic charge carrier mobility.[91b] For example, thin-films of poly(trithieno-diketopyrrolopyrrole) formed by blade-coating shows a 20-fold enhancement in field-effect mobility in the direction of alignment compared to the orthogonal direction.[95] PCDTPT (Figure 2.7) exhibited a one order of magnitude enhancement in field-effect hole mobility along the alignment direction compared with the mobility in a spin-coated isotropic PCDTPT film.[27c] Similar behavior was shown in polymer CP1 (Figure 2.7).[31d] Treatments such as thermal annealing and solvent annealing enhance thin-film molecular ordering for many polymeric semiconductors. These two approaches, however, have not shown obvious effects on thin film anisotropic orientation.

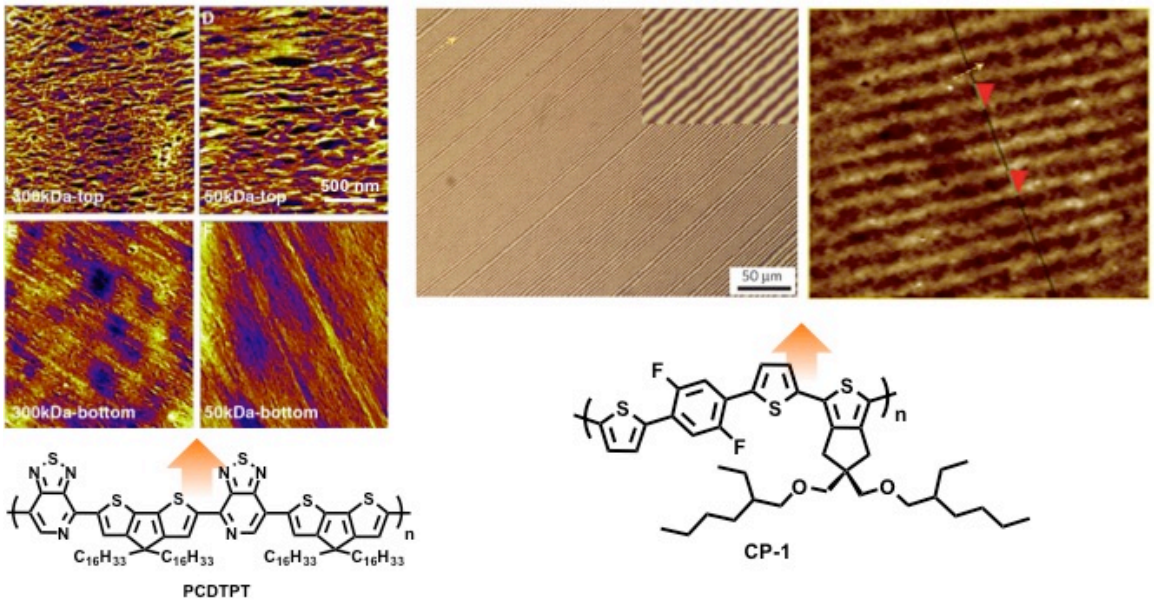

Figure 2.7. Thin film alignments of PCDTPT (in a scale of 500 nm) and CP-1 (in a scale of 50 μm). The figures are reproduced from literatures of Tseng et al.[27c] and Kim et al.[31d].

The MW has a significant impact on the optical, electronic, and mechanic performance of π-conjugated polymers. For instance, with the increase in MW, P3HT thin-films change from a highly multi-crystalline and defective morphology having large domain boundaries (MW < 3 kDa) to more homogeneous-like and uniform characteristics (MW > 18 kDa).[63a, 96] A red-shift in the UV/vis absorption spectra was also established for the increase in MW, demonstrating an enhancement of intra- and inter-molecular interactions within thin-films.[97] Chang et al. proposed that P3HT chain ends induce defects in the nano-scaled domains of thin-films preventing effective charge carrier hopping. The increase in MW of polymer chains reduces the population of chain ends leading to the decrease in defects, and thus enhanced charge carrier mobility. [98] Noriega et al. recently reported that high MW benefits polymeric semiconductors against the disorder within

aggregates to allow more efficient intra- and inter-molecular charge carrier transport through a systematic investigation of 13 π-conjugated polymers.[99] In many cases, there is positive correlation between polymer semiconductor MW and charge carrier mobility and power conversion efficiency for OFETs and OPVs, respectively.[100] One recent example is PCDTPT, which shows a 2-3 fold increase in field-effect mobility as the MW of the polymer was increased from 30 kDa to 300 kDa. In this case, PCDTPT thin-films were spin-cast onto FET device substrates. However, within highly aligned PCDTPT thin-films fabricated via a flow coating approach, the effect of MW is largely eliminated, suggesting that polymer chain alignment might be able to offset defects and disorder originating from low MW materials.[27c]

2.2. Charge Carrier Transport Mechanism and Molecular Design

The charge carrier transport within organic and polymeric semiconductors follows two regimes: i) hopping transport between localized states and ii) band-like transport in delocalized states.[3, 18b]

Within disordered organic and polymeric semiconductors, charge carrier transport is generally described by thermally activated hopping of charges through a distribution of localized states or shallow traps.[3a] That is, the charge transfer characteristics can be described by a self-exchange electron-transfer reaction: a charge carrier is carried from a

charged, relaxed molecule or unit to an adjacent neutral molecule or unit.[19c, 101] This charge carrier distribution is based on van der Waals interactions.[102] A molecule or unit within an oligomer or polymer charged by one hole or electron is termed a polaron (cation or anion, in chemistry terminology).[19a, 23] In comparison to the neutral species with an aromatic configuration, polarons convert to a quinoid configuration, during which polaronic states are formed between the HOMO and LUMO of neutral species leading to a narrowed bandgap, as shown in Figure 1.5. The geometric relaxation between the aromatic and quinoid configurations results in a reorganization energy (λ) during electron transfer.[103] According to the IUPAC gold book, reorganization energy is defined as the Gibbs energy dissipated when a system that has undergone 'vertical' electron transfer (electron transfer obeying the Franck–Condon principle) relaxes to the equilibrium state for its new charge distribution.[104] It describes the hole-vibration or electron-vibration interactions. This hopping transport model hence has strong electron-phonon coupling. The self-exchange electron transfer (hopping) rate (κ_{ET}) is commonly described by semi-classical high-temperature Marcus theory:[19b, 32b, 101]

$$\kappa_{\mathrm{ET}} = A \exp\left(-\frac{\lambda_E}{4k_B T}\right) \qquad \text{Eq. 2.1}$$

where k_B is the Boltzmann constant (8.617 x10^{-5} eV K^{-1}). The pre-factor A depends on the strength of electronic coupling (J). In the case of weak coupling as in non-adiabatic conditions, A is described as $\frac{4\pi^2}{h}\frac{1}{\sqrt{4\pi k_B}}t^2$. The parameter t denotes the transfer integral,

which describes the possibility of intermolecular overlaps of electronic orbitals, or rather, the strength of electronic coupling between neighboring sites. The factor of h is Planck's constant (4.136×10^{-15} eV.s). The corresponding κ_{ET} is expressed as:

$$\kappa_{ET} = \frac{4\pi^2}{h}\frac{1}{\sqrt{4\pi k_B}}t^2\exp\left(-\frac{\lambda_E}{4k_BT}\right) \qquad \text{Eq. 2.2}$$

Unlike the strong atomic bonding within inorganic semiconductors, the *van der Waals* bonding between molecules or units, formed by the intra- (within oligomers and polymers) and inter-molecular overlap of electronic orbitals, provides a weak electronic bandwidth (W_B) at *ca*. 0.1 eV that is two orders of magnitude less than that for silicon. Thus organic materials exhibit relatively low charge carrier mobility.[19c] The bandwidth depends on the strength of electronic coupling described by the transfer integral.[101, 103a] The larger the transfer integral, the greater the bandwidth for electronic coupling between neighboring molecules or units. As depicted in Marcus theory (Eq. 2.2), an increase in temperature allows the charge carrier hopping against the activation energy (reorganization energy, λ_E).[19a, 20b] In OFET devices, the increase in gate voltage might induce more charge carriers to fill existing shallow and deep traps. The additional charges hence require a lower activation energy to hop between molecules or units. The details are described in the Section 2.3.

For organic semiconductors having a highly crystalline microstructure, the charge carrier transport within the crystal lattice follows that of band-like transport between

delocalized states, at a temperature close to or below zero Celsius degree.[3a, 19c, 32b] Organic semiconductors with extensive π-conjugation, such as pentacene, have a transfer integral comparable to, or greater than, the reorganization energy, implying that charge delocalization is possible. Bao and Locklin stated that the activationless (band-like) transport dominates as $2t > \lambda_E$, while the hopping characteristic (localized transport) takes place in the case of $2t < \lambda_E$ derived from Marcus theory.[19c] The reorganization energy and transfer integral correlate to the molecular polarization time (τ_v) and carrier residence time (τ_{res}), respectively. Band-like transport may occur at $\tau_v > \tau_{res}$, and the hopping behavior takes over as $\tau_v < \tau_{res}$.[101] The carrier residence time τ_{res} can be described by:

$$\tau_{res} = \frac{h}{W_B} \approx \frac{2}{3}\frac{10^{-15}}{W_B(eV)} \qquad \text{Eq. 2.3}$$

where W_B refers to the full effective bandwidth. In general, W_B should be on the order of ca. 100 - 200 meV in order to keep $\tau_{res} < \tau_v$. In a tight-binding approximation, $W_B = 4t$ in a one-dimensional infinite stack.[103a]

The charge carrier mobility based on band-like transport is much greater than that based on hopping transport. Experiments indicated that for one material, such as pentacene,[45] rubrene,[36, 105] and BTBT-C8,[39] a single-crystal film can exhibit a mobility (10-30 $cm^2V^{-1}s^{-1}$ in OFET device architectures) that is one to two orders of magnitude higher than that observed in semi-crystalline and amorphous films.[106] Similar trends in mobilities were observed from temperature-dependent time-of-flight and pulse-radiolysis

time-resolved microwave conductivity (PR-TRMC) as well.[3a, 19c, 32b, 101, 107] Calculations for rubrene based on density functional theory (DFT) indicated that the theoretical maximal mobility could be above 100 $cm^2V^{-1}s^{-1}$ at 200K.[3a, 19c, 32b]

With the increase in temperature, however, the weak *van der Waals* bonding within the crystal lattice is easily modulated leading to the reduction of W_B and thus a decrease in the charge carrier mobility.[3a, 20b] Along with this phonon-scattering process, the charge carrier transport behavior turns from band-like transport (electronic coupling) to hopping transport (electron-phonon coupling). Typically, both transport regimes exist within polymeric semiconductor films due to the semi-crystalline feature associated with π-conjugated polymers.[101]

The charge carrier transport mechanism unveiled the significance of the transfer integral and reorganization energy. The transfer integral has a positive correlation with charge carrier mobility in both hopping and band-like regimes; while the reorganization energy has a negative correlation to charge carrier transport in the hopping model (reorganization energy is negligible in the band-like model).[40e, 103b] Thus, a molecular design aimed towards an increase in transfer integral together with decreased reorganization energy is desired.

As a factor of indicating the possibility of electron tunneling between two adjacent molecules or sites, the transfer integral is exponential to the π-π stacking distance

between two species, that is, $t \sim \exp(-d)$, or $t^2 \sim \exp(-2d)$, where d refers to the π-π stacking distance, generally 3.4 – 4 Å in organic and polymeric semiconductors.[101] Thereby a small reduction in π-π stacking distance leads to significant improvement in charge carrier mobility. For instance, the decrease of 0.1 Å might lead to a 23 % of enhancement in mobility (μ) given the relationship $\mu \sim t^2 \sim \exp(-2d)$. Additionally, the transfer integral is sensitive to the orientation and torsion between two adjacent molecules or units, since these two factors influence the overlap of the π systems. Feng et al. reported the transfer integral for discotic liquid crystal materials decreases to half its original value for a system oriented co-facially (0° twist) to one having only 10° of torsion.[103b] Therefore, a rigid, locked molecular configuration for organic semiconductors is beneficial for charge carrier transport performance.

Reorganization energy relates to the hole-vibration and electron-vibration interactions, and decreases with the increase in π-conjugation of organic semiconductors.[19c, 103] That is to say, the more π-electronic delocalization, the less reorganization energy, and thus the higher the charge carrier mobility. For instance, DFT calculations for polyacenes indicated that reorganization energy monotonically decreases while the transfer integral monotonically increases for the progression from naphthalene to pentacene.[19c] The same trend was observed in discotic crystals as well.[103b] For organic semiconductors, π-electronic delocalization correlates with the molecular geometry, that is, an increase in π-

electrons comes along with an expansion in molecular geometry. An enlarged conjugated molecular system leads to a relatively small geometric relaxation and thus a reduced reorganization energy.

As a result of the above effects, having a molecular design that affords enhancement of the π-conjugation length and narrowing of the π-π stacking distance is desirable. From a molecular engineering point of view, the planarization of aromatic cores or polymeric backbones in organic and polymeric semiconductors via the incorporation of fused aromatic units, such as diketopyrrolopyrrole, benzothiadiazole, isoindigo, and naphthalene dicarboxyimide into organic and polymeric systems and the reduction of steric hindrance associated with the aromatic cores or polymeric backbones are will be beneficial to enhancing π-conjugation. Besides the molecular structure, post-deposition processing of semiconductor thin-films might also be able to narrow the π-π stacking distance. The details will be discussed in the sections on molecular design, synthesis and materials processing.

2.3. Synthesis of Organic & Polymeric Semiconductors

Synthetic strategies for homopolymers such as head-to-tail regioregular poly(3-alkylthiophene) were based on Kumada cross-coupling with $Ni(dppp)Cl_2$ or $Pd(PPh_3)_4$ catalysts.[14c, 17b, 50b, 108] To increase the head-to-tail regioregularity, Grignard

metathesis[14c, 108] and Rieke zinc catalyzed polymerizations[17b] were employed as shown in Figure 2.8. Thiophene based homogeneous π-conjugated polymers have been synthesized by oxidative polymerization approaches as well. These reactions are driven by $FeCl_3$ as the oxidant, or by electrochemical oxidation processes.[109]

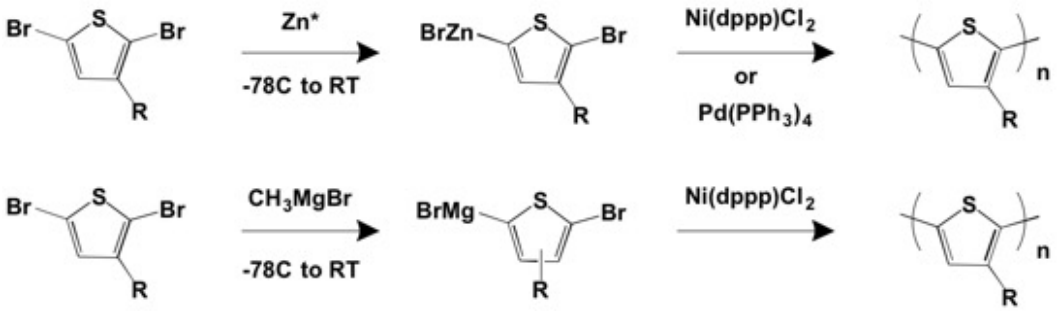

Figure 2.8. Synthetic procedures for poly(alkylthiophene)s[14c, 17b]

Copolymers such as D-A copolymers are accessible through Stille (Figure 2.9),[110] Suzuki (Figure 2.10),[111] and Sonogashira coupling reactions[112] (Figure 2.11) using Pd based catalysts, including commercial tetrakis(triphenylphosphine)palladium(0) ($Pd(PPh_3)_4$), palladium(II) acetate ($Pd(OAc)_2$), bis(triphenylphosphine)palladium(II) dichloride ($Pd(PPh_3)_2Cl_2$), and tris(dibenzylideneacetone)dipalladium(0) ($Pd_2(dba)_3$). Negishi[113] and Heck coupling[114] reactions have not been generally applied in the preparation of π-conjugated polymers, due to their synthetic challenges and random conformational defects that appear along the polymer backbone. Contrary to the chain growth polymerization based synthetic approach that affords P3ATs, the Pd-based

coupling reactions leading to the formation of heterogeneous D-A copolymers are step growth polycondensation reactions.[62]

The optoelectronic performance, e.g. the field-effect mobilities and photovoltaic conversion rate of semiconducting polymer based FETs and OPVs directly correlates to the molecular weight (MW) of the polymer.[55, 100e] To increase MW, the purity of the monomers used in these step-growth polymerizations should be as high as possible (>99%).[16a] However, there are challenges associated with the purification of the trialkylstannyl and boron-functionalized monomers, due to their instability in the ambient environment or to the inherent acidic conditions associated with silica gel chromatography.[33, 115] Hence, copolymerization approaches that do not require trialkylstannyl and boron ester functionalized monomers are highly desirable. Recently, direct hetero-arylation polymerizations have been investigated.[116] Few examples are shown in Figure 2.12, in which the relevant C-H and C-Br bonds were directly coupled with the aid of Pd-catalysts.[117] Monomers having C-H bonds, in general, have higher purity compared with the trialkylstannyl-substituted counterparts. Thus, the polymer prepared by direct hetero-arylation is expected to have a higher MW.[118] The present challenge for hetero-arylation lies in the low selectivity for reaction of C-Br with monomers that have different types of C-H bond (e.g. α-C-H and β-C-H bonds). This random polymerization provides irregular polymeric structures and thereby reduces the

charge carrier transport mobility and photovoltaic performance.[119] The development of catalysts with high selectivity for direct hetero-arylation is desired.

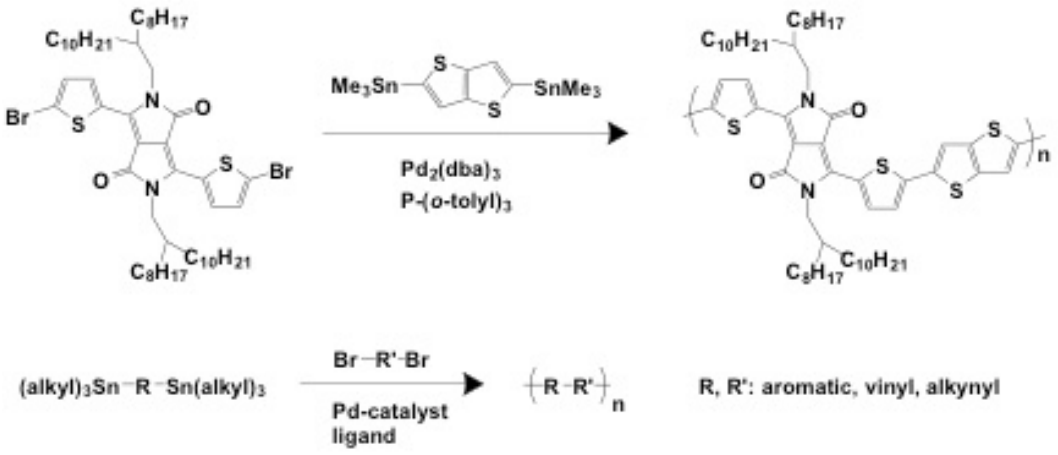

Figure 2.9. General procedure for the preparation of π-conjugated polymers via a Stille coupling approach[27a]

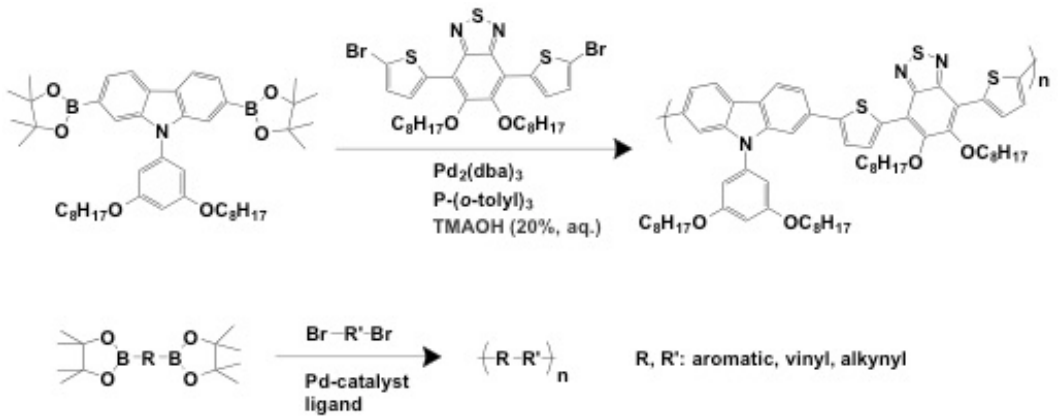

Figure 2.10. General procedure for the preparation of π-conjugated polymers using Suzuki coupling[120]

It is difficult to control the batch-to-batch variations in MW and polydispersity of polymers prepared using a step growth polymerization mechanism. These parameters however, as discussed above, are critical achieving high performance polymeric

semiconductors. Recently, it has been shown that it is feasible to synthesize D-A copolymers via chain growth polymerization approaches. For instance, Senkovskyy et al. demonstrated a Ni-catalyzed chain-growth polymerization leading to poly(NDI2OD-T2) with controlled molecular weight, relatively narrow polydispersity, and specific end-functionality,[121] as shown in Figure 2.12. The reaction was conducted at room temperature over a period of time that was less than 24 hours; and no toxic tin substituents were involved. Schmidt et al. reported that poly(NDI2OD-T2) synthesized by Ni-catalyzed chain-growth polymerization showed similar electron mobility to the same polymer prepared using step growth polycondensation when the materials were processed into roll-to-roll (R2R) inkjet printed OFETs.[122]

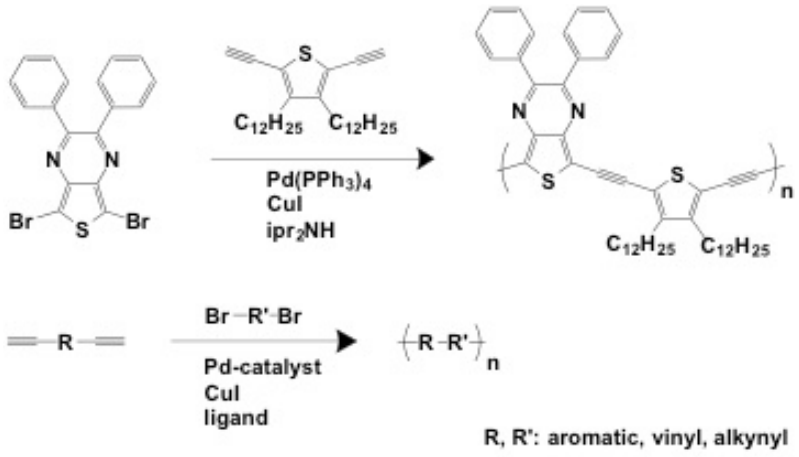

Figure 2.11. General procedure for the preparation of π-conjugated polymers through Sogonashira coupling.[123]

The Pd- and Ni-catalyzed reactions for the synthesis of π-conjugated polymers are conducted in solution, where all monomers, catalysts, and chelates are dissolved with

common organic solvents such as chlorobenzene (CB), chloroform, toluene and xylenes. Alternatively, oxidative chemical vapor deposition (oCVD) was recently introduced by Gleason et al., in which the conducting material, poly(3,4-ethylenedioxythiophene), was synthesized without the need for solvents.[124] This approach requires that the monomer have a low vapor pressure so that it is evaporated easily. The evaporated gas phase monomers were deposited onto substrates inside the CVD chamber at low temperature, in which oxidative polymerization proceeds by $FeCl_3$ catalysis to afford a thin film of poly(3,4-ethylenedioxythiophene).[125]

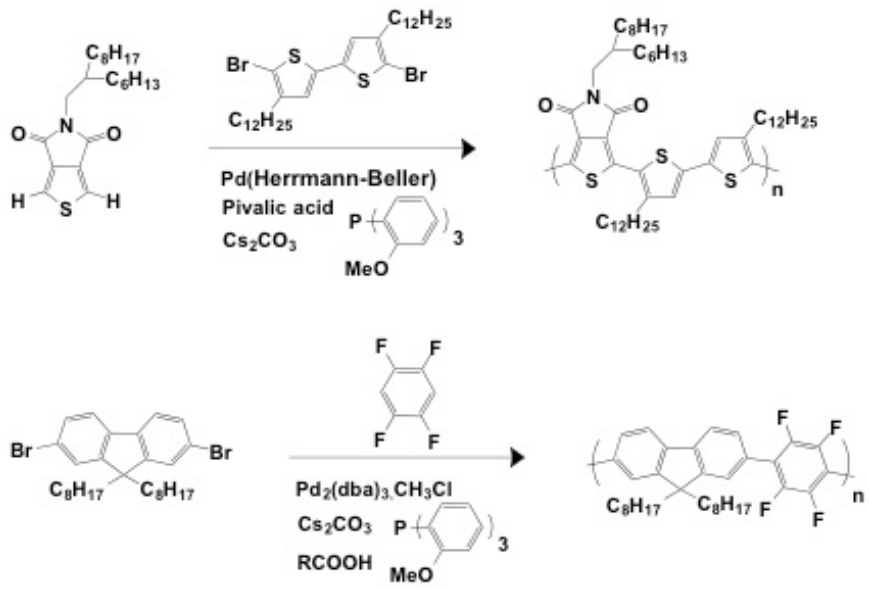

Figure 2.12. Examples of direct hetero-arylation copolymerizations.[116, 117b]

Whether a given D-A copolymer will exhibit electron or hole transport characteristics depends upon the electron deficiency of the individual units. In principal, electron donors consist of electron rich functional groups, such as thiophene, phenyl, oligothiophenes,

fused thiophenes, fused phenyls, vinylene, acetylene, silole, pyrrol, and germole moieties, etc.. Synthetic approaches to the monomers vary. Figures 2.14-2.16 exhibit the strategies that have been used to access some common electron donors (acenes in Figure 2.14, thienoacenes in Figure 2.15 and 2.16). The synthetic pathways to BTBT-C8, DNTT, DNTTT, and TIPS-ADT are shown in Figure 2.14 as well. In contrast, electron acceptors consist of electron-withdrawing functional groups or atoms, such as nitrile (or cyano-, -CN), imine (-C=N-), carbonyl (-C=O), and fluorine (-F), all of which possess relatively high electronegativity. Typical acceptor moieties include naphthalenedicarboximide (NDI), perylenedicarboximide (PDI), benzothiadiazole (BT), difluorobenzothiadiazole (DFBT), pyridal[2,1,3]thiadiazole (PT), benzobisthiazole (BBT), diketopyrrolopyrrole (DPP), isoindigo, fluorineinsoindigo, thienoisoindigo, thienopyrrolodione (TPD), BODIPY, bithiazole, and thiazolothiazole (TzTz). Synthetic strategies to obtain these compounds are shown in Figure 2.18-2.19 Examples of coupling the above electron donors and acceptors to afford p-type, n-type, and ambipolar polymeric semiconductors are shown in Figure 2.20, 2.21, and 2.22, respectively. Figure 2.23 shows synthetic approaches for typical small molecule n-channel materials based on the electron acceptors described above.

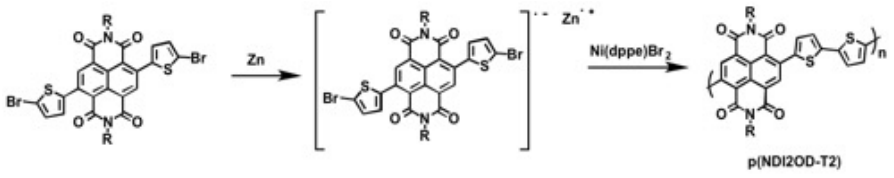

Figure 2.13. Ni-catalyzed chain-growth polymerization leading to poly(NDI2OD-T2)

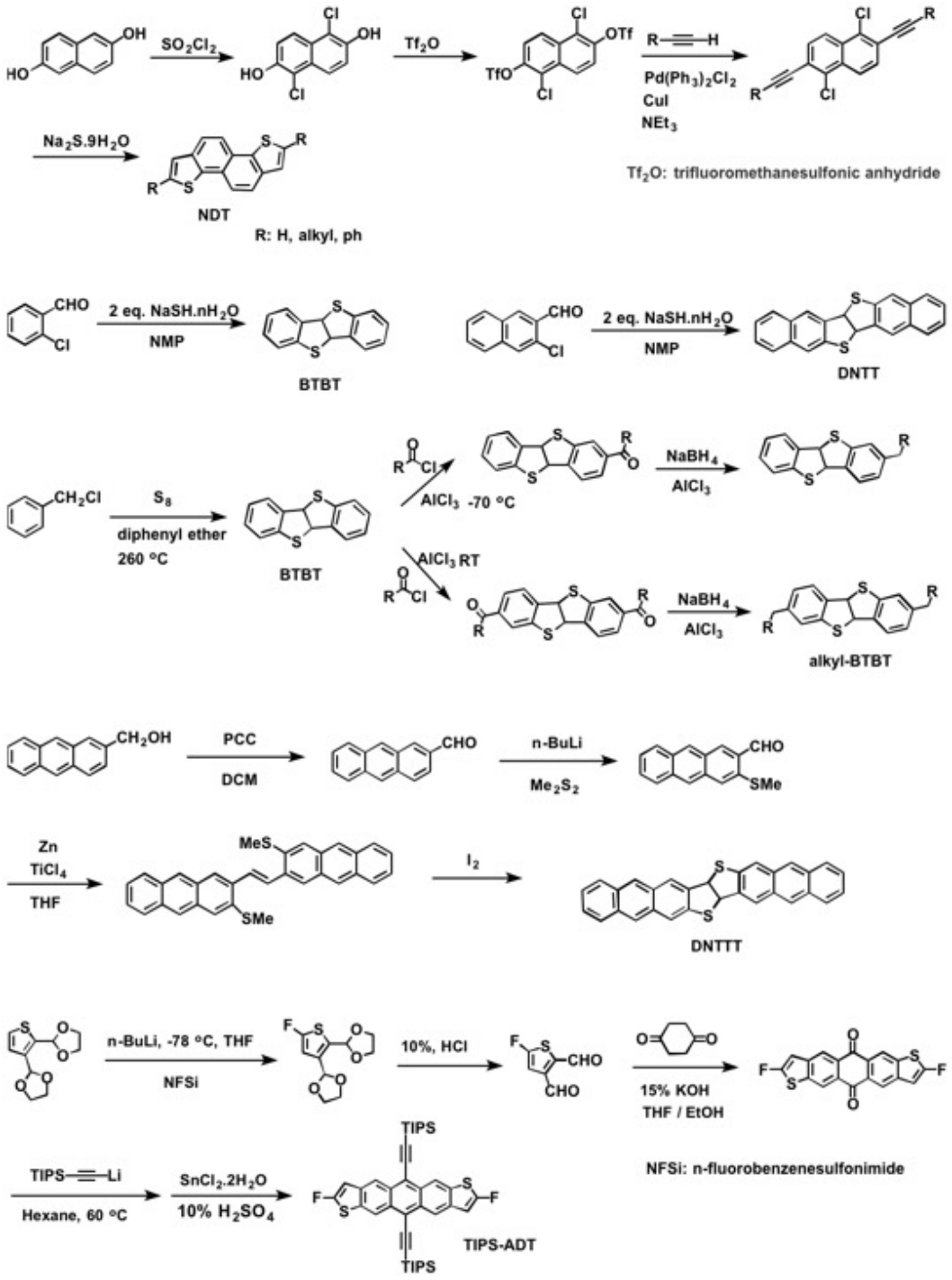

Figure 2.14. Synthetic approaches leading to electron donating acene small molecules.[40a, c, e, f, 126]

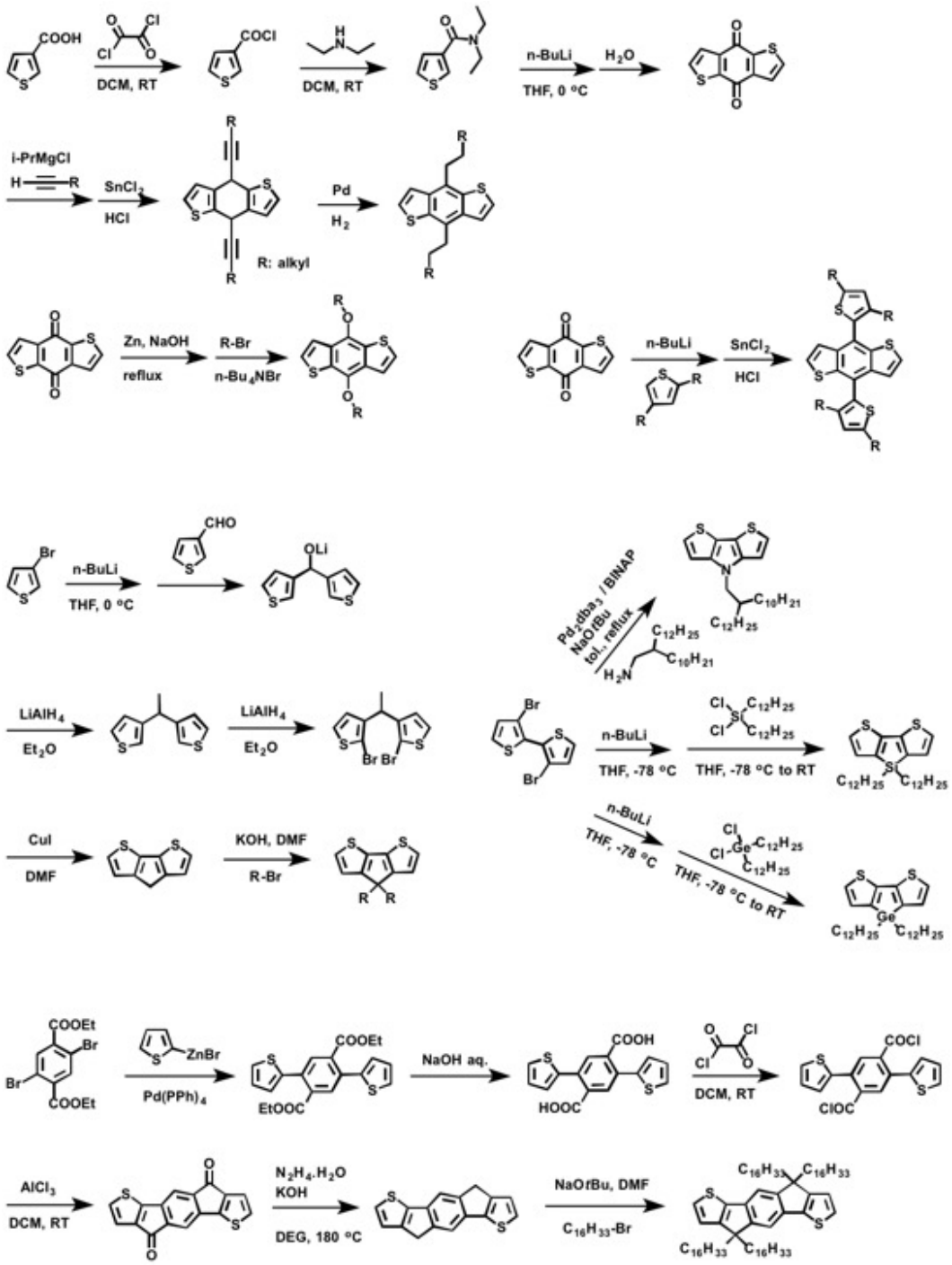

Figure 2.15. Synthetic approaches for the preparation of electron donating thienoacenes.[100a, 127]

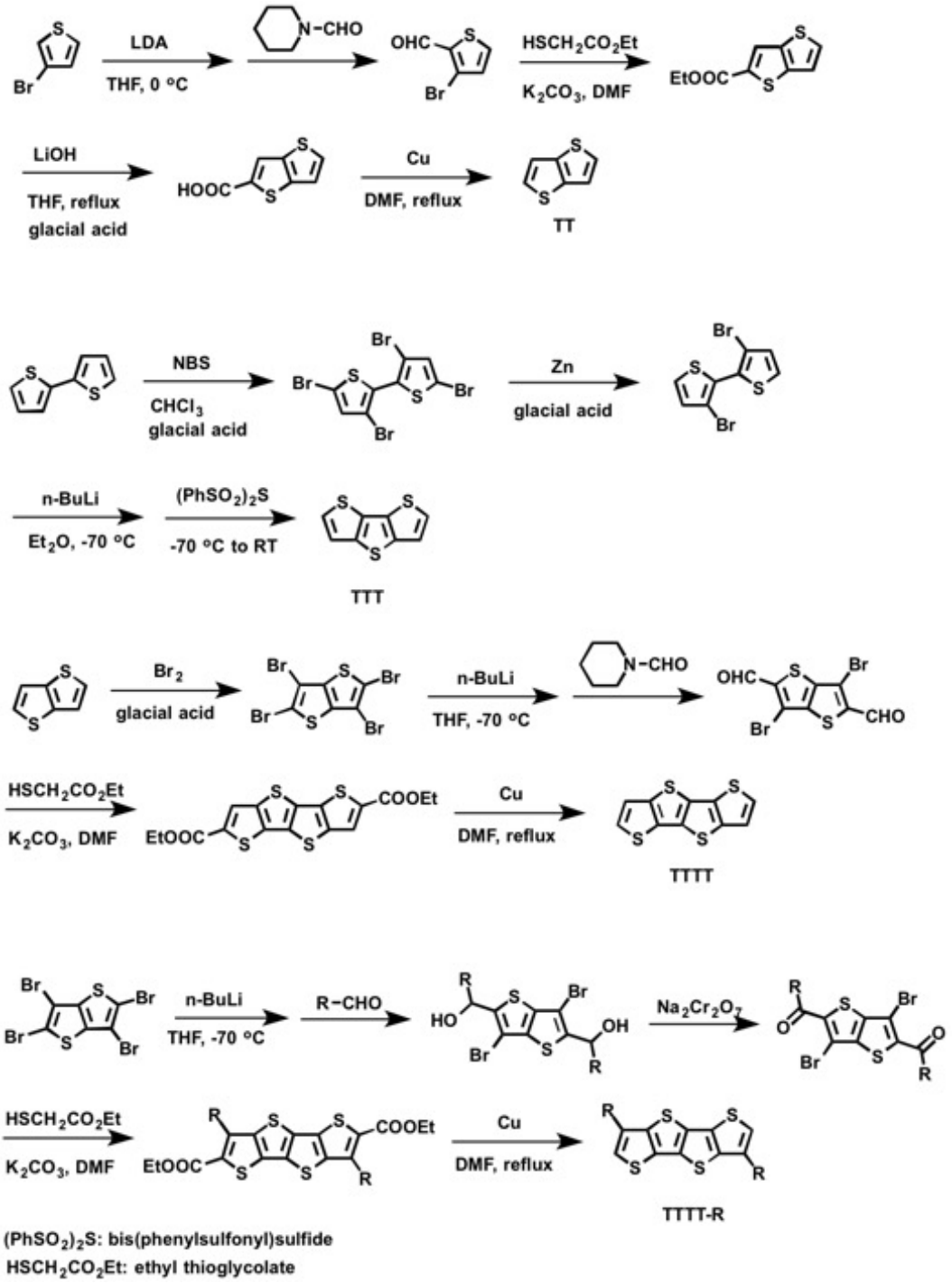

Figure 2.16. Synthetic approaches for the preparation of electron donating thienoacenes.[41d, 79, 128]

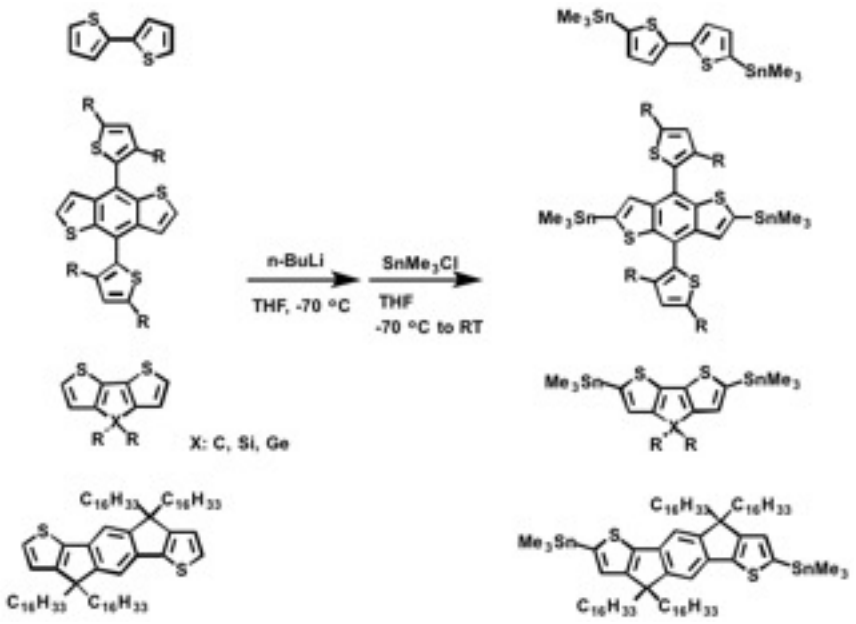

Figure 2.17. The metallization of thienoacenes for subsequent Stille polymerization.[115, 127c, 129]

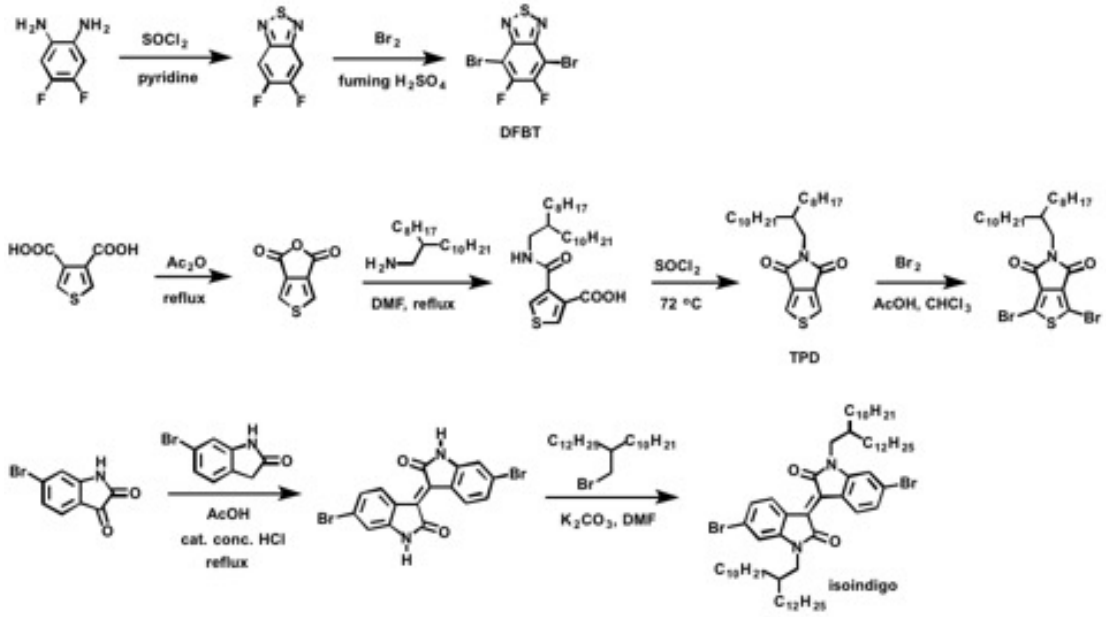

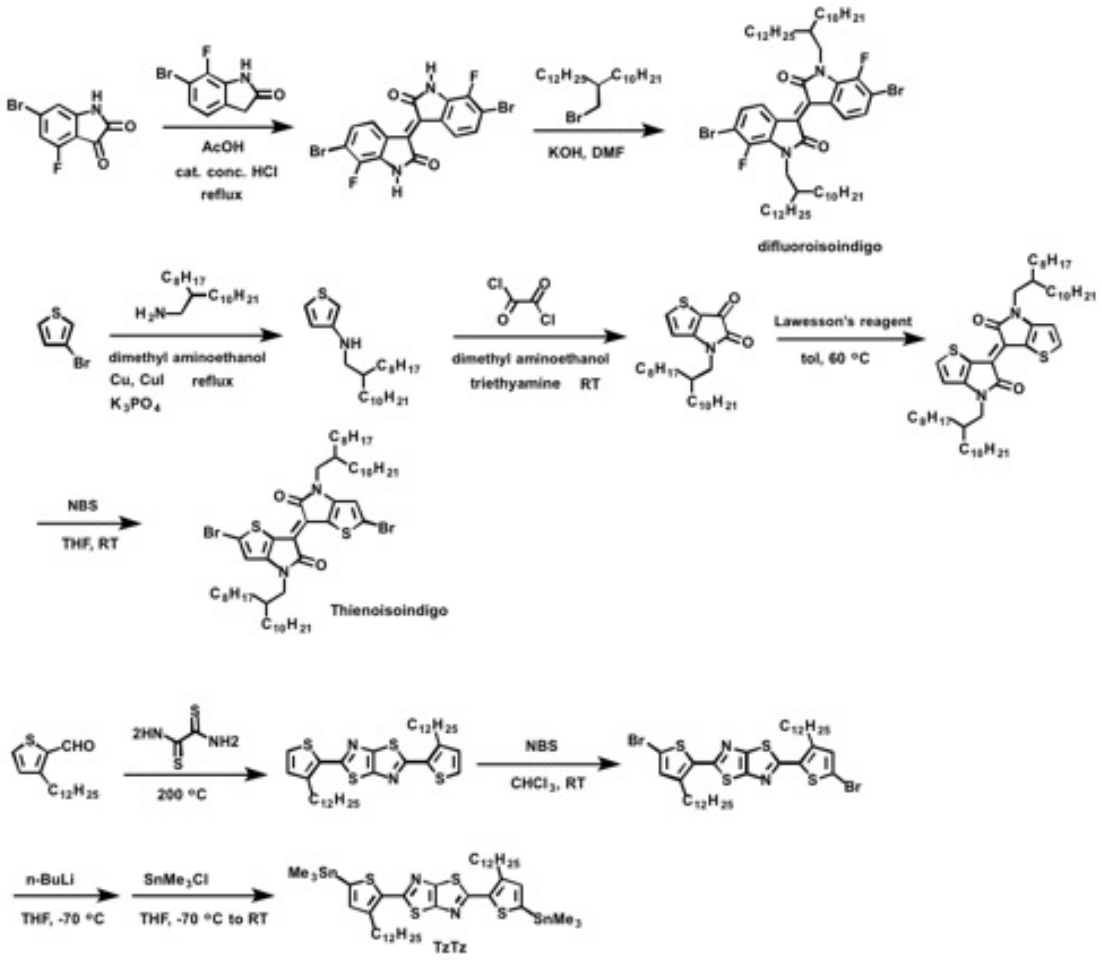

Figure 2.18. Synthetic approaches for the preparation of the electron deficient DFBT, TPD, isoindigo, fluorinated isoindigo, thienoisoindigo, and TzTz derivatives.[11a, 61c, 75b, 80, 130]

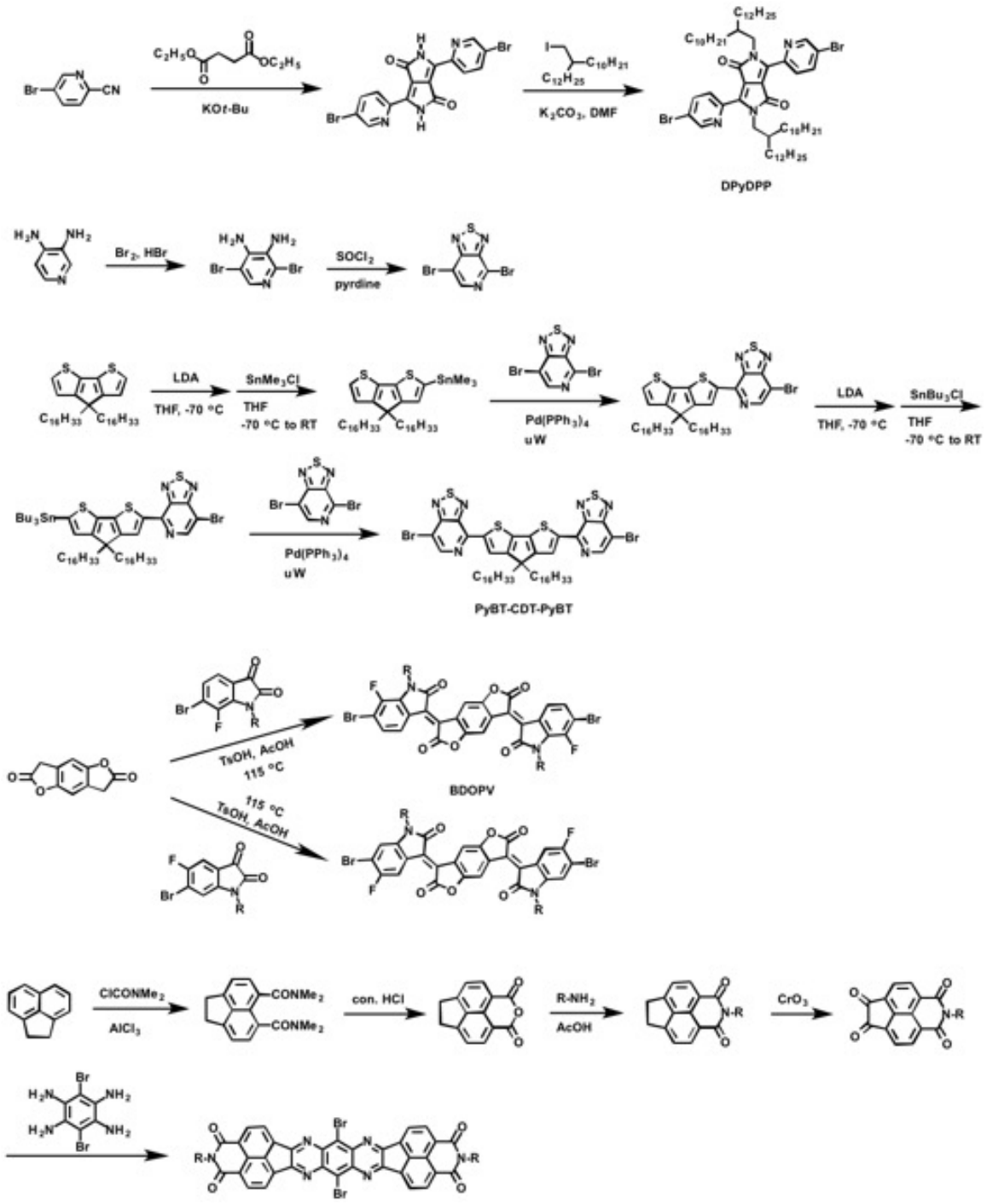

Figure 2.19. Synthetic approaches for the preparation of electron deficient oxoindolinylidenebenzodifurandione,[28c, d] tetraazabenzodifluoranthene diimide,[58] and pyridal- [2,1,3]thiadiazole.[61b]

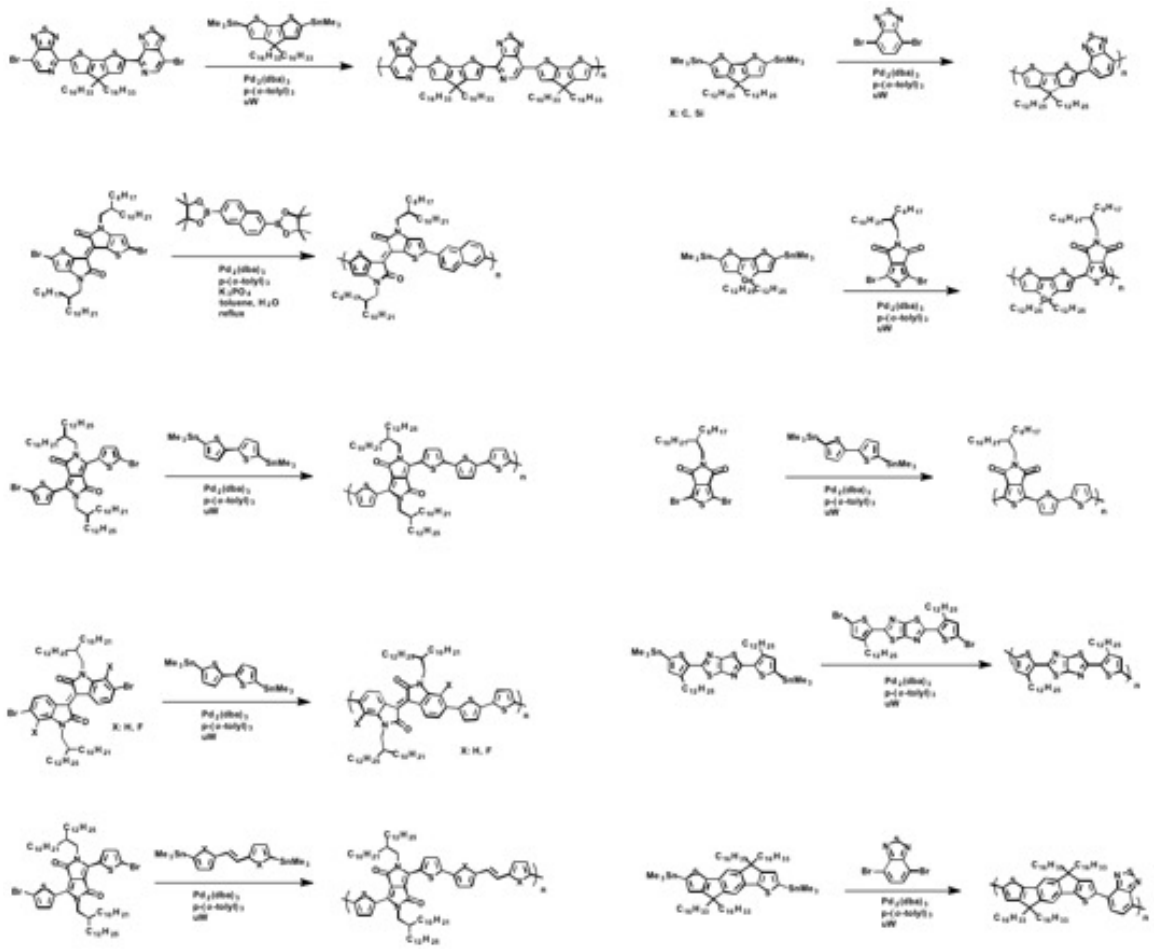

Figure 2.20. Examples of copolymerizations leading to p-type D-A polymeric semicondcutors.[5, 11a, 27d, 61b, 131]

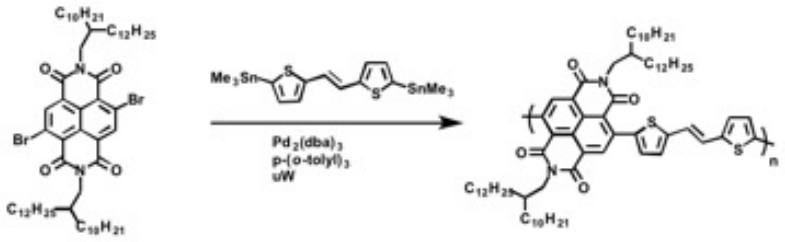

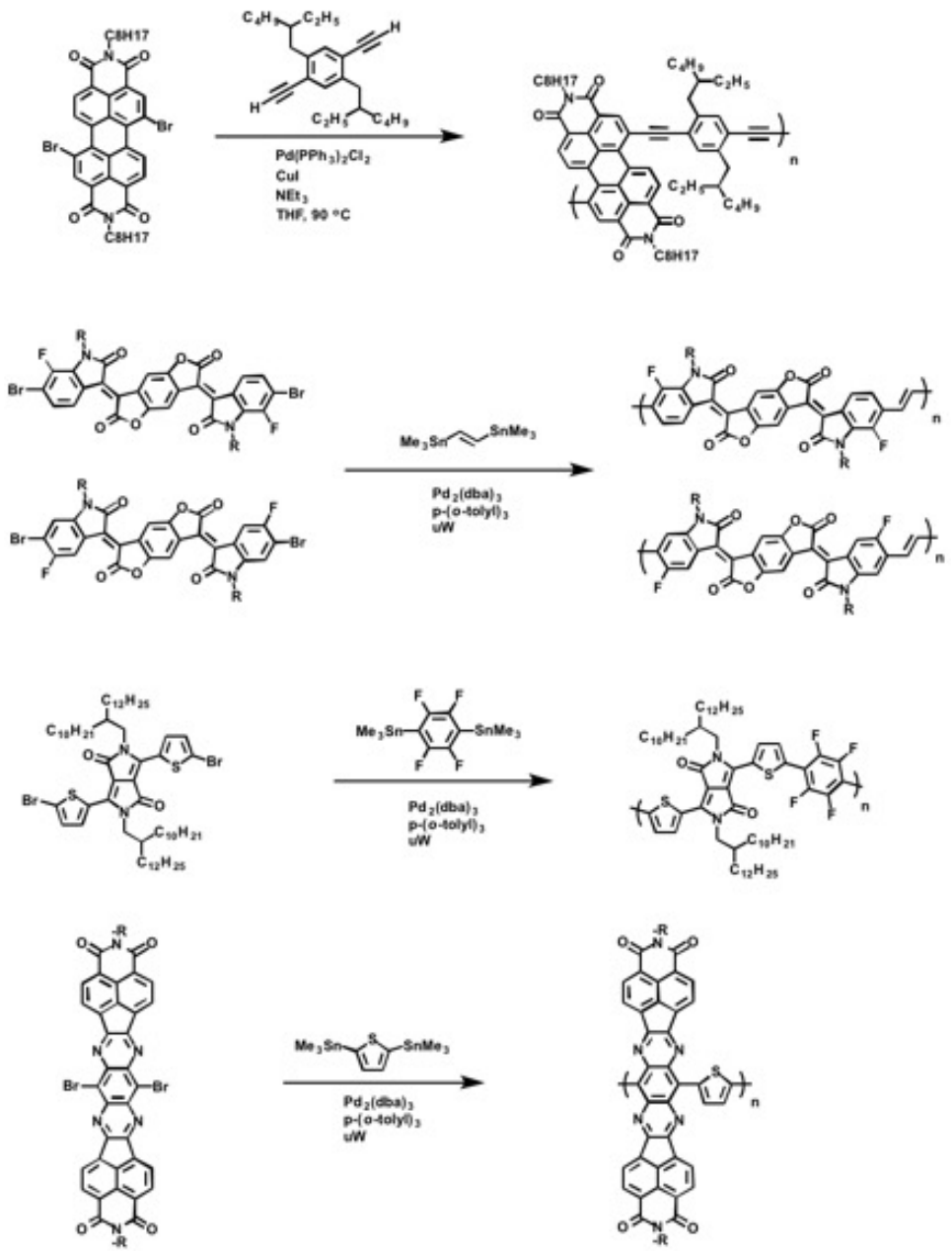

Figure 2.21. Examples of copolymerizations leading to n-type D-A polymeric semicondcutors.[28d, 61e, g]

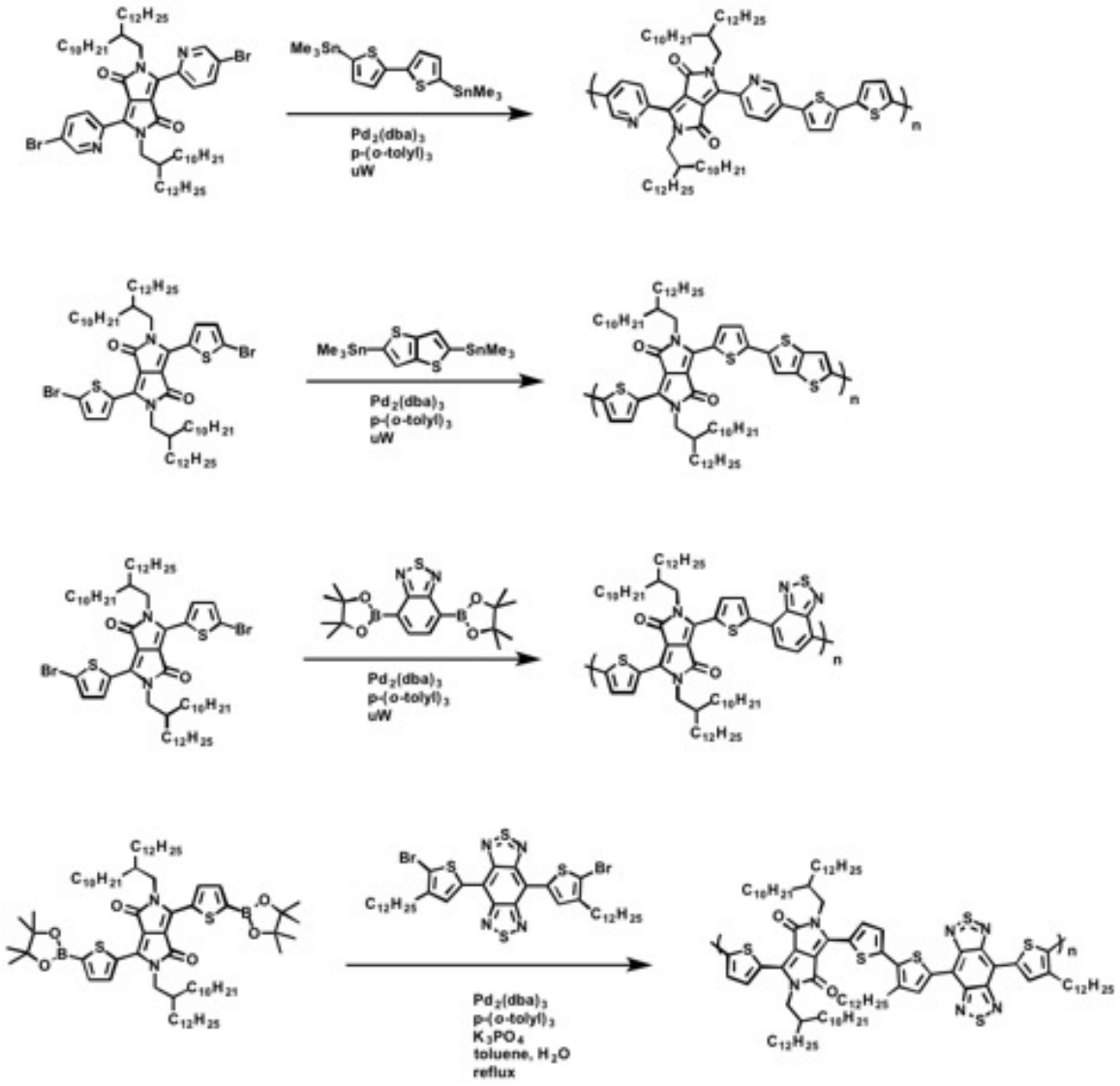

Figure 2.22. Examples of copolymerization affording ambipolar D-A polymeric semicondcutors.[27a, 59, 61f, 132]

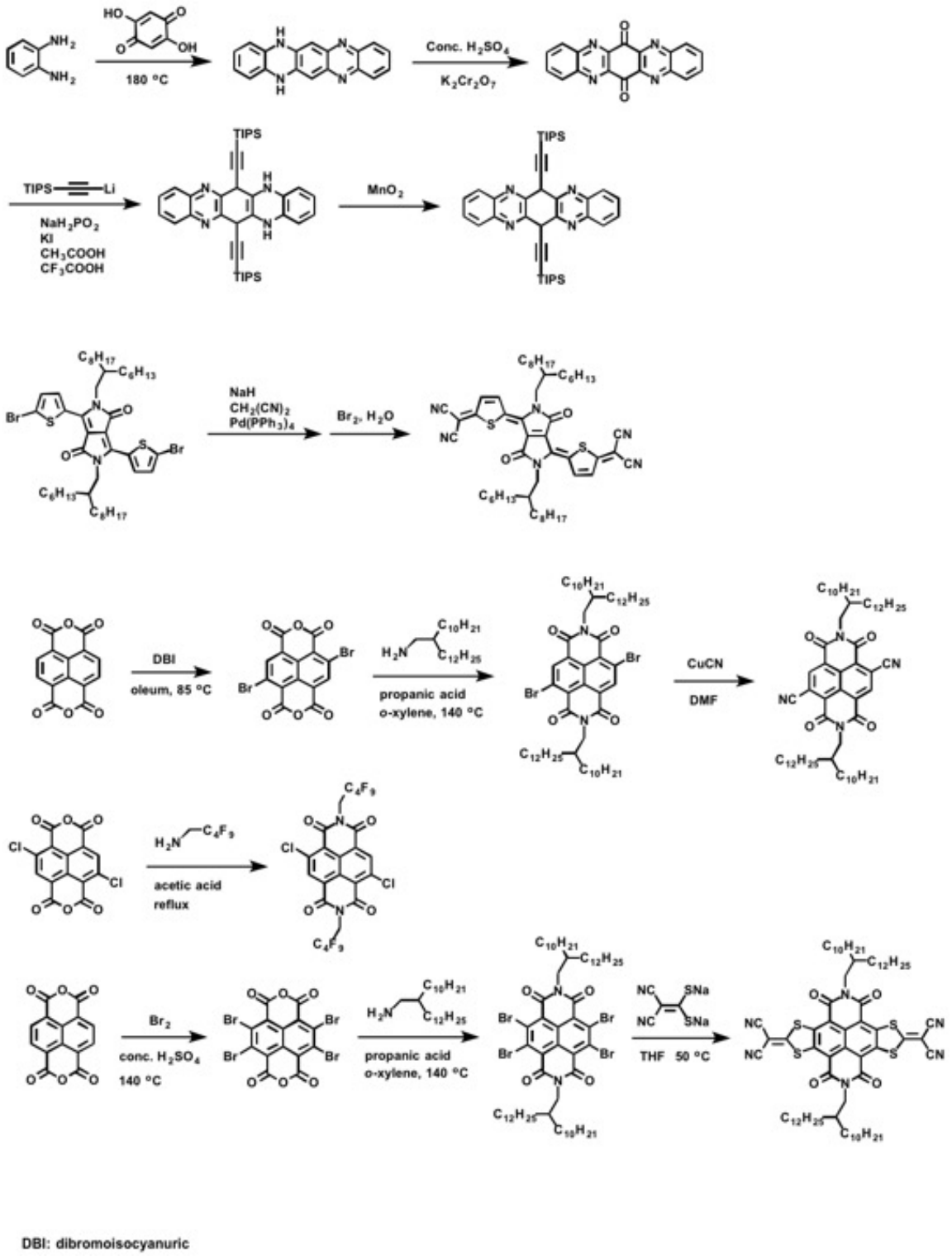

Figure 2.23. Synthetic approaches to selected n-type small molecule semiconductors.[14e, 17d, 40p, r, 133]

For a given moiety, the incorporation of electron donating (low electronegativity) functional groups or atoms tends to increase the HOMO/LUMO energy levels of the unit and the resulting HOMO/LUMO levels of respective molecules and polymers; alternatively, inclusion of electron withdrawing (high electronegativity) functional groups or atoms leads to a decrease the HOMO/LUMO energy levels. For instance, TIPS-TAP (10' in Figure 2.24) which has electron deficient –C=N- bonds, possesses lower HOMO/LUMO levels than TIPS-pentacene (11 in Figure 2.24).[44a] In a comparison of PBDTTT-C to PBDTTT-CF, the incorporation of fluorine into PBDTTT-C leads to 0.1 eV decrease in both HOMO/LUMO energy levels of PBDTTT-C, as shown in Figure 2.26.[14d] It is worthy to notice that the impact of electron-withdrawing functional groups or atoms on the HOMO and LUMO of respective organic molecules and polymers might be distinct. For instance, the nitrile containing CN-PPV exhibits a HOMO and LUMO that are 0.56 eV and 0.59 eV, respectively, lower than MEH-PPV. In a comparison of MEH-PPV with BuEH-PPV, the incorporation of oxygen into the side-chains of MEH-PPV leads to increases in the HOMO and LUMO by 0.31 eV and 0.04 eV, respectively.[32a] Typically, electron donating groups have greater impact on the HOMO than the LUMO of molecules; while electron withdrawing groups tend to have a more significant effect on the LUMO than the HOMO of the corresponding species.

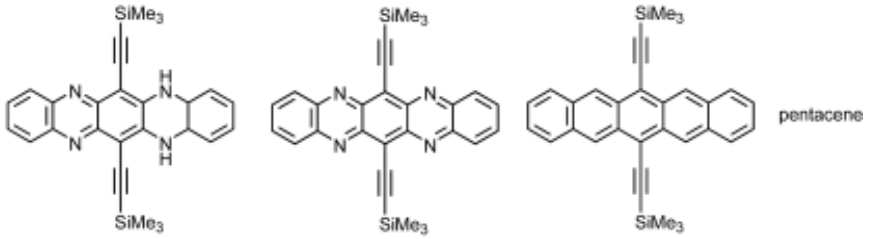

	9'	10'	11	pentacene
HOMO [eV]	–4.93	–5.29	–4.61	–4.60
LUMO [eV]	–2.14	–3.43	–2.71	–2.39
gap [eV]	2.79	1.86	1.90	2.21
experimental [eV]	(**9**: 2.37)	(**10**: 1.82)	(1.92)[a]	(2.11)[b]

Figure 2.24. Calculated (B3LYP 6-31G**//B3LYP 6-31G**) HOMO, LUMO and gap values for pentacene, its dialkynylated derivative and 9' and 10'. [a] For the TIPS-substituted pentacene see: *J. Am. Chem. Soc.* 2001, 123, 9482–9483;[134] [b] spectrochim. Acta Part A1997, 53, 1813–1824.[135] This figure is downloaded from Miao et al.'s literature.[40p]

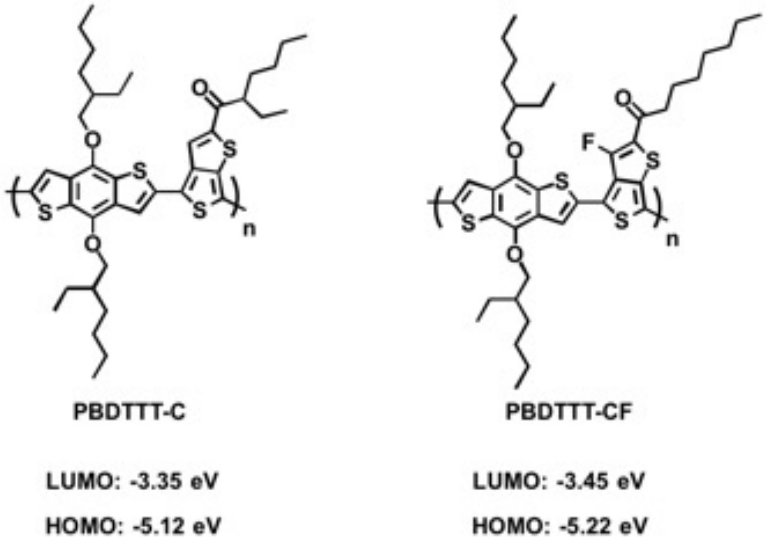

Figure 2.25. The molecular structures of PBDTTT-C and PBDTTT-CF, and their corresponding HOMO and LUMO energy levels.[14d]

2.4. OFET Device Fabrications and Processing

2.4.1. OFET Device Structure and Properties

Four typical organic field-effect transistor (OFET) device configurations of are shown in Figure 2.26, including bottom-gate/bottom contact (BGBC), bottom-gate/top-contact (BGTC), top-gate/bottom-contact (TGBC), and top-gate/top-contact (TGTC) architectures, in which organic or polymeric semiconductors are employed as the charge carrier transport layers.[3, 22a] Each configuration consists of a dielectric layer and three electrodes including the source, drain, and gate electrodes. The source-drain electrodes are typically 0.5 - 2 mm in length and 20 - 100 μm wide. The source electrode is grounded and defined as $V_S = 0$. Unlike inorganic semiconductors, which must be, pre- p- or n-doped, organic and polymeric semiconductors used in OFET architectures should be neutral with no free charge carriers available within the semiconductor layer. However, in a real system, organic semiconducting materials inevitably contain trace amounts of impurities which result from syntheses and purification processes and will act as dopants. An increase in degree of doping can convert organic semiconductors to conducting materials, as the bands formed between the HOMO/LUMO extend and eventually fill the bandgap.

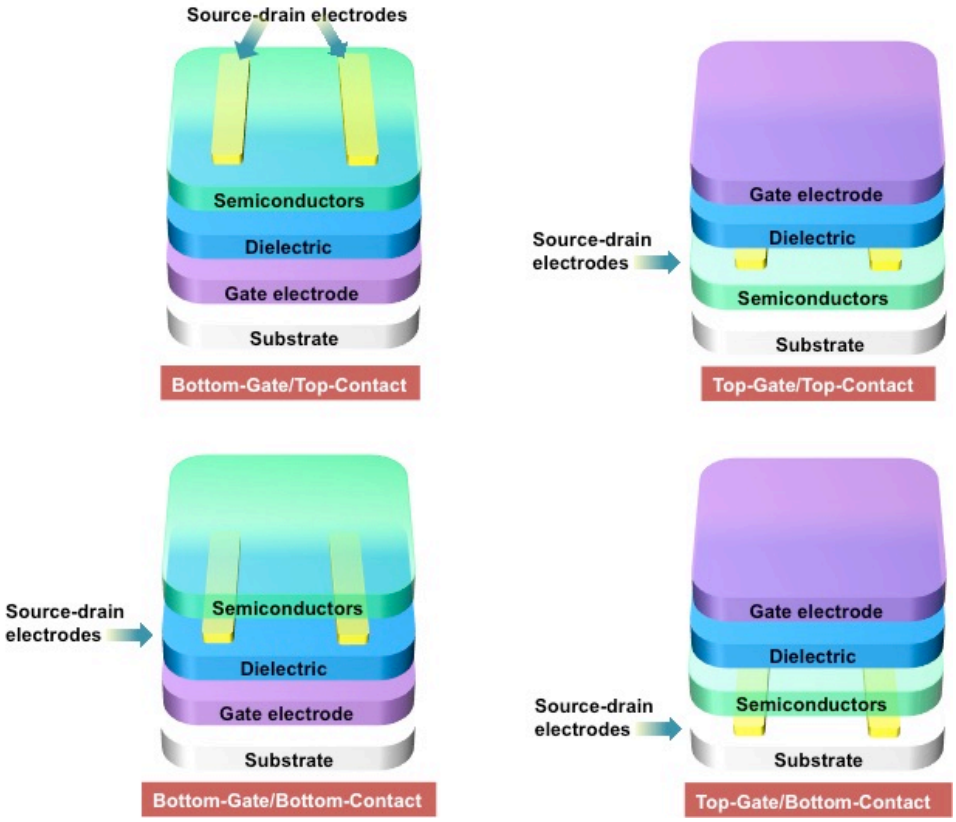

Figure 2.26. Schematic representation of four OFET architectures.

Application of a voltage (V_G) to the gate electrode leads to polarization of the dielectric material and induces charge carrier injection from the source electrode ($V_S = 0$) to the organic/polymeric semiconductor adjacent to the semiconductor-dielectric interface as shown in Figure 2.27. For instance, in BGBC-OFET devices, the application of $V_G < 0$ induces the accumulation of positive charges within the dielectric close to the semiconductor-dielectric interface; and thus leads to hole injection from the source electrode to the semiconductor layer. The injected holes accumulate within the semiconductor adjacent to the semiconductor-dielectric interface. Similarly, the application of $V_G > 0$ induces electron injection and accumulation within semiconductors

close to the semiconductor-dielectric interface, as shown in Figure 2.27. If there is no bias between the source and drain electrodes, that is, $V_{SD} = 0$, the concentration of charge carriers is uniform between the source-drain channel. Once V_{SD} is applied, the movement of charge carriers takes place under the electric field driving force. In the case of $V_G > 0$ and $V_{SD} > 0$, the injected electrons flow from the source to the drain electrode; while for $V_G < 0$ and $V_{SD} < 0$, the injected holes flow from the source to drain electrodes. The schemes describing the effect of V_{SD} on charge carrier transport are shown in Figure 2.28.

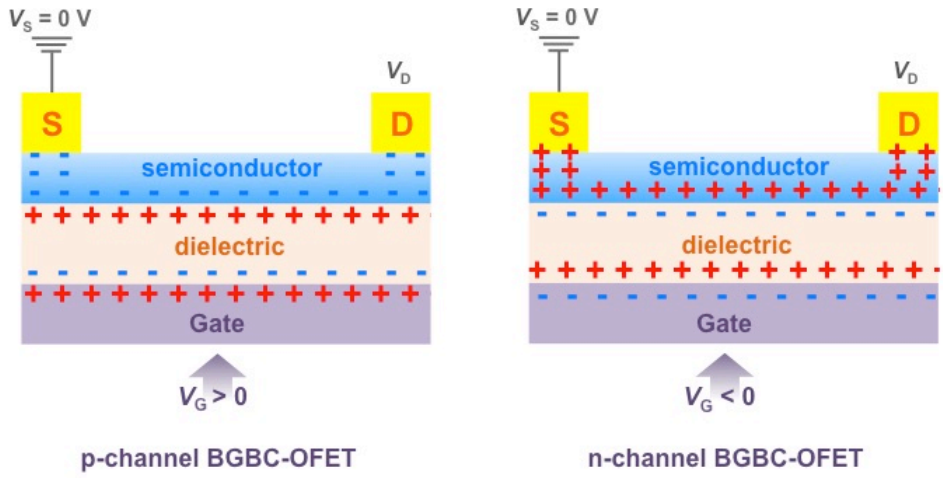

Figure 2.27. Scheme of the effect of gate voltage (V_G) on charge injection into organic/polymeric semiconductors.

It should be stated that charge carrier transport is an intrinsic characteristic of organic semiconducting materials; however, experimentally, results obtained for a given polymer semiconductor, such as in an OFET configuration, Space-Charge-Limited-Current (SCLC), or Time-Resolved Microwave Conductivity (TRMC) characterization, heavily depend on both the material characteristics and device features. For instance, the field-

effect charge carrier mobilities of organic semiconductors could be affected by charge carrier injection between the electrodes and semiconductors, and the interfacial characteristics between the semiconductor and dielectric. Recent studies indicated that by modulating the dielectric material within an FET, some hole transport (p-type) polymeric semiconductors, such as P3HT, poly(2-methoxy-5-(2-ethylhexoxy)-1,4-phenylene vinylene) (MEH-PPV), and poly(9,9-dioctyfluorene), are able to exhibit field-effect electron transport characteristics.[20a]

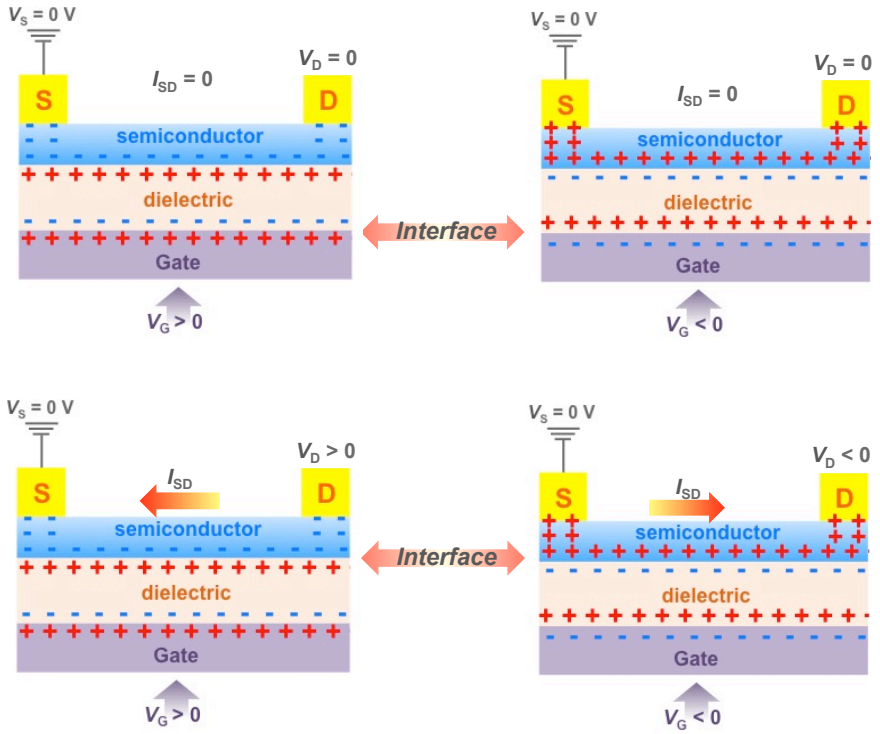

Figure 2.28. Schemes of charge carrier (hole and electron) transport within BGBC-OFET configurations.

In p-channel transistors, holes are injected from the source electrode to the HOMO of the organic or polymeric semiconductor, while in n-channel transistors; electrons are

injected from the source into the LUMO of the semiconductor (Figure 1.5). Please note that an organic or polymeric semiconductor in the charged state (polar or bipolar states) should have a narrower bandgap compared to its neutral state, due to the transformation of organic or polymeric semiconductors from an aromatic configuration to the quinonoid configuration.[19a, 23] The electrode-semiconductor interface follows the Mott-Shottky model where the contact barrier height is given by the difference between the workfunction (φ) of the metal (or conducting polymer) electrode and the HOMO or LUMO of the semiconductor.[3a] It is desirable for the workfunction of the electrode to be close to the semiconductor HOMO or LUMO to reduce contact resistance and gain good ohmic contact.[136] Typically, gold (Au with φ at -5.0 eV), palladium (Pd with φ at -5.0 eV), and platinum (Pt with φ at -5.0 eV) are selected as source and drain electrodes for p-type (hole transport) organic or polymeric semiconductors having a HOMO at between *ca*. -4.8 and -5.3 eV. For example, P3HT, which has a HOMO level at -4.8 eV, exhibits good hole mobility when Au is used as the electrode, but no transport characteristics are observed when silver (Ag with φ at -4.5 eV) is employed for the electrodes. For n-channel transistors where the semiconductor LUMO levels are located at ca. -3.0 - -4.0 eV, calcium (Ca with φ at -2.9 eV) or aluminum (φ at -4.1 eV) are typical candidates for electrode materials. Since Ca is readily oxidized upon exposure to air due to its low workfunction, encapsulation of Ca electrodes with a high workfunction metal, such as Au, is typically necessary.[28a] The workfunction of the metal could be further tuned by

coupling metal with self-assembled monolayers (SAMs), such as alkanethiols and perfluorinated alkanethiols, in which the thiol groups are bonded to the metal surface.[137] The electron donating alkane pushes electrons to the metal leading to an increase in metal workfunction; while the electron withdrawing perfluorinated alkane pulls electrons from the metal resulting in a decrease in metal workfunction. de Boer et al. [138] and Cheng et al.[21] reported a change of 0.6 – 1.1 eV in the workfunction of Ag and Au by SAMs, respectively. Stoliar et al.[139] and Cai et al.[140] reported the effect of the length of alkane chain on the workfunction of metals and the resulting charge carrier transport results with OFETs. Besides reducing the contact resistance, SAM functionalization also improves organic/polymeric semiconductor - metal electrode interfacial contact due to the alkane interactions; and thus leading to an observed increase in mobility. Besides the use of SAMs, Zhou et al. recently reported that polyethylenimine ethoxylated (PEIE) and branched polyethylenimine (PEI) are able to increase the workfunction of metal (Au and Ag) and ITO electrodes.[141] In our study, n-channel OFETs functionalized via PEIE showed a lower threshold voltage (V_T, *vide infra*) and higher current on/off ratio ($I_{ON/OFF}$, *vide infra*) compared with OFETs functionalized via pentafluorobenzene thiol (PFBT), a typical SAM used in OFET applications.

Among the four OFET configurations depicted in Figure 2.26, BGBC and TGTC have source and drain electrodes placed between the semiconductor and dielectric layers that

allow charge carriers to be injected directly into the semiconductor-dielectric interface. Alternatively, semiconductors are placed between the dielectric and two (source and drain) electrodes in BGTC and TGTC configurations, where charge carriers injected from the source electrode need to move across the semiconducting layer (20-50 nm in general depending on coating conditions). In BGBC and BGTC architectures, charge carrier transport occurs at the bottom surface of the semiconductor layer; whereas in BGBC and BGTC architectures, charges are conducted along the top surface of the semiconductor. The morphology of the bottom and top surfaces hence has distinct impact on the four transistor configurations.

The electron traps commonly exist at the semiconductor-dielectric interface, leading to trapped charges.[130d, 142] Thereby, these traps are first refilled before charge carriers can flow through the channel. This fact, together with the contact resistance, would limit the effect of V_G on the charge carriers injected into the channel. The charge carrier density Q_{SD} hence is represented as:[3]

$$Q_{SD} = neh = C_{ox}\,(V_G - V_T) \qquad \text{Eq. 2.2.1}$$

where C_{ox} refers to the capacitance of dielectrics within unit area with the unit of $nF.cm^{-2}$. n denotes the charge density within unit area; and h is the thickness of the charged layer in the channel. The threshold voltage, V_T, includes the impacts of impurities within semiconductors, electron traps within the semiconductor-dielectric interface, and contact

resistance at the metal-semiconductor interface.[143] In general, in p-channel transistors impurities would move V_T positively, the direction is reversed in n-channel transistors.

2.4.2. Linear and Saturated Mobilities

As $V_{SD} << V_G - V_T$, Q_{SD} is reduced from the source (x = 0) to drain electrodes (x = L, the length of channel) in a linear manner (Figure 2.29a):

$$Q_{SD} = n(x)eh = C_{ox}\,(V_G - V_T - V(x)) \qquad \text{Eq. 2.2.2}$$

where V(x) is the impact of source-drain voltage on Q_{SD}, with the boundary conditions of V(x) = 0 at x = 0 and V(x) = V_{SD} at x = L. This regime is defined as the linear regime. The electric current within the charge layer (I_{SD}) in the channel could be treated as:

$$I_{SD} = n(x)ehW\mu E \qquad \text{Eq. 2.2.3}$$

where W is the width of the channel; μ refers to the field-effect charge carrier mobility with the unit of $cm^2V^{-1}s^{-1}$; and E is the electric field between source and drain electrodes equal to dV / dx. Thereby,

$$I_{SD} = C_{ox}(V_G - V_T - V(x))W\mu\frac{dV}{dx} \qquad \text{Eq. 2.2.4}$$

During the charge carrier transport I_{SD} keeps constant along x direction. According to the boundary conditions that V(x) = 0 at x = 0 and V(x) = V_{SD} at x = L, the equation above is integrated as:

$$I_{SD} = \frac{W}{L} C_{ox} \mu ((V_G - V_T) V_{SD} - \frac{1}{2} V_{SD}^2) \quad \text{Eq. 2.2.5}$$

As $V_{SD} << V_G - V_T$ (linear regime), the equation above is simplified as:

$$I_{SD} = \frac{W}{L} C_{ox} \mu \big((V_G - V_T) V_{SD} \big) \quad \text{Eq. 2.2.6}$$

Therefore,

$$\mu_{lin} = \frac{L}{W C_{ox} V_{SD}} \left(\frac{\partial I_{SD}}{\partial V_G} |_{V_{SD}} \right) \quad \text{Eq. 2.2.7}$$

As $V_{SD} = V_G - V_T$, the "pitch-off" appears inside the channel close to the drain electrode as shown in Figure 2.29b and c, in which I_{SD} reaches a saturated value. This regime is defined as the saturated regime. The equation 2.2.5 is converted as:

$$I_{SD} = \frac{W}{2L} C_{ox} \mu (V_G - V_T)^2 \quad \text{Eq. 2.2.8}$$

Therefore,

$$\mu_{sat} = \frac{2L}{W C_{ox}} \left(\frac{\partial I_{SD}^{1/2}}{\partial V_G} |_{V_{SD}} \right)^2 \quad \text{Eq.2.2.9}$$

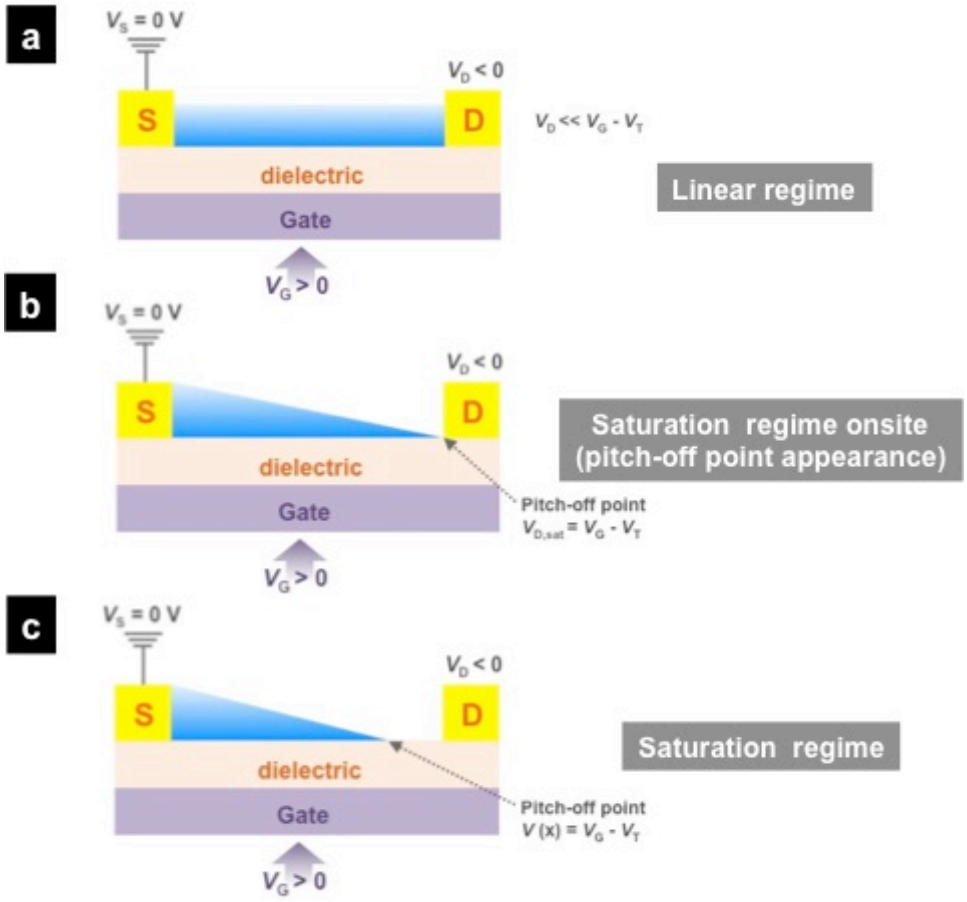

Figure 2.29. Schemes of (a) linear regime with $V_D << V_G - V_T$, (b) the onsite of saturation regime with $V_{D,sat} = V_G - V_T$, where the pitch-off point exhibits at drain electrode; and (c) saturation regime with $V(x) = V_G - V_T$, at which $V_D > V_{D,sat}$.

Figure 2.30 shows typical I_{SD}-V_{SD} (Figure 2.30a), I_{SD}-V_G (Figure 2.30b), and $I_{SD}^{1/2}$-V_G (Figure 2.30c) curves. The I_{SD}-V_{SD} curve is known as the transfer curve. The linear regime is shown at low V_{SD} (< 5V). I_{SD}-V_G and $I_{SD}^{1/2}$-V_G are called output curves for the linear regime and saturated regime, respectively. In the curve of I_{SD}-V_G, there is a turn-on voltage (V_{ON}) referring to the "dramatic" increase in current. In light of impurities and electron traps, V_{ON} typically does not equal zero. V_T is determined from the curve of

$I_{SD}^{1/2}$-V_G as shown in Figure 2.30c. The current on and off ratio, $I_{ON/OFF}$, determined through dividing maximum I_{SD} (I_{ON}) by the minimum I_{SD} (I_{OFF}), demonstrates the change in current between the on and off states. A large value of $I_{ON/OFF}$ indicates that the OFET devices have high sensitivity. Ideally, $I_{ON/OFF}$ is $>10^6$.

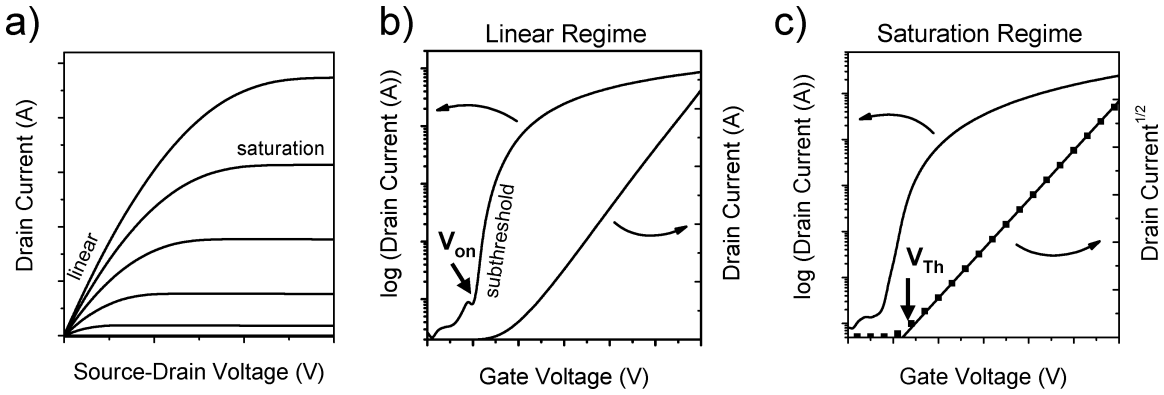

Figure 2.30. The examples of (a) transfer curve of I_{SD}-V_{SD}, (b) linear regime out-put curve of $I_{SD} - V_G$, and saturation regime out-put curve of $I_{SD}^{1/2} - V_G$. This figure is from *Chem. Rev*. 2007, 107, 1296.[3a]

2.4.3. Dielectric materials for OFETs

As discussed above, dielectric materials can significantly impact charge carrier transport. BGBC transistors typical test devices use 200-300 nm of SiO_2 thermally grown onto heavily doped Si gate electrodes.[3b, 18b] In general, defects and silanol groups exist on the surface of SiO_2 that might negatively affect the efficiency of charge carrier transport at the semiconductor-dielectric interface. One approach to address this challenge is to grow a silane or amine based SAM on the top surface of the SiO_2.[144] The silane (active Si-Cl or Si-OMe) or amine (N-H) groups are able to bond to the surface

silanol groups to afford siloxane (Si-O-Si) or silazane (Si-N) bonds, as shown in Figure 2.31.

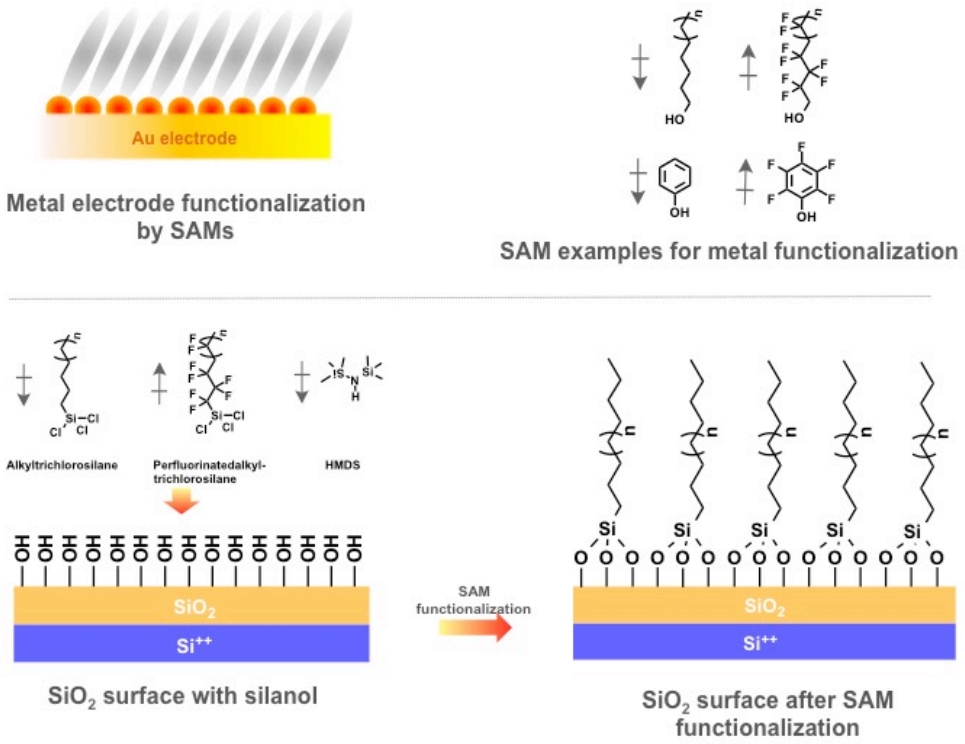

Figure 2.31. Schemes of self-assembly monolayer (SAM) functionalization to metal surface and SiO_2 surface.

Typical silane SAMs include alkyltrichlorosilane, perfluorinated alkyltrichlorosilane, alkyltrimethoxylsilane, and bis(trimethylsilyl)amine (HMDS).[86, 145] The resulting surface turns from hydrophilic (water contact angle < 20°) to hydrophobic (water contact angle > 95° for SAMs with alkyl groups and 80-85° for HMDS). The perfluorinated SAM treated surface in particular shows superhydrophobic characteristics, with a contact angle > 130°, which might lead to polymer ink dewetting on the substrate. The p-channel field-effect transistors often show approximately a 1 order of magnitude enhancement in

hole mobility when a SAM treatment is used in the device fabrication process. Possible reasons include that defects and silanol surface groups were largely eliminated through treatment; and/or that the presence of alkyl chains induces polymer semiconductor packing to turn from a "face-on" orientation to an "edge-on" orientation,[146] which benefits the in-plane carrier transport from source to drain as shown in Figure 2.32.

In the real cases, however, it proves difficult to remove all electron traps with the SAM treatment. Therefore, n-channel transistors which are quite sensitive to electron traps generally require hydrophobic polymers as dielectrics, such as divinyltetramethylsiloxane-bis(benzocyclobutene) (BCB),[20a, 147] amorphous fluoropolymer CYTOP,[20c, 148] ferroelectric polymer (P(VDF-TrFE-CFE)),[149] polystyrene (PS),[150] PVP,[151], PVP:HDA[147b, 152], PMMA,[153], poly(methyl silsesquioxane),[154] and parylene[155]. These polymers have no hydrophilic functional groups and thus minimize electron traps on the dielectric layers. Compared with inorganic dielectrics such as SiO_2, SiN_x, and Al_2O_3, polymeric dielectric materials provide better interfacial interaction with organic and polymeric semiconductors.[156] The resulting n-channel transistors generally show enhanced electron transport characteristics (higher mobility, higher $I_{ON/OFF}$, and reduced V_T) and minimized ambipolar features compared with devices fabricated with SAM pre-treated SiO_2 dielectric layers. For instance, P(NDI2OD-T2) showed an electron mobility close to 1 $cm^2V^{-1}s^{-1}$ based on

OFETs with PS as dielectrics. Further, these amorphous polymer dielectrics can be used in fabrication of flexible and stretchable OFET devices based on PEN or PET substrates. It is worthy to mention that BCB needs to be formed via polymerization at 300-350 °C. It is thus commonly applied on BGTC transistor configurations, before casting organic and polymeric semiconductors; while the fluorinated CYTOP which has a low surface tension is primarily used in TGBC transistor configurations where it is coated on top of organic or polymeric semiconductors.

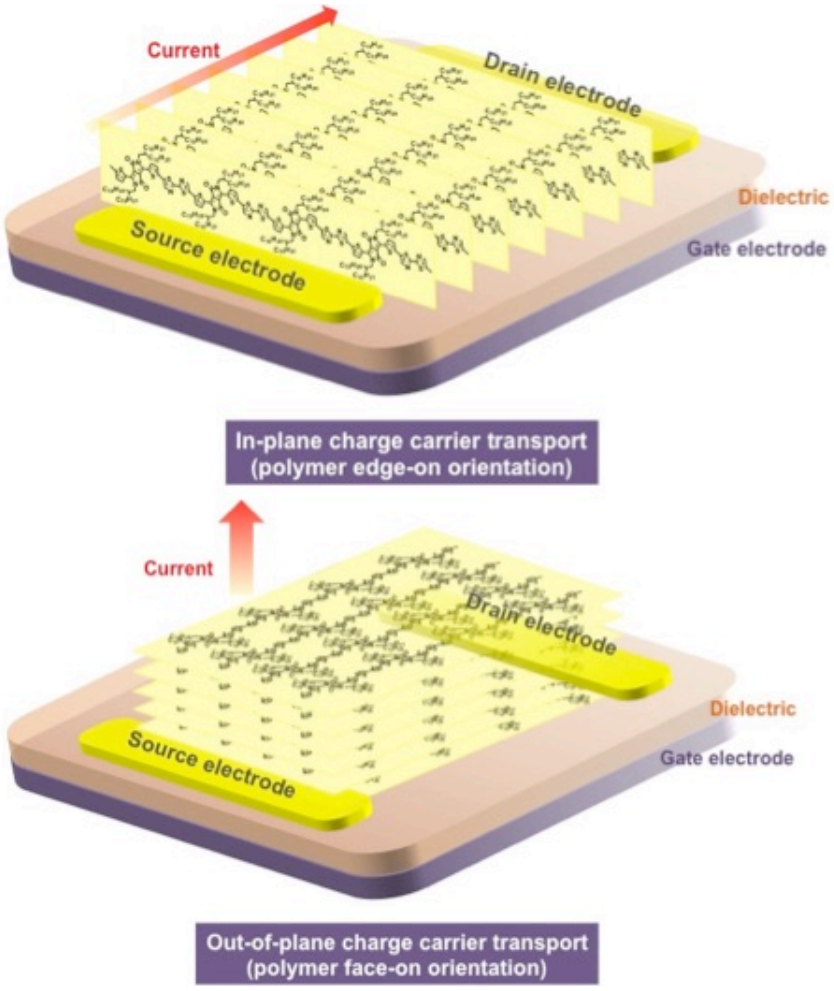

Figure 2.32. Schemes of the in-plane charge carrier tranposrt (polymer edge-on orintation) and out-of-plane charge carrier transport (polymer face-on orientation).

The encapsulation of organic and polymeric FETs is necessary since the devices are in general sensitive to humidity and oxygen. Polymers such as CYTOP and parylene can be combined with inorganic materials including SiO_2, SiN_x, and Al_2O_3 to form organic-inorganic hybrid encapsulation layers.[148b, 157]

2.4.4. Organic and Polymeric Semiconductor Thin-Film Deposition

Small molecule semiconductors are frequently deposited onto FET substrates under high vacuum, where under optimized conditions it is possible to grow single-crystal thin-films. This deposition process needs to be conducted under thermal evaporation rather than electron-beam evaporation conditions due to the high-energy associated with electron-beams: exposure of organic materials to an electron-beam often leads to film damage. Thin-film deposition approaches have significant impacts on the resulting thin-film morphology such as molecular orderings and orientation distributions, and thus the charge carrier transport behavior. Previously, it was thought that small molecule thin-films grown from vacuum deposition are superior to ones fabricated from solution-processes such as spin-coating. The spin-cast films are generally more disordered and have multi-crystalline characteristics compared with thermally deposited counterparts, which can severely limit charge carrier transport efficiency. However, recent studies have shown that for certain organic semiconductors, such as BTBT-C8 and pentacene, single-

crystal thin-films could be formed through inkjet printing and solution shearing coating (blade coating). Yuan et al. recently reported the alignment of BTBT-C8 parallel or perpendicular to source-drain electrodes on OFETs based on an off-center spin coating approach, during which the centrifugal force aligns the thin films. The X-ray scattering characteristics unveiled a new packing structure that differed from the single-crystal film, demonstrating the feasibility that selected meta-stable molecular packing configurations may possess more efficient charge carrier transport pathways compared with the single-crystal packing that is typically observed.[46] It had been previously believed that the molecular packing associated with single crystal materials is the optimum for achieving the highest possible charge carrier transport for any one material.

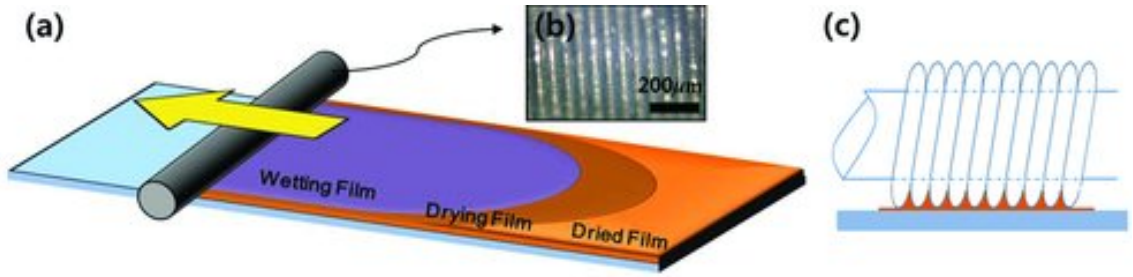

Figure 2.33. Blade coating of polymeric semiconductors onto OFET substrates. The figure is reproduced from *Adv. Mater*. 2013, 25, 4302-4308.[158]

Polymeric semiconductor thin-film formation onto FET substrates is typically carried out through a solution-based process, such as spin-coating, blade-coating, slot-die coating, or inkjet printing. The high MW of polymers prevents film formation via thermal deposition. Spin-coating is widely used to afford uniform and isotropic thin films in lab

environments. Film thickness is typically 50-100 nm, depending on the ink concentration, solvent, spinning speed (500-5000 rpm), and spinning time. However, for large-scale, high speed, and low-cost coating processes, blade coating (which uses a shearing force), gravure coating, or slot-die coating are more efficient.[90, 91b] Khim et al.[158] and Lee et al.[31b, 77] reported high-performance polymer FETs could be achieved through a blade coating process, and as shown in Figure 2.33 and 2.34 field-effect hole mobilities beyond 3 $cm^2V^{-1}s^{-1,}$ respectively, were reported. Compared with spin-coating, the blade coating might induce alignment of polymeric thin-films along the direction of the one dimension applied shearing force, which affords the anisotropic film. Brinkmann's group reported a post-rubbing approach for improving film texture, that is, cycled rubbing of the spin-coated films was done to increase the film orientation. The resulting dichroic ratio was increased for typical polymer semiconductors such as P3HT, PBTTT, and P(NDI2OD-T2), indicative of enhanced alignment within the thin-film. The charge carrier mobility, however, does not show a significant change after this rubbing process.[159] Heeger's group recently introduced a grooved OFET configuration, in which the SiO_2 dielectric surface within the channel was linearly scratched via a mechanical grooving process. The polymeric ink was flowed through the channel and formed a highly aligned texture induced by the grooved patterns. The resulting OFETs exhibited mobilities >50 $cm^2V^{-1}s^{-1}$,[27c, 93a] which is to date, a record mobility for polymeric semiconductors.

An alternative approach for polymeric film formation is based on inkjet printing. The significant operational parameters include ink viscosity and surface tension, which could be manipulated through adjusting the material's concentration in the ink formulation and if necessary, the addition of additives. In comparison to traditional coatings, use of inkjet printing allows fine control of the dose and position of active material and thus, the thickness, size and position of the semiconductor film formed on the device substrate, which potentially reduces ink consumption and issues associated with ink solvent emission; also, expensive photolithographic-patterning of the semiconductor films is avoided. Polymeric field-effect transistors based on inkjet printing have been reported, and similar mobilities compared with transistors fabricated using the spin-coating approach were demonstrated.[148b] Additionally, a push-coating process was introduced using P3HT based transistors which exhibited similar thin film morphology and hole mobility compared with spin-coated P3HT based devices.

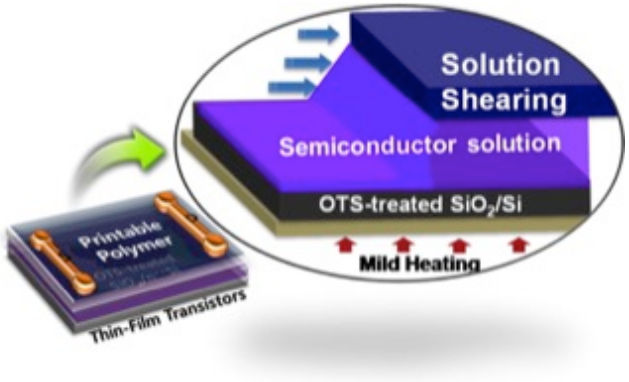

Figure 2.34. Shear force induced coating of polymeric semiconductors onto OFET substrates. The figure is reproduced from *J. Am. Chem. Soc.* 2012, 134, 20713.[77]

2.5. Polymeric Semiconductor Materials Characterization

2.5.1. Molecular Structure Identification

Synthesized organic compounds were characterized using nuclear magnetic resonance spectroscopy (NMR), mass spectrometry (MS), elemental analysis, and Fourier transform infrared spectroscopy (FT-IR). ^{1}H- and ^{13}C-NMR provided the chemical shifts, spin-spin coupling (only ^{1}H-NMR), spinning sidebands (only ^{1}H-NMR), and the relative ratios between peaks of each H and C atom of the compounds measured. If one compound has other elements such as N, F, P, and B, it is recommended to measure the corresponding ^{15}N, ^{19}F, ^{31}P, and ^{11}B NMR spectra. Taken together, NMR information reveals the molecular composition, structure, the relative positions of atoms, as well as the purity of a given compound. The molecular weight (MW) is characterized by the mass spectrum that provides a pattern referring to the distribution of ions by mass, or mass-to-charge ratio. According to the mass spectrum, the mass and particular molecular fragments of a compound can be determined. Electron ionization mass spectroscopy (EI-MS) in general is used to test volatile organic compounds (VOCs) with MWs < 600 Da. For molecules with MWs > 600 Da, matrix-assisted laser desorption/ionization (MADLI) might be applicable. In MALDI analysis, please note that the MW of target molecules should be different from that of the matrix molecule to avoid the noise in the measurement. The elemental compositions of a given compound may be determined through elemental

analysis. For common organic and polymeric semiconductors, the primary elemental compositions contain C, H, O, N, S, and F, among which C, H, N, and S could be determined by combustion analysis, that is, these elements would be converted to CO_2, H_2O, NO_2, and SO_2 under combustion with excess oxygen. Fluorine content is typically analyzed using ion specific electrode (ISE) or ion chromatography. FT-IR spectroscopy can be used to determine what functional groups are incorporated into a compound, such as carbonyl, nitrile, and imide groups on small molecules or polymers. For identification of a compound, ^{1}H-, ^{13}C-, and particular element (if pertinent) NMR spectroscopies mass spectrum are required as well.

2.5.2. Absorption and Fluorescence Spectroscopy

Due to their high degree of π-conjugation, organic and polymeric semiconductors typically have strong absorption in the visible range that can be characterized by UV/vis absorption spectroscopy. The onset positions of absorption patterns for organic and polymeric semiconductors indicate the lowest photon energy that a particular material can absorb to promote electrons from the ground state to the excited state; in other words, the optical gap of these materials to activate the electrons. For organic and polymeric semiconductors, electrons in excited states after photo activation are still bound to holes left in the ground state due to the relatively high binding energy (0.3-0.5 eV), which is a

significant feature in contrast to inorganic semiconductors.[1c, 160] This "hole-electron pair" is termed an exciton; and the energy gap corresponding to the onset position is defined as the optical bandgap (E_g^{opt}). The bandgap (E_g) between the HOMO and LUMO in organic and polymeric semiconductors should be expressed as E_g^{opt} subtracted by the binding energy.[161] Typically, the absorption spectrum of organic and polymeric semiconductors in both solution and solid state are reported. For homooligomers or homopolymers, there is one π - π* transition. For example, in solution regioregular P3HT and octathiophene exhibit a single absorption band with absorption maxima (λ_{max}) at 456 nm and 423 nm, respectively, that correspond to the π - π* transition.[17b, 41b] For D-A oligomers or polymers, donor-acceptor coupling leads to an intramolecular charge transfer (ICT) band, which in general has a lower energy compared with the π - π* transition and thus reduces E_g^{opt}. For instance, in solution, the polymer PBT6[33] and oligomer TTBTT[41a] have ICT bands with λ_{max} at 535 nm and 510 nm, respectively, and π - π* thiophene transitions with λ_{max} at 428 nm and 350 nm, respectively. The absorption spectrum for PBT6 is shown in Figure 3.5 of Chapter 3.

In solution, organic compounds and polymers (solutes) interact with solvents to stabilize the entire solute-solvent system. Because the dipole moments of solutes are different in the ground states and excited states, solvents with distinct polarities have different interactions with solutes in the ground and excited states leading to a change in

the energy gap (E_g) of solutes, a phenomenon known as solvatochromism. The bathochromic and hypsochromic shifts of materials induced by distinct solvents are termed positive and negative solvatochromism, respectively. The solvatochromism of PBT6 in different solvents is discussed in Chapter 3.

Compared with the spectrum of solution, the λ_{max} of absorption for solid organic and polymeric semiconductor films typically displays a red-shift (bathochromic shift), implying an enhancement of π-conjugation arising from planarization of the backbones and an increase in π-π intermolecular interactions. For instance, regioregular P3HT exhibits a shift in λ_{max} from 456 nm in solution to 560 nm in thin-film form;[17b] similarly, for PBT6 λ_{max} shifts from 428 nm (π - π* transition) and 535 nm (ICT band) in solution, to 495 nm (π - π* transition) and 677 nm (ICT band) in thin films.[33] Additionally, in solution, organic or polymeric semiconductors commonly provide featureless, board absorption bands; while vibrational fine structured bands might emerge in film states, indicative of the enhancement in molecular ordering within films after removing solute-solvent interactions. For instance, regioregular P3HT has a broad band with λ_{max} at 456 nm; while its thin films show three vibrational fine shoulders at 526, 560, and 610 nm.[17b] Steyrleuthner et al. introduced the determination of the ordered aggregate ratio within P(NDI2OD-T2) films by comparing the ratio of vibrational bands (ordered aggregates) with the featureless bands (disordered aggregates).[162] The vibrational fine structure

correlates with the vibrational transition during light absorption and emission. The vibrational band with lowest energy might relate to the transition from the ground electronic state (n=0) / ground vibrational state (v=0) to the excited electronic state (n=1) / ground vibrational state (v'=0) in n=1, termed 0-0 transition. Other transitions with higher energy involve an electronic transition in combination with vibrational transitions within the excited electronic state. In other words, the bands labeled such as 0-1, 0-2, etc., represent the electrons that travel higher in energy than the purely electronic transition (0-0). For instance, 0-1 transition denotes the transition from ground electronic state (n=0) / ground vibrational state (v=0) to the excited electronic state (n=1) / excited vibrational state (v'=1) in n=1.[163] In P3HT thin films, for example, the three vibrational bands at 526, 560, and 610 nm refer to transitions of 0-2, 0-1, and 0-0, respectively.[89, 164] The intensity of each vibrational transition is dependent upon the Frank Condon overlap of the ground state and excited state. This introduces the possibility of vibrational information within the electronic spectrum.

Some polymers, such as DPP-based[165] or isoindigo-based materials,[78a] display vibrational fine structures in solution state absorption spectra; and no obvious shift in absorption is apparent when the films are solids. The possible reason is that these polymers have relatively low solubility in common solvents and thus form aggregates within in solutions leading to similar microstructure compared with films. For organic

compounds or polymers showing blue-shifts (hypsochromic shift), H-aggregates might form within the solid materials, which generally quench the fluorescence. Therefore, H-aggregates could be confirmed through measuring the quantum yield of fluorescence emission. Spano et al. stated that π-conjugated polymers like P3HT typically form both J- (strong fluorescence) and H-aggregates within films. J-aggregates are correlated with intrachain interactions; while H-aggregates correlate with interchain interactions. For P3HT films, the increase in the ratio of the 0-0 intensity to 0-1 intensity suggests the transition from H- to J-aggregate behavior.[99, 166] Aggregates in solution might be impacted by thermal energy, that is, heating of solutes could gain sufficient energy to dis-aggregate resulting in the reduction of inter- and/or intra-molecular interactions, and thus the hypsochromic shift, which is termed thermochromism. The thermochromism of PBT6 is discussed in Chapter 3. In addition, the vibrational fine structures in solution phase absorption spectra would fade with an increase in solution temperature, due to the presence of vibrational hot bands and Fermi Resonance.[3a]

In contrast to absorption spectroscopy, fluorescence spectroscopy tests the transition of electron relaxation from the excited electronic state to the ground electronic state, in which light (photons) with certain wavelength emit from the materials. Based on Kasha's rule, electron relaxation occurs at the lowest excited state, that is excited electronic state with n=1 (S1) / ground vibrational state with v=0 at S1, to the ground electronic excited

state with n=0 (S0) and distinct vibrational state at S0, such as v=0, 1, 2, etc. at n=0. For instance, the 0-1 transition in fluorescence represents the electron relaxation from n=1,v'=0 to n=0, v=1. For electrons having an electronic state at S1 with n=1, v'=1, 2, 3, etc., electrons are relaxed from n=1, v'=1, 2, 3, etc. to n=1, v'=0 through the nonradiative vibrational relaxation, during which heat dissipates and thus the emitted photon has lower energy (higher wavelength) than the absorbed photon. The general transitions are shown in a Jablonski diagram. The fluorescence spectra mirror their absorption spectral counterparts. Due to the high sensitivity of the technique, material solution concentrations should keep low (*ca*. 10^{-6} M). High solution concentration, on the one hand, would saturate the fluorescence spectra, while on the other hand, would induce aggregate formation leading to the appearance of aggregation bands or bleaching of fluorescence due to the formation of H-aggregates. Fluorescence spectroscopic analysis is significant to OPV and OLED applications.

2.5.3. Molecular Frontier Orbitals

The IP and EA may be estimated through cyclic voltammetry (CV) or differential pulse voltammetry (DPV), in which, the polymeric thin films (organic small molecules may be dissolved into an electrolyte solution for measurement) cyclically undergo an electrochemical redox process. CV and DPV characterization is carried out in a three-

electrode cell consisting of a platinum button working electrode, a platinum wire counter electrode, and a Ag/Ag+ reference electrode in a 0.1 – 0.5 M solution of electrolyte, which typically is $[nBu_4N]^+[PF_6]^-$ in acetonitrile. The ferrocene/ferrocenium redox couple (Fc/Fc^+) is typically used as the internal standard. Cardona et al.[167] and Stalder et al.[54a] suggested setting the potential of Fc/Fc^+ at -5.08 eV versus vacuum. In the case that Fc/Fc^+ overlaps with the oxidation wave of the sample being measured, $CcPF_6$ redox couple can be used as the internal standard. The redox wave of $CcPF_6$ is 1.33 eV lower than that of $FcPF_6$.[33] Accordingly, $CcPF_6$ has an absolute potential of -3.75 eV versus vacuum. The material is oxidized under a positive scanning voltage (typically from 0 to +2 V for organic and polymeric semiconductors); while it is reduced under negative scanning voltage (0 to -2 V). The onset positions of the oxidation and reduction waves on an *I-V* curve relate to the ionization potential (IP) and electron affinity (EA) of the materials under characterization. The corresponding electronic bandgap (E_g^{elec}) is calculated by taking IP and subtracting the absolute value of EA, that is E_g^{elec} = IP - |EA|.[161] Electrochemically stable materials show constant oxidation and reduction waves under repeated electrochemical scan cycling. Based on Koopmans' theorem, the first IP of the material is identified with the negative of the orbital energy of the HOMO, while EA could be considered as the LUMO energy level. However, this approach is controversial and does not match well with experimental results. It worthies noting that upon CV and DPV characterization, the polymer films cast onto the working electrode

interact with the surrounding liquid electrolyte, which leads to the polymer deviating from the intrinsic state because of the overall experimental conditions. Hence, the experimental results are expected to be different from the intrinsic IP and EA of the materials in question.

A more precise approach to explore the ionization potential of a molecule or polymer is through ultraviolet photoelectron spectroscopy (UPS), in which the molecule, after absorbing an ultraviolet photon, emits an electron from the HOMO and leaves a ground-state ion. This measurement is conducted under an ultrahigh vacuum (UHV) environment at 10^{-9} torr. This environment better resembles real film conditions than the liquid based CV/DPV methodologies. Typically the ultraviolet incident photon is discharged from He I with energy ($h\nu$) of 21.22 eV. The resulting EA hence could be estimated by EA = IP – E_g^{opt} – binding energy.

2.5.4. Thermal Properties

The decomposition temperature (T_d) of organic and polymeric semiconductors is measured by thermal gravimetric analysis (TGA), in which the sample is heated under a nitrogen environment and the sample weight is recorded. The temperature at which the sample weight drops by 5 wt% is termed T_d. This process, however, is not able to detect

changes in molecular structure or cleavage of polymer chains that commonly occurs during the material heating process and may dramatically change materials properties.

Differential scanning calorimetry (DSC) characterizes the thermal transitions of materials under heating and cooling cycles, during which the glass transition temperature (T_g), melting temperature (T_m), and re-crystallization temperature (T_c) are recorded. Materials showing multiple melting and re-ordering temperatures imply the existence of meso-phase transitions. Polarized optical microscopy is employed to confirm the presence of liquid crystalline phases. Organic and polymeric semiconductors having rigid π-conjugated aromatic units with flexible alkyl side chains might form liquid crystalline phases. For instance, the p-type oligomers TPTTPT[41a] and BTBT-C8,[40a] and n-type oligomers substituted NDI[168] and NDI-DTYM2[169] showed liquid crystalline phase transitions in DSC and/or X-ray scattering characterization. For polymers, a lyotropic liquid crystalline phase was observed in P3HT films.[170] PTPhN shows a smectic phase upon thermal cycling.[171] Besides, conjugated polymers PAF,[172] F8T2,[173] PBTTT,[16c] and PQTBTz-C12[145a, 174] were considered as liquid crystalline materials as well. Materials in a liquid crystalline phase are expected to exhibit more long-range order that might enhance macro-scale charge carrier transport, one crucial parameter in organic electronics.[175] Therefore, it is reasonable to thermally anneal organic and polymeric semiconductors, which exhibit a liquid-crystalline meso-phase regime with the aim of

inducing the formation of long-range order within thin-films. For instance, polymer PQTBTz-C12 exhibited an approximate one order of magnitude increase in field-effect hole mobility with the formation of a liquid-crystalline phase upon thermal annealing treatment.[145a] It is worthy to mention that certain alkyl side chains, such as the dodecyl side chain in poly(3-dodecylthiophene), undergo melting and re-ordering transitions upon the thermal heating and cooling process.[176] In DSC characterization, the results shown in the 1st thermal cycling include the thermodynamic history of the material being measured; the transition behaviors shown after the 2nd cycling demonstrate intrinsic thermodynamic properties. Amorphous organic or polymeric materials show no transitions on thermal cycling.

2.5.5. Thin-film surface morphology

Charge carrier transport performance highly correlates with the molecular or polymeric morphology (ordering and orientation), which could be characterized by electronic microscopes, such as atomic force microscopy (AFM), transmission electron microscopy (TEM), and scanning electron microscopy (SEM). Organic and polymeric semiconductors have a variety of nano-scaled morphological features, such as nano-wires shown in P3HT, P(NDI2OD-T2), and PQT-12, nano-fibers shown in PBT6, and nano-terraces appearing in small molecules such as NDI-DTYM2, TIPS-pentacene, and the

polymers PBTTT and pTBTD-OD, under AFM and TEM analysis. An approach to developing polymer semiconductor nanowires with lengths in the range of a tenth of a micron and diameters that are in the range of hundreds of nanometers was recently developed:[177] polymers were completed dissolved into solvents to afford dilute polymeric solutions (0.1-0.5 $g.L^{-1}$) at 40-50 °C. After filtration, the filtrate solution was allowed to site for over 1 week to grow polymeric nanowires. The resulting nanowires exhibited highly ordered structures: for certain nanowires single-crystal regimes were recognized via selected area electron scattering (SAED). This approach has been successfully applied to P3HT,[177d] DPP-based,[177e] benzothiadiazole-based,[177a] and thiazolothiazole-based[177b] D-A polymeric semiconductors; the nanowires were incorporated into OFETs and exhibited much higher field-effect mobilities compared with their thin-films counterparts formed by solution-processing. For instance, P3HT based nanowires exhibited an average μ_h of 3.8 $cm^2V^{-1}s^{-1}$ of; while its μ_h is in the range of 10^{-2} $cm^2V^{-1}s^{-1}$ for solution-processed films.[177c]

For AFM characterization, the roughness suggests the degree of thin-film crystallinity. The film with a high degree of crystallinity possess a high degree of roughness, while amorphous materials exhibit a more uniform film. Typically, polymeric semiconductors have semi-crystalline structures display roughness in the range of 1-10 nm. As discussed above, efficient charge carrier transport takes place close the bottom surface of

semiconductor films in BGBC and BGTC transistors, and the top surface of semiconductor films on TGBC and TGTC counterparts. Organic and polymeric thin-films pre-deposited onto Si-wafers could be isolated after being submerged in hydrofluoric acid. The semiconductor thin-film morphology characterization thereby would be discerned on top surface for TGBC and TGTC transistors and on bottom surface for BGBC and BGTC devices.

High-resolution TEM (HR-TEM) is able to unveil the π-π stacking distance between polymeric chains. For instance, polymers PQT-12,[54b] PDPP2T-TT-OD,[27a] and poly(tetraazabenzodifluoranthene diimide)s[58] showed π-π stacking distances in a range of 3.5 - 4 nm under HR-TEM. The electron-beam intensity should be kept as low as possible (< 200 keV in typical cases) to avoid any damage to organic and polymeric semiconductor thin-films.

2.5.6. Microstructure within Thin-Films

The microstructure of organic and polymeric semiconductor thin-films could be characterized by grazing incidence wide-angle X-ray scattering (GIWAXS).[146a, 178] Herein the grazing angle of the incident beam is necessary due to the thin-film character (nanometer to micrometer scale). With the aim of enhancing the diffraction intensity and reducing substrate scattering, the grazing incidence angle should be below the critical

angle of total reflection from the substrate, but above the critical angle for the organic or polymeric film, In real cases, the incidence angle is set to *ca*. 0.1-1° to enhance the sensitivity to thin-films.[16c, 88, 146a] A synchrotron beamline with a high X-ray photon flux and beam collimation is beneficial to explore polymeric thin-films that typically have weak or low crystallinity.[160] One-dimensional grazing incidence wide-angle X-ray scattering (1D-GIWAXS) merely detects the X-ray diffraction from thin-films in the out-of-plane regime; and two-dimensional grazing incidence wide-angle X-ray scattering (2D-GIWAXS) is able to detect the X-ray diffraction in both the out-of-plane and in-plane regimes, which allows exploration of the material orientations within films, as shown in Figure 2.35. Polymeric semiconductors typically show edge-on orientation and face-on orientation on a substrate. These two orientation schemes and their corresponding 2D-GIWAXS patterns are shown in Figure 2.36. The edge-on orientation accelerates charge carrier transport in the horizontal direction which benefits OFET applications; while the face-on orientation facilitates charge carrier transport in the vertical direction which is beneficial in OPV and OLED applications. Recent investigations indicated that some polymers such as P3HT [146a] and PTzQT[55] showed alternation of orientation in polymer chains from a face-on orientation on a hydrophilic substrate to an edge-on orientation on a hydrophobic substrate.

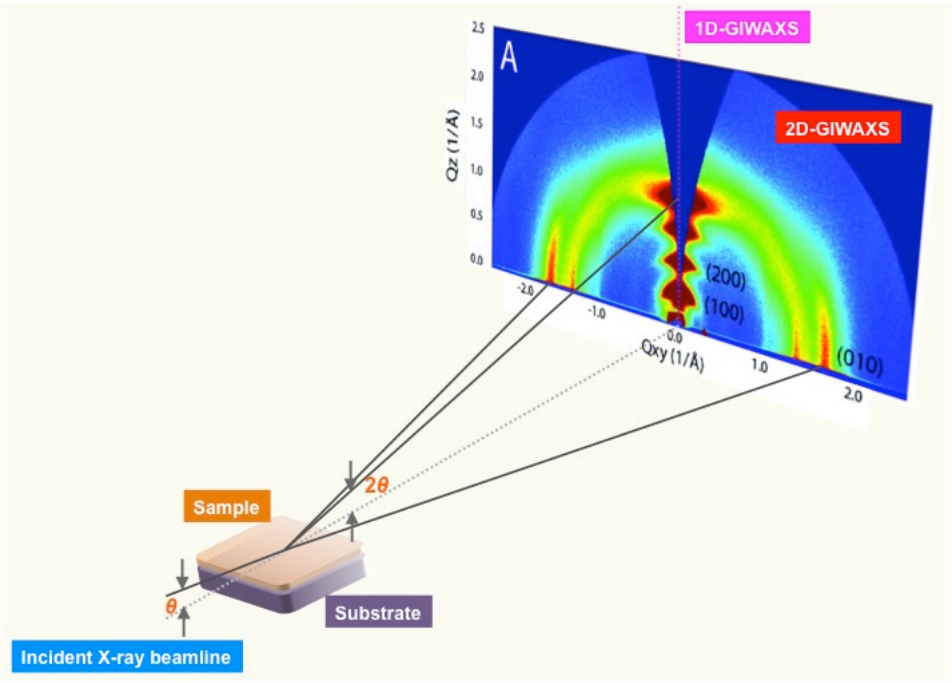

Figure 2.35. The scheme of 2D-GIWAXS characterization to one sample. The incidence and diffraction angles are θ and 2θ, respectively. An edge-on oriented polymer pattern is shown: <100> and <200> are at out-of-plane regime and <010> is at in-plane regime. The magenta colored dash-line in the middle of the 2D-GIWAXS pattern is the diffraction detection region for 1D-GIWAXS.

In general, polymeric semiconductors having an edge-on orientation exhibit <*h*00> patterns in the out-of-plane regime and <010> diffraction in the in-plane regime (Figure 2.36). The <*h*00> unveils the *d*-spacing distance between polymeric backbones separated by alkyl side chains as shown in Figure 2.37, if $h > 2$, that is <100>, <200>, and <300>, etc. are available in 2D-GIWAXS patterns, the polymeric semiconductor measured forms a laminar structure in the crystalline lattice. The corresponding *d*-spacing distance could be calculated based on Bragg's Law. The average molecular length of a methylene bond (-CH_2-) is approximately 1.5 Å, based on which the linear side chain length could be estimated.

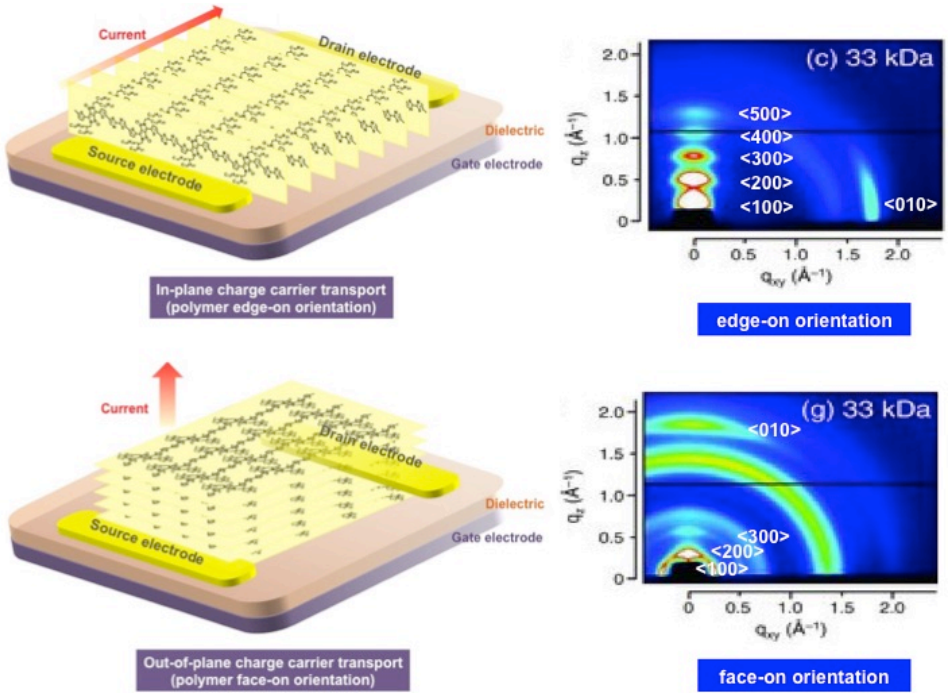

Figure 2.36. Schemes of polymer edge-on orientation and face-on orientation, and their corresponding 2D-GIWAXS patterns. The GIWAXS images were reproduced from literature (*Adv. Mater*. 2012, 24, 425).[55]

If the *d*-spacing distance is less than the total lengths of two side chains, side chain packing within the lattice follows an interdigitated model; otherwise, side chains pack as the end-to-end model (Figure 2.38). The <010> diffraction demonstrates the π-π stacking distance between the polymeric backbone, as shown in Figure 2.36 and 2.37. The typical π-π stacking distance derived from (010) is in the range of 3.5 – 4 Å. Generally, the narrowing of the π-π stacking distance enhances electronic coupling (transfer integral, *vide supra*) between chains leading to enhanced interchain interactions and charge carrier mobility. Oppositely, polymers possessing face-on orientations have <*h*00> in the in-plane regime while <010> in the out-of-plane regime on 2D-GIWAXS patterns, as shown in Figure 2.36.

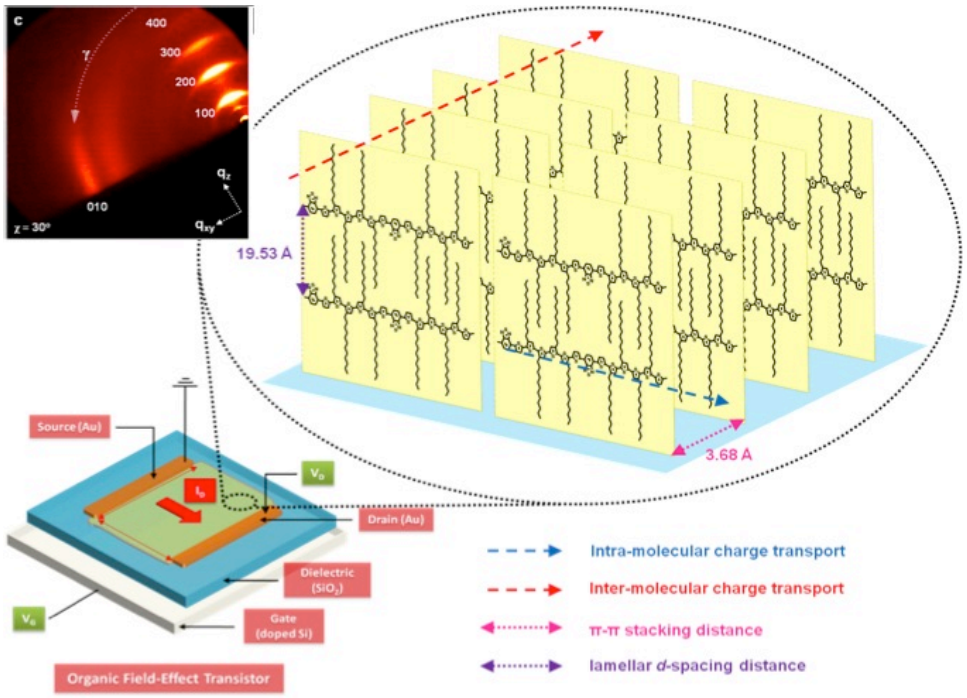

Figure 2.37. The <*h*00> and <010> in 2D-GIWAXS patterns of PBDT6 and their corresponding laminar d-spacing and π-π stacking distances in the edge-on packing.[33]

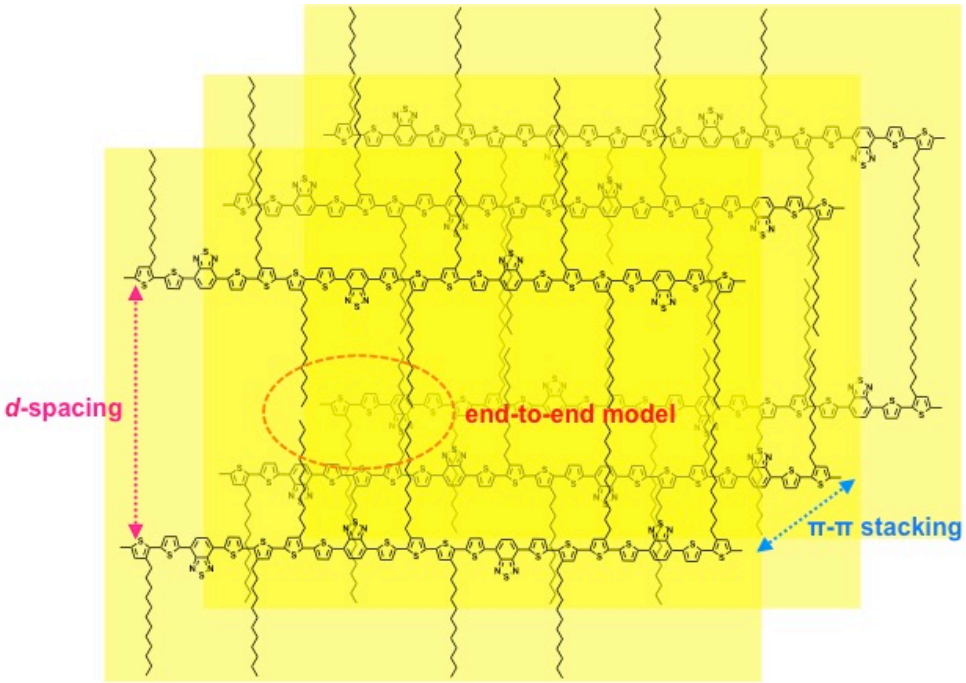

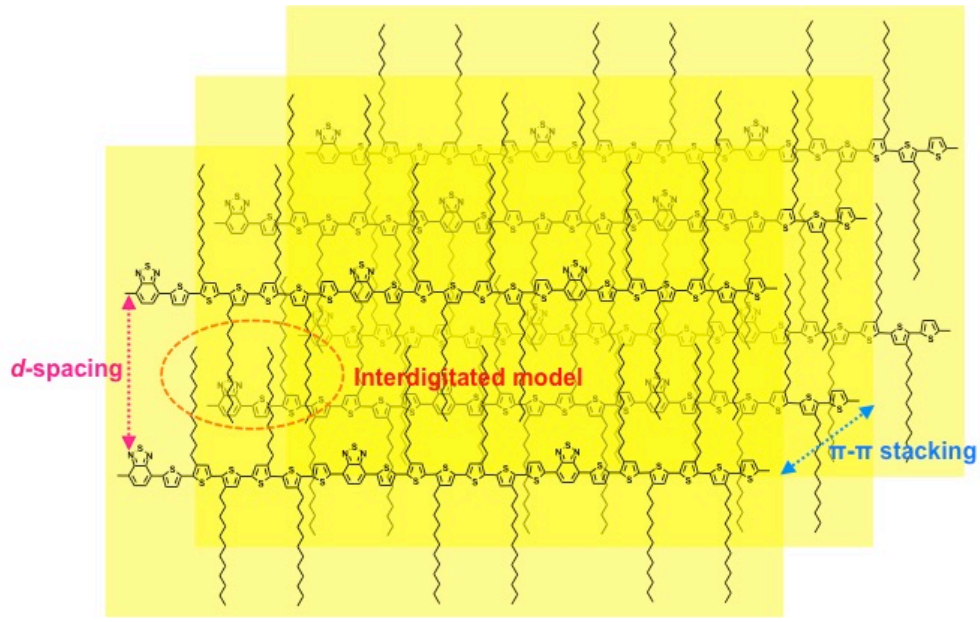

Figure 2.38. Schemes of polymer side chain packing follows end-to-end packing model (up) and interdigitated packing model (down).

The coherence length (τ) along (h00) and (010) can be calculated via the Scherrer equation:

$$\tau = \frac{K\lambda}{\beta Cos\theta} \qquad \text{Eq. 2.3.1.}$$

where K is a dimensionless shape factor (0.9); λ refers to the incidence X-ray wavelength (1.54059 Å in this study); β represents the full-width-at-half-maximum (FWHM, radians) of <100> and <010> peaks along 2θ direction; and θ denotes to Bragg angle. The coherence length indicates the average size of the ordered (crystalline) domains that may be smaller or equal to the grain size within films. The FWHM values for the <200> and <300> diffractions relative to that of the <100> diffraction (i.e., $FWHM_{<200>}/FWHM_{<100>}$ and $FWHM_{<300>}/FWHM_{<100>}$) suggest the cumulative ordering within the crystalline

lattice. The increase of $FWHM_{<200>}/FWHM_{<100>}$ and $FWHM_{<300>}/FWHM_{<100>}$ suggests an increase in the cumulative disorder.[179]

The degree of arc in <*h*00> and <010> diffractions indicates the degree of orientation of polymeric chains on substrates. As shown in Figure 2.36, the narrowing of arc in <100> refers to the increase in the edge-on orientation. The film orientation distribution is investigated by Herman's orientation function (*S*), as shown in Equation 2.3.2 and 2.3.3:

$$f = \frac{\int_0^{\pi/2} I(\chi) Cos^2(\chi)\, Sin(\chi) d\chi}{\int_0^{\pi/2} I(\chi)\, Sin(\chi) d\chi} \qquad \text{Eq. 2.3.2}$$

$$S = \tfrac{1}{2}(3f-1) \qquad \text{Eq. 2.3.3}$$

For instance, Figure 2.39 shows the <100> and <010> peak distributions along with χ, within a polymer PDBTz film cast from *o*-xylene. To simplify the calculation, χ was defined as 0° at the q_z axis (out-of-plane), and as 90° at the q_{xy} axis (in-plane). The $I(\chi)$ term is the <100> or <010> intensity at each χ, and sin(χ) represents a geometric intensity correction factor. The molecular orientation parameter, *f*, refers to the average lattice plane orientation relative to χ_{max}, the azimuthal angle at which $I(\chi)$ approaches the maximum. According to Eq. 2.3.3, S = 1, if on average, the lattice planes completely align parallel to χ_{max}; S = -1/2 if they completely orient perpendicular to χ_{max}; while S = 0 if the lattice planes orient randomly. The detailed discussion of the orientation distribution of polymer PDBTz is shown in Chapter 5. Herman's orientation function

could also estimate the texture of films along a given direction. Lu et al. recently analyzed the texture of P3HT thin-films cast by a micropillar-casting approach via Herman's orientation function, quantitatively demonstrating a high degree of orientation along the texture direction.[180]

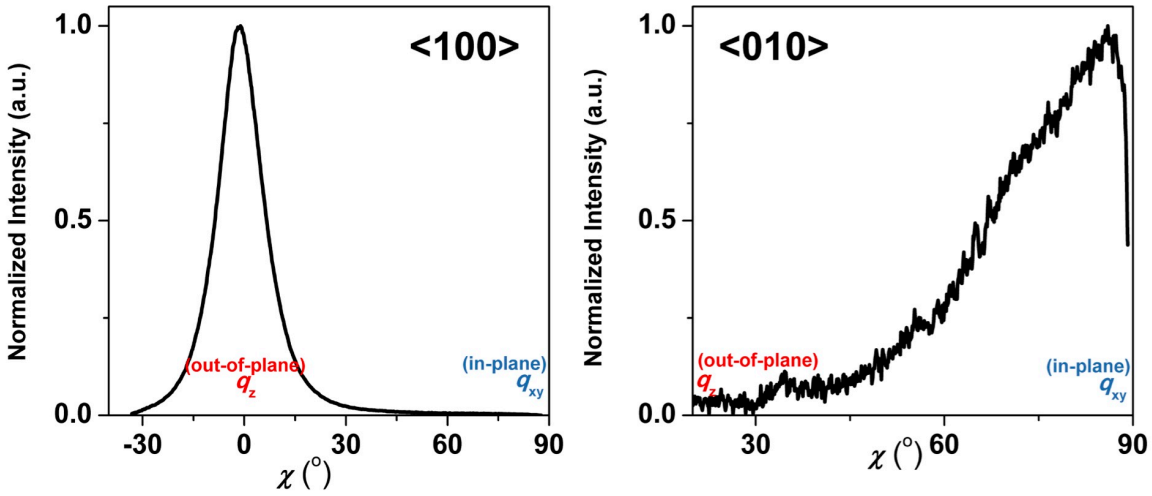

Figure 2.39. The intensity distribution of the <010> and <010> peaks of PDBTz (please see Chapter 5) films along the χ axis from q_z (out-of-plane, $\chi = 0°$) to q_{xy} (in-plane, $\chi = 90°$).

Most polymers have both crystalline and amorphous regions. The degree of crystallinity (DoC) is defined as the ratio of the crystalline region to the amorphous region.[178c] In X-ray scattering patterns, the diffraction peaks fitting the Gaussian distribution denote the diffractions from the crystalline domain; while the board bands in X-ray scattering patterns represent signals from the amorphous region. However, it is quite challenging to determine the reference materials in completely crystalline and entirely amorphous conditions. The alternative analysis is to compare the DoC of one

film to that of the other film cast from the same material to afford the relative degree of crystallinity (rDoC). For rDoC analysis to the anisotropic films, it is necessary to analyze the diffraction patterns over all orientations, in order to eliminate the error originating from the differences in intensities of diffraction peaks measured in the specular geometry.

Besides GIWAXS, neutron scattering and selected area electron diffraction (SAED) coupled with HR-TEM are able to analyze the microstructure of thin films. Small angle X-ray scattering (SAXS) is required to explore the aggregation of polymers within solutions or solids.[88, 181]

2.5.7. Hansen Solubility Parameters

Solute-solvent intermolecular interactions could be estimated via cohesive energy density (*E/V*), an energy required to move a unit volume of molecules from their neighbors to infinite separation.[182] Cohesive energy density could be described via three Hansen Solubility Parameters (HSPs), including the dispersion force solubility parameter (δ_d), dipolar intermolecular force solubility parameter (δ_p), and hydrogen bonding solubility parameter (δ_h), as shown in Eq. 2.3.4:

$$E/V = \delta_d^2 + \delta_p^2 + \delta_h^2 \qquad \text{Eq. 2.3.4}$$

where *E* refers to total cohesive energy required to move molecules having a volume of *V* from neighbors to infinite separation. One polymer and its solvents could be marked on

Hansen Space, a 3-dimensional Cartesian coordinate consisting of 3 HSPs, depending on their HSPs, as shown in Figure 2.40. The distance between polymer and solvent on Hansen Space is termed as R_a:

$$R_a = \sqrt{4(\delta_{d1} - \delta_{d2})^2 + (\delta_{p1} - \delta_{p2})^2 + (\delta_{h1} - \delta_{h2})^2} \qquad \text{Eq. 2.3.5}$$

The less the R_a term is, the less *E/V* between solute and solvent, that is, the less thermodynamic driving force for phase separation of solute from solvent resulting in better solubility. In Figure 2.40, a Hansen sphere of a polymer was determined via locating HSPs as the sphere center and the interaction radius (R_0) as the radius. R_0 is determined by one marginal solvents to the target solute, for example, chloroform is commonly selected as the marginal solvent to P3HT in determining R_0 of P3HT. The relative cohesive energy ($RED = R_a / R_0$) is employed to assess the miscibility between solute and solvent such that: $RED > 1$ suggests a miscible regime, corresponding to the fact that are solvents located within the Hansen sphere in Figure 2.40; for $RED = 1$ the polymer is partially miscible, corresponding to solvents locating at the sphere boundary; and $RED > 1$, solvents locating outside the sphere.

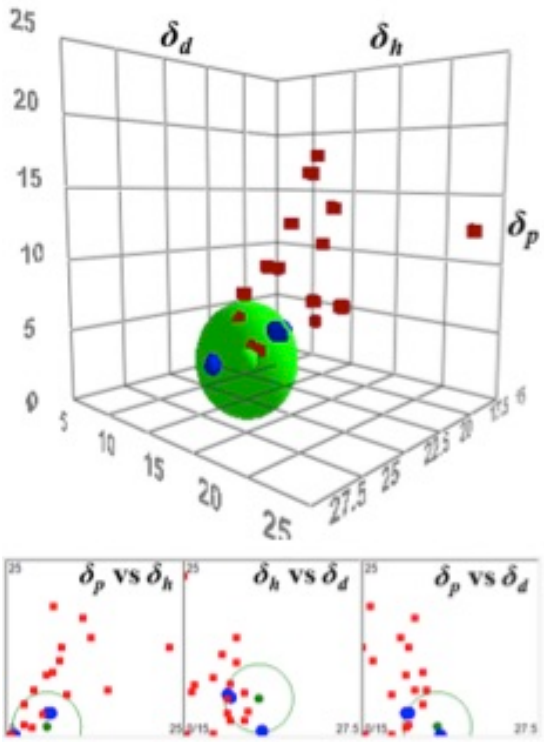

Figure 2.40. Hansen solubility parameter diagrams for PDBTz and selected solvents. Solvents in the green circle are considered to be good solvents for PDBTz; while solvents far away from the green circle are poor solvents.

CHAPTER 3

HIGH CHARGE CARRIER MOBILITY, LOW BANDGAP D-A BENZOTHIADIAZOLE-OLIGOTHIOPHENE BASED POLYMERIC SEMICONDUCTORS

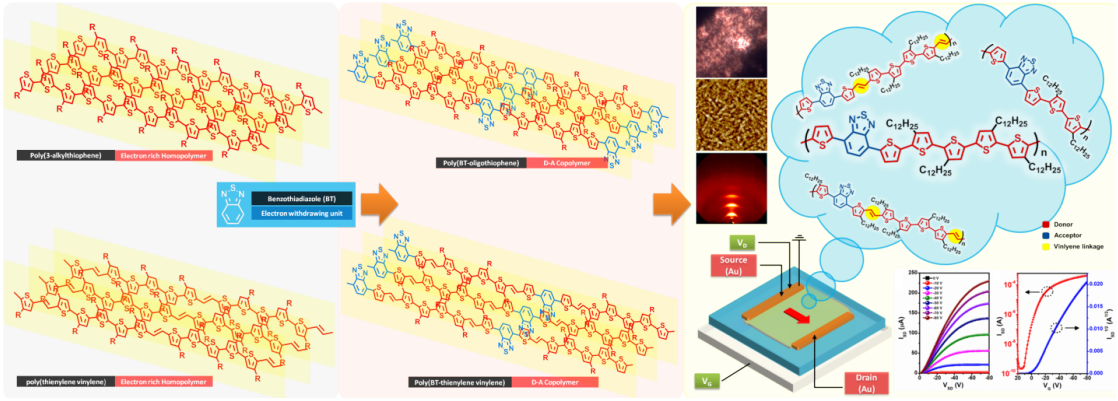

3.1 Abstract:

A series of benzothiadiazole oligothiophene and oligo(thienylene vinylene) donor-acceptor (D-A) copolymers were synthesized and characterized. These low optical bandgap materials (~1.5 eV) are capable of absorbing photons in the range of 400 to 800 nm and exhibit good thermal stability. Their hole mobilities, determined using an organic field effect transistor (OFET) architecture, vary over a range of three orders of magnitude and strongly correlate with the molecular ordering and morphology of the respective thin films. Spin-coated films of the poly(benzothiadiazole-sexithiophene) **PBT6**, which

exhibits a highly crystalline lamellar π-π stacked edge-on orientation on the OFET substrate, possesses a hole mobility of ca. 0.2 cm^2/Vs. Vinylene containing analogs **PBT6V2** and **PBT6V2'** are amorphous and exhibit very low mobilities. The molecular weight of **PBT6** has a strong influence on the electronic properties: a sample with a lower molecular weight exhibits a mobility approximately one order of magnitude lower than the high molecular weight homolog, and the absorption maximum is appreciably blue-shifted. The hole mobility of **PBT6** is further enhanced by a factor of ca. 3 through fabrication of the OFET by drop-casting. OFETs fabricated by this process exhibit mobilities of up to 0.75 cm^2/Vs and $I_{ON/OFF}$ ratios in the range of 10^6 to 10^7. These results demonstrate the potential of incorporating benzothiadiazole units into polythiophene derivatives to develop high mobility semiconducting polymers.

3.2. Introduction

As discussed in Chapter 1 and 2, polymeric semiconductors possess a combination of properties that are advantageous for the fabrication of large-area, light-weight and low-cost flexible plastic electronics.[3b, 16c] Although significant progress has been made, polymeric semiconductors, such as poly(3-hexylthiophene), P3HT,[17b, 89, 183] and poly(2,5-thienylene vinylene)[184] typically exhibit low charge carrier mobility, low ambient stability which limit their commercialization potential.[2b, 3b, 16c] From a

molecular perspective, the charge carrier transport properties and bandgap are determined by intra- and intermolecular π-electronic coupling; while stability in air may be enhanced by incorporating electron deficient groups that lead to a reduction in electron density (and thereby lower IP of polymers).[14d, 129a, 185]

The electron deficient benzothiadiazole (**BT**) unit has recently been explored in the development of organic semiconductors for optoelectronic applications.[71, 186] In this study, we incorporated the **BT** acceptor into electron-rich (donor) polythiophene and poly(thienylene vinylene) chains with the aim of addressing the deficiencies associated with current materials. Four such donor-acceptor (D-A) copolymers have been synthesized and characterized: poly(benzothiadiazole-quaterthiophene) **PBT4**, poly(benzothiadiazole-sexithiophene) **PBT6**, and poly(dithieno-benzothiadiazole-vinylene-quaterthiophene)s **PBT6V2** and **PBT6V2'** as shown in **Figure 3.1.** (the latter pair of polymers differ in the number of dodecyl substituents in each repeat unit).

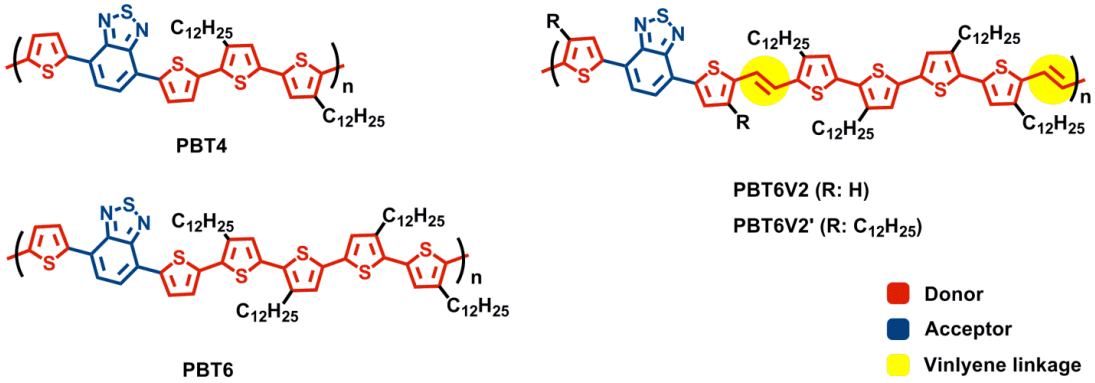

Figure 3.1. Molecular structures of benzothiadiazole-oligothiophene D-A copolymers (**PBT4**, **PBT6**, **PBT6V2** and **PBT6V2'**).

The D-A character is expected to support intramolecular charge transfer (ICT) from the electron donating oligothiophene units to the electron accepting **BT** units. This should result in a decrease in electron density compared to analogous polythiophenes, and thereby improve the ambient stability of the polymers. This feature should also narrow the bandgap, thus extending the photon absorption range to a higher wavelength region relative to polythiophene, which is a crucial factor in the development of efficient OPVs.[187] In addition, the planar nature of the fused heteroaromatic **BT**, in combination with the match between the electronic structures of BT and the donor segments, might facilitate π-π intermolecular interactions between adjacent polymer chains and benefit intermolecular charge carrier mobility.[127i]

The design and syntheses of these BT-oligothiophene polymers are described, along with their optical, thermal, morphological and electronic properties. The hole transport performance of these polymers correlates with molecular order within the films (crystallinity and orientation), molecular configuration (presence of side-chains and vinylene linkages), and molecular weight. Spin-coated semi-crystalline **PBT6** films exhibit hole mobilities of ca. 0.2 $cm^2/V.s$ in an OFET configuration. Fabrication of **PBT6** films by drop-casting resulted in a further increase in hole mobility by a factor of ca. 3, up to 0.75 cm^2/Vs and $I_{ON/OFF}$ ratios in the range of 10^6 to 10^7.

3.3. Results and Discussion

3.3.1. Polymer Design and Synthesis

To evaluate the impact of the ratio of electron-rich thiophene rings to electron-deficient **BT** units on the optical and electronic properties of the resultant polymers, **PBT4** and **PBT6** were designed with four and six thiophene units per **BT** in each repeat unit, respectively. **PBT6** possesses two additional dodecyl-chains per repeat unit relative to **PBT4**, which should favorably impact polymer solubility. In comparison to **PBT6**, **PBT6V2** has an electron rich vinylene linkage connecting quaterthiophene and dithienobenzothiadiazole (**DTB**) units that might elevate the electron donating properties of the donor segment and thereby favor D-A interactions.[188] The incorporation of side chains at the 4-positions of the thiophene rings of the **DTB** units of **PBT6V2** to provide **PBT6V2'** is expected to further improve polymer solubility.

Synthetic routes leading to the four polymers are outlined **Figure 3.2-3.4**. The synthesis of **PBT6** made use of 4,7-bis(3'-dodecyl-[2,2'-bithiophen]-5-yl)benzo[c][1,2,5]thiadiazole, **BDTDTB**, which was synthesized by Pd(0)-catalyzed Stille coupling of 2-thienyltributylstannane to 4,7-dibromobenzo[c][1,2,5]thiadiazole to afford **1**, followed by metallation to afford distannane **M1** and subsequent coupling with **2** (**Figure 3.1**). In preparation for a Stille polymerization, **BDTDTB** was subjected to bromination with NBS to afford dibromo monomer **M2**, and to metallation to give

distannane **M3**. Bithiophene monomers **M4** and **M5** were prepared according to literature procedures (**Figure 3.1**).

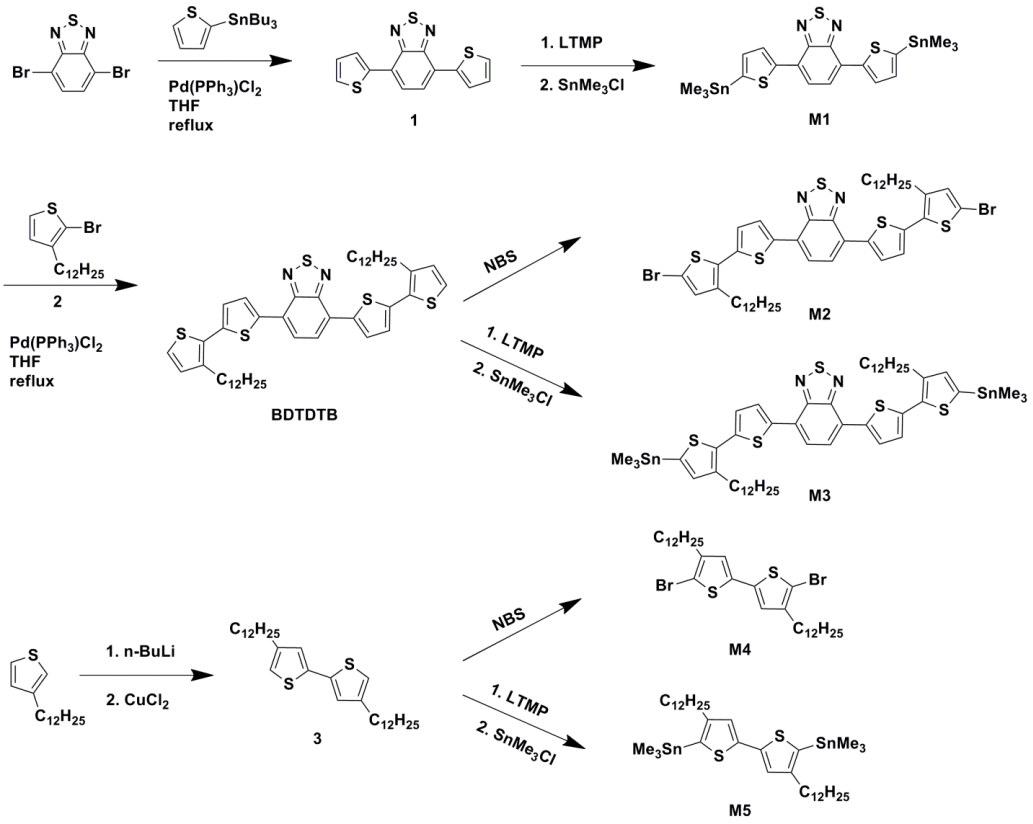

Figure 3.2. Preparation of dibromide and bisstannane monomers **M1-5**.

We envisioned preparing the vinylene polymers **PBT6V2** and **PBT6V2'** by Horner–Wadsworth–Emmons polymerizations of dialdehyde monomer **M8** with bisphosphonate monomers **M6** and **M7**, respectively. Dialdehyde **4** was prepared by a Suzuki coupling of 4,7-dibromobenzo[c][1,2,5]thiadiazole and 5-formylthiophene-2-boronic acid (**Figure 3.3**). Dialdehyde **4** was reduced to diol **5** upon treatment with $NaBH_4$; **5** was then converted to bis(chloromethyl) compound **6** upon reaction with $SOCl_2$. A Michaelis–Arbuzov reaction of **6** with triethyl phosphite afforded bisphosphonate monomer **M6**. To

construct bisphosphonate **M7**, dithienobenzothiadiazole **8** was subjected to a Vilsmeier–Haack reaction to afford dialdehyde **9**,[189] which was converted into the bisphosponate monomer in 3 steps. Monomer **M4** was subjected to Stille coupling with (4-dodecyl-2-thienyl*)*tributylstannane (**7**) to afford quarterthiophene **12**, and a Vilsmeier–Haack reaction provided dialdehyde monomer **M8** (**Figure 3.4**). Attempts to brominate **12** to give monomer **M9** led to the formation of inseparable byproducts as a result of reaction at the β-carbon of the thiophene rings.

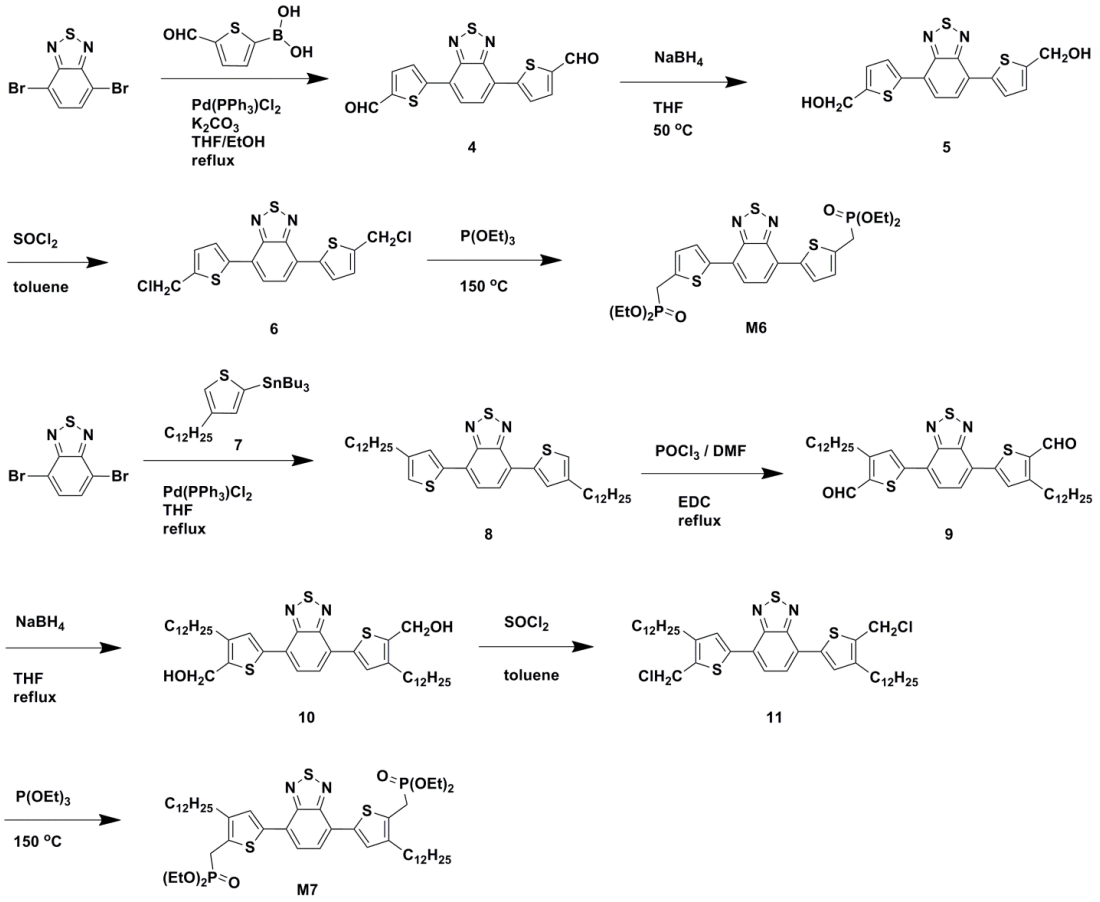

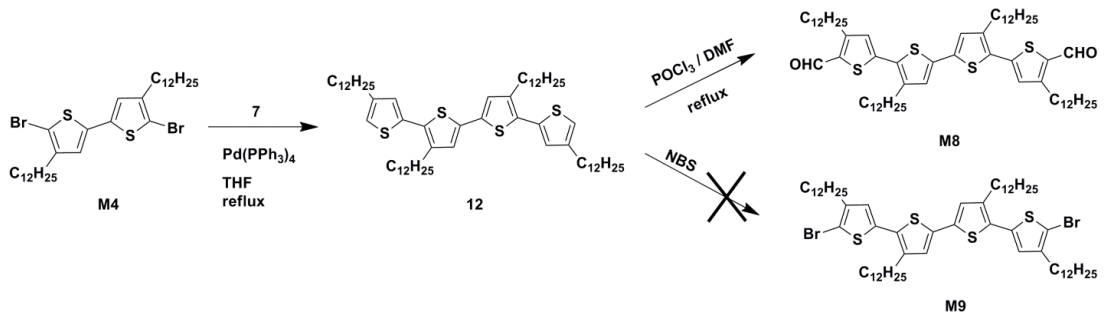

Figure 3.3. Preparation of bisphosphonate and dialdehyde monomers **M6-8**.

PBT4 was prepared by the Stille polymerization of bis(stannane) monomer **M1** and dibromide monomer **M4**. Two routes were explored for the preparation of **PBT6** - Stille copolymerization of (i) bis(stannane) **M3** with dibromide **M4**, and (ii) dibromide **M2** with bis(stannane) **M5**. Gel Permeation Chromatography (GPC) indicated that the molecular weight (MW) of **PBT6** prepared through cross coupling of **M3** with **M4** (number average molecular weight, M_n: 18.1 kDa, degree of polymerization, DP = 13.9) is approximately twice that achieved from the coupling of **M2** and **M5** (labeled as **PBT6(L)**, M_n: 8.6 kDa, DP = 6.6). The lower MW of **PBT6(L)** may be attributed to the low purity of **M5** (which contained ~14% of the monostannyl derivative of **3**, as determined by ^{1}H NMR spectroscopy) that impedes formation of high MW polymer during the step-growth polymerization. The results of GPC characterization of **PBT4**, **PBT6V2** and **PBT6V2'** are shown in **Table 3.1**.

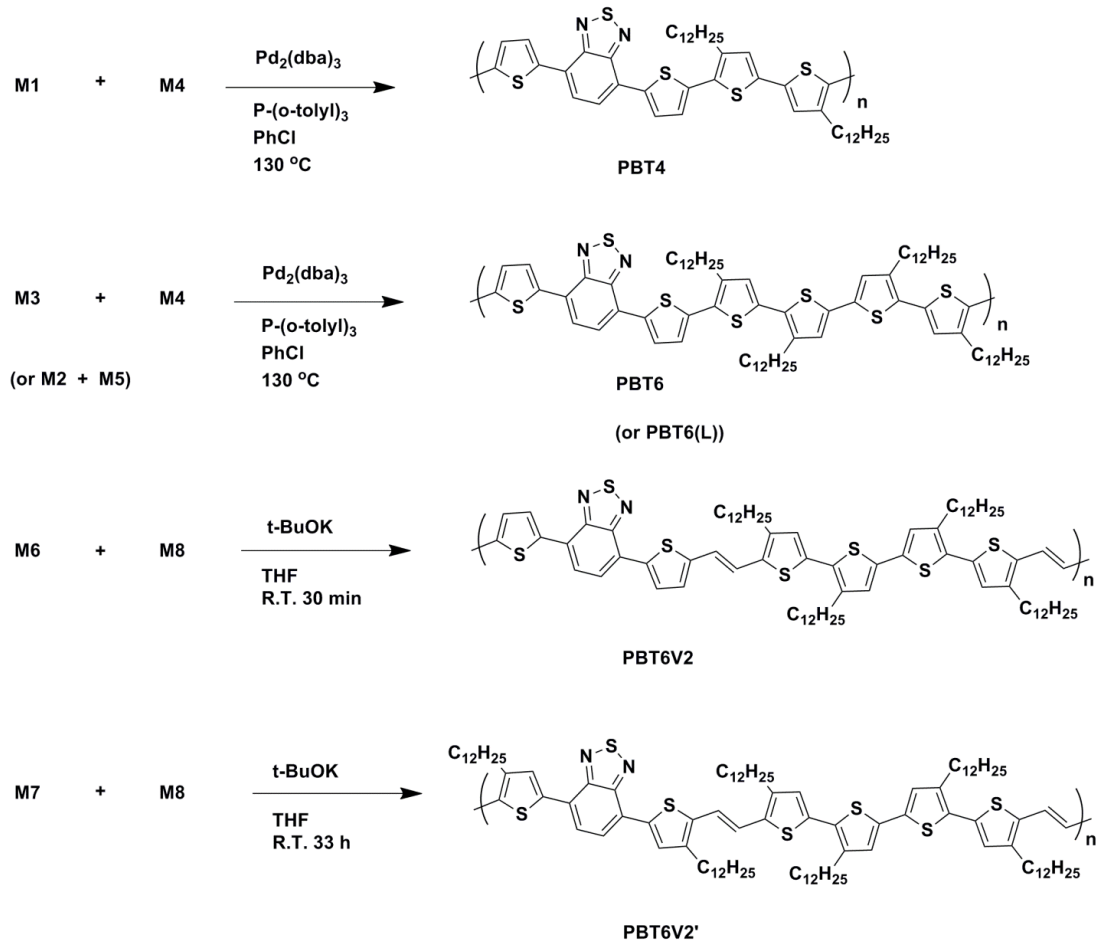

Figure 3.4. Polymerzations of **PBT4**, **PBT6** / **PBT6(L)**, **PBT6V2** and **PBT6V2'**.

3.3.2. Photophysical Properties

The optical absorption spectra of the copolymers (**PBT4**, **PBT6**, **PBT6V2** and **PBT6V2'**) and oligomer BDTDTB are shown in **Figure 3.5**. In solution (**Figure 3.5a**), the copolymers exhibit absorption bands at significantly higher wavelengths than BDTDTB, thereby demonstrating an extension of the conjugation length that results from intramolecular electron delocalization. The same tendency is apparent upon comparison

of the spectra of homologs 4,7-bis(thien-2-yl)-2,1,3-benzothiadiazole (DTB) (λ_{abs} = 308, 446 nm), oligomer BDTDTB (λ_{abs} = 348, 499 nm), and polymer PBT4 (λ_{abs} = 403, 569 nm), as shown in **Figure S3.1** (Supporting Information-1). A bathochromic shift is also apparent for all five materials in going from solution (**Figure 3.5a**) to thin films (**Figure 3.5b**), indicating enhanced order in the solid state that may be ascribed to interchain π-π

Table 3.1. Photophysical (absorption and emission), electrochemical properties and molecular weights of benzothiadiazole-oligothiophene polymers and oligomer.

Sample	λ_{abs} / nm [a]		λ_{em} [b]	E_{opt} [c]	E_{ox} / HOMO [d]	M_n [e]	M_w [f]	PDI
	solution	film	/ nm	/ eV	/ eV	/ kDa	/ kDa	
PBT4	403, 569	456, 656	699	1.52	1.77 / -5.24	5.8	9.7	1.67
PBT6	428, 535	495, 677	666	1.54	1.80 / -5.27	18.1	36.5	2.02
PBT6V2	512, 588	560, 622	730	1.53	1.60 / -5.07	11.3	35.5	3.13
PBT6V2’	473, 582	512, 621	743	1.53	1.72 / -5.19	14.3	42.5	2.98
BDTDTB	348, 499	380, 560	650	1.79	1.79 / -5.26	-	-	-

[a] wavelength of peak maxima in UV/vis spectra; [b] wavelength of maxima in fluorescence spectra (excitation wavelength, λ_{ex} = 450 nm); [c] optical bandgap estimated from onset point (λ_{onset}) of absorption band of thin film: E_{opt} = 1240 / λ_{onset}; [d] E_{ox} was measured in 0.1 M solution of $[n\text{-}Bu_4N]^+[PF_6]^-$ in acetonitrile using $CcPF_6$ as the reference; [e] number average molecular weight; [f] weight average molecular weight

electronic coupling and/or planarization of the copolymer backbone.[190] All of the materials exhibit two absorption bands, as shown in **Figure 3.5**. The bands appearing at the lower wavelength (300-550 nm) correspond to the π-π* transition of the oligothiophene (in **PBT4**, **PBT6** and BDTDTB) or oligo(thienylene vinylene) (in **PBT6V2** and **PBT6V2’**) unit.[191] For instance, the $CHCl_3$ solution bands at λ_{abs} = 403 nm

and 428 nm for **PBT4** and **PBT6**, respectively, correspond to the typical absorption bands of α-quaterthiophene (λ_{abs} = 380 to 396 nm) and α-sexithiophene (λ_{abs} = ca. 426 nm) derivatives.[16b, 192] We propose that the bands at higher wavelengths (400-800 nm) result from intramolecular charge transfer (ICT) between the electron-deficient BT and electron-rich oligothiophene units. This conjecture is confirmed through observation of solvatochromism in the fluorescence and absorption spectra.[127d] For example, solutions of **PBT6** in solvents having different polarities and polarizabilities (**Table S3.1**) exhibit shifts in λ_{em} and λ_{abs} (**Figure 3.6**), indicative of the charge transfer nature of this peak. The ICT results in a narrowing of the optical bandgap (E_g^{opt}). The D-A BT-containing conjugated copolymers prepared here possess lower optical bandgaps as calculated from the onsets of absorbance (*ca*. 1.5 eV, **Figure 3.5b**), than polythiophenes (1.9-2.1 eV)[193] and poly(thiophene vinylenes) (1.7 eV).[194] The absorption bands of these new D-A polymers are well matched to harvest photons throughout the visible region (400-800 nm, **Figure 3.5b**), which makes them particularly interesting candidates for OPV applications.

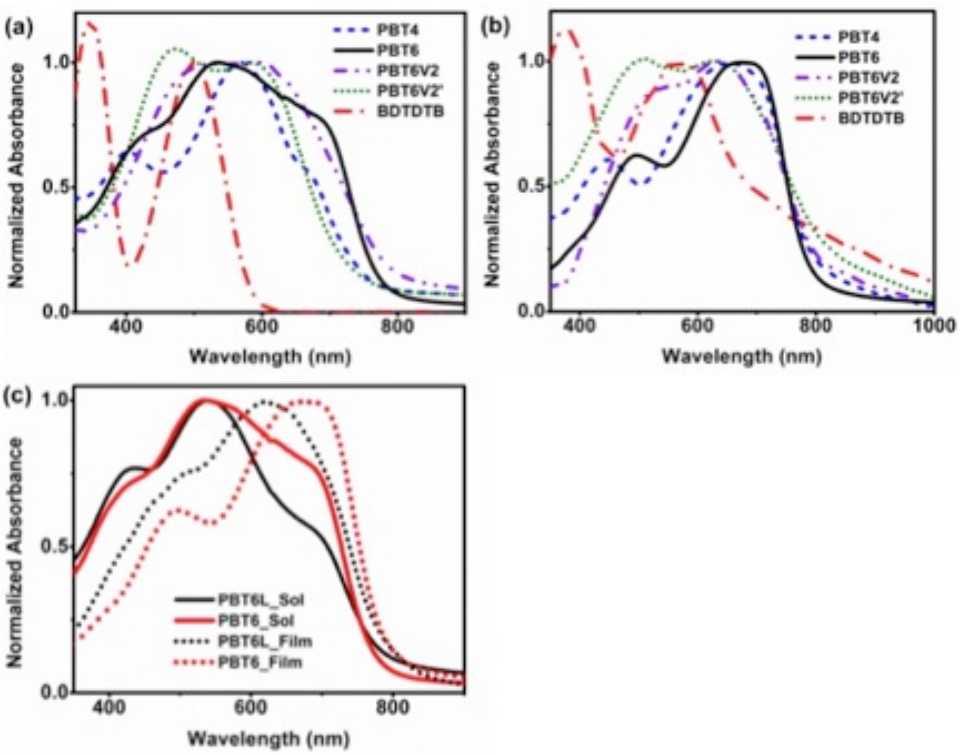

Figure 3.5. Absorption spectra of **PBT4**, **PBT6**, **PBT6V2**, **PBT6V2'** and **BDTDTB** in (a) chloroform ($CHCl_3$) solution and (b) as a thin film; and (c) the absorption spectra of **PBT6** (high MW, M_n: 18.1kDa and PDI: 2.02) and **PBT6(L)** (low MW, M_n: 8.6 kDa and PDI: 1.72) in solution (PBT6_Sol, PBT6L_Sol) and solid film state (PBT6_Film, PBT6L_Film) .

Additional absorption shoulders were observed at 670 nm and 690 nm in purple $CHCl_3$ solutions of **PBT4** and **PBT6** (**Figure 3.5a**) at room temperature. These features vanish upon heating and re-emerge upon cooling (**Figure S3.2 and S3.4**), a similar phenomenon exhibited by P3HT and related conjugated polymers arises from the presence of aggregates.[69, 89, 191a, 195] A thermochromic effect was also observed during the heating-cooling cycles in which λ_{abs} blue-shifted and shoulders vanished upon heating to afford a pink solution while λ_{abs} red-shifted and shoulders re-appeared upon cooling, returning to a purple solution (**Figure S3.2 – 3.4**). The observed aggregates are stable in solution at

room temperature and are not affected by dilution. For example, **Figure S3.5** shows that the shoulder observed in **PBT6** is apparent even in a very dilute solution (10^{-6} M) and that the relative absorbance of the shoulder in comparison to the two main bands remains constant. Compared with **PBT6**, the low MW counterpart, **PBT6(L)** (M_n: 8.6 kDa), displays a much weaker shoulder in the solution absportion spectrum (**Figure 3.5c**), suggesting more limited aggregation in solution likely due to the increased solubility relative to the higher MW material. In the solid state, the λ_{abs} of **PBT6** is red shifted by *ca*. 56 nm relative to **PBT6(L)** (**Figure 3.5c**), suggesting that the increased MW enhances electron delocalization within the system. Similar effects have been observed in P3HT.[97a] We postulate that the higher MW leads to a decrease in the number of defects originating from chain ends embedded within crystalline grains, thus benefiting chain ordering.[196]

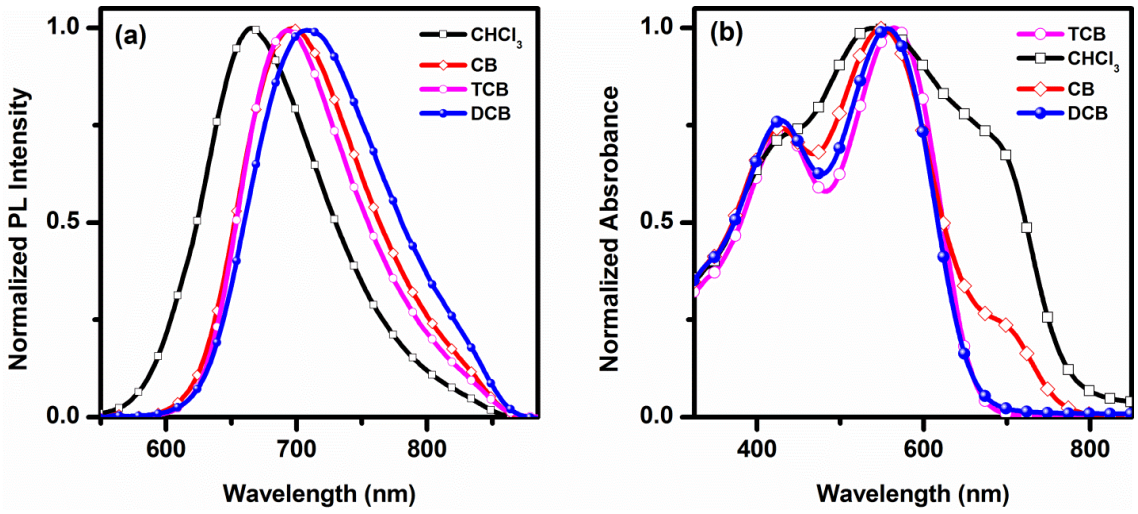

Figure 3.6. The shifts in emission ((a), ca. $2x10^{-6}$ M) and absorption spectra ((b), ca. $3.8x10^{-5}$ M) of **PBT6** in $CHCl_3$, CB, DCB and TCB.

The impact of incorporation of a vinylene linkage within the polymeric backbone on the conjugation length can be seen from the spectra in **Figure 3.5a**. In solution, **PBT6V2** exhibits a red shifted absorption compared to **PBT6**. The introduction of the vinylene moiety might promote D-A ICT due to its electron donating properties. However, **PBT6V2'** displays a blue shift in the absorption compared to **PBT6V2**, which may be attributed to the two dodecyl chains at the 4 positions of the two thiophenes within the **DTB** unit that induce dihedral torsion between the thiophene and vinylene moieties in **PBT6V2'** and thus shorten the conjugation length.[187d, 197] In the solid state, the vinylene linkage has little effect on the absorption maxima, suggesting that the effect of vinylene on the conjugation length is offset by interchain π-π interactions. A similar phenomenon is seen upon comparison of a poly(quarterthiophene)[54b, 198] and a vinylene containing analog,[199] in which the difference in absorption maxima is much larger in solution than in the solid state. All the polymers investigated here show strong photoluminesence with λ_{em} in the range of 666 to 743 nm (**Figure 3.6a**), representing a red shift compared to that of the oligomer **BDTDTB** (λ_{em} = 648 nm, **Figure S3.6**).

3.3.3. Electrochemical Properties

Cyclic voltammetry (CV, **Figure S3.7**) was used to analyze the redox properties of the materials. **PBT4** and **PBT6** have oxidation potentials of +1.77 V and +1.80 V (versus

bis(cyclopentadienyl)cobalt(III) hexafluorophosphate, $CcPF_6$) corresponding to HOMO energy levels at -5.24 eV and -5.27 eV, respectively. P3HT exhibits a HOMO of ca. -5.17 eV under identical conditions, and poly(octylthiophene)s possess HOMOs in the range of -4.97 to -5.07 eV,[109a] thereby indicating the impact of the electron deficient **BT** units in lowering the HOMO energy levels of the copolymers. The observation of lower HOMO energy levels for **PBT4** and **PBT6** may allow for enhanced ambient stability relative to the polythiophene.[71, 185c, 199] **PBT6V2**, having the additional vinylene linkage in the polymer backbone, exhibits an increased HOMO energy (-5.07 eV) compared to the **PBT4** and **PBT6** analogs. This result can be attributed to the incorporation of the vinylene moiety that raises the electron density due to its electron donating properties.[54b, 188, 200] **PBT6V2'**, however, has a lower HOMO of -5.19 eV compared with **PBT6V2**. This may be a result of side chain induced steric hindrance (between the dodecyl group at C-4 of the thiophenes in **DTB** and the vinylene linkage) that shortens the conjugation length and thus offsets the effect of the vinylene unit. No evident reduction peaks were observed in the cyclic voltmmograms, suggesting that all these polymers belong to the class of p-type (hole transport) semiconductors.

3.3.4. Thermal Properties

The thermal characteristics were evaluated using thermogravimetric analysis (TGA), and differential scanning calorimetry (DSC, **Table 3.2**). The decomposition temperatures (T_d), defined as the temperature associated with 5% weight-loss, are in the range of 350-450 °C, indicative of high thermal stability. DSC studies on **PBT4** (shown in **Figure 3.7a**) show the presence of one endothermic peak upon heating, with one exothermic peak during the cooling process, which are associated with melting (T_m = 283 °C) and recrystallization (T_c = 249 °C), respectively. Interestingly, **PBT6** exhibits three endothermic peaks (T_{m1} = 45 °C; T_{m2} = 200 °C and $T_{m2'}$ = 217 °C) upon heating and two exothermic peaks (T_{c1} = 34 °C and T_{c2} = 202 °C) during the cooling process (**Figure 3.7b**), suggesting the existence of a mesophase between T_{m1} and T_{m2}. The temperature below T_{m1} corresponds to a solid phase while the temperature above T_{m2} corresponds to an isotropic phase. As has been suggested for poly(3-dodecylthiophene), P3DDT,[176a, 201] T_{m1} and T_{c1} may represent the melting and crystallization of the dodecyl side chains of **PBT6**; while T_{m2}, $T_{m2'}$ and T_{c2} correspond to the main chain melting and crystallization, respectively. Polarized optical microscopy (POM) demonstrates that a spin-coated film of **PBT6(L)** which melts at ca. 200 °C, displays a birefringent pattern (**Figure S3.10**) at approximately 80 °C upon subsequent cooling. The birefringence remains, even after

cooling to room temperature. No thermal transitions were observed for **PBT6V2**, **PBT6V2'** and **BDTDTB**, suggesting that thin films of these materials are amorphous.

Table 3.2. Thermal decomposition temperatures (T_d [a]) and thermal transition temperatures (T_m [b] and T_c [c]) of polymers and oligomer. Values in parentheses are transition enthalpies (J/g)

Sample	T_d / °C	Heating		Cooling	
		T_{m1} / °C (ΔH_{m1} / J/g)	T_{m2} / °C (ΔH_{m2} / J/g)	T_{c1} / °C (ΔH_{c1} / J/g)	T_{c2} / °C (ΔH_{c2} / J/g))
PBT4	461		283 (2.6)		249 (3.7)
PBT6	438	45 (7.8)	200, 217 (9.7)	34 (7.4)	202 (9.5)
PBT6V2	410	-	-	-	-
PBT6V2'	351	-	-	-	-
BDTDTB	438	-	-	-	-

[a] temperature corresponding to 5% mass loss; [b] melting temperature on heating; [c] crystallization temperature on cooling.

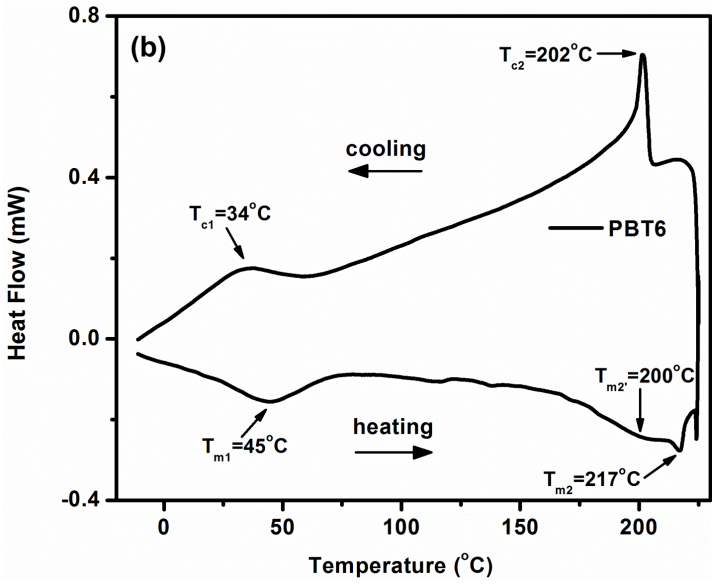

Figure 3.7. The thermal transitions of **PBT6** in DSC:, in the second heating / cooling scan at 10 °C / min.

3.3.5. Thin film Crystallinity and Morphology

The microstructures of polymer films were investigated by 2-dimensional grazing incidence X-ray scattering (2D-GIXS). Polymer films were prepared by drop casting chloroform solutions of the polymers onto Si wafers (300 nm SiO_2 dielectric on heavily doped Si) that had been pretreated with octadecyltrichlorosilane (OTS-18). Samples were tilted at $\chi = 90°$ and 30° to study the X-ray pattern along the q_z (out-of-plane) and q_{xy} (in-plane) axes. **PBT6** exhibited (*h*00) peaks at $2\theta = 4.52°$ (100), 9.08° (200), 13.52° (300) and 18.0° (400) along the q_z axis correpsonding to a lamellar d-spacing of 19.53 Å between polymer chains segregated by dodecyl side chains, and (010) peak at $2\theta = 24.16°$ along the q_{xy} axis arising from π-π stacking (3.68 Å) (**Figure 3.8c, d**). Unlike P3HT,[146a, 202] the variation of intensity at $2\theta = ca.$ 24° along the γ axis indicates a high intensity of (010) peak in the in-plane direction, and a very low intensity in the out-of-plane direction (**Figure 3.8e**), suggesting the formation of a highly ordered, lamellar structure with an edge-on orientation on the substrate.[203] In light of the length of a dodecyl chain (~15 Å), the interlamellar spacing of **PBT6** is consistent with an interdigitated packing mode of the side chains. **PBT4** exhibited a peak at $2\theta = 3.3°$ along the q_z axis corresponding to a lamellar spacing of 26.91 Å (**Figure 3.8a, b**). The peak at $2\theta = 24.40°$ correpsonding to the π-π stacking distance (3.64 Å) is barely perceptible, implying less crystallinity than **PBT6**. The largely lamellar spacing of **PBT4** (26.91 Å) suggests an end-to-end mode of

side-chain packing, similar to that of poly(3-dodecylthiophene) having a d-spacing of ~27.21 Å.[17b] In contrast to **PBT6**, **PBT4** exhibits a largely arcing diffraction for lamellar d-spacing and its π-π stacking peaks are equally weak in both the in-plane and out-of-plane orientations (**Figure S3.11c,d**), signifying no preferential orientation. **PBT6** thus appears to adopt a much more highly oriented configuration on the substrate than **PBT4**. Two-dimensional transmission wide-angle X-ray diffraction (2D-WAXD) of a **PBT6** drop-cast film indicates a π-π stacking distance of 3.65 Å (**Figure S3.12**), comparable to the 2D-GIXS result.

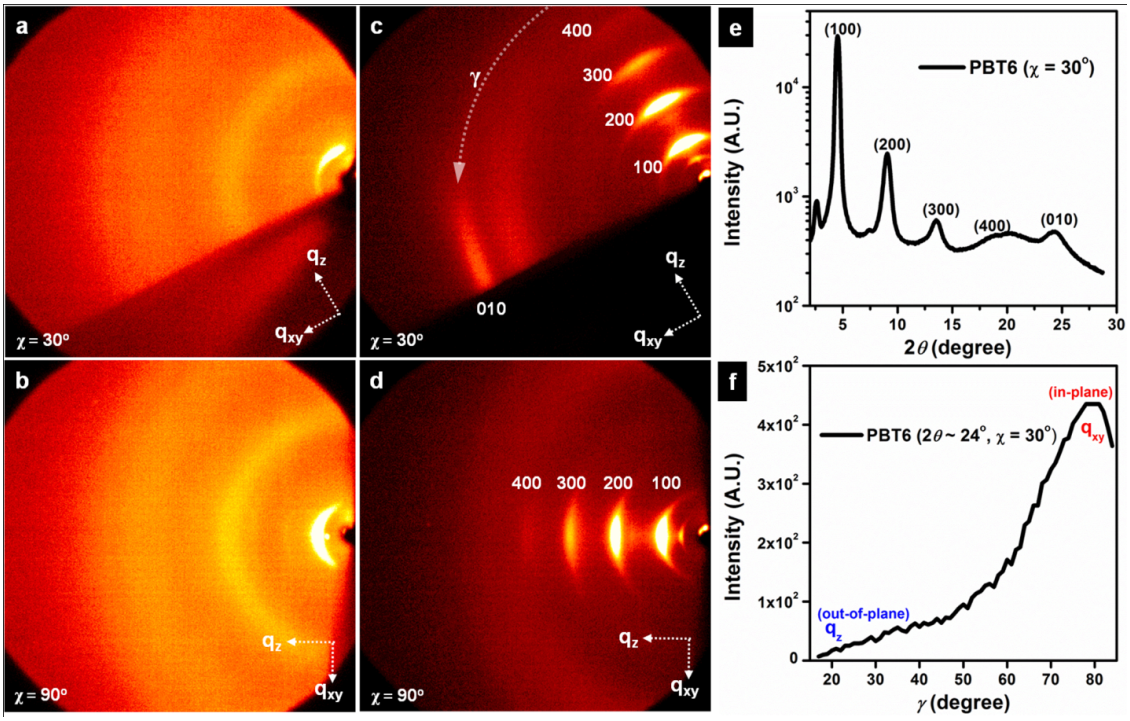

Figure 3.8. 2D-GIXS area detector images of **PBT4** drop-cast film (annealed at 200 °C for 4 h) at (a) χ = 30° and (b) χ = 90°; **PBT6** drop-cast film (without annealing) at (c) χ = 30° and (d) χ = 90°. The integrated intensity diffraction pattern corresponding to **PBT6** drop-cast film at χ = 30° is shown in (e); the integrated diffraction patterns for a, b and d are shown in **Figure S3.12**. The intensity variation scanning at 2θ = ca. 24° along γ axis

from q_z (out-of-plane) to q_{xy} (in-plane) is shown in (c, f). The scheme of sample tilting method is also in **Figure S3.12.**

The intensities of lamellar spacing and π-π stacking peaks of **PBT4** were clearly enhanced by thermal annealing of a film at 200 °C for 4 h, as shown by one-dimensional X-ray diffraction (1D-XRD, **Figure S3.13**). For **PBT6**, a highly crystalline XRD pattern is obtained on as-deposited films without the need for extended annealing (**Figure 3.8** and **S3.14**). As observed during DSC analysis, **PBT6** undergoes side-chain recrystallization at T_{c1} = 34 °C which is close to room temperature and hence the side-chains in **PBT6** may have sufficient thermal energy to facilitate assembly into a highly crystalline structure. **PBT6** was annealed at temperatures from 75 °C up to 250 °C (i.e. within mesophase and isotropic phase) followed by subsequent cooling to room temperature. The corresponding 1D-XRD patterns measured at room temperature (**Figure S3.14**) indicate that the high crystallinity of **PBT6** is maintained after annealing up to 170 °C, clearly decreased after annealing at 200 °C and could not be detected after annealing at 250 °C, suggesting that the order is retained in the solid and mesophases (< 180 °C) and that the high temperature transition in the DSC corresponds to melting to an isotropic phase. **PBT6V2** and **PBT6V2'** display no XRD patterns, consistant with an amorphous structure as previously suggested by the lack of thermal transitions in the DSC analysis.

The surface morphologies of the polymer thin films were evaluated using atomic force microscopy (AFM) in the tapping mode. Nano-fiberous features with a width of 40-50

nm and length of 200-300 nm were observed for as-spun films of **PBT6** (**Figure 3.9c,d**) consistent with a high degree of crystallinity as observed through GIXS and XRD measurements. This morphology is largely lost upon annealing at 250 °C followed by subsequent quenching to room temperature, which correlates with the loss of diffraction peaks in the XRD at the higher transtition observed in the DSC. **PBT4** films display fewer surface features (**Figure 3.9a,b**), and **PBT6V2** and **PBT6V2'** are largely amorphous. In combination, the results of analyses by DSC, XRD and AFM indicate that the degree of molecular ordering in a polymer thin film architecture for this series of D-A copolymers follows the sequence: **PBT6** > **PBT4** > **PBT6V2** ~ **PBT6V2'**.

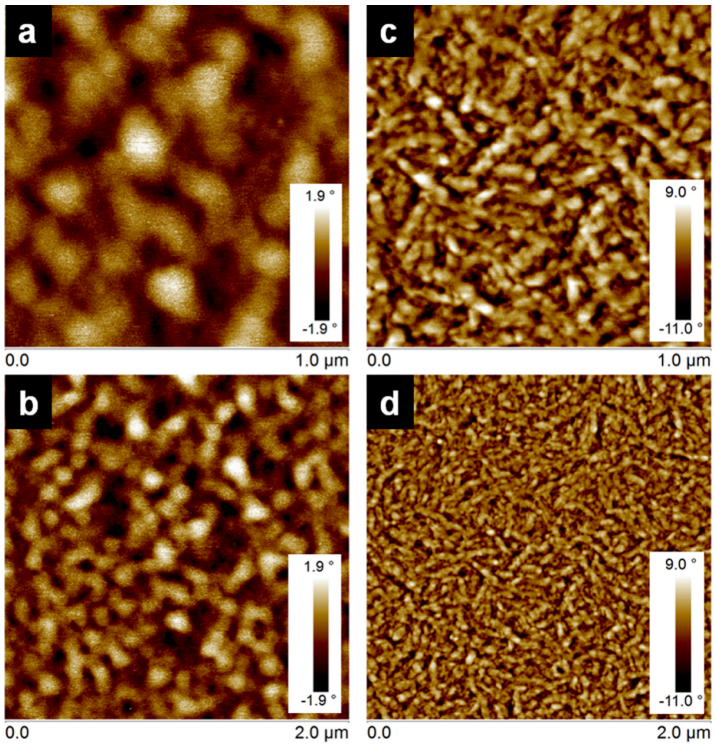

Figure 3.9. Tapping mode AFM phase images of **PBT4,** (a) and (b); and **PBT6** (c) and (d). Films were prepared by spin-coating 8 mg/mL solutions of polymer in DCB onto OTS-18 pre-treated Si substrates.

3.3.6. Field Effected Mobility Characterization

Bottom gate, bottom contact OFET devices were used to evaluate the charge transport properties of the D-A copolymers (**Figure S3.15**). DCB was selected as the processing solvent because no aggregation was observed in this solvent, in contrast to solutions in $CHCl_3$ and CB (**Figure 3.6b**); TCB was not considered because its high boiling point severely limits the efficiency of solvent evaporation. Polymer solutions in DCB (8 mg/mL) were spin-cast onto OTS-18 pre-treated SiO_2 dielectric (300 nm) grown onto heavily doped Si substrates. The channel between gold source and drain electrodes was 50 μm long and 2 mm wide. The output and transfer curves for devices fabricated with **PBT6** and **PBT4** are shown in **Figure 3.10**. **PBT6** exhibits a hole mobility (μ_h) of 0.2 cm^2/Vs, which is *ca*. one order of magnitude higher than its low MW counterpart, **PBT6(L)** (0.029 cm^2/Vs, **Table 3.3**), indicating the impact of MW on charge carrier transport. **Figure S3.17** demonstrates that drop-cast films of **PBT6** are smoother and more uniform than those of **PBT6(L)**, supporting the premise that increased MW facilitates formation of more uniform thin films, a key factor associated with processing and application of polymer thin film technologies. **PBT4** exhibits a moderate mobility of 0.01 cm^2/Vs, ascribable to its lower crystallinity compared to **PBT6** which may originate from its low MW. Higher MW analogs could not be obtained due to the limited solubility of the polymer in the polymerization solvent. The solubility of **PBT4** might be improved

by incorporating longer branched alkyl side-chains. Recently reported polymers with the same main-chain structure as **PBT4**, but substituted with long branched 2-octyldodecyl appendages possess higher MW and mobilities of 0.02-0.2 cm^2/Vs.[71, 203c] The amorphous vinylene-containing counterpart, **PBT6V2** exhibits a low μ_h of 10^{-4} cm^2/Vs, and no appreciable field-effect hole or electron transport was detected for **PBT6V2'**.

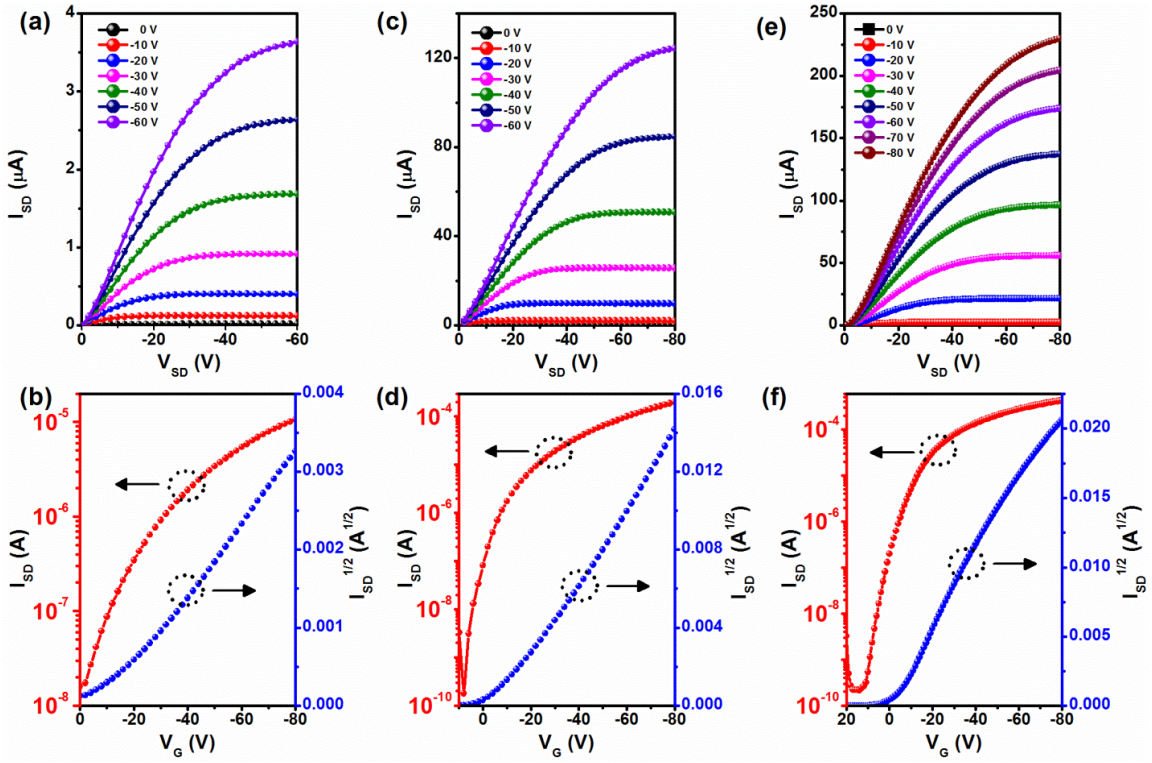

Figure 3.10. Output (up row) and transfer (down row, V_{SD} = -80 V) characterizations of OFETs (channel size: 50 μm long x 2 mm wide) based on spin-coated **PBT4** films (a, b), spin-coated **PBT6** films (c, d) and drop-cast **PBT6** films (e, f).

The differences in the hole mobilities are consistent with the thin film morphologies of the respective polymers. The much higher degree of molecular ordering of **PBT6** and **PBT4** relative to **PBT6V2** and **PBT6V2'** improves their ability to undergo interchain charge hopping, which in turn leads to enhanced mobilities. The incorporation of the

vinylene linkage in the latter two polymers causes a reduction in the crystalinity of thin films and a concomitant decrease in mobility. No charge carrier transport was detected in **BDTDTB**. It is noteworthy that a previously reported oligomeric compound having the same backbone as **BDTDTB** but two dodecyl chains on the α-carbons rather than β-carbons of the peripheral thiophene units, exhibits a liquid crystalline phase and has a μ_h of 10^{-3} cm^2/Vs in solution-processed FETs.[186a] Using the combined results, it is evident that the relative position of side chains plays a significant role in determining intermolecular interactions and charge carrier transport properties in these materials.

PBT6 devices prepared via spin-casting were annealed at distinct temperatures within both the mesophase and the isotropic phase (as determined by DSC, **Figure S3.18**). The values of μ_h and current on/off ratio ($I_{ON/OFF}$) measured at room temperature increased from 0.14 cm^2/Vs and 10^4, respectively, for samples that were not annealed, up to 0.25 cm^2/Vs and 10^6 after annealing at 70 °C (i.e., within mesophase). However, these values decreased to 0.075 cm^2/Vs and 10^4 upon annealing in the isotropic phase (250 °C). This result is consistent with the observed decrease in crystallinity of **PBT6** through XRD (**Figure S3.14**) and AFM (**Figure S3.19**) analysis. The threshold voltage ranged from 4.7 to -18 V upon annealing and no obvious hysteresis was observed (**Figure S3.20**).

The hole transport properties of **PBT6** were further investigated using films drop-cast from DCB. Films formed at room temperature exhibited a mean value for μ_h of 0.17

cm^2/Vs. After thermal annealing at 80 °C for 24 h, μ_h was increased by a factor of ~3 (mean 0.5 cm^2/Vs) with a maximal value of μ_h as high as 0.75 cm^2/Vs and $I_{ON/OFF}$ of 10^6 - 10^7.

Table 3.3. Hole transport properties of polymers spin-coated (except "PBT6 (drop-casting)") onto OTS-18 pretreated OFETs substrates (channel size: 50 μm of long x 2 mm wide)

Polymers	Hole mobility, μ_h / cm^2/V.s [a]	$I_{ON/OFF}$	Threshold voltage, V_T / V
PBT4	0.01[b]	10^3	-4.9
PBT6	0.2 (0.25) [c]	10^6	-2.3 – -3.2
PBT6(*drop-casting*) [d]	0.5 (0.75)	10^6 - 10^7	-0.5 - -5.5
PBT6(L)	0.029 [e]	10^5	
PBT6V2	2.2 x 10^{-4} [f]	10^4	-8.7
PBT6V2'	-	-	-

[a] values in parentheses are maximal mobilities attained; [b] annealed at 200 °C for 1 h; [c] annealed at 115 °C for 1 h; [d] PBT6 was drop-casted onto FETs annealed at 80 °C for 24 h; [e] annealed at 115 °C for 1 h; [f] annealed at 200 °C for 1 h

3.4. Conclusions

Four benzothiadiazole-oligothiophene D-A copolymers were synthesized by Stille coupling (**PBT4** and **PBT6**) or by Horner–Wadsworth–Emmons polymerization (to prepare analogs containing vinylene linkages **PBT6V2** and **PBT6V2'**). These low optical bandgap polymers (~1.5 eV) exhibit the ability to harvest photons at 400-800 nm, possess good thermal stability, and **PBT6**, in particular, displays a mesophase. The hole transport

performance of spin-cast thin films of these polymers in bottom gate bottom contact OFET devices correlates well with their propensity to form ordered structures (**PBT6** > **PBT4** > **PBT6V2** ~ **PBT6V2'**) as verified by DSC, XRD and AFM. **PBT6**, having a highly crystalline lamellar π stacked structure that adopts an edge-on orientation on an OFET substrate exhibits a hole mobility of *ca.* 0.2 cm^2/Vs. The vinylene analogs **PBT6V2 and PBT6V2'**, which are largely amorphous, showed much lower mobilities. Molecular weight has a significant impact on the mobility of **PBT6**. The use of a drop-casting process for the formation of the semiconducting layer results in a further increase in the mobility of the polymer by a factor of ~3, with mobilities as high as 0.75 cm^2/Vs. This work demonstrates the potential for building high mobility semiconducting polymers by incorporation of **BT** acceptor units into polythiophene derivatives, and the significant role of processing on the charge transport performance of **BT**-oligothiophene based polymeric semiconductors. **PBT6** could serve as a platform for the investigation of structure-property-processing relationships associated with charge transport in D-A copolymers.

Supporting Information

The synthetic details of preparing monomers and polymers, characteristic methods, OFETs fabrications and Figure S3.1 – S3.20 are included in supporting information-1.

CHAPTER 4

ENHANCING FIELD-EFFECT MOBILITY OF CONJUGATED POLYMERS THROUGH RATIONAL DESIGN OF BRANCHED SIDE CHAINS

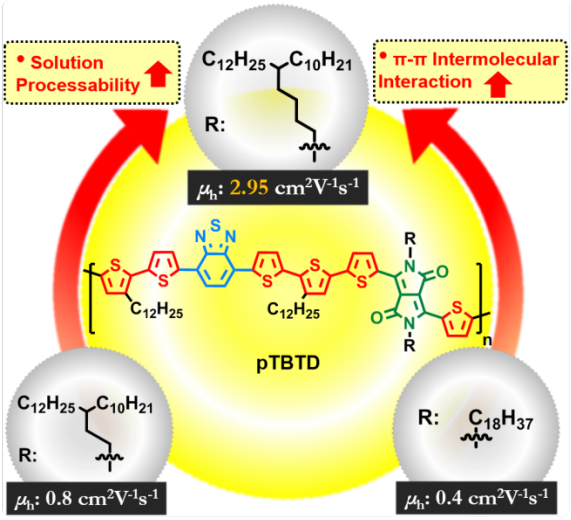

4.1. Abstract

The design of π-conjugated semiconducting polymers possessing effective π-π intermolecular interactions coupled with good solution processability remains a challenge. Here we report structure-property relationships associated side chain molecular structure with resultant π-π intermolecular interactions, polymer solubility, and in turn charge carrier transport, based on a donor-acceptor(1)-donor-acceptor(2) polymer: 5-Decylheptadecyl (**5-DH**), 2-tetradecyl (**2-DT**) and linear *n*-octadecyl (**OD**) chains were

substituted onto a polymer backbone consisting of terthiophene units (**T**) between two different electron acceptors, benzothiadiazole (**B**) and diketopyrrolopyrrole (**D**), **pTBTD**, to afford **pTBTD-5DH**, **pTBTD-2DT**, and **pTBTD-OD**, respectively. In the **5-DH** side chain the branching position is remote from the conjugated polymer backbone, whereas it is proximal in the **2-DT** side chain. The systematic investigation of these polymers demonstrates that incorporation of branched side chains where the branching position is remote from the polymer backbone merges the advantages of improved solubility that emanates from branched units with effective π-π intermolecular interactions normally associated with the presence of linear chains on conjugated polymers. **pTBTD-5DH** exhibits superior qualities with respect to the degree of polymerization, solution processability, π-π interchain stacking, and charge carrier transport relative to the other analogs. **pTBTD-5DH** exhibited a field-effect hole mobility of up to 2.95 $cm^2V^{-1}s^{-1}$, a factor of 3 - 7 times that achieved with **pBDT6-DT** and **pBDT6-OD**.

4.2. Introduction

Side chain engineering has a significant potential to aid the development of high performance semiconducting π-conjugated polymers for optoelectronic applications. Optimization of the solution processability and intermolecular interactions in thin films of these materials is important in the design of new polymeric semiconductors. Here we

describe the influence of the structure of side chains on the solubility and interchain interactions that govern charge carrier transport in a new low bandgap polymer.

We recently introduced poly(benzothiadiazole-*alt*-sexithiophene), **pBT6**, a polymeric semiconductor composed of alternating benzothiadiazole (acceptor) and sexithiophene (donor) units with *n*-dodecyl side chains to impart solubility. It displays a bandgap of 1.5 eV and a hole mobility of up to 0.75 $cm^2V^{-1}s^{-1}$.[33] To further enhance the semiconducting performance of this class of materials, we incorporated diketopyrrolopyrrole units as a second acceptor into the structure of **pBT6**. The new polymer consists of electron-donating terthiophene units (**T**) between two different electron acceptors, benzothiadiazole (**B**) and diketopyrrolopyrrole (**D**), in an alternating arrangement to afford the donor-acceptor(1)-donor-acceptor(2) (**D-A-D-A'**) copolymer, **pTBTD**, as shown in **Figure 4.1**. Diketopyrrolopyrrole and its isomer have been reported as attractive acceptors in the development of semiconductors for use in high performance polymer-based organic field effect transistors (OFETs) and organic photovoltaics, exhibiting mobility and power conversion efficiency beyond 1 $cm^2/V^{-1}s^{-1}$ [27a, 132b, 177e, 204] and 7%, respectively.[62, 205] The **D-A-D-A'** nature of the new copolymers is expected to: (i) lower the HOMO energy level of the polymer; (ii) enhance intramolecular charge transfer and (iii) enhance π-π intermolecular interactions due to the coplanar nature of diketopyrrolopyrrole.[5, 204a, 205a]

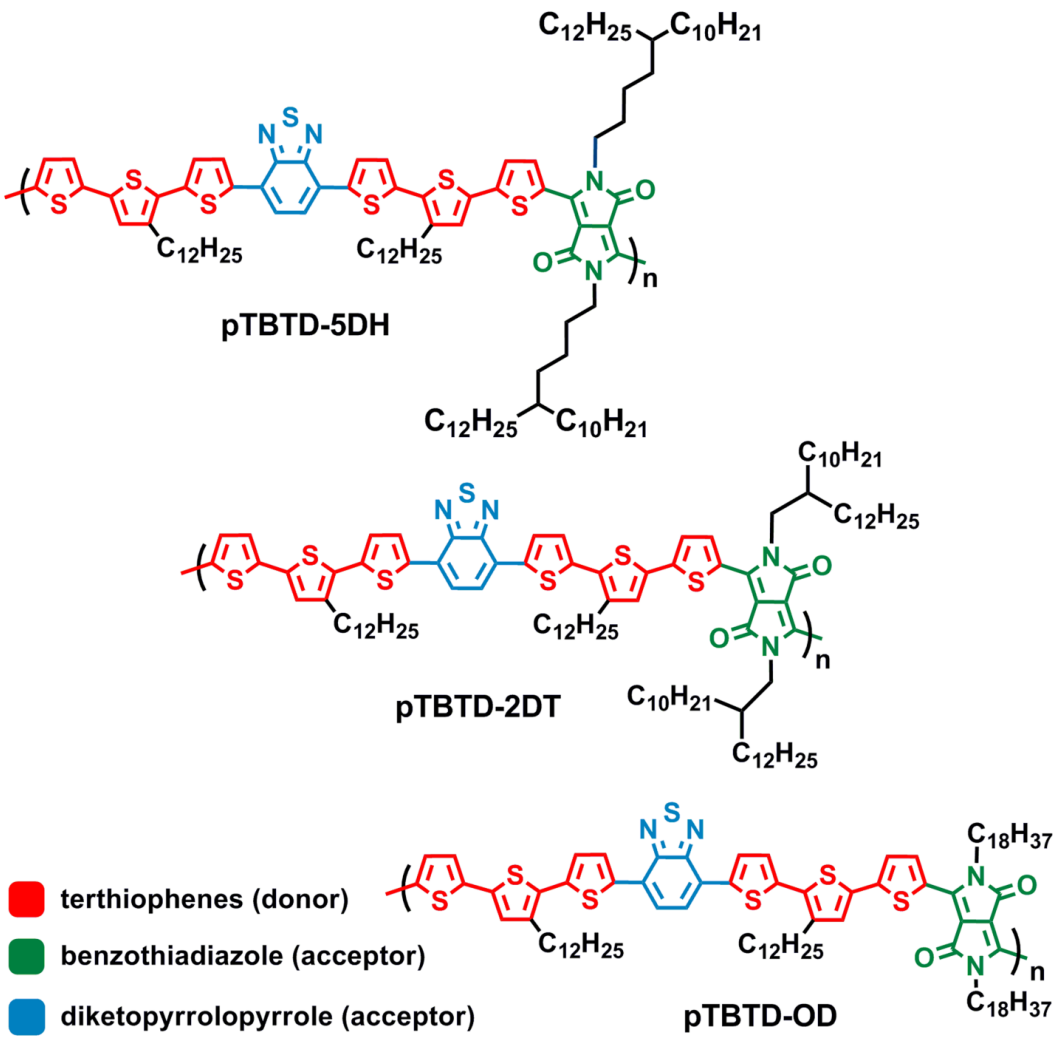

Figure 4.1. Molecular structures of **TBTD** polymers substituted with branched side chains that are (i) remote (**pTBTD-5DH**) or (ii) close to (**pTBTD-2DT**) the conjugated polymeric backbone, and (iii) the linear side chain (**pTBTD-OD**).

Incorporation of branched side-chains improves polymer solubility compared with analogs with linear side chains.[2b, 64, 206] However, branched side chains in which the branched point is close to the polymer backbone (e.g., 2-octyldodecyl, 2-decyltetradecyl) interferes with close packing of the polymers and weakens π-π intermolecular interactions between conjugated backbones, compared to analogs with linear side chains.[207] Therefore, a design strategy that merges the advantages afforded by both

linear and branched side chains is worthy of investigation. Here we describe the introduction of 5-decylheptadecyl (**5-DH**), 2-tetradecyl (**2-DT**), and *n*-octadecyl (**OD**) side chains onto the **TBTD** polymer, to afford **pTBTD-5DH**, **pTBTD-2DT**, and **pTBTD-OD**, respectively (**Figure 4.1**). The side chain branching position is either remote (**5-DH**) or close (**2-DT**) to the polymer backbone. This design strategy of moving the branch point of the side chain away from the **pTBTD** backbone in **5-DH** was intended to reduce steric hindrance between chains while maintaining, or even improving, polymer solubility relative to that of analogous polymers with either branched (**2-DT**) or linear (**OD**) side chain. Recent reports have suggested the effectiveness of controlling the separation of branches in the side chain from the polymer backbone in tuning intermolecular self-assembly, charge carrier mobility,[31b, 61a, 77] and photocurrents.[31e] A comparison of the properties of the three **pTBTD** analogs allows us to systematically investigate the effect of the variation of side chain structure on polymer solution processability, degree of polymerization, molecular ordering and orientation, and macroscopic charge carrier transport properties.

4.3. Results

4.3.1. Polymer Synthesis.

The syntheses of the **TBTD** polymers are outlined in **Figure 4.2**, complete synthetic details are provided in the Supporting Information-2 (S.I.). Commercially available 2-decyl-1-dodecanol, **1**, was converted to bromide **2**, which was then chain-extended by reaction with allylmagnesium chloride. The resulting alkene, **3**, was subjected to hydroboration–oxidation to afford alcohol **4**, which was subsequently converted to bromide **5**.[208] 3,6-Di(2-thienyl)diketopyrrolopyrrole, **6**, was alkylated with **5** to afford the **5-DH** substituted acceptor compound, **7a**, and with **2** and 1-bromooctadecane to afford **7b** and **7c**, respectively. It is noteworthy that the dialkylation of **6** with the 5-decyl-substituted compound to afford **7a** proceeds in high yield (>80%), which is similar to the yield of **7c** formed by alkylation of **6** with the linear side chain, and significantly higher than the yield of **7b** (30%) in which the side chain in the 2-position hinders nucleophilic substitution. The low yield for alkylation of diketopyrrolopyrrole with branched alkyl halides was recently reported as a common problem.[207a, 209] Accordingly, moving the branching position further from the electrophilic site affords a more efficient monomer synthesis. Solutions of **7a-c** afforded similar absorption spectra (absorption maximum, λ_{max}, at 548 nm, **Figure S4.1a**); while in the thin-film an obvious bathochromic shift was observed for the sequence of **7b** (pink, λ_{max} = 515 nm) to **7c** (purple, λ_{max} = 610 nm) and

7a (purple, λ_{max} = 630 nm), as shown in **Figure 4.2** and **Figure S4.1b**. These results indicate that the steric hindrance arising from branching of the side chain close to the diketopyrrolopyrrole core (i.e., **2-DT**) disrupts π-π intermolecular interactions. Moving the branching away from diketopyrrolopyrrole unit (i.e., **5-DH**) relieves this hindrance and results in **7a** having a similar λ_{max} as the linear analog **7c**.

Table 4.1. Molecular weights and photophysical properties of **TBTD** polymers

Polymer	M_n / kDa	PDI	DP [a]	Absorption maximum / eV		E_g^{opt} / eV [b]
				Solution	Film	
pTBTD-5DH	44	2.3	24	1.60, 2.99	1.58, 1.72, 2.98	1.26
pTBTD-5DH(H)	50	2.1	27	1.60, 2.99	1.58, 1.72, 2.98	1.26
pTBTD-2DT	28	2.5	16	1.60, 1.72, 3.03	1.58, 1.73, 2.97	1.30
pTBTD-OD	14	2.5	9	1.94, 3.24	1.56, 1.69, 2.93	1.26

[a] Degree of polymerization, calculated from M_n divided by molecular weight of repeating unit; [b] optical bandgap, estimated from the thin film absorption band onset point (λ_{onset}): E_{opt} = 1240 / λ_{onset}.

TBTD polymers were prepared by Stille step-growth polymerization of 3,6-di(5-bromo-2-thienyl)-*N*,*N*-dialkyldiketopyrrolopyrrole monomers **M1a-c** and bis-stannane monomer **M2**[33] under microwave irradiation (180 °C for 30 min, **Figure 4.2**), followed by precipitation and subsequent purification by Soxhlet extraction. **pTBTD-5DH** was removed from the Soxhlet thimble with chloroform. The residue in the thimble was dissolved in hot 1,2-dichlorobenzene to afford a higher molecular weight sample, **pTBTD-5DH(H)**. The **2-DT** and **OD** analogs were prepared under the same conditions and extracted from the Soxhlet thimble with chloroform and chlorobenzene, respectively.

Gel permeation chromatography (GPC; 135 °C with 1,2,4-trichlorobenzene as eluent, **Table 4.1**) gave number-average molecular weights (M_n) of **pTBTD-5DH** and **pTBTD-5DH(H)** of 44 kg/mol and 50 kg/mol, respectively, approximately twice that of **pTBTD-2DT** (28 kg/mol) and four times that of **pTBTD-OD** (14 kg/mol) prepared in the same manner. This result suggests that the **5-HD** side chains allow the polymerization to proceed to give higher molecular weight by maintaining solubility of the growing polymer. No shoulders were observed on the GPC peaks (**Figure S4.2** in S.I.), indicative of no aggregation of polymer chains. Efforts to prepare lower molecular weight **pTBTD-5DH** using milder reaction conditions (160 °C for 30 min), afforded samples exhibiting no substantial change in M_n (44 kg/mol, PDI: 2.3, **Figure S4.2e**), suggesting that the incorporation of **5-DH** facilitates preparation of relatively high molecular weight polymers, a desirable characteristic for high performance polymer semiconductors.[96b, 99]

4.3.2 Photophysical Properties.

The UV-visible absorption spectra of the **TBTD** polymers are shown in **Figure 4.3**. In solution (**Figure 4.3a**), **pTBTD-5DH** exhibits a similar absorption onset as **pTBTD-2DT**, suggesting a similar extent of π-conjugation within the polymer backbone. The absorption maximum analog with linear side chains, **pTBTD-OD**, is shifted to higher

energy by 0.33 eV in comparison to the maxima of **pTBTD-5DH** and **pTBTD-2DT**. For thin films (**Figure 4.3b**), the absorption maximum of **pTBTD-OD** is red-shifted by 0.23

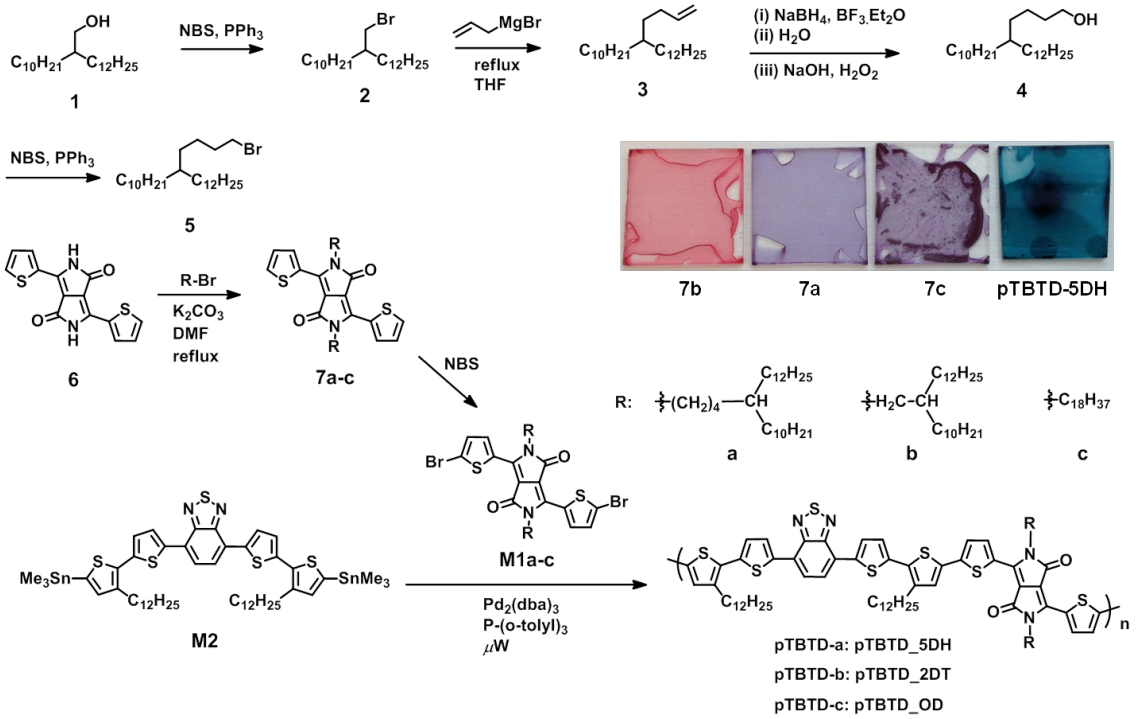

Figure 4.2. Synthesis of **TBTD** polymers. Images inserted represent spin-coated films of compound **7a-c** (1500 rpm from 10 mg/ml in chloroform), and **pTBTD-5DH** (1500 rpm from 8 mg/ml in *o*-dichlorobenzene) on glass wafers.

eV compared to the maximum recorded in solution, consistent with planarization of the polymer backbone and enhanced π-π interchain interactions. Both **pTBTD-5DH** and **pTBTD-OD** exhibit relatively lower optical bandgaps (E_g^{opt}, 1.26 eV in **Figure 4.3**) than **pTBTD-2DT** (1.30 eV) in thin-film form. This suggests that moving the branching of side chains away from the polymer backbone enhances π-conjugation compared to analogs in which the branching is close to the conjugated backbone; and provides **pTBTD-5DH** with photophysical properties that are similar to the analog with linear side

chains. Finally, it should be noted that the absorption peaks of films of **pTBTD-OD** exhibit a significant tail due to reflectivity. This arises from the low solubility of the linear side chain polymer analog, which results in formation of films with high surface roughness. All of the **pTBTD** polymers were thermally annealed at between 100 and 300 °C under inert atmosphere (**Figure S4.3**); no change was observed in the absorption spectra upon annealing, demonstrating the high thermal stability of the films.

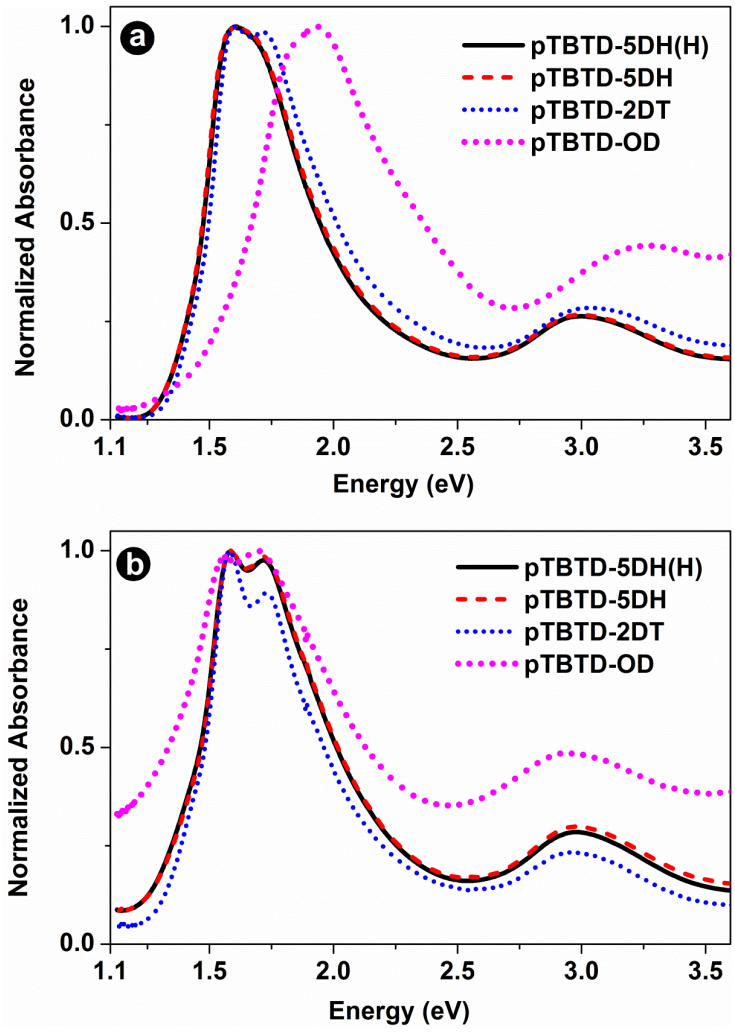

Figure 4.3. Absorption spectra of **TBTD** polymers: (a) in solution (1,2-dichlorobenzene) at room temperature; and (b) thin film at room temperature.

4.3.3. Electrochemistry.

Cyclic voltammetry (CV) and differential pulse voltammetry (DPV) were employed to investigate the redox properties of thin films of **TBTD** polymers (**Figure S4.4**). All of the **pTBTD** polymers exhibited an oxidation onset between 0.41 and 0.54 V versus Fc/Fc^+ (-4.8 eV versus vacuum) by CV, and between 0.45 and 0.50 V versus Fc/Fc^+ by DPV, as shown in **Table 4.2**. These values correspond to HOMO energy levels of -5.2 to -5.3 eV. The oxidation of all of the **pTBTD** polymers displayed good reversibility (e.g., **pTBTD-5DH** shown in **Figure 4.4**), demonstrating the oxidative stability of these polymers. **pTBTD-5DH** (**Figure 4.4** and **Figure S4.4**) and **pTBTD-OD** (**Figure S4.4**) exhibited a second oxidation peak at between 1.2 and 1.4 eV versus Fc/Fc^+, suggesting the presence of both polaronic and bipolaronic states in these polymers. No reduction peaks were evident in the CV or DPV of these materials.

4.3.4. Ionization Potentials.

The HOMO energy levels determined by CV and DPV include the impact of penetration of the electrolyte which swells the polymer films, and thereby changing film morphology during the oxidation process.[167, 210] Accordingly, we chose to characterize films of **pTBTD** polymers by ultraviolet photoelectron spectroscopy (UPS) to determine the intrinsic work functions (ϕ) and ionization potentials (IP) (**Figure S4.5**). The

resulting HOMO energy levels of **pTBTD** are between at -4.9 and -5.1 eV for as-spun films (**Table 4.2**), which are approximately 0.2 – 0.3 eV higher than those obtained by CV and DPV. After thermal annealing, **pTBTD-5DH**, **pTBTD-2DT** and **pTBTD-OD** exhibited a *ca.* 0.1 eV decrease in IP to between 4.8 and 5.0 eV. This decrease is attributed to enhancement of molecular ordering upon thermal annealing, confirmed by subsequent X-ray scattering and AFM characterization (*vide infra*). LUMO energy levels of **pTBTD** are *ca.* -3.7 eV, based upon the common estimation that $E_{LUMO} = E_{HOMO} - E_g^{opt}$ (optical bandgap), without consideration of the exciton binding energy (0.3–1.0 eV).[1c, 211]

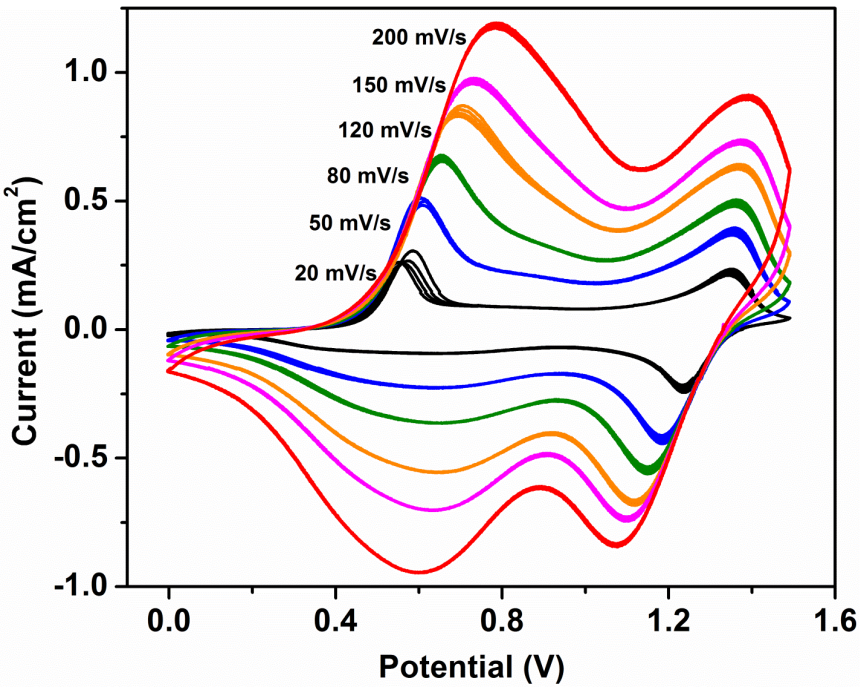

Figure 4.4. Cyclic voltammograms of a drop-cast film of **pTBTD-5DH** on a platinum electrode (in 0.5M Bu_4NPF_6/acetonitrile) at scan rates between 20 mV/s and 200 mV/s (five cycles at each scan rate).

Table 4.2. Redox properties, HOMO, LUMO and work-function energy levels of **TBTD** polymers

Polymers	CV			DPV			UPS				
	1^{st} E_{ox} [a] / V	2^{nd} E_{ox} [b] / V	HOMO / eV	1^{st} E_{ox} [c] / V	2^{nd} E_{ox} [d] / V	HOMO / eV	$IP_{as\text{-}spun}$ eV	$\phi_{as\text{-}spun}$ / eV	$IP_{annealed}$ / eV	$\phi_{annealed}$ / eV	LUMO [e] / eV
pTBTD-5DH	0.47	1.23	-5.27	0.45	1.35	-5.25	5.04	4.46	4.94	4.31	3.78
pTBTD-2DT	0.54	n/a	-5.34	0.49	n/a	-5.29	5.04	4.52	4.86	4.28	3.74
pTBTD-OD	0.41	n/a	-5.21	0.5	1.38	-5.3	5.06	4.59	4.95	4.32	3.8

[a] 1^{st} oxidation peak upon CV; [b] 2^{nd} oxidation peak upon CV; [c] 1^{st} oxidation peak upon DPV; [d] 2^{nd} oxidation peak upon DPV; [e] LUMOs were calculated from $IP_{as\text{-}spun}$ substituted by E_g^{opt} (Table 1).

4.3.5. Thermal Properties.

The **TBTD** polymers decompose at temperatures greater than 360 °C (see TGA characterization, **Table 4.3** and **Figure S4.6a**), indicative of high thermal stability. All **TBTD** polymers show the presence of two endothermic transitions upon heating (T_{h1} and T_{h2}), and two exothermic transitions during the cooling process (T_{c1} and T_{c2}, see DSC characterization, **Table 4.3** and **Figure S4.6b-d**), revealing the presence of ordered phases. The lower temperature transitions (T_{h1} and T_{c1}) most likely correspond to the disordering and reordering processes associated with the side chains; while those at higher temperature (T_{h2} and T_{c2}) represent a polymer backbone phase transition before entering an isotropic phase. X-ray scattering (*vide infra*) indicated an improvement in crystallinity and molecular ordering of **TBTD** polymers after thermal annealing beyond

T_{h2} and T_{c2} and at up to 350 °C, suggesting that the melting point of the **TBTD** polymers is even higher (above the onset of decomposition).

Table 4.3. Thermal decomposition temperature (T_d) and thermal transition temperatures (T_g[a)], T_h[b)], and T_c[c)]) of **TBTD** polymers.

Polymer	T_d / °C	T_g / °C	Heating		Cooling	
			T_{h1} / °C (ΔH, J/g)	T_{h2} / °C (ΔH, J/g)	T_{c1} / °C (ΔH, J/g)	T_{c2} / °C (ΔH, J/g)
pTBTD-5DH	412	n/a	-44 (3.76)	70	-47 (1.31)	65
pTBTD-2DT	400	32	-4 (0.1)	91 (0.3)	-38 (0.2)	61 (0.3)
pTBTD-OD	360	n/a	-6 (3.3)	90 (0.1)	-11 (4.9)	62 (0.1)

[a)] T_g: glass transition temperature; [b)] T_h: phase transition temperature upon heating process; [c)] T_c: phase transition temperature upon cooling process.

4.3.6. Thin-Film Crystallinity and Morphology.

Polymer thin-film microstructures were investigated by two-dimensional grazing incidence wide angle X-ray scattering (2D-GIWAXS, **Figure 4.5**). Films were prepared by drop-casting 1,2-dichlorobenzene-solutions of the polymers onto a Si substrate (300 nm SiO_2 dielectric on heavily p-doped Si) that had been pre-functionalized with octadecyltrichlorosilane (OTS-18). All **TBTD** polymers exhibited well-defined (h00) diffraction patterns along the q_z (out-of-plane) axis corresponding to a highly ordered lamellar structure; and (010) peaks along the q_{xy} (in-plane) axis arising from π-π stacking of polymer backbones. For example, **pTBTD-5DH(H)**, exhibits a (100) peak at 2θ =

3.59°, (200) at 2θ = 7.17°, (300) at 2θ = 10.75°, and (400) at 2θ = 14.37°, corresponding to a lamellar *d*-spacing distance of 24.55 Å between polymer chains segregated by a combination of **5-DH** and dodecyl side chains (on the diketopyrrolopyrrole units and thiophene units, respectively). A (010) peak at 2θ = 24.79° indicates a 3.59 Å π-π stacking distance. Results for other **TBTD** polymers are shown in **Table 4.4**. The lamellar spacing suggests that the polymer side-chains are highly interdigitated in the crystalline phase. Similar to our benchmark polymer, **pBT6**,[33] the variation of intensity of **pTBTD** at 2θ = *ca*. 24.5° along the γ axis indicates high (010) peak intensity in the in-plane direction, and a very low intensity in the out-of-plane direction (**Figure S4.7**). These results suggest the formation of highly ordered lamellar structures with edge-on orientation relative to the substrate surface (**Scheme S4.1**). **pTBTD-5DH** and **pTBTD-5DH(H)**, in which the branching of side chain is remote from the backbone exhibit a similar π-π stacking distance (3.6 Å) to the linear analog, **pTBTD-OD** (3.62 Å), which is smaller than the **2-DT** analog (3.73 Å). These results reveal a benefit derived from moving the branching position further from the polymer backbone whereby steric hindrance that impedes π-π stacking in the **2-DT**-substituted polymer is relieved in the **5-DH** analog, thereby allowing for closer π-π intermolecular interactions between conjugated chains. This is a critical feature for enhancing charge carrier transport. Thermal annealing of the **TBTD** polymers resulted in an increase in the intensity of both the (*h*00) and (010) diffraction peaks, signifying an increase in the degree of crystallinity.

The full-width-at-half-maximum (FWHM) of the (100) diffraction peak (**Table 4.4**) decreased upon thermal annealing, corresponding to an increase of the coherence length of crystalline domains along the (100) axis.[63a, 89]

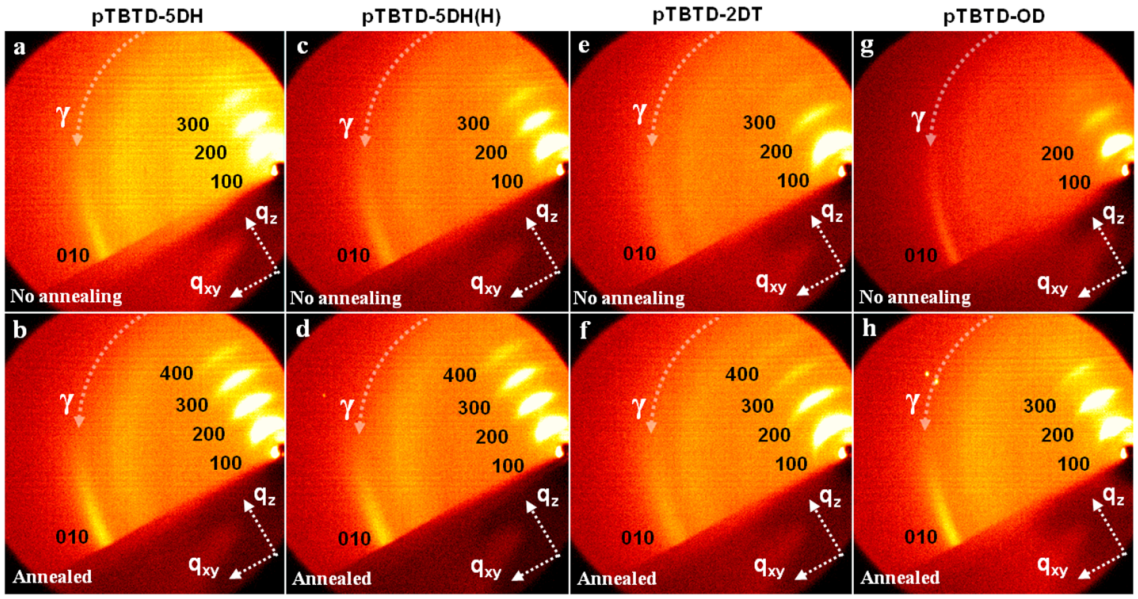

Figure 4.5. 2D-GIWAXS area detector images of **pTBTD** drop-cast films: (a,b) **pTBTD-5DH**; (c,d) **pTBTD-5DH(H)**; (e,f) **pTBTD-2DT**; (g,h) **pTBTD-OD**. Top row, as-spun films; bottom row, samples after annealed at 200 °C (**pTBTD-OD** at 300 °C) for 30 min followed by rapidly cooled to room temperature.

To gain further understanding of the impact of thermal annealing on the molecular ordering of **TBTD** polymers, films were annealed at 100 - 375 °C and characterized using one-dimensional grazing incidence X-ray scattering (1D-GIXS), as shown in **Figure 4.6**. Upon increasing the annealing temperature to as high as 375 °C, a temperature close to the onset of decomposition (*vide supra*), all of the **TBTD** polymers exhibited an increase in the intensity of the (*h*00) lamellar diffraction peak with a concomitant decrease in the FWHM of the (*h*00) diffraction peaks (**Figure 4.7a**).

Table 4.4. 2D-GIWAXS peak assignments and corresponding distances of **TBTD** polymers before and after thermal annealing.

Polymer	As-spun film				After annealing [a)]			
	2θ / °		distance / nm	FWHM	2θ / °		Distance / nm	FWHM
pTBTD-5DH(H)	3.55	(100)	24.88	0.73	3.60	(100)	24.55	0.45
	7.13	(200)			7.17	(200)		
	10.66	(300)			10.7	(300)		
	n/a				14.3	(400)		
	24.75	(010)	3.59		24.79	(010)	3.59	
pTBTD-5DH	3.55	(100)	24.88	0.66	3.55	(100)	24.88	0.48
	7.04	(200)			7.09	(200)		
	10.58	(300)			10.61	(300)		
	n/a				14.11	(400)		
	24.55	(010)	3.62		24.66	(010)	3.61	
pTBTD-2DT	4.10	(100)	21.56	0.95	4.00	(100)	22.07	0.64
	8.22	(200)			7.95	(200)		
	12.21	(300)			11.94	(300)		
	n/a				15.83	(400)		
	24.18	(010)	3.68		23.84	(010)	3.73	
pTBTD-OD	3.96	(100)	22.29	0.97	3.96	(100)	22.29	0.43
	7.90	(200)			7.99	(200)		
	n/a				12.01	(300)		
	24.76	(010)	3.59		24.60	(010)	3.62	

[a)] **pTBTD-5DH** and **pTBTD-2DT** were annealed at 200 °C for 30 min; **pTBTD-5DH(H)** and **pTBTD-OD** were annealed at 300 °C for 30 min.

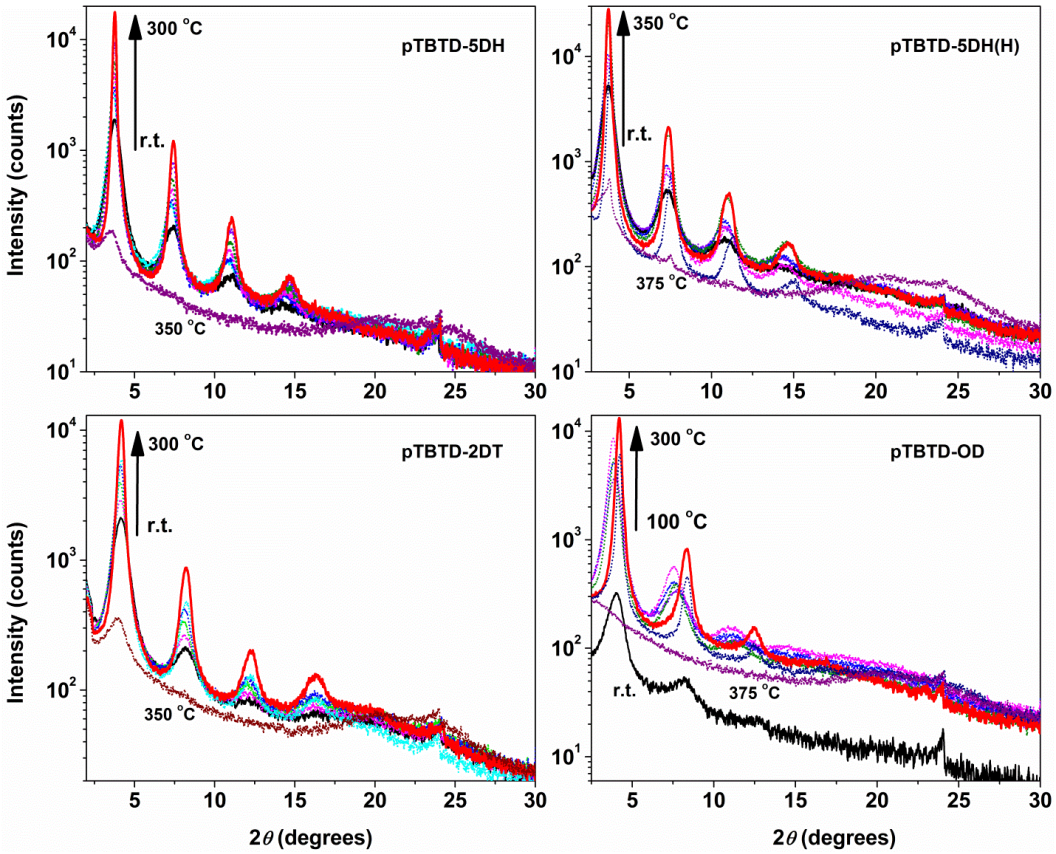

Figure 4.6. 1D-GIXS patterns of **pTBTD** drop-cast films. Films were drop-casted at room temperature; annealed at 100 °C for 30 min, then at 150 °C, 200 °C, 250 °C, 300 °C, 350 °C, and 375 °C for 30 min at each temperature.

The surface morphologies of **TBTD** polymer films were explored using tapping-mode atomic force microscopy (AFM), as shown in **Figure 4.8** (phase images) and **Figure S4.8b** (height images). Polymer films were spin-coated onto Si substrates (300 nm SiO_2 dielectric on heavily p-doped Si) that had been pre-functionalized with OTS-18. The as-spun films appeared highly ordered with a nano-fibrillar texture for **pTBTD-5DH**, **pTBTD-5DH(H)**, and **pTBTD-2DT**, and a nano-granular character was observed for the linear side chain analog, **pTBTD-OD**, which are consistent with the high crystallinity revealed by GIXS. All polymer films prepared here exhibited an increase in surface

roughness with increased annealing temperature over the range of 100 to 300 °C (**Figure 4.7b**), further supporting an increase in crystallinity and molecular ordering. In combination, the results from GIXS and AFM indicate that the degree of crystallinity and grain size of **TBTD** polymer can be improved by annealing at temperatures up to 300-350 °C. Given the importance of molecular order in determining the charge transport in π-conjugated polymers, we went on to investigate the impact of thermal annealing on the charge carrier transport properties.

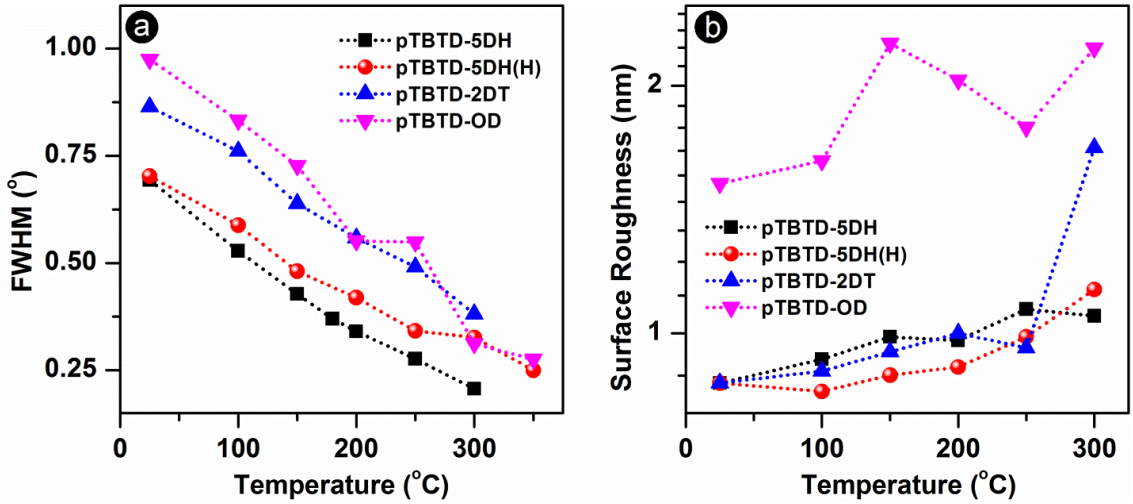

Figure 4.7. (a) FWHM of (100) diffraction peak of **TBTD** polymer films via 1D-GIXS as a function of annealing temperature; (b) surface roughness of **TBTD** polymer films measured by tapping mode AFM as a function of annealing temperature.

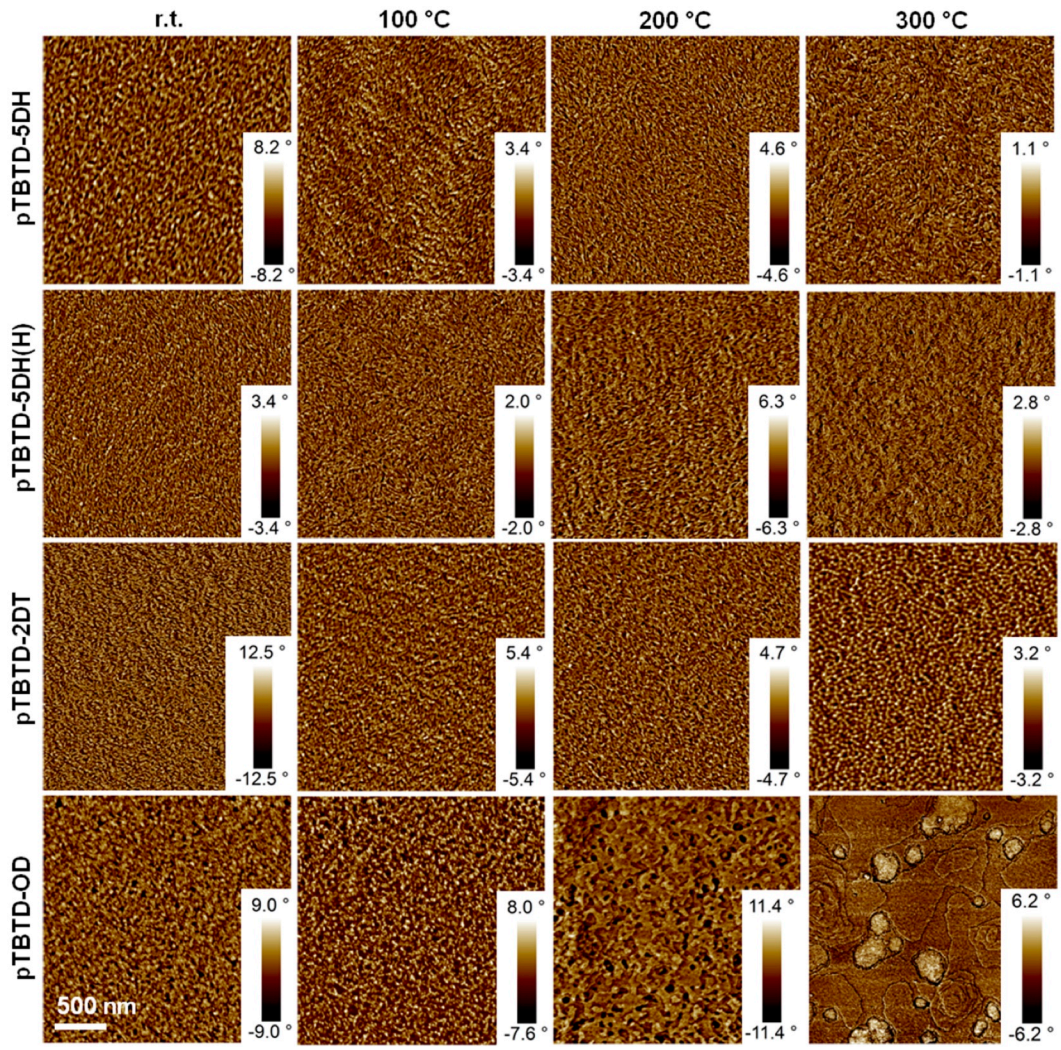

Figure 4.8. Tapping mode AFM phase images of **TBTD** polymers recorded as as-spun films (r.t.) and after annealing at 100 °C, 200 °C, and 300 °C for 30 min at each temperature followed by rapidly cooled to room temperature. Results recorded at room temperature after annealing at 150 °C and 250 °C for 30 min at each temperature are shown in Figure S4.8a.

4.3.7. Field-Effect Mobility.

The charge carrier transport properties of the **TBTD** polymers were investigated using a bottom-contact-bottom-gate organic field-effect transistor (OFET) device architecture. Solutions of the polymers in 1,2-dichlorobenzene (5–8 mg/mL) were spin-coated or drop-

cast onto OFET substrates (300 nm of SiO_2 dielectric grown on heavily n-doped Si) that had been pre-treated with OTS-18 (see fabrication details in S.I.). The channel between gold source and drain electrodes was 50 μm long and 2 mm wide. **pTBTD-5DH** and **pTBTD-5DH(H)** are more soluble in 1,2-dichlorobenzene than **pTBTD-2DT** and **pTBTD-OD**, indicating that the **5-DH** side chain maintains solubility of the polymer that is observed for other branched chains. **pTBTD-OD** did not fully dissolve even upon heating solution to 145 °C, leading to formation of non-uniform films. The output and transfer curves for devices fabricated with the **TBTD** polymers are shown in **Figure 4.9**, and the resulting mobilities calculated from the saturation regime are listed in **Table 4.5** (and **Table S4.1** at S.I.). **pTBTD-5DH** and **pTBTD-5DH(H)** exhibited higher field effect hole mobilities than **pTBTD-2DT** and **pTBTD-OD**. In particular, **pTBTD-5DH(H)** exhibited average and maximum hole mobility measurements of 2.32 and 2.95 $cm^2V^{-1}s^{-1}$ after annealing devices at 300 °C for 30 min. These values are *ca.* 3-4 times greater than those recorded for **pTBTD-2DT** (average, 0.4 $cm^2V^{-1}s^{-1}$; maximum, 0.81 $cm^2V^{-1}s^{-1}$) and *ca.* 8 times the mobility of **pTBTD-OD** (average, 0.3 $cm^2V^{-1}s^{-1}$, maximum, 0.34 $cm^2V^{-1}s^{-1}$). The significant increase in mobility has its origin in the combination of improved polymer solubility, enhanced π-π intermolecular interactions, and an increased degree of polymerization that result from the presence of branching of the side chain remote from the conjugated main chain of the polymer.

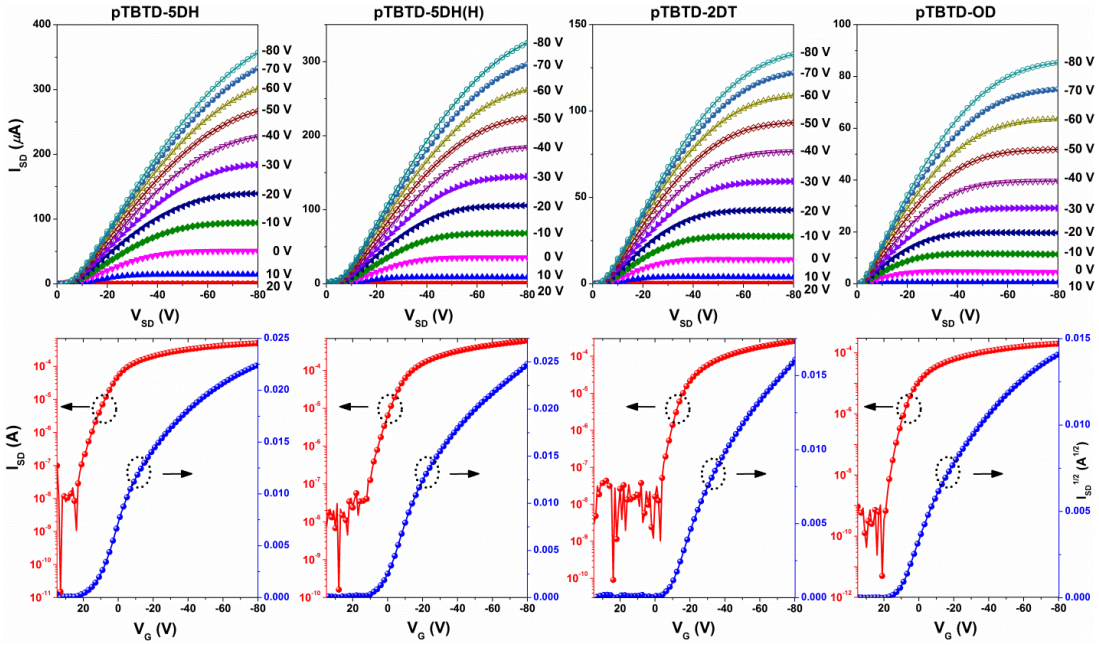

Figure 4.9. Output (top row) and transfer (bottom row, V_{SD}= -80 V) **TBTP** polymers measured in OFETs with channel size of 50 μm long x 2 mm wide.

OFET devices fabricated with the series of **TBTD** polymers were annealed at temperatures ranging from 100 to 300 °C to further understand the impact of thermally induced molecular ordering on charge carrier transport (**Table S4.1**). **pTBTD-5DH(H)**, **pTBTD-5DH** and **pTBTD-OD** exhibited an increase in hole mobility upon increasing the annealing temperature (**Figure S4.9**). For example, **pTBTD-5DH(H)** exhibited a hole mobility of up to 2.95 $cm^2V^{-1}s^{-1}$ after annealing at 300 °C compared to an average mobility of 1.02 $cm^2V^{-1}s^{-1}$ for as-spun films. However, no mobility improvement was observed upon thermal treatment of **pTBTD-2DT**.

Table 4.5. Hole-transport properties of **TBTD** polymers based OFET devices [a].

Samples	Annealing temp[b] / °C	Film processing	Hole mobility ($cm^2V^{-1}s^{-1}$)		$I_{ON/OFF}$	$V_{TH, avg}$ / V
			Avg	Max		
pTBTD-5DH(H)	n/a	spin-coat	1.02	1.34	10^4-10^6	11.7
	300	spin-coat	2.32	2.95	10^5-10^6	12.8
pTBTD-5DH	n/a	spin-coat	0.62	0.68	10^5-10^7	-13.2
		drop-cast	0.43	0.62	10^5-10^6	-0.5
	300	spin-coat	1.74	2.00	10^5-10^6	13.1
		drop-cast	1.06	1.21	10^5-10^7	5.4
pTBTD-2DT	n/a	spin-coat	0.49	0.77	10^6-10^6	8.8
		drop-cast	0.32	0.48	10^5-10^7	-21.4
	300	spin-coat	0.40	0.54	10^6-10^7	-2.7
		drop-cast	0.40	0.81	10^5-10^7	-7
pTBTD-OD	n/a	spin-coat	0.05	0.07	10^4-10^5	7.3
		drop-cast	0.04	0.06	10^3-10^5	6.4
	300	spin-coat	0.30	0.34	10^6-10^7	7
		drop-cast	0.16	0.27	10^4-10^6	-4.6

[a] Characterization results were based on 5 – 8 of devices for each fabrication conduction; [b] OFET devices were thermally annealed at 300 °C for 30 min. 'n/a' denotes no annealing (as-spun films). The results of thermal annealing at 100 - 250 °C are listed in **Table S4.1** (see S.I.).

Drop cast films showed a *ca*. 30-40% lower hole mobility than spin coated films (**Table 4.5** and **Table S4.1**), a trend which is opposite to that observed for the parent **pBT6**.[33] This may be explained by the formation of polycrystalline thick films of the **pTBTD** polymers during the slow solvent evaporation associated with drop casting (see

experimental details in S.I.). Grain boundaries in such films block efficient charge carrier hopping and result in lower mobilities.[16c, 146b]

4.4. Discussion.

The characterization results of **TBTD** polymers raises important points regarding side chain engineering as an approach to optimize the semiconducting properties of conjugated polymers. First, incorporation of an alkyl branch remote from the conjugated polymer backbone, illustrated here with the **5-DH** side chain, provides materials (i.e., **pTBTD-5DH**) with a solubility that is close (or even superior) to that of polymers bearing side chains that are branched close to the backbone (e.g., **2-DT** side chains on **pTBTD-2DT**). The solubility of the **TBTD** polymer series follows the sequence of **pTBTD-5DH** (and **pTBTD-5DH(H)**) ≥ **pTBTD-2DT** >> **pTBTD-OD**. This solubility improvement has two notable consequences: (i) the polymerization of **pTBTD-5DH** proceeds to higher molecular weight, and (ii) **pTBTD-5DH** gives rise to higher quality films than **pTBTD-OD**.

Second, **5-DH** side-chains impart **pTBTD-5DH** (and its corresponding dithienyldiketopyrrolopyrrole derivative **7a**) with π-π intermolecular interactions similar to that of the linear 1-octadecyl analog, **pTBTD-OD** (and its corresponding dithienyldiketopyrrolopyrrole derivative **7c**). This is in contrast to the case of the side

chain with a branch position proximal to the backbone, **pTBTD-2DT** (and **7b**), as has also been reported for a different D-A conjugated polymer by Fréchet et al.[206a] The interchain distances follow the sequence of **pTBTD-5DH** (3.6 Å) ≈ **pTBTD-OD** (3.62 Å) < **pTBTD-2DT** (3.73 Å) from 2D-GIWAXS; and compounds **7a** and **7c** are bathochromatically shifted from **7b** (**Figure 4.2** and **Figure S4.1b**) in the film state.

Thus, the use of side chains in which branch points are incorporated remote from the polymer backbone combines the superiority of branched side chains to improve polymer solubility (and in turn the degree of polymerization) with that of linear chains in facilitating dense π-π interchain stacking by lowering steric hindrance. In contrast, side chains that are branched close to the backbone increase steric hindrance, and linear side-chains limit solubility. Efficient charge carrier transport within polymeric semiconductors requires strong microscale π-π intermolecular interactions for effective charge carrier hopping; and good polymer solubility to facilitate formation of dense, continuous films and thereby avoid macroscale thin-film structural defects[212]. The side chains of **pTBTD-5DH** provide this combination of features to afford a material with significantly higher charge carrier mobility than **pTBTD-2DT** and **pTBTD-OD** in OFET devices.

4.5. Conclusion

We have developed a low bandgap **D-A-D-A'** polymer semiconductor, **pTBTD**, in which a linear side chain (**OD**) and side chains with branches remote (**5-DH**) and proximal (**2-DT**) were incorporated onto the backbone to afford **pTBTD-5DH**, **pTBTD-2DT** and **pTBTD-OD**, respectively. The systematic investigation of these three polymers demonstrates, for the first time, that the incorporation of side chains in which the branch position is remote from the polymer backbone combines the benefit of branched side chains in improving solubility with linear chains in promoting efficient π-π inter-molecular interactions. This provides a polymer with enhanced solution processability, a higher degree of polymerization, close π-π intermolecular stacking, and, in turn, superior macroscale charge carrier transport. These results underscore the significance of understanding structure-property relationships associated with the structure of side chains on conjugated polymers, and demonstrate the promising potential of developing high-performance organic semiconductors *via* side chain engineering.

Supporting Information

The synthetic details of preparing monomers and polymers, characteristic methods, OFETs fabrications, **Scheme S4.1**, **Table S4.1** and **Figure S4.1** – **S4.9** are included in supporting information-2.

CHAPTER 5

MOLECULAR ENGINEERING OF NON-HALOGENATED SOLUTION-PROCESSABLE BITHIAZOLE BASED ELECTRON TRANSPORT POLYMERIC SEMICONDUCTORS

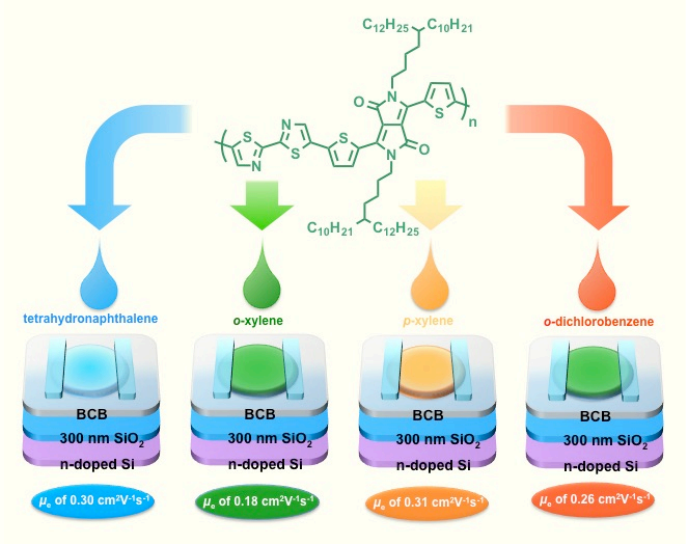

5.1. Abstract:

The electron deficiency and *trans* planar conformation of bithiazole is potentially beneficial for the electron transport performance of organic semiconductors. However, the incorporation of bithiazole into polymers through a facile synthetic strategy remains a challenge. Herein, 2,2'-bithiazole was synthesized in one step and copolymerized with dithienyldiketopyrrolopyrrole to afford poly(dithienyldiketopyrrolopyrrole-bithiazole), **PDBTz**. **PDBTz** exhibited electron mobility reaching 0.3 $cm^2V^{-1}s^{-1}$ in organic field-effect

transistor (OFET) configuration; this contrasts with a recently discussed isoelectronic conjugated polymer comprising an electron rich bithiophene and dithienyldiketopyrrolopyrrole, which displays merely hole transport characteristics. This inversion of charge carrier transport characteristics confirms the significant potential for bithiazole in the development of electron transport semiconducting materials. Branched 5-decylheptacyl side chains were incorporated into **PDBTz** to enhance polymer solubility, particularly in non-halogenated, more environmentally compatible solvents. **PDBTz** cast from a range of non-halogenated solvents exhibited film morphologies and field-effect electron mobility similar to those cast from halogenated solvents.

5.2. Introduction

The development of high efficiency, air stable electron transport polymeric semiconductors for organic electronic devices has attracted much attention due to their importance in the fabrication of organic p-n junction devices, such as complementary-metal-oxide-semiconductor (CMOS)-like logic circuits,[6, 29d] thermoelectrics,[13b] hetero-junction photovoltaics,[2b, 213] and organic light-emitting diodes.[214] For example, a combination of hole transport and electron transport semiconductors with comparable mobility values is required to implement CMOS-like logic, which is widely used in digital integrated circuits including microprocessors, microcontrollers, and static random

access memory devices.[6, 17c, 41c] Significant advances in the development of hole transport polymeric semiconductors have led to materials that demonstrate field-effect hole mobilities of up to 20 $cm^2V^{-1}s^{-1}$.[27c, 61a] However, less progress has been made towards the development of electron transport counterparts.[28d, e, 29a, 162b] The more limited advances in this instance result from challenges associated with the stabilization and delocalization of LUMO, or EA, of π-conjugated polymers.[1a, 20a, 29a, 214a] Stabilization of the LUMO means raising the electron affinity, which can be realized by materials that consist of electron-deficient conjugated repeat units.[1a, 14d, 29a, 33] The LUMO delocalization can be enhanced by backbone planarization and inter-chain stacking.[32b]

The 2,2'-bithiazole unit exhibits a number of features that could be attractive in the search for electron transport conjugated polymers. The presence of electronegative nitrogen atoms lowers the EA in comparison to analogs that consist of electron rich units such as thienyl derivatives.[177b, 215] The *trans* conformation of bithiazole (with a dihedral angle between the thiazole rings close to 180°, as confirmed by density functional theory, DFT, in this study, *vide infra*) can promote polymer backbone planarity, which extends intrachain π-conjugation and interchain π-π stacking, in comparison to analogs such as biphenyl that is not coplanar.[216] Thiazole has a large dipole moment of 1.6 D;[217] an antiparallel alignment between the two thiazole moieties within bithiazole leads to a net

zero dipole, which is one driving force for planarization of bithiazole. Additionally, the large dipole of the thiazole unit could impart strong dipole-dipole interactions between bithiazole-based polymer chains.[218]

The bithiazole unit has been primarily used to build up hole transport donor-acceptor π-conjugated copolymers; since the previous standpoints took account of bithiazole as a weak acceptor. Recent studies indicated the feasibility of bithiazole in developing electron transport small molecular semiconductors;[218-219] and in few cases, bithiazole-based polymers were able to exhibited ambipolar properties.[107] The development of bithiazole based electron transport polymeric semiconductors hence could be expected, though no study has been reported yet. One significant challenge lies in the development of an efficient synthetic pathway to incorporate bithiazole units into π-conjugated molecules and polymers.[215b, 218] Herein 2,2'-bithiazole was synthesized in one step, and copolymerized with a second electron deficient monomer, dithienyl diketopyrrolopyrrole (TDPP), to afford the first example of a bithiazole based electron transport polymer, poly(dithienyldiketopyrrolopyrrole-bithiazole), **PDBTz**, as shown in **Figure 5.1**. An isoelectronic conjugated polymer consisting of alternating electron rich 2,2'-bithiophene units and TDPP (PDQT, see structure shown in **Figure 5.2**) exhibits pure hole transport behavior.[53, 203d, 220] Through comparison of **PDBTz** with PDQT, we set out to explore

the capability of bithiazole on tailoring hole and electron transport characteristics, with the expectation that the bithiazole analog would enhance electron transport behavior.

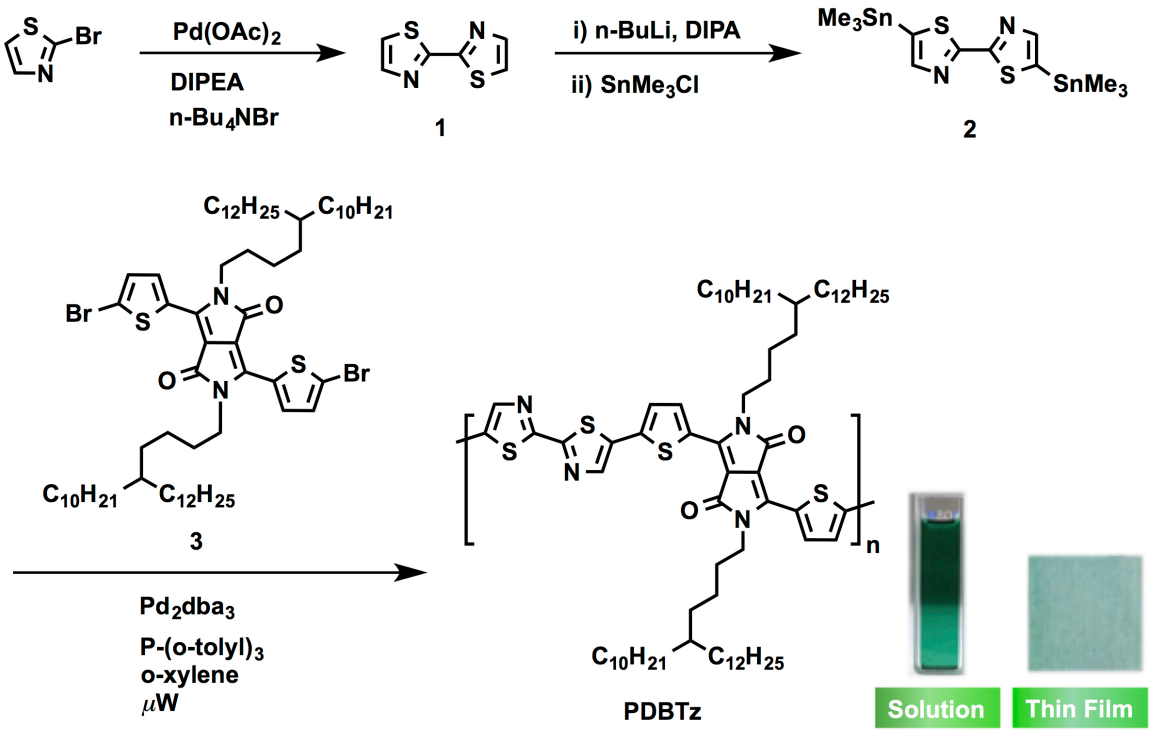

Figure 5.1. The synthetic route to prepare **PDBTz**. The inserted image (bottom right) shows a **PDBTz** solution in *o*-dichlorobenzene (DCB) and a spin-coated film of **PDBTz** from DCB (5 mg mL^{-1}) on a glass substrate.

Side chain substitution on the bithiazole and dithienyl groups was avoided to minimize steric effects within the **PDBTz** backbone. Branched 5-decylheptadecyl (5-DH) side chains were utilized as they had been shown in our previous study to facilitate both polymer solubility and effective π-π inter-chain interactions by virtue of having a branch point remote from the polymeric main chain.[34] Such a side chain was incorporated into the TDPP unit to promote π-π inter-chain interactions and solubility in a wide range of

solvents including non-halogenated options such as xylenes or 1,2,3,4-tetrahydronaphthalene (THN), which are more eco-friendly than halogenated alternatives.

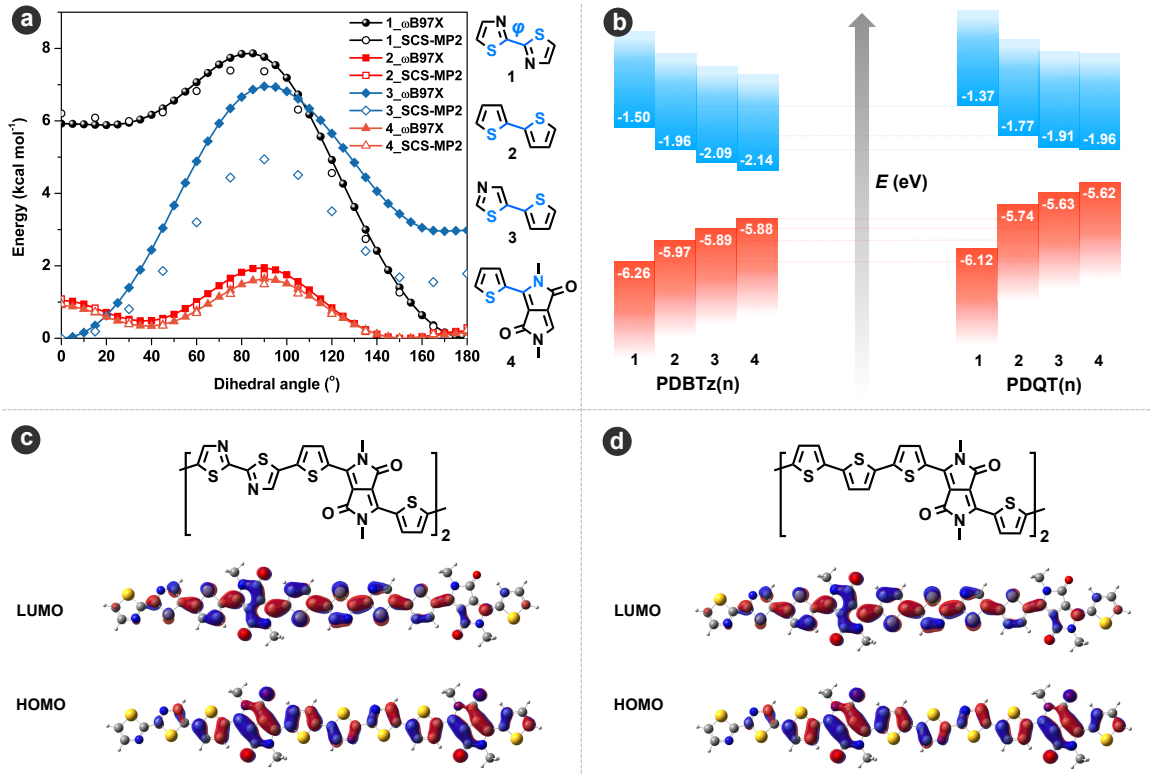

Figure 5.2. (a) DFT (tuned-ωB97X) and SCS-MP2 torsional energies of **PDBTz** subunits at different dihedral angles; dihedral angles (φ) for the subunits are highlighted in blue. (b) DFT HOMOs and LUMOs of the monomer (n=1), dimer (n=2), trimer (n=3), and tetramer (n=4) of **PDBTz** and PDQT. Illustrations of the DFT frontier molecular orbitals for the dimers of (c) **PDBTz** and (d) PDQT.

Current semiconducting polymer solution-processes for organic electronic devices primarily depend on the use of halogenated solvents such as chlorobenzene, *o*-dichlorobenzene (DCB), or 1,2,4-trichlorobenzene (TCB), which present significant health and environmental challenges and severely limit their future application. Thus,

materials that can be processed from non-halogenated media are highly desirable.[30, 221] However, few such examples have been reported, and electron transport polymeric semiconductors processable from non-halogenated solvents are especially rare.[17c] Here, **PDBTz** thin-film OFETs fabricated using non-halogenated *o*-xylene, *p*-xylene, and THN, as well as DCB were investigated. This allowed for a systematic study of solvent on semiconducting polymer thin-film ordering, texture, charge carrier transport performance, and the practicality of developing high mobility n-channel OFET devices via more environmentally-benign processing.

5.3. Results

5.3.1. Polymer Synthesis, Solubility, and Thermal Properties

The synthesis of **PDBTz** is outlined in **Figure 5.1**, and complete synthetic details are provided in the Supporting Information-3 (**S.I.**). Commercially available 2-bromothiazole was homocoupled to afford 2,2'-bithiazole, **1**.[222] Metallation of **1** afforded distannane monomer **2**.[215c] Conversion of **1** to **2** approached 100 % based on ^{1}H NMR analysis. However, **2** has limited stability: de-metallation of 25-30 mol% of **2** back to **1** takes place within one week (**Figure S5.6**, **S.I.**). Hence, the polymerization should be carried out with freshly prepared monomer. **PDBTz** was prepared by Stille step-growth

polymerization of monomer **2** with 3,6-bis(5-bromo-2-thienyl)-*N,N*-di(5-decylheptadecyl)diketopyrrolo-pyrrole monomer (**3**)[34] under microwave irradiation (160 °C for 2 h). The crude polymer was purified through precipitation from methanol followed by Soxhlet extraction to afford **PDBTz** that was further characterized. Gel permeation chromatography (GPC; 135 °C with TCB as eluent) indicated a number-average molecular weight (M_n) of 64 kg mol^{-1}, which corresponds to a degree of polymerization (DP) of 53, as shown in **Table 5.1**. The relatively large PDI of 3.6 is likely due to the polymer aggregation in solution.

Table 5.1. PDBTz molecular weight, photophysical, and thermal properties

Polymer	Mn [kDa]	PDI	DP	Absorption maximum [eV]		E_g^{opt} [eV]	T_d [a)] [°C]	T_h [b)] [°C]	T_c [c)] [°C]
				Solution	Film				
PDBTz	64	3.6	53	1.62, 1.77, 2.78, 3.82	1.62, 1.78, 2.77, 3.80	1.33	417	-44	-47

[a)] T_d: glass transition temperature; [b)] T_h: phase transition temperature upon heating process; [c)] T_c: phase transition temperature upon cooling process.

The attainment of relatively high molecular weight material suggested that the resulting polymer has good solubility in *o*-xylene. Process solvents have a significant influence on the molecular ordering, morphology, and charge carrier mobility of thin-film polymeric semiconductors. Hence, the characterization and processing of **PDBTz** in *o*-xylene along with two other similar non-halogenated solvents, *p*-xylene and THN, were explored. The theoretical solubility of **PDBTz** was estimated using the Hansen solubility

parameter space (R_a),[30a, 182a] which describes the difference in Hansen solubility parameters (HSPs) of **PDBTz** (1) and solvents (2), as shown in E.q. 5.1:

$$R_a = \sqrt{4(\delta_{d1} - \delta_{d2})^2 + (\delta_{p1} - \delta_{p2})^2 + (\delta_{h1} - \delta_{h2})^2} \qquad \text{E.q. 5.1}$$

where δ_d, δ_p, and δ_h refer to the dispersion force solubility parameter, dipolar intermolecular force solubility parameter, and hydrogen bonding solubility parameter, respectively. Lower values of R_a predict a lower cohesive energy density difference between **PDBTz** and a solvent, which corresponds to a weaker thermodynamic driving force for phase separation of solute from solvent and a higher solubility of the polymer.[182d] The pertinent physical properties of **PDBTz** and the four solvents (DCB, *o*-xylene, *p*-xylene, and THN) are listed in **Table 5.2** (the experimental and calculation details are provided in the **S.I.**). Solutions of **PDBTz** in the two xylenes exhibit similar R_a values as for **PDBTz** in DCB, whereas the corresponding value for THN is much lower. These results suggest similar or even better **PDBTz** solubility in the non-halogenated solvents than in DCB. Experimental results indicate that **PDBTz** possesses solubility in the range of 5-9 mg mL^{-1} in the four solvents at 90 ^oC. **PDBTz** exhibits the lowest solubility in *p*-xylene (5 mg mL^{-1}), while the solubility is highest with THN (9 mg mL^{-1}).

PDBTz is stable up to 410 °C (see TGA characterization, **Table 5.2** and **Figure S5.7**), indicating high thermal stability. The polymer exhibits one endothermic (T_h = -44 °C) and one exothermic transition (T_c = -47 °C) upon heating and cooling, respectively (see

DSC characterization, **Table 5.2** and **Figure S5.7**). In light of prior results using the same substituent, this most likely corresponds to the disordering and reordering processes associated with the 5-DH side chains.[34]

Table 5.2. Hansen solubility parameters (δ_d, δ_p, and δ_h) and boiling points (b.p.) for **PDBTz** dichlorobenzene (DCB), *o*-xylene, *p*-xylene and tetrahydronaphthalene (THN).

	δ_d [a] [$MPa^{1/2}$]	δ_p [b] [$MPa^{1/2}$]	δ_h [c] [$MPa^{1/2}$]	R_a [d] [$MPa^{1/2}$]	b.p. [°C]
PDBTz	20.0	1.2	5.1		n/a
DCB	19.2	6.3	3.3	5.64	180
o-Xylene	17.8	1.0	3.1	4.84	144
p-Xylene	17.6	1.0	3.1	5.20	138
THN	19.6	2.0	2.9	2.47	207

[a] δ_d: dispersion force solubility; [b] δ_p: dipolar intermolecular force solubility; [c] δ_h: hydrogen bonding solubility. [d] R_a: Hansen solubility parameters space (HSP difference between **PDBTz** and solvents) calculated by E.q. 5.1.

5.3.2. Photophysical Properties

The spectroscopic features of **PDBTz** solutions in the different solvents are quite similar. Peaks are observed at ca. 325, 446, 702, and 767 nm in the spectra of **PDBTz** in each solvent, as shown in **Figure 5.3a**. The bands with λ_{max} at *ca*. 446, 702, and 767 nm may be ascribed to TDPP units since solutions of the analogous diketopyrrolopyrrole-*oligo*thiophene polymers exhibit similar features;[53, 61a, 203d, 220] while the **PDBTz** band at λ_{max} of 325 nm was assigned to the bithiazole units, given that 2,2'-bithiazole (compound

1) in THF exhibits an absorption band with λ_{max} at 320 nm (**Figure 5.3a**). The absorption spectra of **PDBTz** thin-films (**Figure 5.3b**) are essentially identical to those of the solution spectra, suggesting a similar rigid polymer chain conformation in the solid state as in solution. Based on the absorption onset, the optical band gap (E_g^{opt}) of **PDBTz** is estimated as 1.33 eV. The increase in the intensity of the peak at 697 nm relative to that at 765 nm for the film (**Figure 5.3b**) in comparison to the solution (**Figure 5.3a**) suggests that **PDBTz** favors the interchain excitonic coupling[166a, b] in thin films. **PDBTz** films cast from solutions in DCB, *o*-xylene, *p*-xylene, and THN exhibit similar spectroscopic characteristics, which indicates similar thin-film microstructure (ordering and orientation) for all of the systems, although the film prepared using *p*-xylene is likely to form a stronger interchain excitonic coupling.

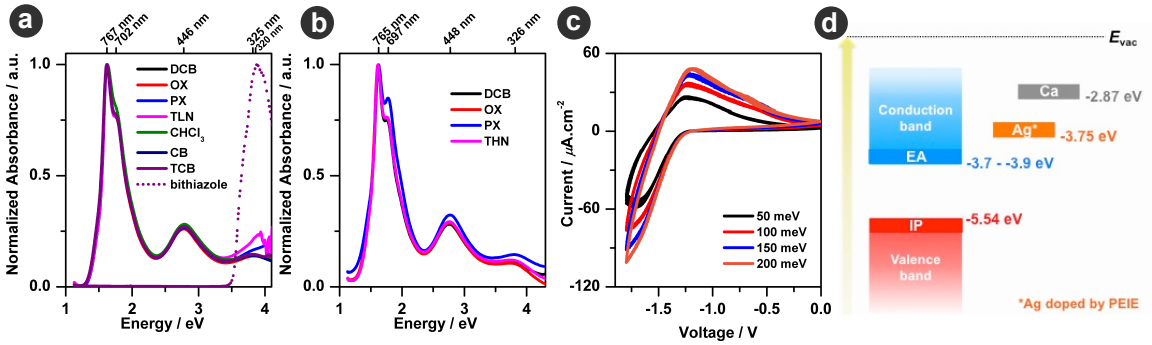

Figure 5.3. The photophysical and electrochemical properties of **PDBTz**: (a) UV/vis absorption spectra of **PDBTz** in solution (DCB: *o*-dichlorobenzene, OX: *o*-xylene, PX: *p*-xylene, THN: tetrahydronapthalene, $CHCl_3$: chloroform, CB: chlorobenzene, TCB: 1,2,4-trichlorobenzene); (b) UV/vis absorption spectra of **PDBTz** thin-films; (c) cyclic voltammograms of a drop-cast film of **PDBTz** on a platinum electrode (in 0.5 M Bu_4NPF_6/acetonitrile) at scan rates between 20 mV s^{-1} and 200 mV s^{-1} (five cycles at each scan rate); (d) Ionization potential (IP) and electron affinity (EA) of **PDBTz** and workfunctions of Ca and PEIE doped Ag.

5.3.3. Characterization of Electronic Structure

The redox potentials of **PDBTz** thin-films were investigated using cyclic voltammetry (CV) and differential pulse voltammetry (DPV) (**Figure S5.9**). **PDBTz** exhibits an onset for reduction at -1.30 V versus Fc/Fc^+ (-5.08 eV versus vacuum[54a, 167]) by CV, and -1.18 V (versus Fc/Fc^+) by DPV, as shown in **Table 5.3**, which corresponds to an electron affinity of -3.8 to -3.9 eV. The reversibility of the reduction, as shown in **Figure 5.3c**, demonstrates the stability of reduced **PDBTz** as an electron carrier. However, **PDBTz** exhibits an irreversible electrochemical oxidation process as demonstrated by both CV and DPV, with a peak onset at +0.82 V (versus Fc/Fc^+) by CV and +0.66 V (versus Fc/Fc^+) by DPV (**Figure S5.9b**). These electrochemical results are opposed to the typical hole transport polymeric semiconductors that have a reversible oxidation while no obvious reduction.[33-34, 203d]

Thin films of **PDBTz** were characterized by ultraviolet photoelectron spectroscopy (UPS) to determine the intrinsic ionization potential (IP) and work function (φ) (**Figure 5.3**, **Figure S5.10**). The 5.54 eV **PDBTz** ionization potential suggests good ambient stability towards oxidation.[1a] Taking into account an optical gap of *ca*. 1.33 eV and an exciton binding energy in the range of 0.3-0.5 eV,[161] would lead to an electron affinity on the order of -3.7 to -3.9 eV, which is consistent with the CV/DPV estimate. Such an

electron affinity implies a good ambient stability for electron transport organic semiconductors.[29a, 214a]

Table 5.3. **PDBTz** ionization potential and electron affinity.

Polymer	UPS			DPV		CV	
	IP [a] [eV]	ϕ [eV]	EA[b] [eV]	E_{red} [c] [V]	EA [eV]	E_{red} [c] [V]	EA [eV]
PDBTz	5.54	4.90	-3.7 - -3.9	-1.18	-3.90 [d]	-1.30	-3.75 [d]

[a] IP: ionization potential; [b] EA: electron affinity, taking into account an optical gap of *ca*. 1.33 eV and an exciton binding energy in the range of 0.3-0.5 eV; [c] E_{red}: reduction potential; [d] calculated from onsets for reduction versus Fc/Fc+ (-5.08 eV versus vacuum[54a, 167]) + 5.08 eV.

5.3.4. Field-effect electron transport

PDBTz charge carrier transport properties were studied using organic field-effect transistors (OFETs) with top-contact/bottom-gate (TCBG) and bottom-contact/top-gate (BCTG) architectures, as shown in **Figure 5.4**. With the aim of minimizing barriers to electron injection, and taking into account the electron affinity of **PDBTz** (in the range of -3.8 to -3.9 eV), calcium (work function, φ = 2.9 eV)[28a] and ethoxylated polyethylenimine (PEIE) doped silver (φ = 3.7 eV)[141] were selected as source and drain electrodes in TCBG and BCTG devices, respectively (**Figure 5.2d**). TCBG and BCTG OFETs were initially fabricated based on spin-coated **PDBTz**/DCB solutions (5 mg mL^{-1}). The results are listed in **Table 5.4**.

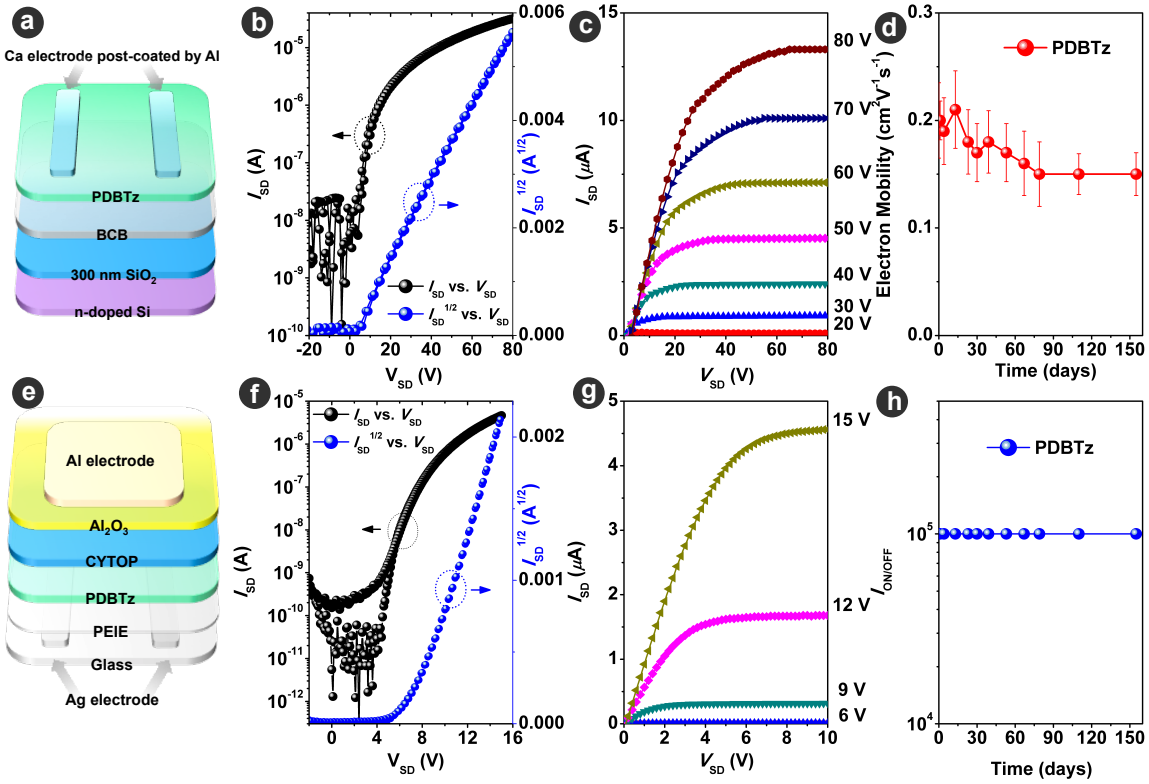

Figure 5.4. I-V curves for **PDBTz**-based OFETs with bottom-gate/top-contact (a) and top-gate/bottom-contact (e) architectures, and their corresponding transfer (b and f) and output (c and g) plots; effect of OFET stability under ambient conditions (25 °C and 55-60 %RH) on electron mobility (d) and $I_{ON/OFF}$ (h).

OFETs making use divinyltetramethylsiloxane-bis(benzocyclobutene) (BCB)[20a, 28a] as the dielectric layer to minimize electron traps exhibited ideal n-channel I-V transfer characteristics, with average and maximum electron field-effect mobility values (μ_e) of 0.17 and 0.26 $cm^2V^{-1}s^{-1}$, respectively, and a current on/off ratio ($I_{ON/OFF}$) greater than 10^5. Comparable electron transport performance was determined for **PDBTz**-based BCTG OFETs with CYTOP/Al_2O_3 as dielectric and encapsulation bilayers. BCTG devices were characterized based on a 10 V source-drain voltage (V_{SD}) and a gate voltage (V_G) in a range of 0 to 16 V, revealing the feasibility of using **PDBTz** for high performance

devices under relatively low operating voltages. Notably, the **PDBTz** devices exhibited similar performance to those prepared with poly(NDI2OD-T2) (0.1 $cm^2V^{-1}s^{-1}$), a benchmark electron transport polymeric semiconductor, based on our previous study.[141] Both **PDBTz** device architectures exhibited excellent n-channel transistor behavior with low (4-8 V) threshold voltages (V_{th}) and negligible hysteresis (**Figure 5.4b,f**). The device performance was determined after thermal annealing at 150 °C. To explore **PDBTz** air stability, devices encapsulated by a CYTOP layer (**S.I.**) were stored at 25 °C and 55-70 % RH, and were characterized periodically over 4 months. No appreciable changes were observed in $I_{ON/OFF}$ and only a small decrease in μ_e was observed over this period (**Figure 5.4d,h**). The ambient stability correlates with the low polymer frontier energy levels. Further enhancement of device stability against O_2 and H_2O is expected through inorganic/organic multilayer encapsulation.[157a]

PDBTz possesses similar solubility in non-halogenated *o*-xylene, *p*-xylene, and THN, as in DCB (*vide supra*). **PDBTz** OFET devices were also fabricated by spin-coating polymer solutions in *o*-xylene (5 mg mL^{-1}), *p*-xylene (4 mg mL^{-1}) and THN (5 mg mL^{-1}) to evaluate the impact of solution-processing from non-halogenated vs. halogenated solvents. As shown in **Figure 5.4**, **PDBTz** electron transport performance in BGTC devices was comparable in devices fabricated from all four solvents, with an average μ_e

of 0.18 $cm^2V^{-1}s^{-1}$. A maximum value of μ_e (0.3 $cm^2V^{-1}s^{-1}$) was obtained in devices prepared from THN and *p*-xylene.

Table 5.4. Electron transport properties of PDBTz fabricated on top-contact/bottom-gate and bottom-contact/top-gate OFETs [a)]

Solvent	TCBG				BCTG			
	$\mu_{e,FET}$ [$cm^2V^{-1}s^{-1}$]		$I_{ON/OFF}$	V_{th} [V]	$\mu_{e,FET}$ [$cm^2V^{-1}s^{-1}$]		$I_{ON/OFF}$	V_{th} [V]
	avg.	max			avg	max		
DCB	0.17 (±0.05)	0.26	10^5	5.5 (±1.2)	0.17 (±0.04)	0.21	10^5	7.8 (±0.4)
o-Xylene	0.14 (±0.04)	0.18	10^5	8.0 (±1.2)	0.08	0.08	10^4	0.8
p-Xylene	0.24 (±0.06)	0.31	10^5	4.0 (±1.0)	0.08 (±0.002)	0.08	10^3	0.8 (±0.3)
THN	0.18 (±0.07)	0.30	10^5	6.0 (±3.5)	0.09 (±0.007)	0.11	10^3	0.1 (±0.1)

[a)] BGTC characterization results were based on 5–8 of devices for each fabrication conduction; TGBC characterization results were 3 – 6 of devices for each fabrication conduction. These OFET devices were thermally annealed at 150 °C for 30 min.

5.3.5. Thin film morphology and microstructure

The surface morphologies of **PDBTz** films that were prepared by spin-casting from the four solutions onto BCB modified Si substrates were characterized using tapping-mode atomic force microscopy (AFM). All of the films exhibited similar nanostructured morphologies with similar grain sizes of 30-60 nm and surface roughness of 1.04-1.38 nm, as shown in **Figure 5.5**. This suggests comparable contact between spin-coated films and the source-drain electrodes of TCBG OFETs.

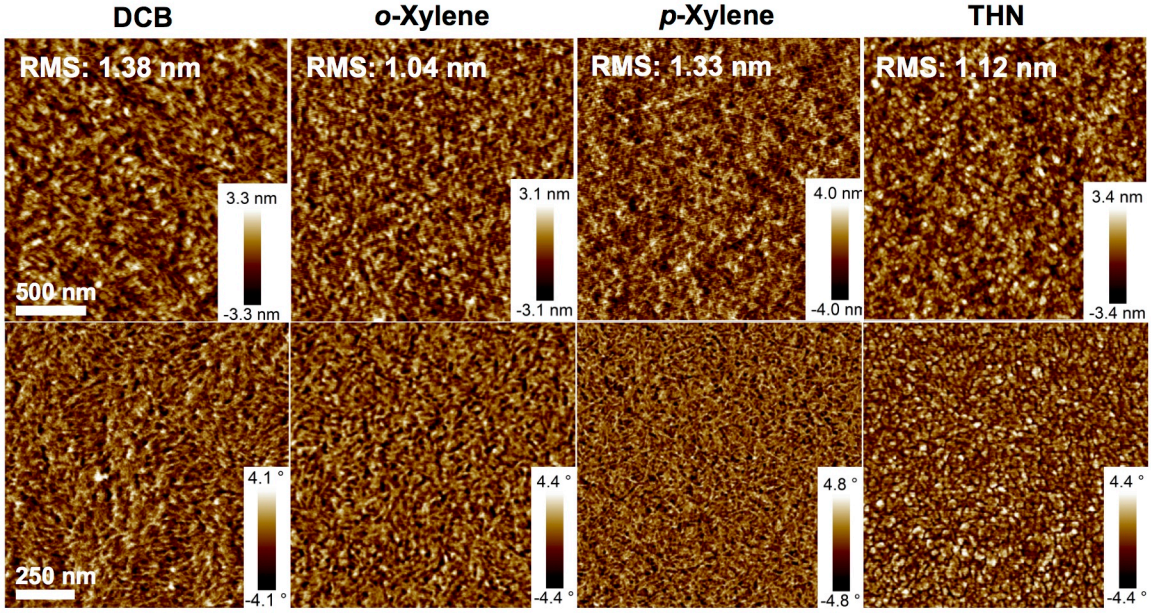

Figure 5.5. Tapping mode AFM height (top row) and phase (bottom row) images of **PDBTz** recorded after annealing each film at 150 °C for 30 min followed by rapid cooling to room temperature.

The polymer films were investigated further by two-dimensional grazing incidence wide angle X-ray scattering (2D-GIWAXS) to explore the relationship between film microstructure and electron transport performance. Films were prepared from drop-cast PDBTz solutions in DCB, *o*-xylene, *p*-xylene, and THN onto Si substrates (300 nm SiO_2 dielectric on heavily p-doped Si) that had been functionalized with cross-linked BCB. X-ray scattering patterns, before and after thermal annealing at 150°C, were similar for each sample, regardless of solvent, as shown in **Figure 5.6**. All of the films exhibited well-defined <*h*00> diffraction patterns along the q_z (out-of-plane) axis that is attributed to a highly ordered lamellar *d*-spacing structure between polymer chains that are segregated by 5-DH chains. In addition the films exhibited <010> peaks along the q_{xy} (in-plane) axis

arising from π–π stacking of PDBTz backbones. The spacing distances (**Figure 5.7a, e**), full-width-at-half-maximum (FWHM, **Figure 5.7b, f**), coherence length (mean size of ordered crystalline domains, **Figure 5.7c, g**), and relative degrees of crystallinity[162b] (rDoC, **Figure 5.7d**) indicated by the <100> and <010> peaks are similar for PDBTz films from all four solutions both before and after annealing. In light of the length of a heptadecyl chain in an all-trans conformation (*ca*. 17.5 Å), the PDBTz lamellar *d*-spacing (24-25 Å) suggests that the side chains are interdigitated within the crystalline lattice.

The **PDBTz** <100> and <010> patterns exhibit highly anisotropic distributions along with the azimuthal angle, χ, as seen in **Figure 5.6**. This was quantitatively evaluated by Herman's orientation function (*S*, the calculation details are provided in **S.I.**).[223] Results of this analysis are shown in **Table 5.5**. The four **PDBTz** films exhibited essentially identical *S* values that approached 0.9 for the <100> diffraction, which is regarded as a high value for a polymer system and is indicative of a high degree of alignment parallel to χ_{max}; on the other hand, χ_{max} for <100> is close to zero. These results quantitatively demonstrate that all four **PDBTz** films have average lattice planes oriented normal to the q_{xy} axis, which corresponds to an edge-on orientation, as shown in **Scheme S5.1**. The $\Delta\chi_{FWMH}$ term refers to the full width at half maximum of peak intensity along the χ axis. All four films display a value of $\Delta\chi_{FWMH}$ in a range of 9 to 13° for the <100> diffraction. Such a narrow distribution further confirms a high degree of orientation along χ_{max}. A

similar phenomenon is observed for the <010> pattern: the four samples have an *S* value of approximately 0.8 at $\chi_{max} \approx 86°$. These results are also consistent with a highly aligned edge-on orientation for the average lattice planes, which mirrors the <100> analysis. In summary, all four **PDBTz** films exhibit a highly edge-on aligned orientation irrespective of casting solvents.

Table 5.5. Hermans' orientation function of <100> and <010> peaks in **PDBTz** films cast from DCB, *o*-xylene, *p*-xylene and THN, before and after annealing

Solvent	RT [a]						150 °C [b]					
	<100>			<010>			<100>			<010>		
	S [c]	χ_{max} [d]	$\Delta\chi_{FWHM}$ [e]	S	χ_{max}	$\Delta\chi_{FWHM}$	S	χ_{max}	$\Delta\chi_{FWHM}$	S	χ_{max}	$\Delta\chi_{FWHM}$
DCB	0.85	1.8	12.3	0.66	4.5	21.3	0.83	1.9	11.7	0.62	3.5	23.1
o-Xylene	0.88	1.9	9.7	0.76	3.8	19.7	0.90	1.1	7.6	0.77	4.4	19.2
p-Xylene	0.87	2.8	10.9	0.81	4.6	17.0	0.89	1.4	8.4	0.79	4.0	19.0
THN	0.87	2.1	10.9	0.72	4.0	23.9	0.90	1.7	9.3	0.73	4.0	19.4

[a] **PDBTz** films as-spun from four solutions; [b] **PDBTz** films were thermally annealed at 150 °C for 30 min; [c] Hermans' orientation function; [d] the azimuthal angle at which X-ray scattering intensity reaches the maximum; [e] absolute values of χ distribution corresponding to full width at half maximum of peak intensity.

The FWHM values for the <200> and <300> diffractions relative to that of the <100> diffraction (i.e., $FWHM_{<200>}/FWHM_{<100>}$ and $FWHM_{<300>}/FWHM_{<100>}$) underwent no obvious change upon annealing (**Figure 5.7**h), which demonstrates identical enhancement in the lattice cumulative order.[179] After annealing, all **PDBTz** films exhibited a reduction in FWHM and corresponding improvement in coherence length for both <100> and <010> patterns (**Figure 5.7**b, f and c, g), together with a 3-10% increase

in rDoC, which correlate well with the observed increase in electron mobility upon annealing. In consideration of the subtle increase in orientation distribution within all four **PDBTz** films after thermal annealing, as shown by changes in S and $\Delta\chi_{FWMH}$ (**Figure 5.7**), annealing primarily impacts **PDBTz** ordering and grain size, while crystallite growth likely proceeds equally along each orientation distribution direction. The microstructure and morphology analyses demonstrate that the processing solvents have similar effect on the morphology, molecular ordering, orientation, and rDoC of **PDBTz** films, in good accord with very similar electron transport properties for the respective samples.

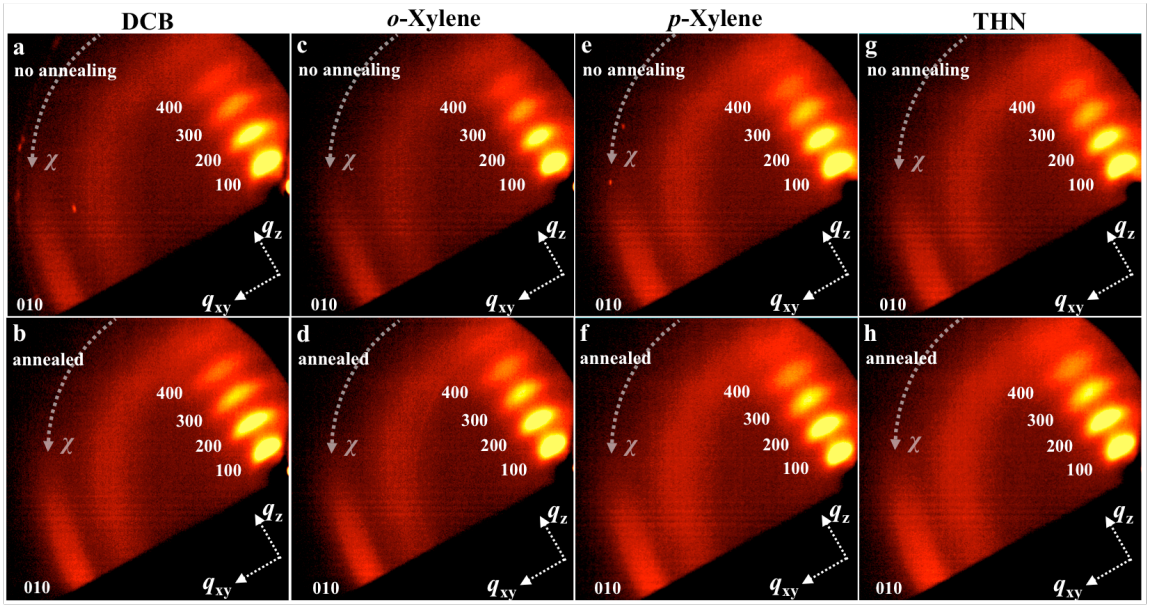

Figure 5.6. 2D-GIWAXS area detector images of **PDBTz** films cast from DCB (a, b); *o*-xylene (c, d); *p*-xylene (e, f); and THN (g, h) solutions, respectively. Top row, as-spun films; bottom row, samples after annealing at 150 °C for 30 min followed by rapid cooling to room temperature.

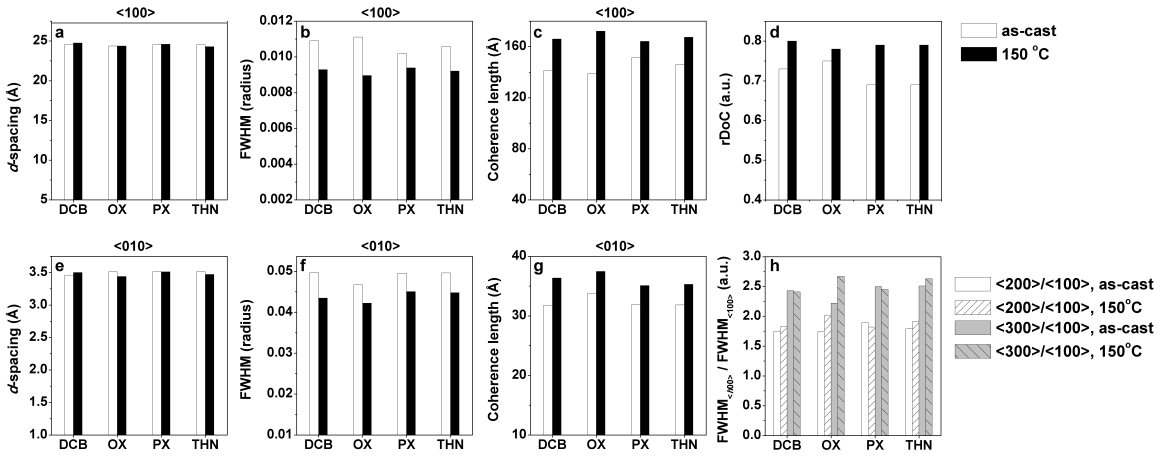

Figure 5.7. *d*-spacing (a and e), FWHM (b and f), and coherence length (c and g) for PDBTz cast from DCB, *o*-xylene (OX), *p*-xylene (PX), and tetrahydronaphthalene (THN) solutions, respectively, along the <100> and <010> peaks. The relative degree of crystallinity (rDoC, d). Hollow bars: as cast films; black bars: films after 150 °C/30 min anneal. (h) Relative FWHMs of <200> and <300> to those of <100>: $FWHM_{<200>}/FWHM_{<100>}$ and $FWHM_{<300>}/FWHM_{<100>}$ for as cast films (bars with no oblique line) and films after thermal annealing at 150 °C for 30 min (bars with oblique lines).

5.3.6. Comparison of PDBTz with PDQT

Several groups have reported the copolymerization of bithiophene-containing monomers and TDPP to afford poly(diketopyrrolopyrrole-quaterthiophene), PDQT,[53, 203d, 220] whose chemical structure is shown in **Figure 5.2d**. Electrochemical studies of PDQT reveal reversible oxidation, and hole transport properties are observed in OFETs prepared from this material. In contrast, **PDBTz**, where the bithiophene segment of each PDQT repeat unit is replaced by bithiazole, displays reversible electrochemical reduction and electron transport behavior. This shift from hole transport for PDQT to electron

transport for **PDBTz** clearly demonstrates a significant impact for bithiazole to instill electron transport characteristics.

For a side-by-side comparison of these two polymers, **PDBTz** was applied to BCBG transistors with Au (φ = 5.1 – 5.5 eV) as source-drain electrodes, which have the same electrode-injection condition to PDQT based device. The results exhibited a 0.2-0.3 $cm^2/V^{-1}s^{-1}$ of μ_e similar to those shown in TCBG and BCTG transistor configurations. A weak hole mobility (μ_h, in a order of 10^{-3} $cm^2/V^{-1}s^{-1}$) was observed due to the close φ of Au to the HOMO of **PDBTz**. This much greater μ_e than μ_h suggests bithiazole-based counterpart is more favorable to electron transport.

Density functional theory (DFT) calculations using tuned-ωB97X/cc-pVDZ were utilized to first explore the torsional potentials of **PDBTz** and PDQT subunits; the results were compared to reference single-point SCS-MP2 calculations (**Figure 5.2a**, see **S.I.** for details).[224] Tuned-ωB97X calculations were also carried out for the monomer through tetramer of **PDBTz** and PDQT. The calculations indicate that within one **PDBTz** repeat unit, the bithiazole segment adopts a *trans* coplanar conformation with a dihedral angle (φ) of 180° between the two thiazole rings (**Figure 5.2a**). This contrasts with the bithiophene moiety within one PDQT repeat unit, in which the two rings are twisted at an angle of 155° (**Figure 5.2a**). Expectedly, replacing bithiophene with bithiazole stabilizes both the LUMO and HOMO levels of **PDBTz** by about 0.2-0.3 eV compared to PDQT

(**Figure 5.2b**). Interestingly, as shown in **Figure 5.2c**, both the LUMO and HOMO wavefunctions are delocalized along the **PDBTz** backbone.

5.4. Conclusion

An electron transport polymeric semiconductor, **PDBTz**, was prepared upon copolymerization of the electron deficient bithiazole with dithienyldiketopyrrolopyrrole. **PDBTz** has a low optical bandgap (1.33 eV) and high electron affinity (-3.7 – -3.9 eV). **PDBTz** based thin-film OFETs exhibited an electron mobility reaching 0.3 $cm^2V^{-1}s^{-1}$ with $I_{ON/OFF}$ greater than 10^5. No substantial performance changes were observed in $I_{ON/OFF}$ and a small decrease in μ_e was noted upon storing **PDBTz** OFETs encapsulated by CYTOP at 25 °C and 55-70 % RH over 4 months. Incorporation of 5-DH side chains instilled **PDBTz** with good solubility in non-halogenated xylenes and THN, in comparison to halogenated DCB. **PDBTz** films cast from these four solvents displayed similar morphologies (ordering and texture) and field-effect electron mobility. The results demonstrate the feasibility for developing high performance electron transport materials that are compatible with more environmentally benign process options. DFT calculations demonstrated that the incorporation of bithiazole induces a more planar geometry and lowers both the LUMO and HOMO energy levels compared to bithiophene, a typical

electron rich building block used to develop electron transporting polymeric semiconductors.

Many current electron transport and ambipolar polymeric semiconductors are based upon copolymerization of bithiophene with electron acceptors, such as naphthalenedicarboximide, perylenedicarboximide, or isoindigo derivatives.[17c, 28e, 57, 225] In this study, bithiazole has been shown as a promising building block for the next generation of electron transport polymeric semiconductors with enhanced mobility and stability.

Supporting Information

The synthetic details of preparing monomers and polymers, characterization methods, OFET fabrications, computational details, **Scheme S5.1-5.2**, and **Figure S5.1 – S5.11** are included in the Supporting Information.

CHAPTER 6

CONCLUSION

This dissertation discusses the rational molecular engineering of donor-acceptor π-conjugated semiconducting copolymers and their applications to OFET devices.

Chapter 1 and 2 introduced recent advances surrounding the development of high-performance organic and polymeric semiconductors and summarized crucial methodologies in organic and polymeric semiconducting material synthesis, characterization, and OFET device fabrication and processing.

Chapter 3 discussed the incorporation of an electron deficient benzothiadiazole into an electron rich polythiophene system to afford PBT6, which has a relatively lower HOMO due to the electron deficiency of benzothiadiazole and enhanced intra-molecular charge transfer due to the donor-acceptor coupling. Applied to OFETs, PBT6 exhibits ordered inter-chain π-π stacking and thus displayed a high hole mobility of up to 0.75 $cm^2V^{-1}s^{-1}$, approximately a one order of magnitude enhancement compared with electron rich thiophene polymers. This result indicated the potential of developing high-performance polymeric semiconductors via D-A coupling. This study demonstrated that the molecular weight has a strong influence on the field-effect mobility as well: a PBT6 sample with a lower molecular weight exhibits a mobility approximately 1 order of magnitude lower than the high molecular weight homologue.

In Chapter 4, a 2nd electron deficient diketopyrrolopyrrole (DPP) group was incorporated into poly(oligothiophene-*co*-benzothiadiazole) to afford a donor–acceptor(1)-donor–acceptor(2) polymer, pTBTD, with enhanced intra-molecular interactions. Polymer side chains impact the polymer solution processability and polymer inter-chain π-π interactions. In this study, three side chains including the branched 5-DH, 2-DT, and linear n-octadecyl (OD) chains are substituted onto pTBTD, which demonstrated that the incorporation of branched side chains like 5-DH having the branching position remote from the polymer backbone have the advantages of both improved solubility from branched units and effective π–π intermolecular interactions compared with counterparts having branched chains close to the polymer backbone as in 2-DT and linear side chains such as OD. The resultant field-effect hole mobility for the 5-DH polymer was above 3 $cm^2V^{-1}s^{-1}$, which is 3-8 times of pTBTD-2DT and pTBTD-OD.

In Chapter 5, electron deficient bithiazole moieties were incorporated with dithieno-diketopyrrolopyrrole to afford a poly(diethino-diketopyrrolopyrrole-bithiazole), PDBTz. The enhanced electron deficiency of PDBTz compared with PBT6 and pTBTD lowered the frontier orbitals of PDBTz and hence allowed PDBTz to convert to an n-channel (electron transport) semiconductor in contrast to the p-type (hole transport) PBT6 and pTBTD. PDBTz was solution-processed onto OFET substrates using non-halogenated solvents including xylenes and tetralin. The resultant thin-film OFET devices based on

these non-halogenated solvents exhibited similar film morphology and field-effect electron mobilities as the counterparts based on halogenated solvents, indicative of the practicality of developing high mobility OFET devices through more environmentally-benign processing.

CHAPTER 7

FUTURE WORKS

As discussed in Chapter 2, the performance of p-type, hole transport, polymeric semiconductors has improved significantly in recent years. However, challenges related to the development of their n-type counterparts with high electron mobility and good ambient stability remain. As discussed in Section 2.2, electron mobility correlates with the transfer integral and reorganization energy, which might be improved through increasing polymer MW, π-conjugation along the polymeric backbones, and decreasing the possibility of steric hindrance between chains thereby narrowing the π-π stacking distance. The incorporation of electron withdrawing functional groups or units is expected to deepen the electronic states, thus leading to enhanced resistance to oxidation.

Currently accessible n-type polymers such as P(NDI2OD-T2) and PDBTz still have electron rich units in their backbones giving rise to relatively high HOMO energy levels which lead to decreased air stability. Our future studies would be engaged in development of π-conjugated polymers having "all-electron-deficient" backbones accessed by synthesis of acceptor-acceptor polymers. Three possible synthetic strategies are described below:

7.1. Dithiazolodiketopyrrolopyrrole based Copolymers

The dithieno-diketopyrrolopyrrole units within PDBTz possess two electron rich thiophenes. As discussed in Chapter 5, the thiazole unit has a higher electron-deficiency than thiophene due to the electron withdrawing imide (-C=N-) bond within thiazole itself. Herein, it is proposed that the two thiophene units within dithieno-diketopyrrolopyrrole could be replaced by two thiazole units to afford the new dithiazolo-diketopyrrolopyrrole (DTzDPP). Figure 6.1 shows its molecular structure and one possible synthetic approach. The two 5-decylheptadcyl side chains would be incorporated into DTzDPP to improve the solubility of DTzDPP and the corresponding polymers in common organic solvents. In one approach, DTzDPP is brominated and then coupled with bistrimethylstannyl bithiazole to afford the poly(tetrathiazolo-*co*-diketopyrrolopyrrole), PDPPTz4, as shown in Figure 6.1. Additionally, DTzDPP could be brominated and then copolymerized with hexamethylditin to afford poly(dithiazolo-diketopyyrolopyrrole) (PDTzDPP). Preliminary results suggest that DTzDPP can be readily synthesized with high purity. Both PDPPTz4 and PDTzDPP are expected to have lower HOMO/LUMO energy levels, improved electron mobility and increased ambient stability compared with PDBTz. A systematic investigation of the optical and electronic properties of PDQT, PDBTz, and PDPPTz4 and PDTzDPP is proposed.

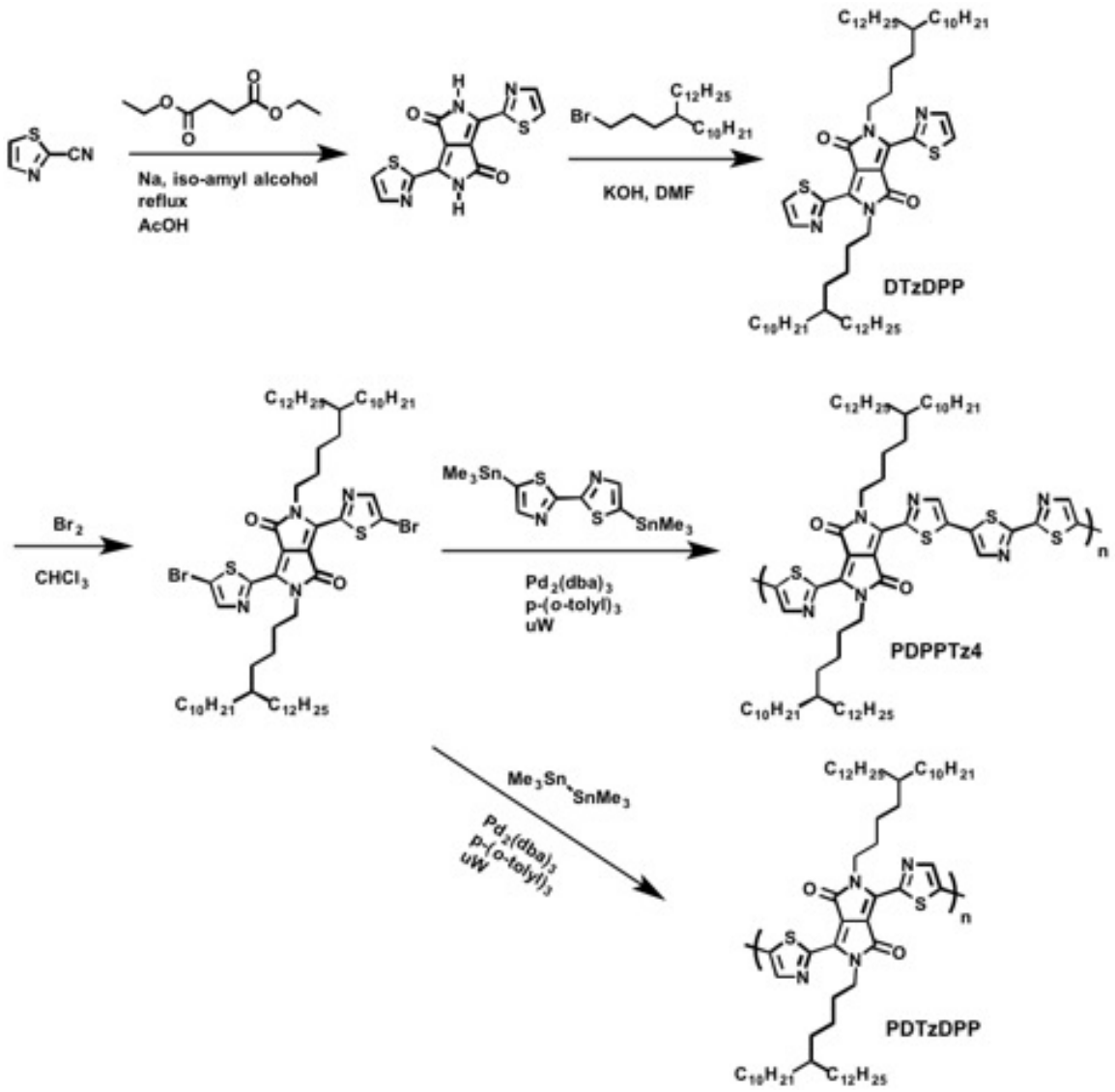

Figure 7.1. Synthetic strategy for the synthesis of DTzDPP and PDPPTz4 and PDTzDPP

7.2. Bithiazole-Naphthalenedicarboximide based Copolymers

The current commercially available electron transport polymer semiconductor, P(NDI2OD-T2), consists of electron rich bithiophene derivatives co-polymerized with electron deficient naphthalene diimide (NDI) substituents. The electron-donating

characteristics of bithiophene weaken the electron deficiency of the resultant polymer. Herein, it is proposed to substitute bithiophene with the electron deficient bithiazole moiety, to afford poly(bithiazole-naphthalene diimide), PNDITz2, as shown in Figure 6.2. Branched 5-decylheptadecyl side chains will be incorporated into NDI. As we demonstrated in our investigations with hole transporting polymers, use of 5-decylheptadcyl groups which have branching points remote from the polymer backbone rather than the 2-decyldodecyl side chains incorporated into P(NDI2OD-T2), , is expected to enhance π-π interchain interactions while maintaining good solubility.

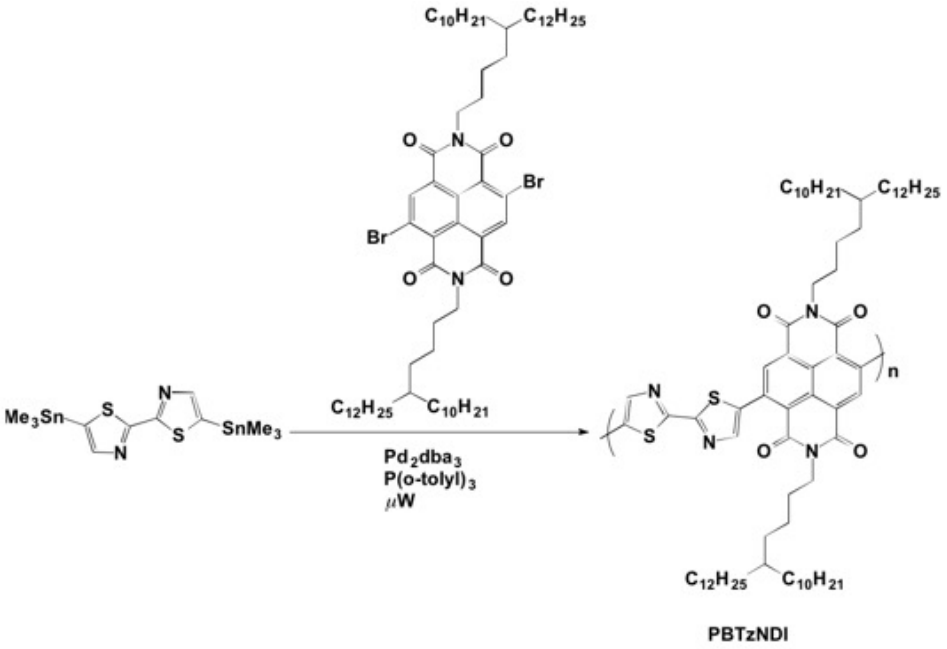

Figure 7.2. Synthetic procedure proposed for the preparation of PNDITz2.

7.3. Fluorine-based all electron-acceptor copolymers.

(*E*)-1,2-bis(2,3,5,6-tetrafluorophenyl)ethane (BTFPhV) is a strongly electron deficient material due to the incorporation of eight fluorine atoms into the structure. The vinylene linkage between the two tetrafluophenyl groups is expected to minimize torsion between the tetra-fluophenyl groups. BTFPhV is proposed to be functionalized with bistrimethylstannyl groups and copolymerized with DTzDPP brominated monomers to afford poly(bis(2,3,5,6-tetrafluorophenyl)ethane-dithiazolo-diketopyrrolopyrrole), PF4PDPP, as shown in Figure 6.3. In a manner similar to DTzDPP, BTFPhV is expected to be able to couple with the alternative electron-withdrawing moieties such as NDI and insoindigo units to afford all-electron-deficient π-conjugated polymers.

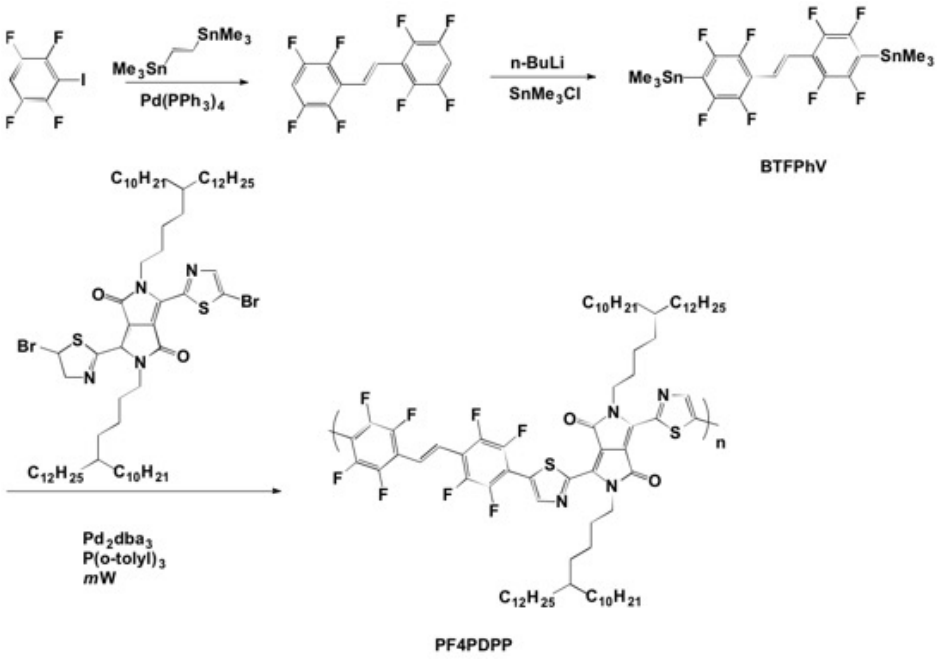

Figure 7.3. Synthetic strategy of affording BTFPhV and PF4PDPP

7.4. Applications of n-type polymeric semiconductors

The n-type π-conjugated polymers synthesized above would be employed in the fabrication of n-channel OFETs to investigate their electron transport performance. These device samples would be stored in ambient conditions and 50-70% of relative humidity (RH) and measured periodically to evaluate their air stability. In combination with p-type polymeric semiconductors, these n-type electron transport counterparts would be used to fabricate p-n junction complementary metal-oxide semiconductor like (CMOS-like) logic circuits.[17c] CMOS devices are widely used in digital integrated circuits including microprocessors, microcontrollers, and static random access memory devices. The CMOS-like circuits are proposed to be fabricated on flexible PEN or PET substrates in order to investigate the feasibility of using these polymeric semiconductors in flexible electronics applications.

The n-type materials would also be n-doped with organic dopants such as 1H-benzimidazole (DMBI),[226] benzimidazolium (DMBI-I),[227] fluorosilane,[228] or rhodocene dimer salts[229] to explore the viability of high electron mobility polymers for organic thermoelectric device (OTED) applications,[13b, 230] including organic Seebeck thermoelectric generators and solid-state Peltier coolers, together with p-doped p-type organic or polymeric semiconductors. Thermoelectric devices are able to harvest waste heat and partly convert it electric energy (Seebeck generator). During this process, heat is

released from the materials having a high temperature to materials having a low temperature, leading to the cooling of the high temperature materials (Peltier cooler). As shown in Figure 6.4 from Snyder's review,[13d] in OTEDs both p- and n-doped semiconductors carry out heat transfer from the high temperature end to the other, low temperature end, during which free charge carriers (holes in p-type, and electrons in n-type semiconductors) diffuse from the high temperature regime to the cool temperature regime. The resultant charge concentration gradient gives rise to an electrostatic potential and thereby generates a current in a circuit. The ideal thermoelectric materials are semiconductors that are so heavily doped that their transport properties resemble metals. In OTEG, as shown in Figure 6.4, each p-n junction unit was coupled together by the metal wires, in which the current flowed. Heat is transported vertically through the p-n junction. The thermal conductivity (κ) of both p- and n-doped semiconductors would be evaluated. The maximum efficiency of the OTEG would be determined by its figure of merit (zT),

$$zT = \frac{\alpha^2 T}{\rho\kappa}$$

where zT depends on Seebeck coefficient (α), absolute temperature (T), electrical resistivity (ρ), and κ. Compared with inorganic semiconductors, organic and polymeric semiconductors might enable development of light-weight and flexible thermoelectric

generators and Peltier coolers. Such devices might be attractive for next-generation wearable computing that requires flexibility, light-weight, and efficient heat dissipation.

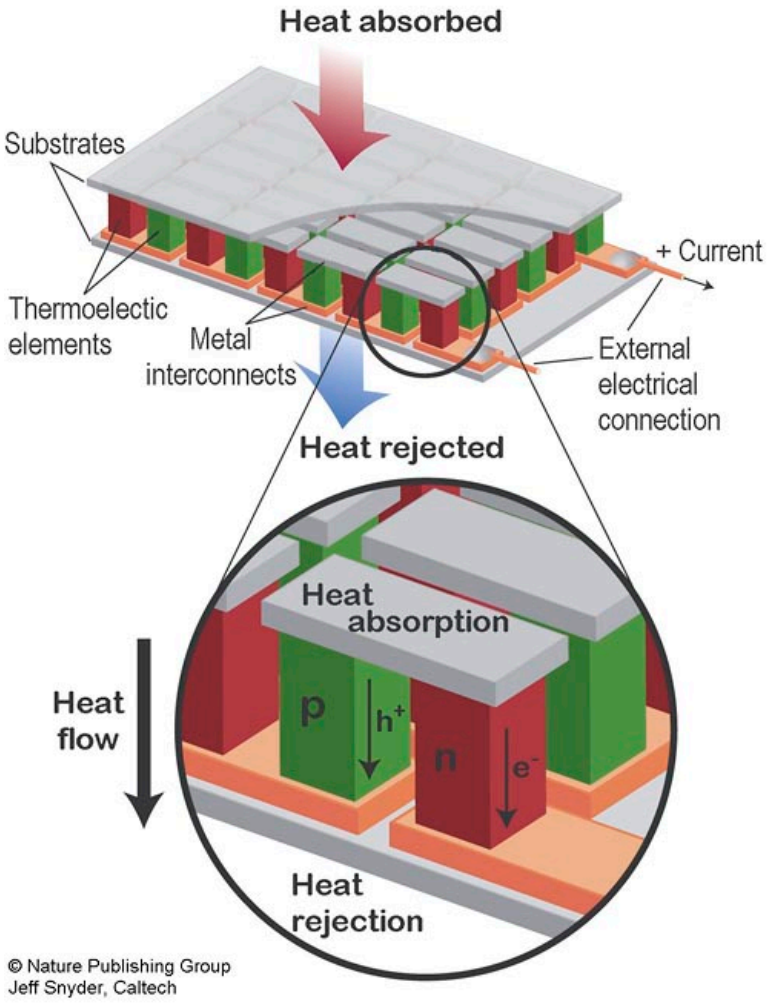

Figure 7.4. The scheme of p-n junction thermoelectric generators and solid-state Peltier coolers. This scheme is downloaded from Prof. Jeff Snyder's thermoelectrics group website.

SUPPORTING INFORMATION

Please see supporting information-1 (for Chapter 3) in page 184, supporting information-2 (Chapter 4) in page 250, and supporting information-3 (for Chapter 5) in page 294.

SUPPORT INFORMATION-1

FOR CHAPTER 3

Materials and Methods

All solvents (chloroform, toluene, ethanol, THF, 1,2-dichloroethane, DMF, dichloroethane (EDC), chlorobenzene, 1,2-dichorobenzene (DCB), 1,2,4-trichlorobenzene) were purchased as anhydrous grade solvents from Sigma-Aldrich. THF and toluene were distilled over sodium with benzophenone as the indicator. bis(triphenylphosphine)palladium(II) dichloride ($Pd(PPh_3)_2Cl_2$), 4,7-dibromobenzo[c]-1,2,5-thiadiazole, hexamethyldisilazane (HMDS), 2-(tributylstannyl)thiophene, tris(dibenzylideneacetone)dipalladium(0) ($Pd_2(dba)_3$), tri(o-tolyl)phosphine ($P(o\text{-}tolyl)_3$), bis(cyclopentadienyl)cobalt(III) hexafluorophosphate ($CcPF_6$), were purchased from Sigma-Aldrich. 5-formylthiophene-2-boronic acid was purchased from Frontier Scientific, Inc., 3-dodecylthiophene was purchased from either Sigma-Aldrich or Rieke Metals, n-octadecyltrichlorosilane (OTS-18) was purchased from Acros Organics, 1H,1H,2H,2H-perfluorodecyltriethoxysilane (FDTS) was purchased from Gelest, Inc., and tetra-n-butylammonium hexafluorophosphate ($[nBu_4N]^+[PF_6]^-$) was purcahsed from TCI America. Silica gel was purchased from Sorbent Technologies (Premium Rf™, porosity: 60Å; particle size: 40-75 μm).

^{1}H NMR and ^{13}C NMR spectra were recorded using a Varian Mercury Vx 400 (400 MHz) nuclear magnetic resonance spectrometer. Compounds were dissolved in deteurated solvents at room temperature; spectra of polymers were recorded in 1,1,2,2-tetrachloroethane-d_2, $C_2D_2Cl_4$, at 80 °C or 95 °C. Electron ionization mass spectra (EI-MS) were recorded using a Waters AutoSpec; while matrix-assisted laser desorption/ionization mass spectral (MALDI-MS) mesurements were conducted on a Bruker Autoflex III Smartbeam instrument. Molecular weights of **PBT4**, **PBT6**, **PBT6(L)** and **PBT6V2'** were measured using a PL-GPC 220 instrument (courtesy of the Prof. Richard F. Jordan Research Group in the Department of Chemistry at the University of Chicago) using TCB as the mobile phase (stabilized with 125 ppm butylated hydroxytoluene) at 135 °C; the molecular weight of **PBT6V2** was measured on a Waters Associates GPC V2000 liquid chromatography system using an internal differential refractive index detector at 40 °C and HPLC grade THF as the eluent. UV-Vis absorption spectra and fluorescence spectra were recorded on an Agilent 8453 UV-Visible Spectrophotometer and Shimadzu RF-5301PC Fluorescence Spectrometer, respectively. Electrochemical redox potentials of polymer films (drop cast onto the platinum button working electrode from hot $CHCl_3$ solution) were carried out in a three-electrode cell consisting of a platinum button working electrode, a platinum wire counter electrode, and a Ag/Ag^+ reference electrode in a 0.1 M solution of $[nBu_4N]^+[PF_6]^-$ in acetonitrile. The $CcPF_6$ redox couple was used as the internal standard, to prevent overlap with the

oxidation wave of the polymers. **Figure S3.7a** shows the redox wave of $CcPF_6$, which is 1.33 eV lower than that of $FcPF_6$ (-4.80 eV versus vacuum). Accordingly, $CcPF_6$ has an absolute energy of -3.47 eV versus vacuum. A cyclic voltammetry (CV) was performed on a CHI Instruments 620D Electrochemical Analyzer/Workstation with a scan rate of 50 mV/s. The thermal decomposition temperature of polymer powders were investigated with a Perkin-Elmer Pyris 1 thermogravimetric analyzer (TGA) in a nitrogen atmosphere (25 mL/min) with a heating rate of 10 °C/min. Thermal transitions of polymers were measured with a TA Q200 Differential Scanning Calorimeter (DSC) in a nitrogen atmosphere (50 mL/min) with a heating/cooling rate of 10 °C/min. 1D-XRD measurements were performed on a PANalytical X-ray diffractometer and reflectometer (operating voltage of 45 kV and current of 40 mA) equipped with a Cu K_α X-ray irradiation source (λ = 1.541 Å), and at a fixed incidence angle of 1°. 2D-GIXS measurements were carried out using a Bruker-AXS Microdiffractometer (operating voltage of 45 kV and current of 40 mA) with a 0.8 mm collimator, K_α monochromator, Hi-Star area detector, and Eulerian cradle sample holder, at a fixed incidence angle (0.2° for **PBT6** and 1.2° for **PBT4**), and a 90° or 30° out-plane tilt angle, γ. 2D-WAXD measurements were conducted using a Rigaku MicroMax 002 X-ray source (operating voltage of 45 kV and current of 0.65 mA) CuK_α radiation filtered by confocal optic system (λ = 1.5418 Å) and equipped with a Rigaku R-axis IV++ detector. Polymer films for XRD characterization were prepared by drop casting chloroform solutions of the

polymers onto octadecyltrichlorosilane (OTS-18) pre-treated SiO_2 dielectric (300 nm)/n-doped Si substrates. The morphology of polymer thin films deposited on FET devices were measured with a Veeco Digital Instruments Dimension 3100 scanning probe microscope in the tapping mode with a silicon etched probe tip.

Table S3.1. λ_{abs} and λ_{em} of **PBT6** in solvents possessing distinct polarities and polarizabilities

	λ_{abs} (nm) **[a]**	λ_{em} (nm) **[b]**	ε **[c]**	n_D **[d]**	polarity **[e]**	polarizability **[f]**
$CHCl_3$	536	666	4.81	1.4458	0.36	0.2105
CB	550	696	5.62	1.5248	0.38	0.2345
DCB	557	710	9.93	1.5514	0.43	0.2420
TCB	566	692	2.24	1.5717	0.23	0.2475

[a] peak with maximal intensity in absorption spectra (ca. $3.8x10^{-5}$ M) of PBT6 (Figure 3b); [b] peak with maximal intensity in fluorescence spectra (ca. $2x10^{-6}$ M) of PBT6 (Figure 3a); [c] dielectric constant; [d] refractive index; [e] calculated from $(\varepsilon - 1) / (2\varepsilon + 1)$[1]; [f] calculated from $(n^2 - 1) / (2n^2 + 1)$[1]

Positive solvatochromism is displayed in both absorption and fluorescence spectra from $CHCl_3$, to CB, and to DCB (λ_{abs} and λ_{em} are red shifted along with the increase in solvent polarity). Interestingly, λ_{abs} is also red shifted along with the increase in electronic polarizabilities of the solvents.

Synthetic Details

All reactions were carried out under an argon atmosphere using a standard Schlenk line technique. The compounds 4,7-di(thiophen-2-yl)benzo[c][1,2,5]thiadiazole (**1**),[2] 4,7-bis(5-(trimethylstannyl)thiophen-2-yl)benzo[c][1,2,5]thiadiazole (**M1**),[3] 2-bromo-3-

dodecylthiophene (**2**),[4] 4,4'-didodecyl-2,2'-bithiophene (**3**),[4b,5] 5,5'-dibromo-4,4'-didodecyl-2,2'-bithiophene (**M4**),[6] 4,7-bis(5-formyl-2-thiophenyl)-2,1,3-benzothiadiazole (**4**),[7] 4,7-bis(3-bis(methylenediethyl phosphonate)-thiophen-2-yl)-2,1,3-benzothiadiazole (**M6**),[8] 2-tributylstannyl-4-dodecylthiophene (**7**),[9] 7-bis(4-n-dodecylthiophen-2-yl)-2,1,3-benzothiadiazole (**8**)[10] were prepared following published procedures.

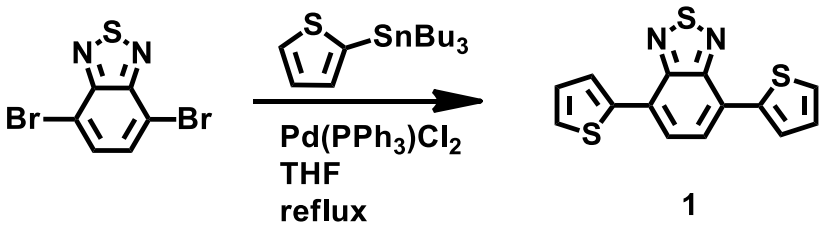

4,7-di(thiophen-2-yl)benzo[c][1,2,5]thiadiazole (1): 4,7-dibromobenzo[c]-1,2,5-thiadiazole (5.0 g, 17 mmol, 1.0 eq.), 2-(tributylstannyl)thiophene (14.6 g, 39 mmol, 2.3 eq.) and $Pd(PPh_3)_2Cl_2$ (1.194 g, 1.7 mmol, 0.1 eq.) were dissolved into THF (125 mL) under argon. After purged by argon for 30 min, the reaction mixture was heated to 75 °C and heated at reflux for 19 h, before cooling to room temperature. D.I. H_2O (100 mL) was added and the mixture was extracted into CH_2Cl_2 (3 x 30 mL). The combined organic solution was washed with brine (3 x 100 mL), dried over anhydrous $MgSO_4$, and concentrated under reduced pressure after filtration. The resulting dark brown residue was purified by column chromatography (silica gel, hexane/CH_2Cl_2, 4:1, v/v). The final product was recrystallized from ethanol to afford orange needle-like crystals (yield: 65

%). ^{1}H NMR (400 MHz, $CDCl_3$) δ 8.13 (dd, J = 3.7, 1.1 Hz, 2H), 7.89 (s, 2H), 7.46 (dd, J = 5.1, 1.1 Hz, 2H), 7.22 (dd, J = 5.1, 3.7 Hz, 2H). ^{13}C NMR (101 MHz, $CDCl_3$) δ 152.75, 139.51, 128.17, 127.66, 126.96, 126.09, 125.88. EI-MS (m/z): 299.9 [M^+]; HRMS: [M^+] calcd for $C_{14}H_8N_2S_3$, 299.9846; found, 299.9850, Δ = 1.3 ppm.

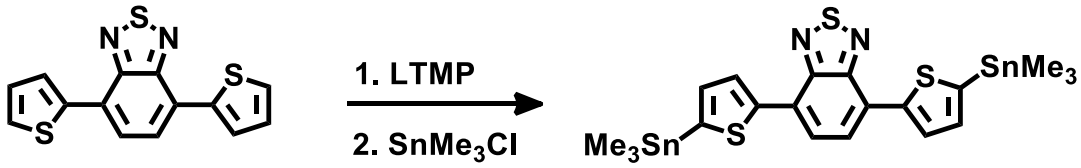

1 M1

4,7-bis(5-(trimethylstannyl)thiophen-2-yl)benzo[c][1,2,5]thiadiazole (M1): 2,2,6,6-tetramethylpiperdine (1.46 mL, 8.66 mmol, 2.6 eq.) was dissolved into dry THF (20 mL) under argon. n-butyllithium (3.46 mL of a 2.5 M solution in hexane, 8.66 mmol, 2.6 eq.) was added into the solution rapidly at -78 °C. The resulting solution was stirred at -78 °C for 30 min, and was warmed to room temperature and stirred for 10 min, to afford lithium 2,2,6,6-tetramethylpiperidide (LTMP). The solution was cooled to -78 °C and **1** (1.0 g, 3.33 mmol, 1.0 eq.) in THF (15 mL) was added in a dropwise manner, during which time the colorless solution turned purple. The resulting solution was stirred at -78 °C for 45 min; and trimethyltin chloride (8.32 mL of a 1.0 M solution in THF, 8.33 mmol, 2.5 eq) was then added in a dropwise manner, during which time the solution turned from purple to orange. The solution was then warmed to room temperature and was stirred for 12 h.

Brine (20 mL) was added and the mixture was extracted into CH_2Cl_2 (3 x 30 mL), washed with brine (3 x 60 mL), dried over anhydrous $MgSO_4$, and concentrated under reduced pressure after filtration. The residue was recrystallized from ethanol to give orange needle-like crystals (yield: 90%). ^{1}H NMR (400 MHz, $CDCl_3$) δ 8.18 (d, J = 3.5 Hz, 2H), 7.88 (s, 2H), 7.30 (d, J = 3.4 Hz, 2H), 0.43 (s, 18H). ^{13}C NMR (101 MHz, $CDCl_3$) δ 152.86, 145.25, 140.45, 136.30, 128.59, 126.03, 126.01, -7.93. EI-MS (m/z): 625.9 [M^+]; HRMS: [M^+] calcd for $C_{20}H_{24}N_2S_3Sn_2$, 627.9163; found, 627.9146, Δ = 2.7 ppm.

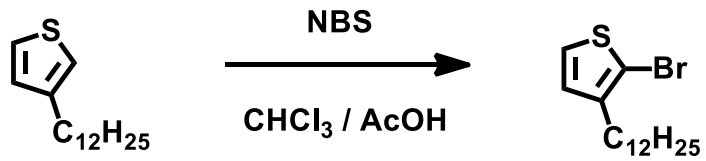

2

2-bromo-3-dodecylthiophene (2): NBS (3.53 g, 19.8 mmol, 1 eq.) was dissolved in $CHCl_3$/acetic acid (70 ml, 1:1, v/v) and the solution was added dropwise to 3-dodecylthiophene at 0 °C (5.0 g, 19.8 mmol, 1.0 eq.) using an addition funnel. The solution was stirred at room temperature in the dark, for 15 h, under argon. D.I. H_2O (50 mL) was added and the mixture was extracted into Et_2O (3 x 30 mL). The combined organic solution was washed with brine (3 x 50 mL), dried over anhydrous $MgSO_4$, and concentrated under reduced pressure after filtration. An orange oil was used in the next

step without further purification (yield: ~90 %). ^{1}H NMR (400 MHz, $CDCl_3$) δ 7.18 (d, J = 5.6 Hz, 1H), 6.79 (d, J = 5.6 Hz, 1H), 2.56 (t, J = 8 Hz, 2H), 1.57 (p, J = 8 Hz, 2H), 1.37 – 1.20 (m, 18H), 0.88 (t, J = 6.8 Hz, 3H).

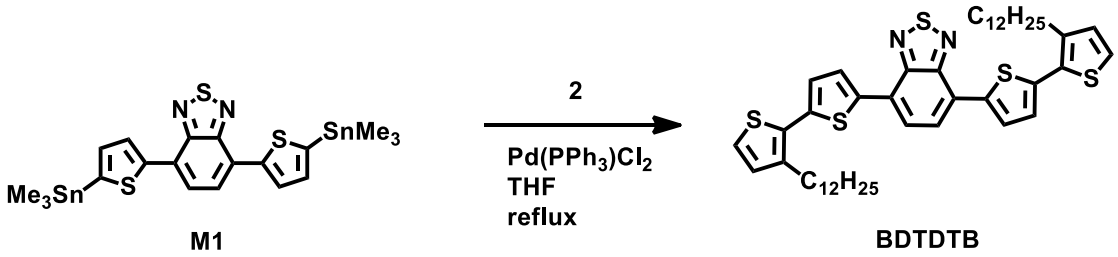

4,7-bis(3'-dodecyl-[2,2'-bithiophen]-5-yl)benzo[c][1,2,5]thiadiazole (BDTDTB): **M1** (1.0 g, 1.6 mmol, 1.0 eq.), **2** (1.19 g, 3.59 mmol, 2.25 eq.) and $Pd(PPh_3)Cl_2$ (70 mg, 9.6 μmol, 0.06 eq.) were dissolved into THF (38 mL) under argon. After purged by argon for 30 min, the mixture was heated to 75 °C and heated at reflux for 24 h. D.I. H_2O (100 mL) was added and the mixture was extracted into CH_2Cl_2 (3 x 30 mL). The combined organic solution was washed with brine (3 x 100 mL), dried over anhydrous $MgSO_4$, and concentrated under reduced pressure after filtration. The resulting dark purple residue was purified by column chromatography (silica gel, hexane/CH_2Cl_2, 7:2, v/v), and further purified by column chromatography (silica gel, hexane/CH_2Cl_2, 100:20, v/v), to afford a purple solid (yield: 35%). ^{1}H NMR (400 MHz, $CDCl_3$) δ 8.12 (d, J = 3.9 Hz, 2H), 7.87 (s, 2H), 7.22 (d, J = 3.9 Hz, 5.2 Hz, 4H), 6.98 (d, J = 5.2 Hz, 2H), 2.85 (t, J = 8 Hz, 4H), 1.68 (p, J = 8 Hz, 4H), 1.45 - 1.16 (m, 36 Hz), 0.86 (t, J = 7.2 Hz, 6H). ^{13}C NMR (101 MHz, $CDCl_3$) δ 152.76, 140.38, 139.14, 138.05, 130.76, 130.42, 128.27, 126.96, 125.83,

125.52, 124.32, 32.15, 30.92, 29.93, 29.92, 29.89, 29.86, 29.78, 29.70, 29.60, 29.59, 22.92, 14.35. MALDI-MS (m/z): 800.3 [M^+]; HRMS: [M^+] calcd for $C_{46}H_{60}N_2S_5$, 800.3339; found, 800.3360, Δ = 2.6 ppm.

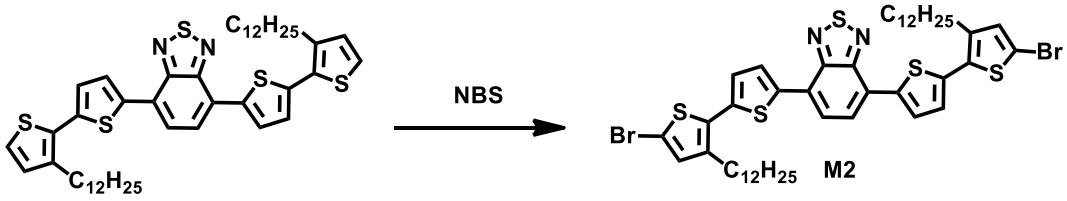

4,7-bis(5'-bromo-3'-dodecyl-[2,2'-bithiophen]-5-yl)benzo[c][1,2,5]thiadiazole (M2): NBS (92 mg, 0.51 mmol, 2.05 eq.) was dissolved into $CHCl_3$/acetic acid (20 mL, 1:1, v/v) and dropwise added into **BDTDTB** (200 mg, 0.25 mmol, 1.0 eq.) in anhydrous $CHCl_3$/acetic acid (20 mL, 1:1, v/v) at 0 ˚C using an addition funnel. The resulting mixture was stirred in the dark at 0 ˚C for 3 h, followed by stirring at room temperature for 12 h. The mixture was then poured into D.I. H_2O (50 mL), and was extracted into CH_2Cl_2 (3 x 30 mL). The combined organic solution was washed with brine (3 x 50 mL), dried over anhydrous $MgSO_4$, and concentrated under reduced pressure after filtration. The product was washed with methanol (3 x 20 mL) and isolated as a purple solid. ^{1}H NMR (400 MHz, $CDCl_3$) δ 8.09 (d, J = 3.9 Hz, 2H), 7.86 (s, 2H), 7.16 (d, J = 3.9 Hz, 2H), 6.93 (s, 2H), 2.78 (t, J = 7.6 Hz, 4H), 1.64 (p, J = 7.6 Hz, 4H), 1.43 – 1.16 (m, 36H), 0.86 (t, J = 6.9 Hz, 6H). ^{13}C NMR (101 MHz, $CDCl_3$) δ 152.68, 140.93, 139.57, 136.68, 133.04, 132.22, 128.21, 127.28, 125.76, 125.53, 111.09, 32.15, 30.77, 29.92, 29.91,

29.89, 29.82, 29.66, 29.65, 29.59, 29.55, 22.92, 14.35. MALDI-MS (m/z): 958.2 [M^+]; HRMS: [M^+] calcd for $C_{46}H_{58}Br_2N_2S_5$, 956.1558; found, 956.1570, Δ = 1.3 ppm.

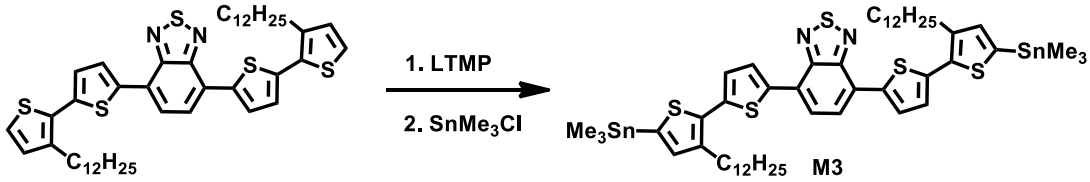

4,7-bis(3'-dodecyl-5'-(trimethylstannyl)-[2,2'-bithiophen]-5yl)benzo[c][1,2,5]thia-diazole (M3): 2,2,6,6-tetramethylpiperidine (47 mg, 0.33 mmol, 2.67 eq.) in THF (1 mL) was cooled to -78 ˚C under argon, followed by the addition of n-butyllithium (0.13 mL of a 2.5 M solution in hexane, 0.33 mmol, 2.6 eq.). The resulting solution was stirred at -78 °C for 30 min, and was warmed to room temperature and stirred for 10 min, to afford lithium 2,2,6,6-tetramethylpiperidide (LTMP). It was subsequently cooled down to -78 ˚C and **BDTDTB** (100 mg, 0.13 mmol, 1.0 eq.) in THF (3.2 mL) was added in a dropwise manner. After stirring at -78 ˚C for 1 h, $SnMe_3Cl$ (0.34 mL of a 1.0 M solution in THF, 0.33 mmol, 2.67 eq.) was added in a dropwise manner. The resulting solution was then warmed to room temperature and stirred for 12 h. After poured into D.I. H_2O (50 mL), the mixture was extracted into CH_2Cl_2 (3 x 15 mL), washed with brine (3 x 30 mL), dried over anhydrous $MgSO_4$, and concentrated under reduced pressure after filtration. The final product was washed with methanol (3 x 20 mL) and isolated as a purple solid. ^{1}H NMR (400 MHz, $CDCl_3$) δ 8.13 (d, J = 3.9 Hz, 2H), 7.86 (s, 2H), 7.20

(d, J = 3.5 Hz, 2H), 7.04 (s, 2H), 2.79 (t, J = 8 Hz, 4H), 1.65 – 1.74 (m, 4H), 1.40 – 1.16 (s, 36H), 0.86 (t, J = 6.8 Hz, 6H), 0.40 (s, 18H).

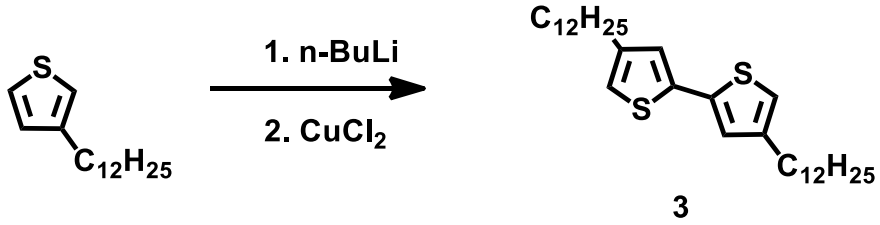

3

4,4'-didodecyl-2,2'-bithiophene (3): n-butyllithium (19.0 mL of a 2.5 M solution in hexane, 47.52 mmol, 1.2 eq.) was added dropwise into 3-dodecylthiophene (10.0 g, 39.6 mmol, 1.0 eq.) and tetramethylethylenediamine (TMEDA, 7.1 mL, 47.52 mmol, 1.2 eq.) in Et_2O (80 mL) at -78 ˚C under argon. The resulting solution was warmed to room temperature within 20 min, and heated to 40 ˚C for 1 h, followed by cooling down to -78 ˚C. The anhydrous $CuCl_2$ (6.39 g, 47.52 mmol, 1.2 eq.) was rapidly added into the solution at -78 °C. The resulting slurry was stirred at room temperature for 15 h. The crude product was extracted into hexane (5 x 50 mL), washed with brine (3 x 100 mL), dried over anhydrous $MgSO_4$, and concentrated under reduced pressure after filtration. The resulting residue was purified by column chromatography (silica gel, hexane). The final product was recrystallized from EtOH/acetone (1:1, v/v) to afford a light-yellow solid (yield: 45 %). ^{1}H NMR (400 MHz, $CDCl_3$) δ 6.97 (d, J = 1.4 Hz, 2H), 6.76 (d, J = 1.4 Hz, 2H), 2.56 (t, J = 7.6 Hz, 4H), 1.61 (p, J = 7.6 Hz, 4H), 1.43 – 1.19 (m, 36H), 0.88

(t, J = 6.8 Hz, 6H). ^{13}C NMR (101 MHz, $CDCl_3$) δ 144.20, 137.58, 125.02, 118.91, 32.15, 30.75, 30.62, 29.90, 29.89, 29.87, 29.82, 29.69, 29.59, 29.54, 22.92, 14.35. EI-MS (m/z): 502.4 [M^+]; HRMS: [M^+] calcd for $C_{32}H_{54}S_2$, 502.3667; found, 502.3667, Δ = 0 ppm.

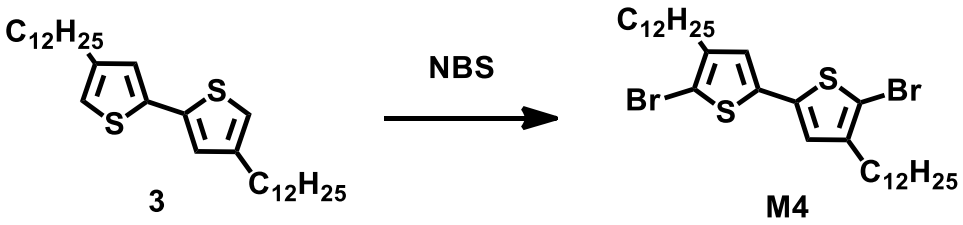

5,5'-dibromo-4,4'-didodecyl-2,2'-bithiophene (M4): NBS (726 mg, 4.08 mmol, 2.05 eq.) in $CHCl_3$/AcOH (50 mL, 1:1, v/v) was dropwise added into **3** (1.0 g, 1.99 mmol, 1.0 eq.) in $CHCl_3$/AcOH (20 mL, 1:1, v/v) at 0 ˚C using an addition funnel. The resulting mixture was stirred at room temperature under dark for 12 h, and was then poured into D.I. H_2O (50 mL). The mixture was extracted into CH_2Cl_2 (3 x 50 mL), washed with brine (3 x 50 mL), dried over anhydrous $MgSO_4$, and concentrated under reduced pressure after filtration. The product was washed with methanol (3 x 20 mL) and isolated as a yellow powder (yield: 91%). ^{1}H NMR (400 MHz, $CDCl_3$) δ 6.77 (s, 2H), 2.51 (t, J = 8 Hz, 4H), 1.57 (p, J = 7.6 Hz, 4H), 1.43 – 1.19 (m, 36H), 0.88 (t, J = 6.9 Hz, 6H). ^{13}C NMR (101 MHz, $CDCl_3$) δ 143.18, 136.36, 124.67, 108.06, 32.15, 29.90, 29.87, 29.84, 29.77, 29.61, 29.59, 29.42, 22.92, 14.36 (Note: some peaks in ^{13}C NMR spectrum

overlap). EI-MS (m/z): 660.2 [M^+]; HRMS: [M^+] calcd for $C_{32}H_{52}Br_2S_2$, 658.1857; found, 658.1877, Δ = 3.0 ppm.

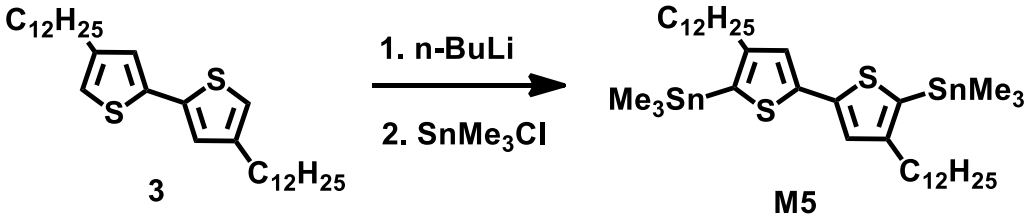

(4,4'-didodecyl-[2,2'-bithiophene]-5,5'-diyl)bis(trimethylstannane) (M5): n-butyllithium (0.62 mL of a 2.5 M solution in hexane, 1.55 mmol, 2.6 eq.) was added dropwise into **3** (300 mg, 0.60 mmol, 1.0 eq.) in THF (5 mL) at -78 ˚C. The solution was stirred at -78 ˚C for 30 min, at room temperature for 1 h, and cooled down to -78 ˚C, followed by the dropwise addition of $SnMe_3Cl$ (1.8 mL of 1.0 M solution in THF, 1.79 mmol, 3.0 eq.). The resulting solution was stirred at room temperature for 10 h, and was then poured into D.I. H_2O (30 mL). The mixture was extracted into hexane (3 x 20 mL), washed with brine (3 x 50 mL), dried over anhydrous $MgSO_4$, and concentrated under reduced pressure after filtration. The resulting brown-yellow oil was recrystallized from hexane at -78 ˚C to afford yellow oil containing 84.5 wt% of **M5** and 15.6 wt% of **(4,4'-didodecyl-[2,2'-bithiophen]-5-yl)trimethylstannane (M5')**. ^{1}H NMR (400 MHz, $CDCl_3$) of **M5** δ 7.10 (s, 2H), 2.54 (t, J = 7.6 Hz, 4H), 1.59 (p, J = 8 Hz, 4H), 1.37 – 1.20 (m, 36 H), 0.88 (t, J = 6.8 Hz, 6H), 0.37 (s, J = 18H). ^{1}H NMR (400 MHz, $CDCl_3$) of

M5' δ 7.11 (s, 1H), 6.97 (d, J = 1.6 Hz, 1H), 6.75 (d, J = 1.6 Hz, 1H), 2.54 (t, J = 7.6 Hz, 4H), 1.59 (p, J = 8 Hz, 4H), 1.37 – 1.20 (m, 36 H), 0.88 (t, J = 6.8 Hz, 6H), 0.38 (s, J = 9H).

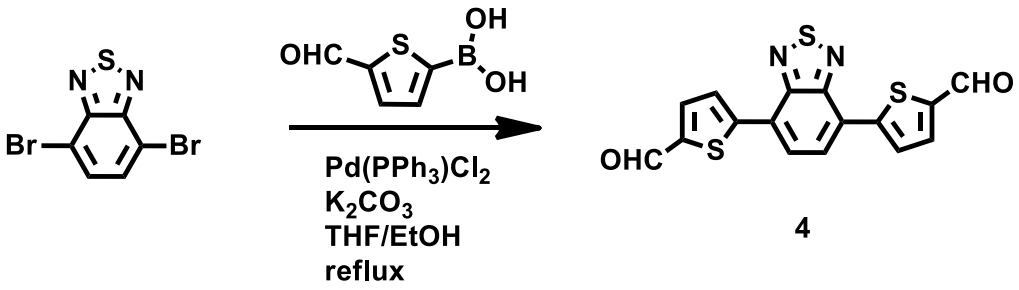

4,7-bis(5-formyl-2-thiophenyl)-2,1,3-benzothiadiazole (4): Na_2CO_3 (19.47 g, 183.6 mmol, 12.0 eq.) was dissolved into D.I. H_2O (92 mL) to make a 2.0 M aq. solution of Na_2CO_3. 5-formylthiophene-2-boronic acid (6.0 g, 38.3 mmol, 2.5 eq.) was dissolved into ethanol (50 mL). The two solutions were then bubbled with argon for 2 h. Degassed Na_2CO_3 aq. solution and 5-formylthiophene-2-boronic acid solution were added to the solution of 4,7-dibromobenzo[c]-1,2,5-thiadiazole (4.5 g, 15.3 mmol, 1.0 eq.) and $Pd(PPh_3)_2Cl_2$ (1.0 g, 1.42 mmol, 0.09 eq.) in toluene (60 mL) under argon. After purged by argon for 30 min, the solution was stirred at 50 °C for 18 h, during which time the organe solution turned to a red slurry. D.I. water (100 mL) was added at room temperature and the red residue was collected by filtration, washed with methanol (3 x 20 mL) followed by $CHCl_3$ (3 x 20 mL). The pure product was recrystallized from $CHCl_3$ to afford a red solid (yield: 35%). ^{1}H NMR (400 MHz, $CDCl_3$) δ 10.00 (s, 2H), 8.26 (d, J =

4.0 Hz, 2H), 8.06 (s, 2H), 7.87 (d, J = 4.0 Hz, 2H). FT-IR (KBr, cm-1): ν = 3088 (m), 2839 (w), 2815 (w), 1646 (s), 1523 (w), 1450 (s), 1233 (s), 820 (m). EI-MS (m/z (%)): 355.9 (100) [M^+], 354.9 (50) [$M^+ - H$]; HRMS: [M^+] calcd for $C_{16}H_8N_2O_2S_3$, 355.9740; found, 355.9748, Δ = 2.2 ppm.

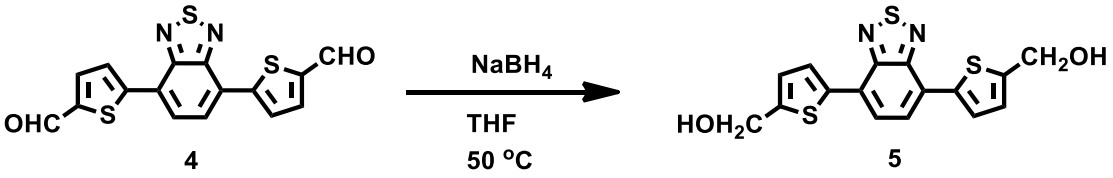

4,7-bis(5-hydroxylmethyl-thiophen-2-yl)-2,1,3-benzothiadiazole (5): $NaBH_4$ (102 mg, 2.7 mmol, 3.0 eq.) was added to **4** (0.32 g, 0.9 mmol, 1.0 eq.) in THF (25 mL) under argon. The mixture was heated to 50 °C for 12 h, before cooling to room temperature. D. I. H_2O (50 mL) was added and the resulting mixture was stirred at room temperature for 30 min. The mixture was collected by filtration, washed with brine (3 x 20 mL), followed by methanol (3 x 20 mL), to afford red solid that was used in the next step without further purification (yield: 70 %). ^1H NMR (400 MHz, DMSO-d_6) δ 8.01 (s, 2H), 7.99 (d, J = 3.8 Hz, 2H), 7.07 (d, J = 3.7 Hz, 2H), 5.62 (s, 2H), 4.69 (s, 4H). EI-MS (m/z): 360.0 [M^+]; HRMS: [M^+] calcd for $C_{16}H_{12}N_2O_2S_3$, 360.0074; found, 360.0061, Δ = 3.6 ppm.

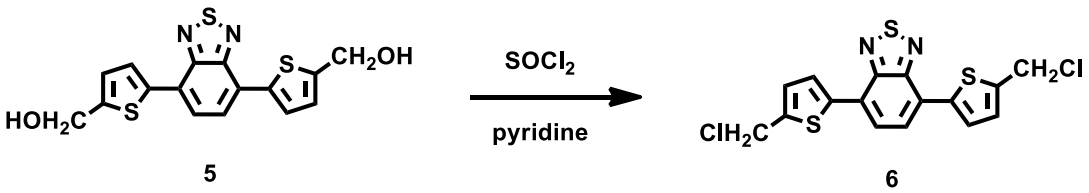

5 6

4,7-bis(5-chloromethyl-thiophen-2-yl)-2,1,3-benzothiadiazole (6): diol **5** (650 mg, 1.8 mmol, 1.0 eq.) and anhydrous pyridine (0.9 mL, 10.8 mmol, 6.0 eq.) were dissolved into toluene (45 mL) at 0 °C. Thionyl chloride (1.2 mL, 15.8 mmol, 8.8 eq.) was then added in a dropwise manner at 0 °C. The resulting mixture was stirred at 0 °C for 1h followed by stirring at room temperature for 10 h, under argon. The excess thionyl chloride and toluene was removed under reduce pressure. The residue was washed with methanol (3 x 20 mL) and isolated as a dark-red solid, which was employed to the next step without further purification (yield: 65 %). ^{1}H NMR (400 MHz, $CDCl_3$) δ 7.95 (d, J = 3.8 Hz, 2H), 7.85 (s, 2H), 7.18 (dt, J = 3.8, 0.7 Hz, 1H), 4.87 (d, J = 0.5 Hz, 2H). EI-MS (m/z): 395.9 [M^+]; HRMS: [M^+] calcd for $C_{16}H_{10}Cl_2N_2S_3$, 395.9395; found, 395.9383, Δ = 3.0 ppm.

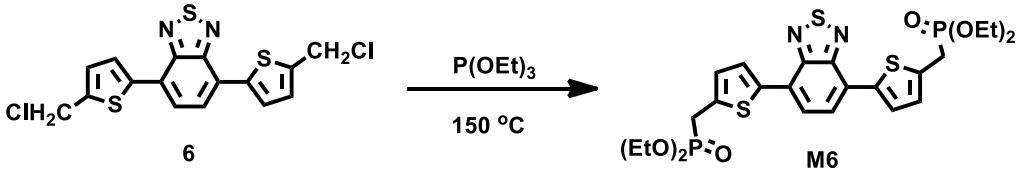

6 M6

4,7-bis(3-bis(methylenediethylphosphonate)-thiophen-2-yl)-2,1,3-benzothiadiazol-e (M6): bis(chloromethyl) compound **6** (627 mg, 1.58 mmol, 1.0 eq.) was mixed with

$P(OEt)_3$ (4.1 mL, 23.7 mmol, 15.0 eq.). The resulting mixture was stirred at 148 °C for 8 h under argon. The excess $P(OEt)_3$ was removed by vacuum distillation (*ca.* 10^{-4} torr) at 60 °C. The dark red crude product was purified by column chromatography (silica gel, EtOAc/MeOH, 105:10, v/v) and isolated as a dark-red gel-like solid (yield: 34 %). ^{1}H NMR (400 MHz, $CDCl_3$) δ 7.97 (d, J = 3.7 Hz, 2H), 7.79 (s, 2H), 7.07 (t, J = 3.6 Hz, 2H), 4.16 – 4.07 (m, 8H), 3.45 (d, J = 24 Hz, 4H), 1.31 (t, J = 8 Hz, 12H). ^{13}C NMR (101 MHz, $CDCl_3$) δ 152.69, 138.93 (138.88), 134.50 (134.40), 128.68 (128.59), 127.84 (127.80), 125.87, 125.56, 62.82 (62.75), 29.30 (27.87), 16.67 (16.61). (Note: values inside brackets refer to coupled peaks due to heteronuclear coupling of carbon-13 to phosphorus-31) EI-MS (m/z): 600.0 [M^+], 463.0 (55) [$M^+ - C_4H_{10}O_3P$], 325.9 (43) [$M^+ - C_8H_{20}O_6P_2$]; HRMS: [M^+] calcd for $C_{24}H_{30}N_2O_6P_2S_3$, 600.0742; found, 600.0741, Δ = 0.2 ppm.

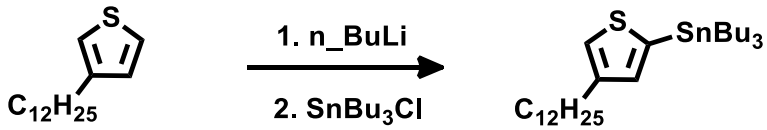

7

2-tributylstannyl-4-dodecylthiophene (7): 3-dodecylthiophene (3.0 g, 15.3 mmol, 1.0 eq.) and tetramethylethylenediamine, TMEDA, (2.75 mL, 18.5 mmol, 1.2 eq.) were dissolved into THF (35 mL) under argon. n-butyllithium (7.33 mL of a 2.5 M solution in hexane, 18.5 mmol, 1.2 eq.) was dropwise added at -78 °C. The resulting solution was

stirred at -78 °C for 40 min followed by warming to room temperature and stirred for an additional 1.5 h. The resulting light-yellow solution was again cooled to -78 °C and tributyltin chloride (5.18 mL, 19.1 mmol, 1.25 eq.) was added in a dropwise manner. The solution was stirred at room temperature for 8 h, and was poured into D.I. H_2O (50 mL). The mixture was extracted into CH_2Cl_2 (3 x 30 mL), washed with brine (3 x 30 mL), dried over anhydrous $MgSO_4$, and concentrated under reduced pressure after filtration, to afford a yellow color oil, which was employed to the subsequent step without further purification (yield: ~90 %). ^{1}H NMR (400 MHz, $CDCl_3$) δ 7.19 (s, 1H), 6.97 (s, 1H), 2.65 (t, J = 8 Hz, 2H), 1.65 – 1.61 (m, 2H), 1.59 – 1.50 (m, 6H) 1.41 – 1.20 (m, 24H), 1.14 – 1.05 (m, 6H), 0.91 – 0.88 (m, 12H).

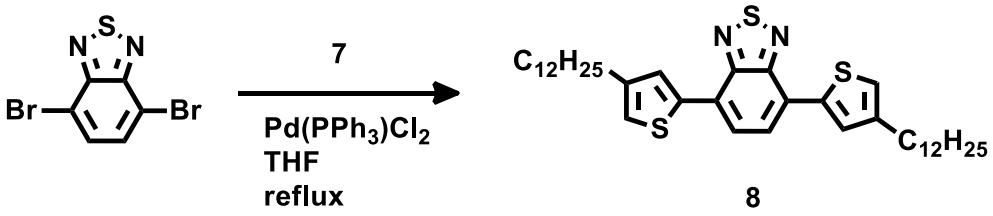

8

4,7-bis(4-n-dodecylthiophen-2-yl)-2,1,3-benzothiadiazole (8): 4,7-dibromobenzo[c]-1,2,5-thiadiazole (1.39 g, 4.75 mmol, 1.0 eq.), **7** (6.42 g, 11.9 mmol, 2.5 eq.) and $Pd(PPh_3)_2Cl_2$ (0.33 g, 0.48 mmol, 0.1 eq.) were dissolved into THF (45 mL) under argon. After purged by argon for 30 min, the solution was heated to 73 °C and heated at reflux for 36 hours, before cooling to room temperature. D.I. H_2O (60 mL) was added and the

mixture was extracted into CH_2Cl_2 (3 x 30 mL). The combined organic solution was washed with brine (3 x 50 mL), dried over anhydrous $MgSO_4$, and concentrated under reduced pressure after filtration. The dark red residue was purified by column chromatography (silica gel, hexane/DCM, 100:15 to 100:30, v/v) and was isolated as a red solid (yield: 82 %). ^{1}H NMR (400 MHz, $CDCl_3$) δ 7.98 (d, J = 1.4 Hz, 2H), 7.83 (s, 2H), 7.04 (d, J = 1.3 Hz, 2H), 2.69 (t, J = 8 Hz, 4H), 1.65 – 1.74 (m, 4H) 1.43 – 1.19 (m, 36H), 0.88 (t, J = 7.3 Hz, 6H). ^{13}C NMR (101 MHz, $CDCl_3$) δ 152.86, 144.59, 139.22, 129.22, 126.25, 125.75, 121.74, 32.15, 30.88, 30.74, 29.91, 29.90, 29.88, 29.85, 29.72, 29.60, 29.59, 22.92, 14.35. EI-MS (m/z): 636.3 [M^+]; HRMS: [M^+] calcd for $C_{38}H_{56}N_2S_3$, 636.3602; found, 636.3606, Δ = 0.6 ppm.

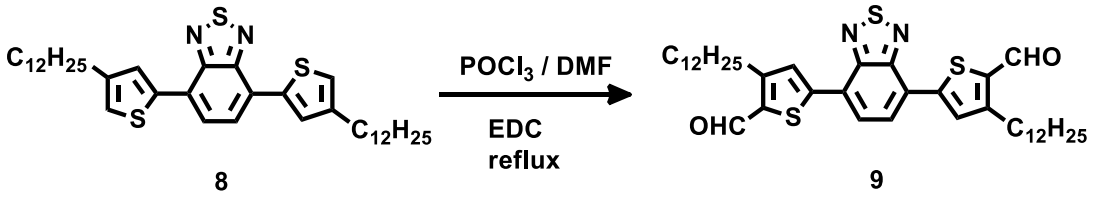

4,7-bis(4-n-dodecylthiophen-5-formyl-2-yl)-2,1,3-benzothiadiazole (9): compound **8** (2.26 g, 3.55 mmol, 1.0 eq.) was dissolved into EDC (60 mL) under argon. The solution was cooled to 0 °C, followed by the addition of DMF (5.5 mL, 70.96 mmol, 20.0 eq.) and subsequently the dropwise addition of phosphoryl chloride, $POCl_3$, (5.62 mL, 60.32 mmol, 17.0 eq.). The resulting mixture was heated to 90 °C and heated at reflux for 12 h, before cooling to room temperature. Sodium acetate aqueous solution (1.0 M in D.I. H_2O,

200 mL) was added. The resulting mixture was stirred vigorously for 1.5 h, and was neutralized by addition of a NaOH aqueous solution. The mixture was extracted into CH_2Cl_2 (3 x 50 mL). The combined organic solution was washed with brine (3 x 50 mL), dried over anhydrous $MgSO_4$, and concentrated under reduced pressure after filtration. The brown residue was purified by column chromatography (silica gel, CH_2Cl_2) to afford an orange solid, which was then recrystallized from ethanol to afford an orange, cotton-like solid (yield: 90 %). ^{1}H NMR (400 MHz, $CDCl_3$) δ 10.11 (s, 2H), 8.10 (s, 2H), 8.01 (s, 2H), 3.04 (t, J = 8 Hz, 4H), 1.78 (p, J = 4Hz, 4H), 1.40 – 1.25 (m, 36H), 0.87 (t, J = 6.8 Hz, 6H). ^{13}C NMR (101 MHz, $CDCl_3$) δ 182.19, 153.37, 152.38, 146.72, 138.10, 131.23, 126.97, 126.40, 31.89, 31.50, 29.64, 29.61, 29.54, 29.53, 29.39, 29.35, 29.33, 28.67, 22.67, 14.10. EI-MS (m/z): 692.3 [M^+]; HRMS: [M^+] calcd for $C_{40}H_{56}N_2O_2S_3$, 692.3488; found, 692.3504, Δ = 2.3 ppm.

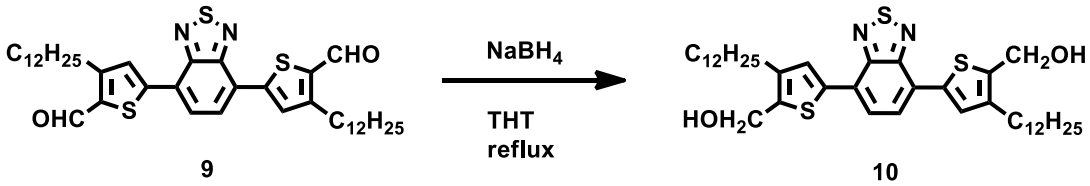

9 10

4,7-bis(4-n-dodecylthiophen-5-hydroxylmethyl-2-yl)-2,1,3-benzothiadiazole (10): sodium borohydride, $NaBH_4$ (84 mg, 2.25 mmol, 3.0 eq.) (*note: too much $NaBH_4$ could reduce benzothiadiazole to 1,2-phenylene-diamine*) was added to **9** (0.52 g, 0.75 mmol, 1.0 eq.) in THF (35 mL) under argon. The mixture was heated to 73 °C and heated of

reflux for 8 h, before cooling to room temperature. D. I. water (45 mL) was added and the resulting mixture was stirred at room temperature for 2 h. The mixture was extracted into $CHCl_3$ (3 x 20 mL). The combined organic solution was washed with brine (3 x 20 mL), dried over anhydrous $MgSO_4$, and concentrated under reduced pressure after filtration. The resulting red precipitate was washed with methanol (3 x 20 mL) to afford target product (yield: 76 %). ^{1}H NMR (400 MHz, DMSO-d_6) δ 7.97 (s, 2H), 7.92 (s, 2H), 5.47 (s, 2H), 4.63 (d, J = 5.4 Hz, 4H), 1.60 – 1.55 (m, 4H), 1.36 – 1.15 (m, 36H), 0.84 – 0.78 (t, 6H). (Note: 4 protons in the region of about 2 to 3 ppm corresponding to Th–CH_2– were obscured by a large proton peak from water in the DMSO-d_6 solvent. (Th: thiophene)).

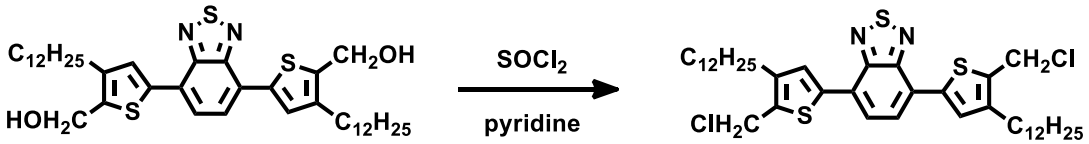

10 11

4,7-bis(4-n-dodecylthiophen-5-chloromethyl-2-yl)-2,1,3-benzothiadiazole (11): diol **10** (0.5 g, 0.72 mmol, 1.0 eq.) and anhydrous pyridine (0.35 ml, 4.3 mmol, 6.0 eq.) were dissolved into toluene (35 mL). Thionyl chloride (0.52 mL, 7.2 mmol, 10.0 eq.) was added in a dropwise manner at 0 °C. The resulting mixture was stirred at room temperature for 15 h under argon. The excess thionyl chloride and toluene were removed under reduced pressure. The mixture was extracted into CH_2Cl_2 (3 x 30 mL). The

combined organic solution was washed with brine (3 x 30 mL), dried over anhydrous $MgSO_4$, and concentrated under reduced pressure after filtration. The resulting dark-red precipitate was washed with methanol (3 x 20 mL) and was employed in the next step without further purification (yield: 78%). ^{1}H NMR (400 MHz, $CDCl_3$) δ 7.88 (s, 2H), 7.82 (s, 2H), 4.83 (s, 4H), 2.69 (t, J = 8 Hz, 4H), 1.75 – 1.65 (m, 4H), 1.30 - 1.20 (m, 36H), 0.87 (t, J = 6.8 Hz, 6H).

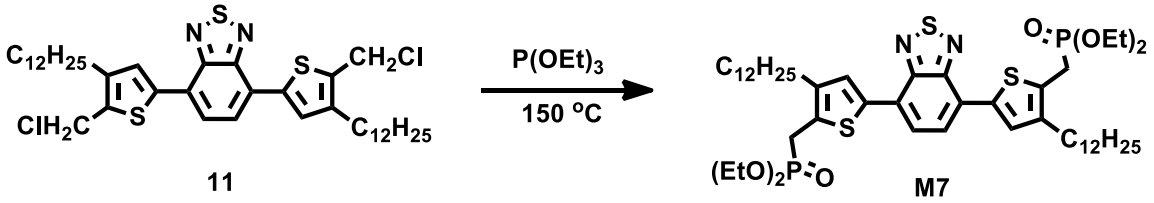

11 M7

4,7-bis(3-bis(methylenediethyl phosphonate)-4-n-dodecylthiophen-2-yl)-2,1,3-benz othiadiazole (M7): bis(chloromethyl) compound **11** (418 mg, 0.57 mmol, 1.0 eq.) was blended with triethyl phosphate, $P(OEt)_3$ (2 mL, 11.38 mmol, 20.0 eq.). The resulting mixture was stirred at 140 °C for 12 h under argon. The excess $P(OEt)_3$ was removed by vacuum distillation (10^{-4} torr) at 60 °C. The dark red crude product was purified by column chromatography (silica gel, EtOAc) and isolated as dark-red solid (yield: 47 %). ^{1}H NMR (400 MHz, $CDCl_3$) δ 7.93 (s, 2H), 7.77 (s, 2H), 4.11 (dq, J = 14.1, 7.1 Hz, 8H), 3.37 (d, J = 21.0 Hz, 4H), 2.63 (t, J = 6.9 Hz, 4H), 1.66 (p, J = 7.8 Hz, 4H), 1.44 – 1.21 (m, 48H), 0.87 (t, J = 6.9 Hz, 6H). ^{13}C NMR (101 MHz, $CDCl_3$) δ 152.66, 142.24 (142.14), 137.14 (137.10), 129.44 (129.40), 127.78 (127.66), 125.67, 125.34, 62.65

(62.59), 32.06, 30.69, 30.67, 29.83, 29.82, 29.79, 29.77, 29.72, 29.50, 28.69, 28.68, 27.44 (26.00), 22.83, 16.63 (16.57), 14.27 (Note: values inside brackets refer to coupled peaks due to heteronuclear coupling of carbon-13 to phosphorus-31). MALDI-MS (m/z (%)): 936.5 (50) [M^+], 799.4 (100) [$M^+ - C_4H_{10}O_3P$]; HRMS: [M^+] calcd for $C_{48}H_{78}N_2O_6P_2S_3$, 936.4464; found, 936.4497, Δ = 3.5 ppm.

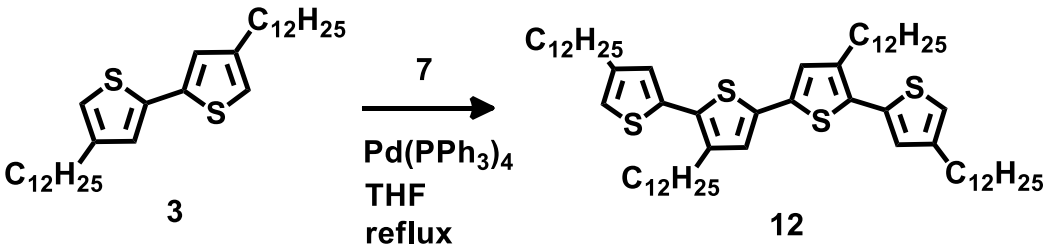

3',4,4'',4'''-tetradodecyl-2,2':5',2'':5'',2'''-quaterthiophene (12): **3** (1.23 g, 1.86 mmol, 1.0 eq.), **7** of (3.42 g, 4.47 mmol, 2.4 eq.), and $Pd(PPh_3)_4$ (0.43 g, 0.37 mmol, 0.2 eq.) were dissolved into toluene (35 mL) under argon. After purged with argon for 30 min, the solution was heated to 120 °C and heated of reflux for 24 h, before cooling to room temperature. D.I. H_2O (50 mL) was added and the mixture was extracted into CH_2Cl_2 (3 x 30 mL). The combined organic solution was washed with brine (3 x 30 mL), dried over anhydrous $MgSO_4$, and concentrated under reduced pressure after filtration. The brown residue was purified by column chromatography (silica gel, hexane/DCM, 100:5, v/v), to afford an orange solid (yield: 55%). ^1H NMR (400 MHz, $CDCl_3$) δ 6.96 (s, 2H), 6.95 (d, J = 1.4 Hz, 2H), 6.88 (d, J = 1.4 Hz, 2H), 2.71 (t, J = 7.6 Hz, 4H), 2.60 (t, J

= 7.4 Hz, 4H), 1.68 – 1.60 (m, 8H), 1.42 - 1.18 (m, 72H), 0.88 (t, J = 6.7 Hz, 12H). ^{13}C NMR (101 MHz, $CDCl_3$) δ 143.87, 140.23, 135.82, 134.83, 130.18, 127.30, 126.51, 120.15, 32.16, 30.72, 30.65, 29.92, 29.89, 29.85, 29.77, 29.68, 29.60, 29.58, 22.93, 14.35. MALDI-MS (m/z): 1002.7 [M^+]; HRMS: [M^+] calcd for $C_{64}H_{106}S_4$, 1002.7171; found, 1002.7177, Δ = 0.6 ppm.

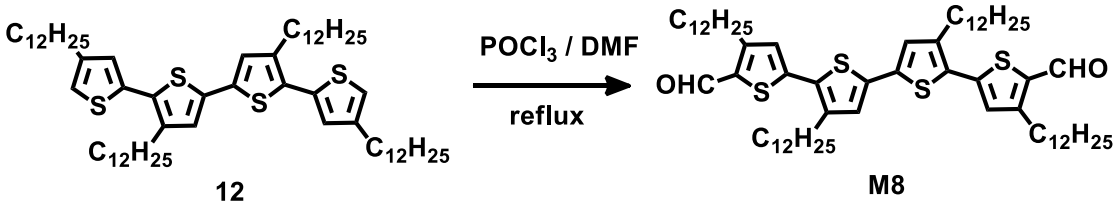

3',4,4'',4'''-tetradodecyl-[2,2':5',2'':5'',2'''-quaterthiophene]-5,5'''-dicarbaldehyde (M8): DMF (2 mL, 24.9 mmol, 25.0 eq.) was added to **12** (1.0 g, 1.0 mmol, 1.0 eq.) in EDC (40 mL) at 0 °C under argon, followed by the addition of phosphoryl chloride, $POCl_3$, (1.9 mL, 19.9 mmol, 20.0 eq.) in a dropwise manner. The resulting solution was heated to 90 °C and heated of reflux for 12 h, before cooling to room temperature. The sodium acetate aqueous solution (100 mL of 1.0 M solution) was added for hydrolysis and the mixture was further stirred for 1 h at room temperature. The mixture was extracted into CH_2Cl_2 (3 x 30 mL). The combined organic solution was washed with brine (3 x 30 mL), dried over anhydrous $MgSO_4$, and concentrated under reduced pressure after filtration. The residue was washed with methanol (3 x 50 mL) and isolated as a red powder (yield: 90%). ^{1}H NMR (400 MHz, $CDCl_3$) δ 10.01 (s, 2H), 7.05 (s, 2H),

7.04 (s, 2H), 2.94 (t, J = 7.8 Hz, 4H), 2.79 (t, J = 7.8 Hz, 4H), 1.74 – 1.64 (m, 8H), 1.44 – 1.15 (m, 72H), 0.87 (t, J = 6.8 Hz, 12H). ^{13}C NMR (101 MHz, $CDCl_3$) δ 181.84, 153.53, 144.95, 143.26, 136.66, 136.27, 129.64, 128.55, 127.71, 32.14, 31.64, 30.44, 29.87, 29.85, 29.75, 29.69, 29.58, 29.57, 28.70, 22.91, 14.34. MALDI-MS (m/z): 1058.7 [M^+]; HRMS: [M^+] calcd for $C_{66}H_{106}O_2S_4$, 1058.7071; found, 1058.7076, Δ = 0.5 ppm.

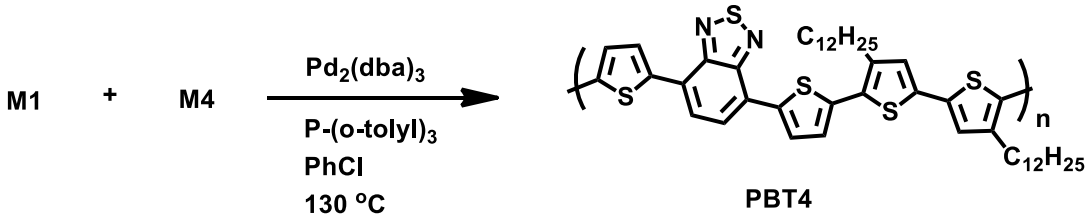

PBT4

Poly(benzothiadiazole-quaterthiophene) (PBT4): **M1** (95 mg, 0.15 mmol, 1.0 eq.), **M4** (100 mg, 0.15 mmol, 1.0 eq.), $Pd_2(dba)_3$ (15 mg, 15 μmol, 0.1 eq.), and P(o-tolyl)$_3$ (20 mg, 60 μmol, 0.4 eq.) into chlorobenzene (10 mL) under argon. The resulting mixture was stirred at 130 ˚C for 3 days and was then poured into methanol (300 mL) to quench the polymerization. The precipitated powders were collected by filtration and then washed by Soxhlet extraction sequentially using methanol (12 h), acetone (12 h), hexane (12 h), and $CHCl_3$ (4 h). The $CHCl_3$ solution was collected and then concentrated under reduced pressure. The concentrated solution was added in a dropwise manner to methanol (200 mL). The precipitate was collected by filtration from methanol followed by drying under vacuum at room temperature for 12 h to afford a black polymer powder (50 mg,

yield: 42%). ^{1}H NMR (400 MHz, $C_2D_2Cl_4$ at 80 °C) δ 8.21 – 8.16 (br, 2H), 7.93 (d, 2H), 7.32 (d, 2H), 7.14 (s, 2H), 2.95 – 2.86 (m, 4H), 1.84 – 1.75 (m, 4H), 1.42 – 1.14 (m, 36H), 0.92 (t, J = 6.7 Hz, 6H). GPC (TCB, 135 °C): M_n = 5.8 kDa, M_w = 9.7 kDa, PDI = 1.67, DP = ca. 7.3.

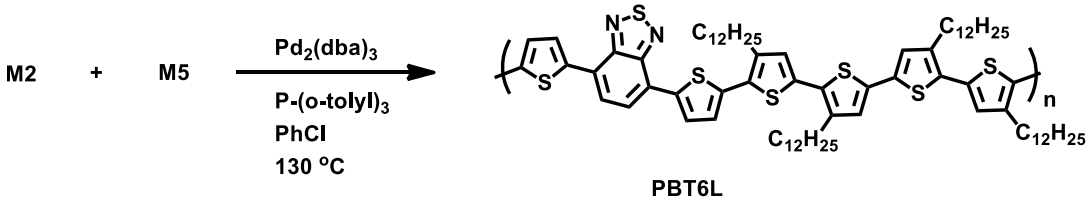

PBT6L

Poly(benzothiadiazole-sexithiophene) (PBT6(L)): **M2** (100 mg, 0.10 mmol, 1.0 eq.), **M5** mixture (109 mg, including 0.10 mmol of **M5**, 1.0 eq.; 0.02 mmol of **M5'**, 0.2 eq.), $Pd_2(dba)_3$ (5 mg, 5 μmol, 0.05 eq.), and P(o-tolyl)$_3$ (6.4 mg, 20.8 μmol, 0.2 eq.) into chlorobenzene (6.9 mL) under argon. The resulting mixture was stirred at 130 ˚C for 3 days, after which it was poured into methanol (300 mL) to quench the polymerization. The precipitated powders were collected by filtration and then washed by Soxhlet extraction sequentially using methanol (12 h), acetone (12 h), hexane (12 h), and $CHCl_3$ (2 h). The $CHCl_3$ solution was collected and then concentrated under reduced pressure. The concentrated solution was added in a dropwise manner to methanol (200 mL). The precipitate was collected by filtration from methanol followed by drying under vacuum at room temperature for 12 h to afford a black fine powder (95 mg, yield: 71%). ^{1}H NMR (400 MHz, $C_2D_2Cl_4$ at 95 °C) δ 8.19 (d, J = 2.4 Hz, 2H), 7.94 (s, 2H), 7.32 (d, J = 2.8 Hz,

2H), 7.15 – 7.04 (br, 4H), 2.98 – 2.90 (m, 4H), 2.90 – 2.79 (m, 4H), 1.87 – 1.73 (m, 8H), 1.42 – 1.11 (m, 72 H), 0.93 (t, J = 6.2 Hz, 12H). GPC (TCB, 135 °C): M_n = 8.6 kDa, M_w = 14.8 kDa, PDI = 1.72, DP = ca. 6.6.

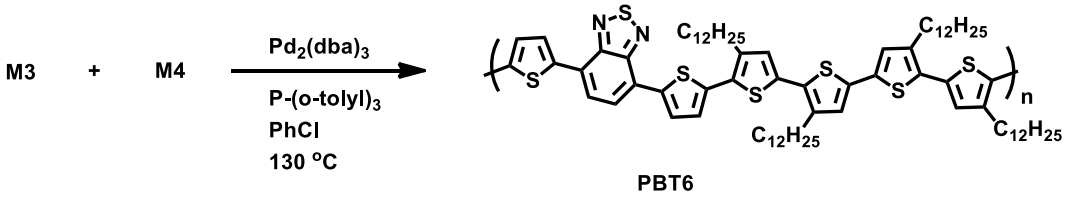

PBT6

poly(benzothiadiazole-sexithiophene) (PBT6): **M3** (112 mg, 0.1 mmol, 1.0 eq.), **M4** (66 mg, 0.1 mmol, 1.0 eq.), $Pd_2(dba)_3$ (5 mg, 5 μmol, 0.05 eq.), and P(o-tolyl)$_3$ (13 mg, 40 μmol, 0.4 eq.) were dissolved into chlorobenzene (6.6 mL) under argon. The resulting mixture was stirred at 130 ˚C for 5 days and was then poured into methanol (300 mL) to quench the polymerization. The precipitated powders were collected by filtration and then washed by Soxhlet extraction sequentially using methanol (12 h), acetone (12 h), hexane (12 h), and $CHCl_3$ (1 h). The $CHCl_3$ solution was collected and then concentrated under reduced pressure. The concentrated solution was added in a dropwise manner to methanol (200 mL). The precipitate was collected by filtration from methanol followed by drying under vacuum at room temperature for 12 h to afford the black polymer powder (94 mg, yield: 72%). ^{1}H NMR (400 MHz, $C_2D_2Cl_4$ at 95 °C) δ 8.20 (s, 2H), 7.94 (s, 2H), 7.32 (s, 2H), 7.09 (s, 4H), 2.98 – 2.90 (m, 4H), 2.90 – 2.81 (m, 4H), 1.88 – 1.73

(m, 8H), 1.42 – 1.12 (m, 72H), 0.93 (t, J = 6.8 Hz, 12H). GPC (TCB, 135 °C): M_n = 18.1 kDa, M_w = 36.5 kDa, PDI = 2.02, DP = ca. 13.9

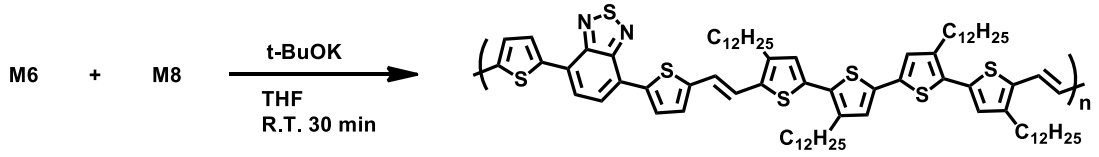

PBT6V2

Poly(dithieno-benzothiadiazole-vinylene-quaterthiophene) (PBT6V2): **M6** (50 mg, 83 μmol, 1.0 eq.) in THF (1.5 mL) was added to **M8** (90 mg, 83 μmol, 1.0 eq.) in THF (2 mL). Potassium *tert*-butoxide (0.33 mL of a 1.0 M solution in THF, 332 μmol, 4.0 eq.) was added in a dropwise manner to the solution at room temperature. The resulting mixture was immediately turned from red-orange to dark-purple with an enhancement in viscosity. The polymerization was quenched after 30 min by pouring the mixture into methanol (300 mL). The precipitated powders were collected by filtration and then washed by Soxhlet extraction sequentially using methanol (12 h), acetone (12 h), hexane (12 h), and $CHCl_3$ (6 h). The $CHCl_3$ solution was collected and then concentrated under reduced pressure. The concentrated solution was added in a dropwise manner to methanol (200 mL). The precipitate was collected by filtration from methanol followed by drying under vacuum at room temperature for 12 h to afford the black polymer powder (15 mg, yield: 13%). ^{1}H NMR (400 MHz, $C_2D_2Cl_4$ at 95 °C) δ 8.15 (s, Th-H), 7.91 (s, BT-H), 7.34 – 7.31 (br, =CH-), 7.22 (s, Th-H), 7.07 (s, Th-H), 7.00 (s, Th-H), 6.97 – 6.95 (br,

=CH-), 2.85 (s, Th-CH_2-), 2.78 (s, Th-CH_2-), 1.82 – 1.69 (br, -CH_2-), 1.42 – 1.11 (m, -CH_2-), 0.94 (s, -CH_3). (Th: thiophene, BT: benzothiadiazole). GPC (THF, 40 °C): M_n = 11.3 kDa, M_w = 35.5 kDa, PDI = 3.13, DP = ca. 8.4.

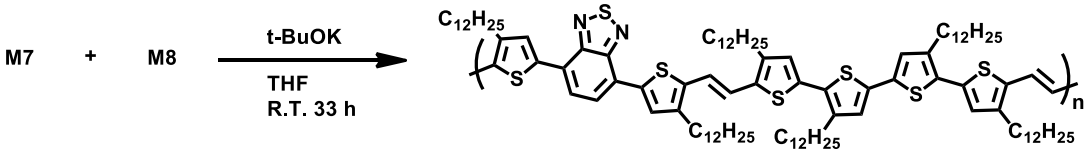

PBT6V2'

Poly(didodecylthieno-benzothiadiazole-vinylene-quaterthiophene) (PBT6V2'): **M7** (70 mg, 75 μmol, 1.0 eq.) in THF (1.5 mL) was added into **M8** (80 mg, 75 μmol, 1.0 eq.) in THF (2 mL). Potassium *tert*-butoxide (0.3 ml of a 1.0 M solution in THF, 0.3 mmol, 4.0 eq.) was then added in a dropwise manner to the solution at room temperature. The mixture was immediately turned from red-orange to dark-purple with an enhancement in viscosity. The polymerization was quenched after 33 h at room temperature by pouring the mixture into methanol (300 mL). The precipitated powders were collected by filtration and then washed by Soxhlet extraction sequentially using methanol (12 h), acetone (12 h), hexane (12 h), and $CHCl_3$ (6 h). The $CHCl_3$ solution was collected and then concentrated under reduced pressure. The concentrated solution was added in a dropwise manner to methanol (200 mL). The precipitate was collected by filtration from methanol followed by drying under vacuum at room temperature for 12 h to afford the black polymer powder (20 mg, yield: 16%). ^{1}H NMR (400 MHz, $C_2D_2Cl_4$ at

95 °C) δ 8.04 (s, Th-H), 7.88 (s, BT-H), 7.17 – 7.00 (br, Th-H, =CH-), 2.89 – 2.81 (br, Th-CH_2-), 2.81 – 2.72 (br, Th-CH_2-), 1.86 – 1.67 (m, -CH_2-), 1.43 – 1.11 (m, -CH_2-), 0.93 (s, -CH_3). GPC (TCB, 135 °C): M_n = 14.3 kDa, M_w = 42.5 kDa, PDI = 2.98, DP = ca. 8.5.

(Note that during Soxhlet extraction, almost all **PBT4** and all **PBT6** residues, after washing sequentially with methanol, acetone and hexane, were soluble in $CHCl_3$, while only 20~30 wt% of the purified **PBT6V2** and **PBDT6V2'** polymers could be solubilized, suggesting that HWE polymerization may facilitate development of high MW, but also insoluble material.)

OFET Device Fabrication and Measurement

The bottom contact, bottom gate FET devices were fabricated on a heavily doped silicon wafer <100> as the gate electrode with a 300 nm thick layer of thermally grown SiO_2 as the gate dielectric which has a capacitance of approximately 1.15 x 10^{-4} F/m^2. Au source and drain contacts with a fixed channel size (50 μm in length and 2 mm in width) were deposited onto the SiO_2 layer using a conventional photolithography lift-off process followed by E-beam evaporation of 50 nm Au contacts with 3 nm of Cr as the adhesion layer. Prior to deposition of semiconducting polymer film, the devices were cleaned by sonication in acetone for 30 min and subsequently rinsed sequentially with acetone, methanol and isopropanol, followed by drying under a flow of nitrogen. The SiO_2 surface

was pretreated by exposing the devices under UV/ozone for 15 min followed by immersion into a 2.54 x 10^{-3} M (1 μL/mL) solution of OTS-18 in anhydrous toluene for 10 min, in nitrogen rich environment. The devices were then cleaned by sonication in toluene for 10 min, followed by rinsing with acetone, methanol and isopropanol, and drying under a flow of nitrogen. For the spin-coating process, a hot polymer solution (8 mg/mL in DCB) was spin-coated onto OTS-18 pretreated FET substrates at 1000 rpm for 1 min in air. The resulting OFET devices were annealed in a vacuum oven (66.19 torr) at 200 °C (**PBT6** at 115 °C) for 1 h and subsequently cooled to room temperature under vacuum over a period of 8 h.

In the study of the relationship between **PBT6** mobility and annealing temperature, the OFET devices having a spin-coated **PBT6** film were dried at room temperature inside a nitrogen-filled glovebox, and annealed at the given temperature on a hotplate for 2 h, followed by rapidly cooling to room temperature within 2 min inside a glovebox.

For drop-cast processing, a hot solution (8 mg/mL of **PBT6** solution in DCB) was drop-cast onto OTS-18 pretreated FET substrates inside a glovebox. The resulting OFET devices were dried inside the glovebox at room temperaure for 17 h. The device characteristics of these as-cast thin-film OFETs were initially measured; and then the devices were annealed at 80 °C on a hotplate for 24 h followed by rapidly cooling to room temperature within 2 min inside a glovebox.

FET devices with HMDS modified dielectric were prepared by inserting the UV/ozone cleaned devices into a vacuum oven filled with HMDS vapor at room temperature for 10 min, followed by rinsing with acetone, methanol and isopropanol, and drying in a flow of nitrogen. FET devices with FDTS modified dielectric were prepared by immersing the UV/ozone cleaned devices into 22.76 x 10^{-3} M (10 μL/mL) FDTS in anhydrous toluene for 1 h, in nitrogen rich environment. The devices were then cleaned by sonication in toluene for 10 min followed by rinsing with acetone, methanol and isopropanol, and finally drying under a flow of nitrogen.

All OFET characterization was performed using a probe station inside a nitrogen filled glovebox using an Agilent 4155C semiconductor parameter analyzer. The FET mobilities were calculated from the saturation regime (V_{SD} = - 80 V, V_{SD} = - 100 V for **PBT6V**) in the transfer plots of V_G vs. I_{SD} by extracting the slope of the linear range of V_G vs. $I_{SD}^{1/2}$ plot and using the following equation:

$$\left.\frac{\partial I_{SD}^{1/2}}{\partial V_G}\right|_{V_{SD}} = \left(\mu_h C_{ox}(\frac{W}{2L})\right)^{1/2}$$

where I_{SD} and V_{SD} are the source-drain current (A) and source-drain voltage (V), respectively; V_G is the gate voltage (V) scanning from 20 to -80 V (20 to -60 V to **PBT6(L)** and **PBT6V**) in the transfer plot; C_{ox} is the capacitance per unit area of the gate dielectric layer, 1.15 x 10^{-4} F/m^2; W and L refer to the channel length (50 μm) and width (2 mm); μ_h represents the hole mobility in the saturation regime (cm^2/Vs).

In the following equation:

$$I_{SD} = \mu_h C_{ox} (\frac{W}{2L})(V_G - V_T)^2$$

the threshold voltage, V_T, was calculated by extrapolating $V_T = V_G$ at $I_{SD} = 0$ in the V_G vs. $I_{SD}^{1/2}$ curve in the saturation regime (V_{SD} = - 80 V). Current on and off ratio, $I_{ON/OFF}$, was determined through dividing I_{SD} at V_G = -80 V (I_{ON}) by the minimum I_{SD} at around V_G = 0~20 V (I_{OFF}).

Devices maintained in a nitrogen filled glovebox have exhibited stability in excess of 3 months. Upon storage in an ambient air environment, device performance begins to degrade after 3 to 5 days.

The mobilities of **PBT6** on HMDS and FDTS-treated substrates were 0.15 cm^2/Vs and 0.092 cm^2/Vs, respectively, after annealing at 80 °C for 24 h (**Table S3.2**). The lower mobility of **PBT6** on these self-assembled monolayers compared with that on OTS-18 might emanate from the long aliphatic chain of OTS-18 relative to HMDS that may promote an edge-on orientation of the polymer chain thus benefiting field effect hole transport between the source and drain electrodes; the strong hydrophobilicity of FDTS likely inhibits favorable polymer chain orientation.

Table S3.2. Effect of self-assembled monolayers and drop-casting process on the hole transport property of PBT6 based on OFETs annealed at 80 °C for 24 h (channel size: 50 μm of long x 2 mm of wide)

SAMs	Spin-coated film			Drop-casted film		
	μ_h (cm^2/Vs)	$I_{ON/OFF}$	$_T$ (V)	μ_h (cm^2/V.s)	$I_{ON/OFF}$	V_T (V)
HMDS	0.15	10^5	-7.5	0.055	10^5	-6.4
FDTS	-[b]	-	-	0.092	10^5	-3.4

[a] values in parentheses are maximal mobilities attained; [b] no uniform film was developed on FDTS pre-coated device due to high contact angle.

Figures

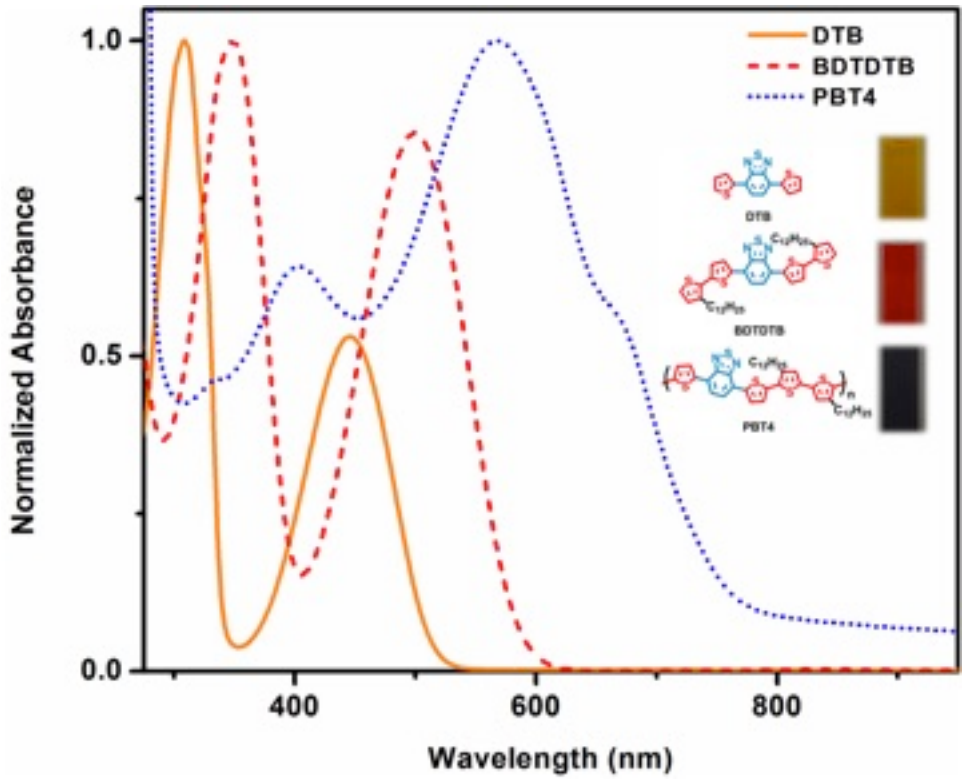

Figure S3.1 The shift of absorption band upon extending from the small molecule (**DTB**) to the oligomer (**BDTDTB**), and polymer (**PBT4**)

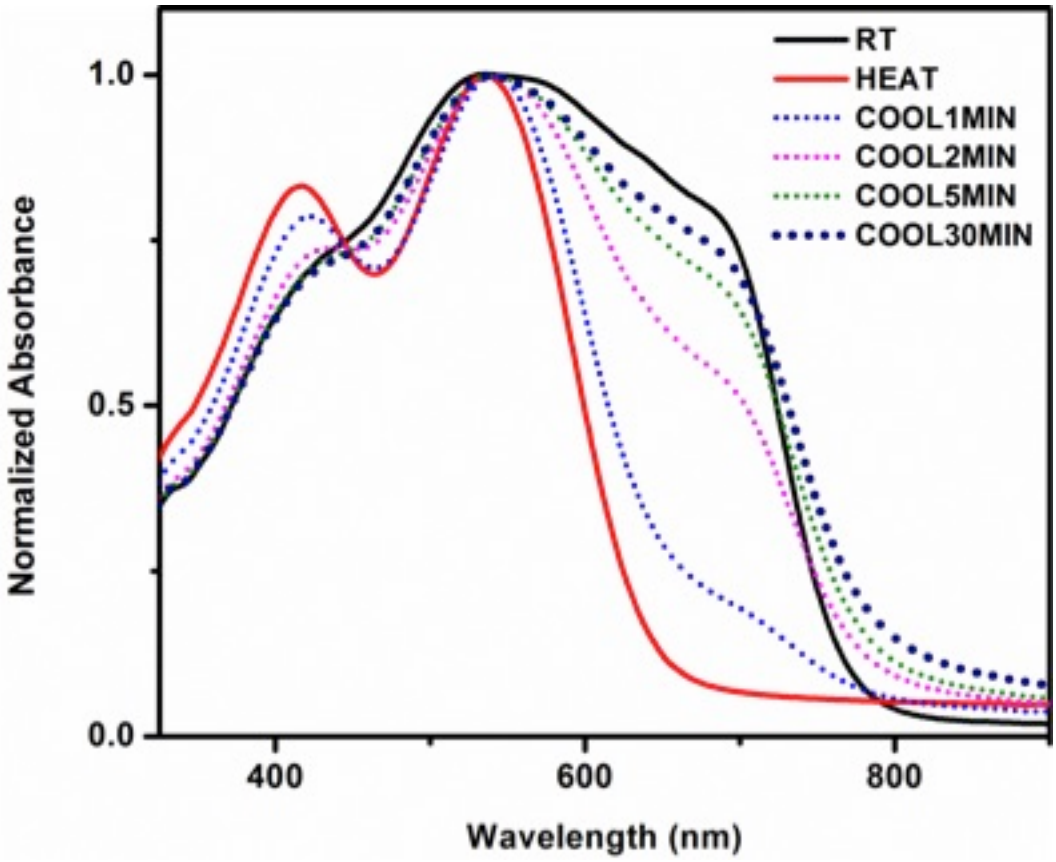

Figure S3.2a. Thermochromism of **PBT6** in $CHCl_3$ solution (3.8×10^{-5} M): (i) room temperature; (ii) after heating (under heat gun for 1 min); (iii) additional 1 min of cooling after heating; (iv) additional 2 min of cooling; (v) additional 5 min of cooling; (vi) additional 30 min of cooling

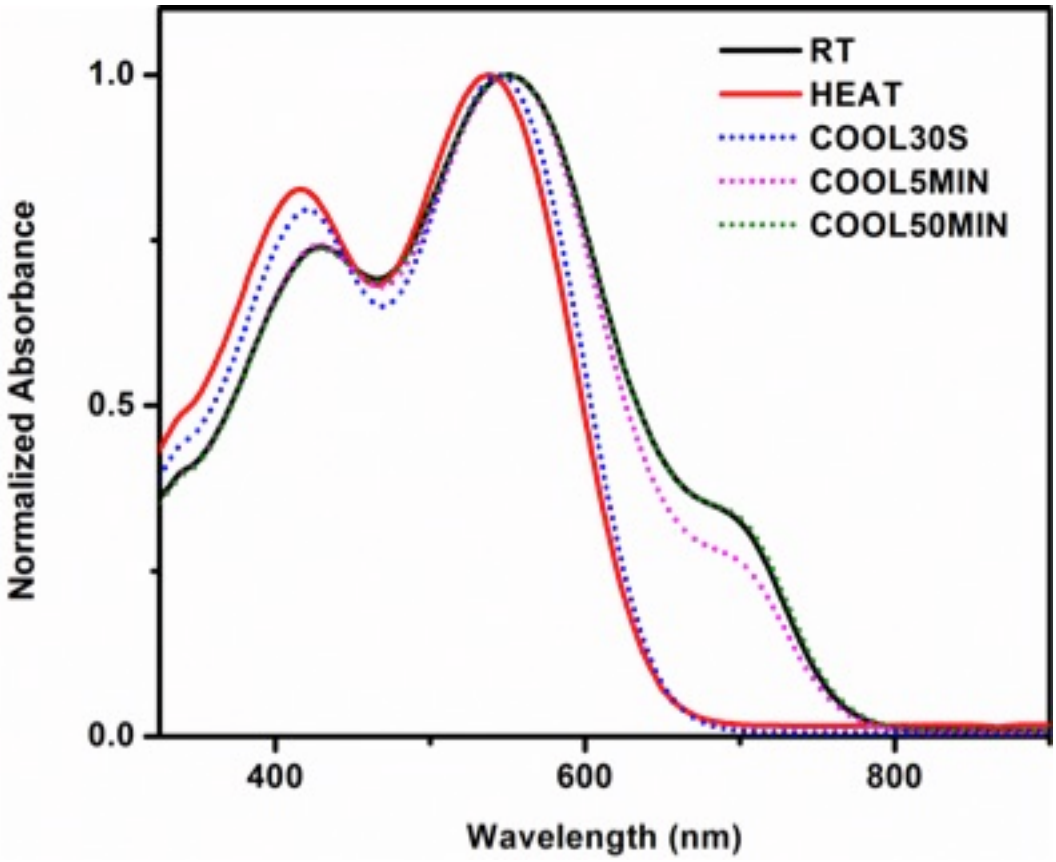

Figure 3.2b. Thermochromism of **PBT6** in CB solution (3.8 x 10^{-5} M): (i) room temperature; (ii) after heating (under heat gun for 1 min); (iii) additional 30s of cooling after heating; (iv) additional 5 min of cooling; (v) additional 50 min of cooling

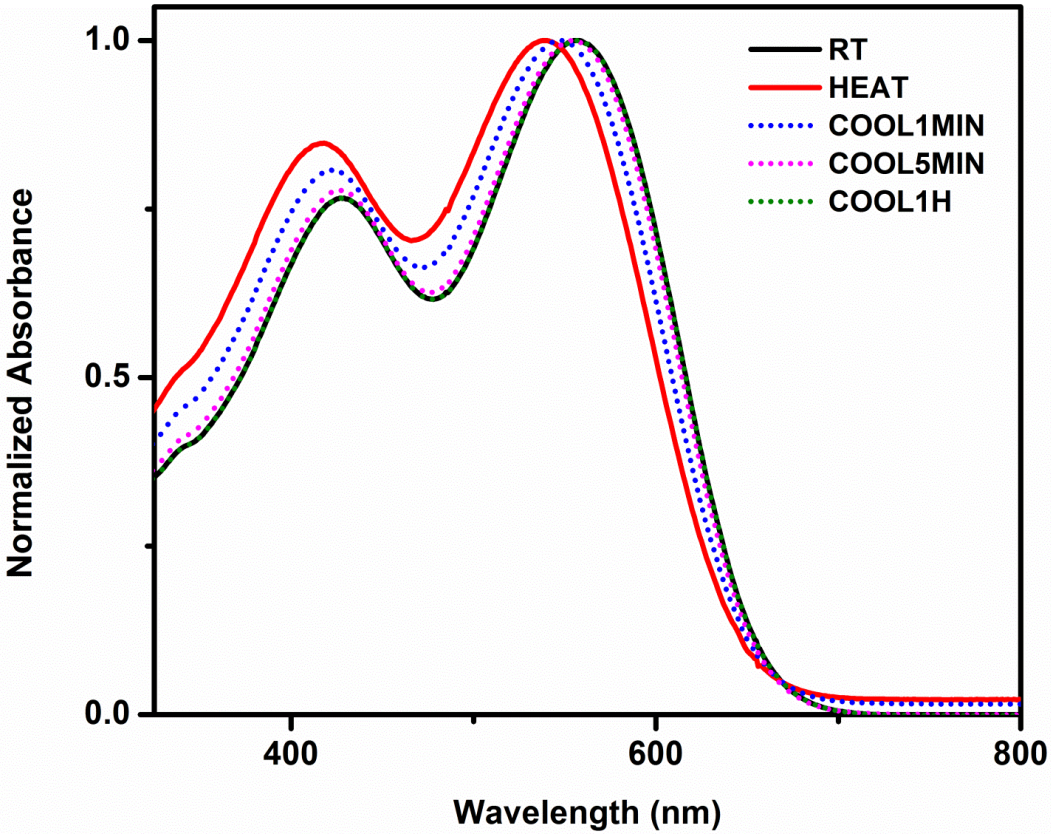

Figure S3.3. Thermochromism of **PBT6** in DCB solution (1 x 10^{-5} M): (i) room temperature; (ii) after heating (under heat gun for 3 min); (iii) additional 1 min of cooling after heating; (iv) additional 5 min of cooling; (v) additional 1 h of cooling

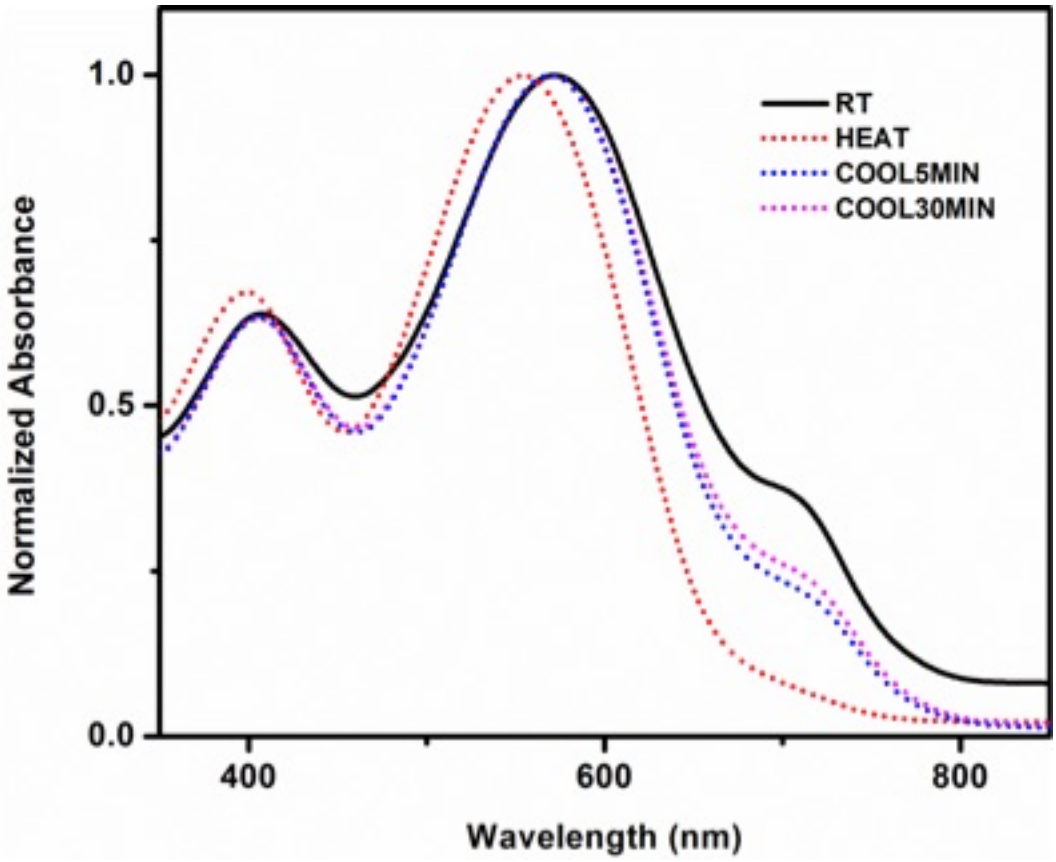

Figure S3.4. Thermochromism of **PBT4** in CB solution (2 x 10^{-5} M): (i) room temperature; (ii) after heating (heat gun for 1 min); (iii) additional 5 min of cooling after heating; (iv) additional 30 min of cooling

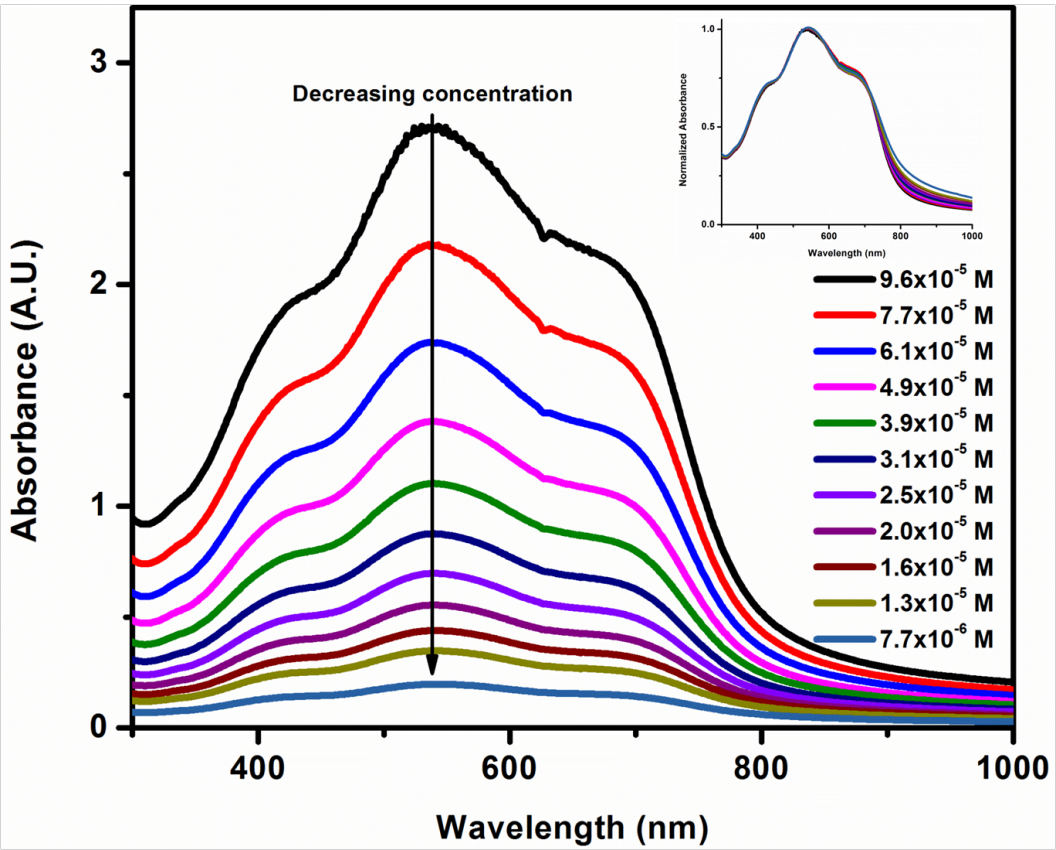

Figure S3.5. The change of absorbance in **PBT6** in $CHCl_3$ solution upon stepwise dilution from 9.6 x 10^{-5} M to 7.7 x 10^{-6} M. The inset is the figure of normalized absorbance versus wavelength setting the absorbance at 539 nm as 1.0, signifying the relative absorbance of the shoulder at λ = 689 nm compared to the primary bands remains constant.

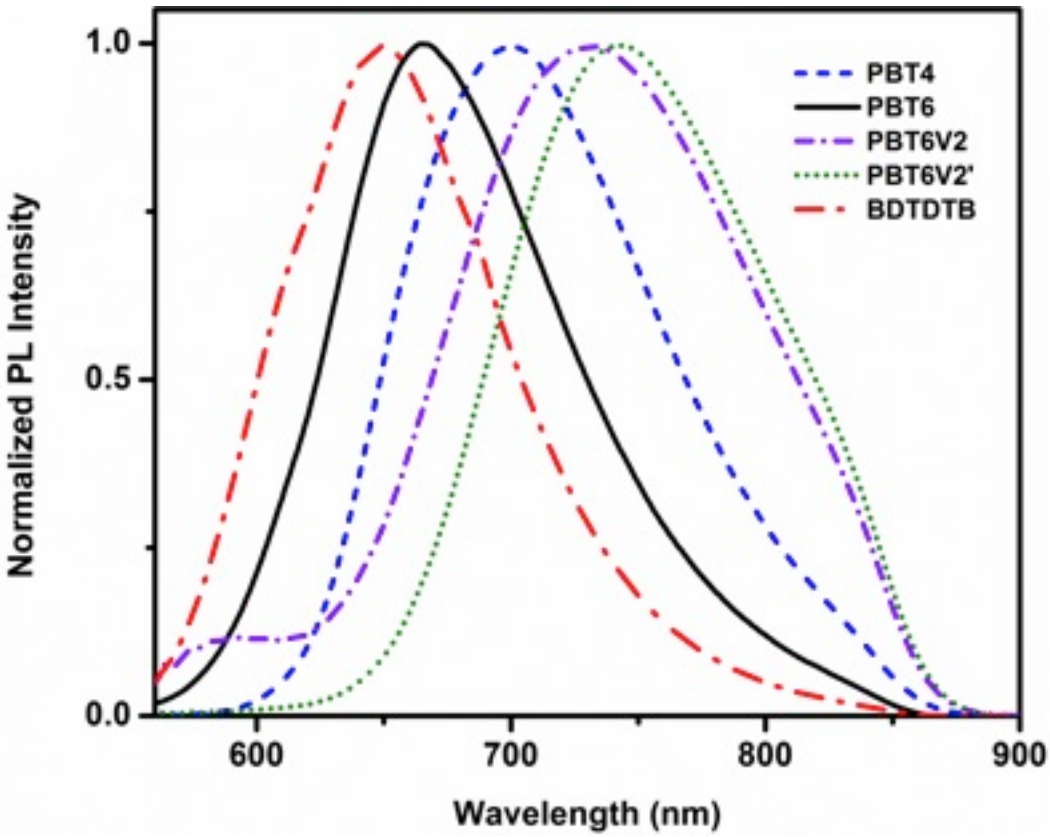

Figure S3.6. Normalized photoluminescence spectra (excitation wavelength, λ_{ex} = 450 nm) of **PBT4**, **PBT6**, **PBT6V**, **PBT6VD** and **BDTDTB** in $CHCl_3$ solution

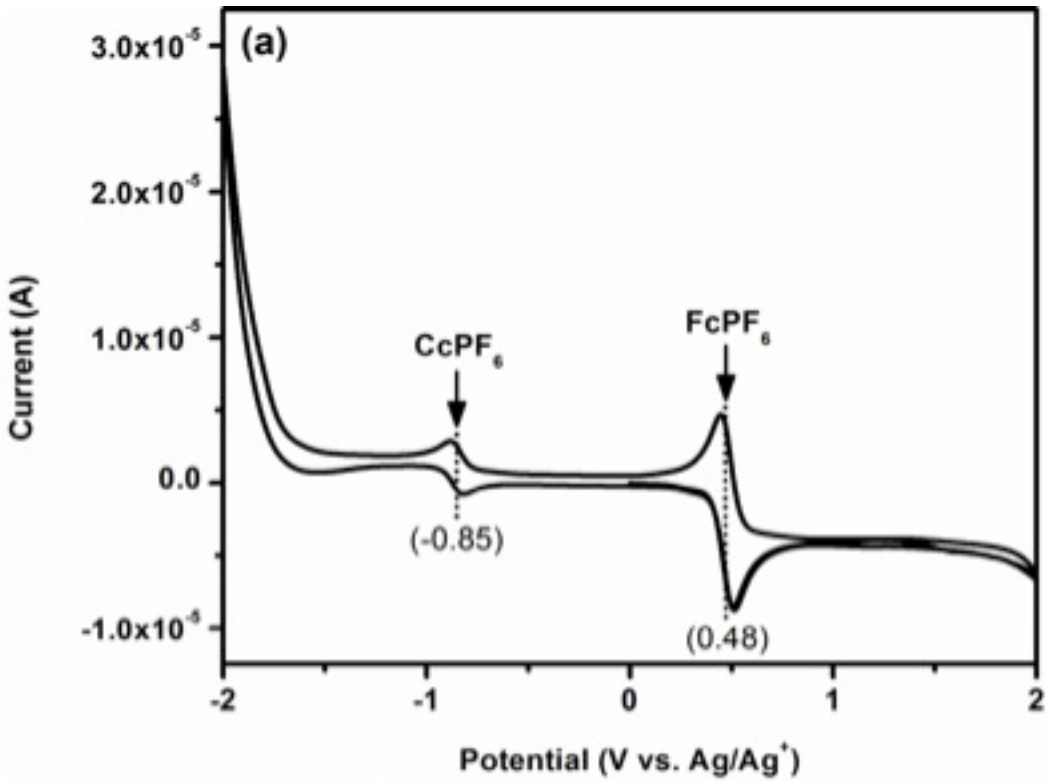

Figure S3.7a. Cyclic voltammogram of bis(cyclopentadienyl)cobalt(III) hexafluorophosphate (cobaltocenium hexafluorophosphate, $CcPF_6$) and ferrocenium hexafluorophosphate ($FcPF_6$) in a 0.1 M solution of $[n\text{-}Bu_4N]^+[PF_6]^-$ in acetonitrile.

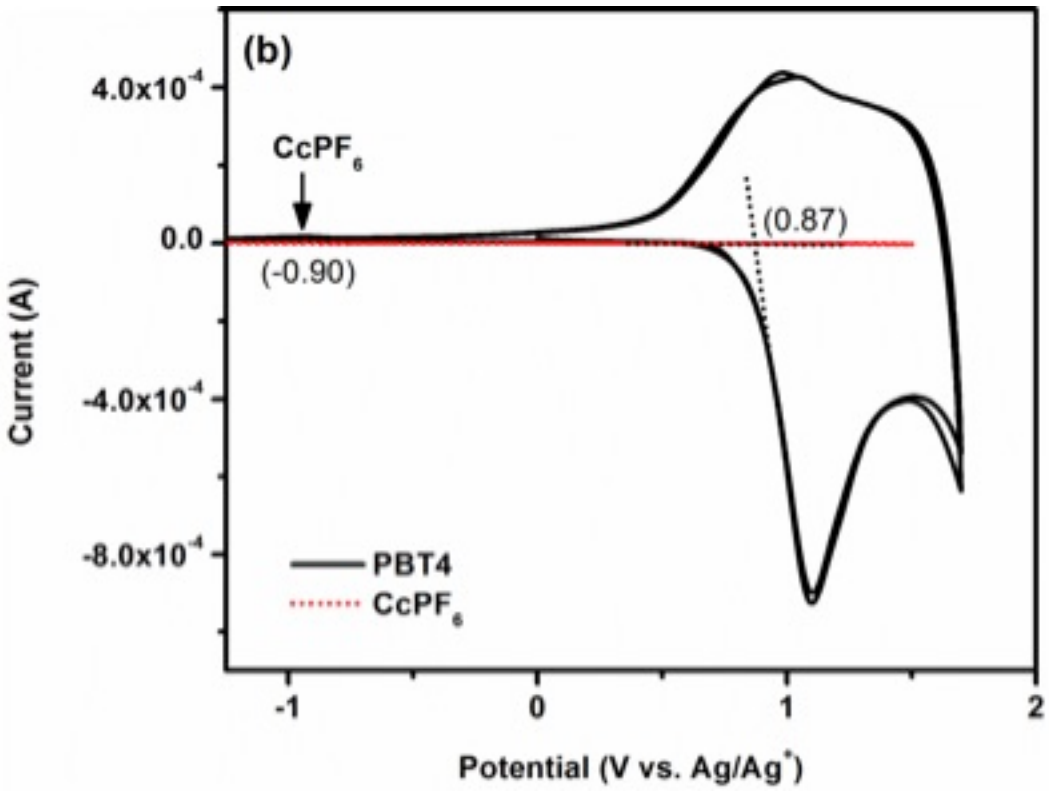

Figure S3.7b Cyclic voltammogram of **PBT4** with CcPF6 as internal reference in a 0.1 M solution of $[n\text{-}Bu_4N]^+[PF_6]^-$ in acetonitrile.

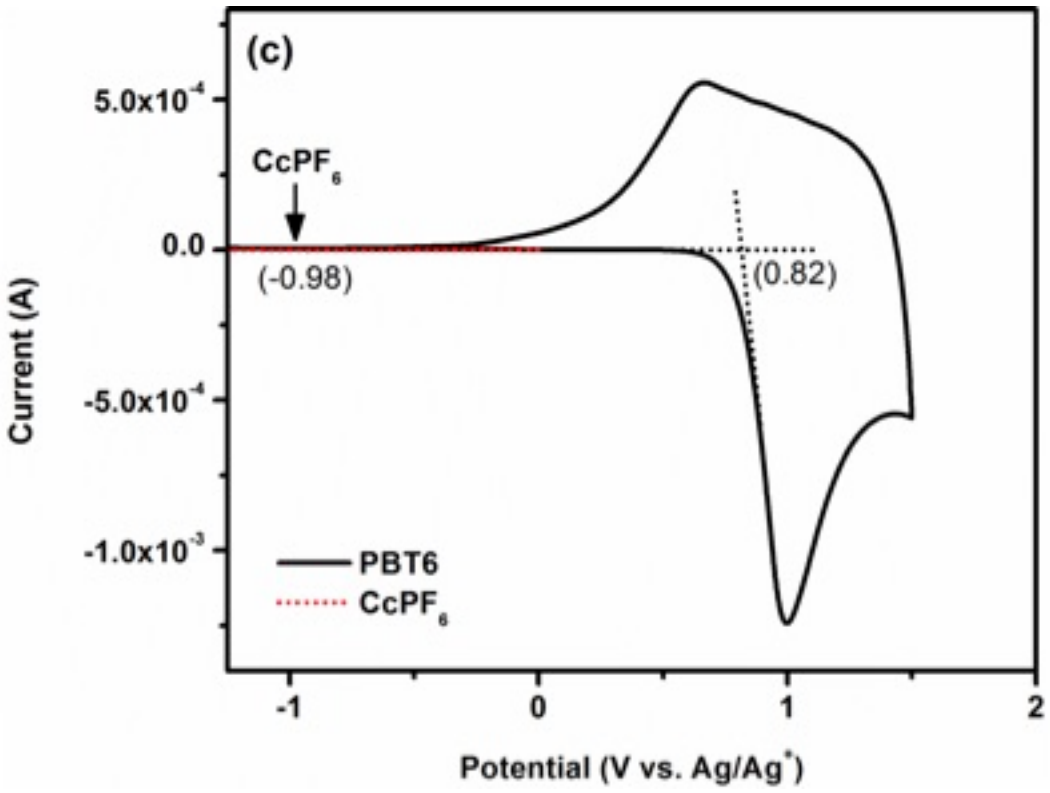

Figure S3.7c Cyclic voltammogram of **PBT6** with $CcPF_6$ as internal reference in a 0.1 M solution of $[n\text{-}Bu_4N]^+[PF_6]^-$ in acetonitrile.

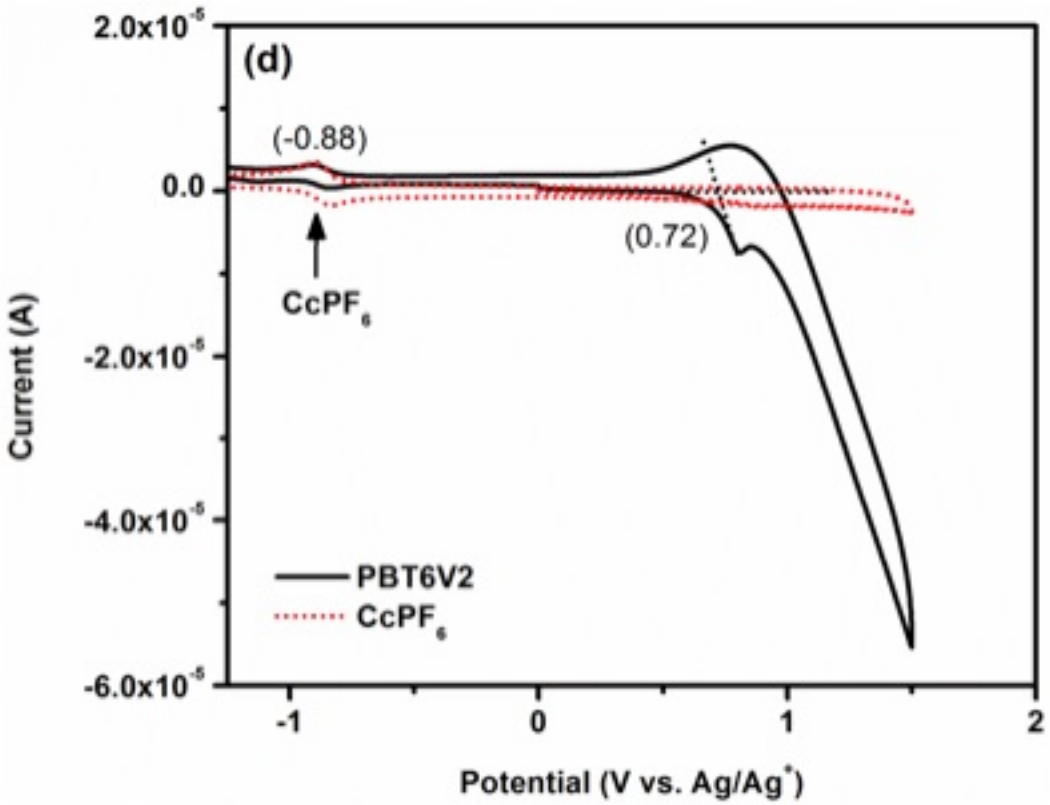

Figure S3.7d Cyclic voltammogram of **PBT6V2** with $CcPF_6$ as internal reference in a 0.1 M solution of $[n\text{-}Bu_4N]^+[PF_6]^-$ in acetonitrile.

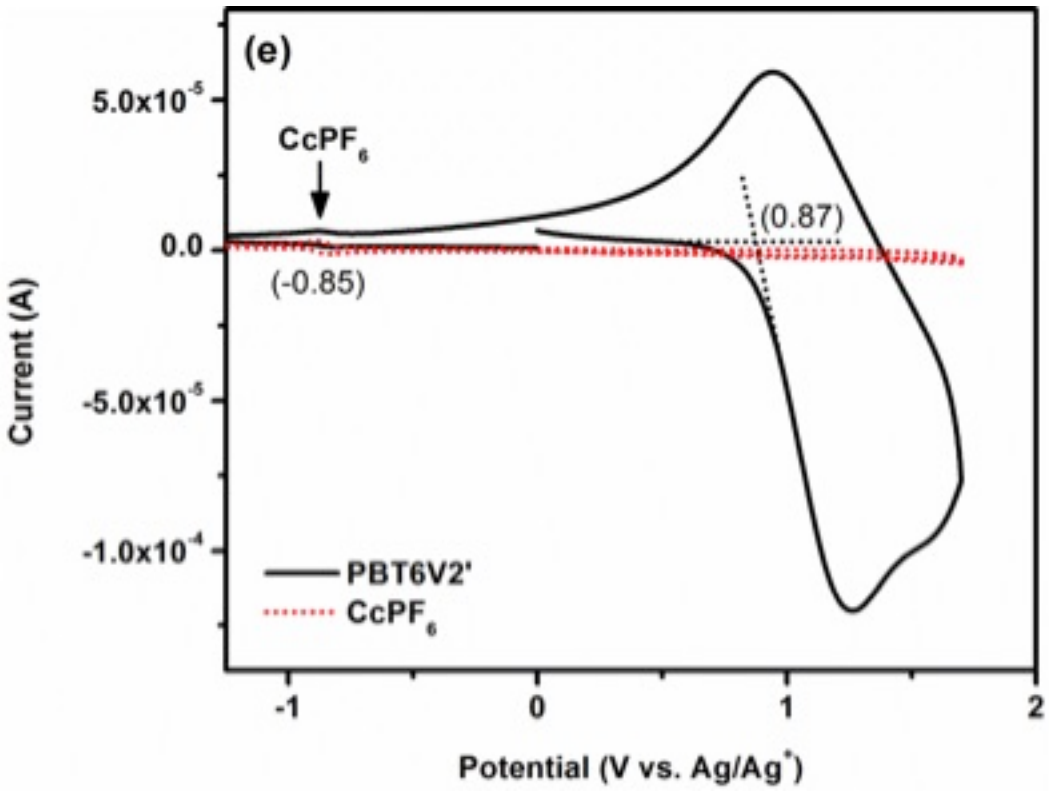

Figure S3.7e Cyclic voltammogram of **PBT6V2'** with $CcPF_6$ as internal reference in a 0.1 M solution of $[n\text{-}Bu_4N]^+[PF_6]^-$ in acetonitrile.

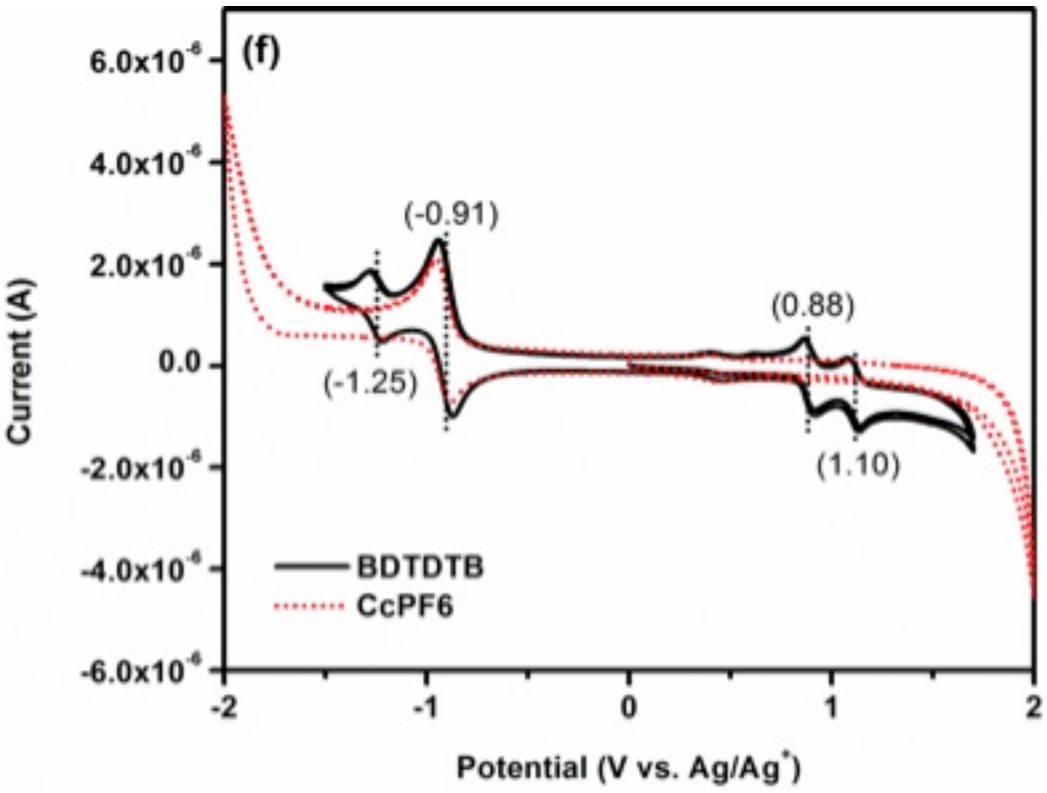

Figure S3.7f Cyclic voltammogram of **BDTDTB** with $CcPF_6$ as internal reference in a 0.1 M solution of $[n\text{-}Bu_4N]^+[PF_6]^-$ in acetonitrile.

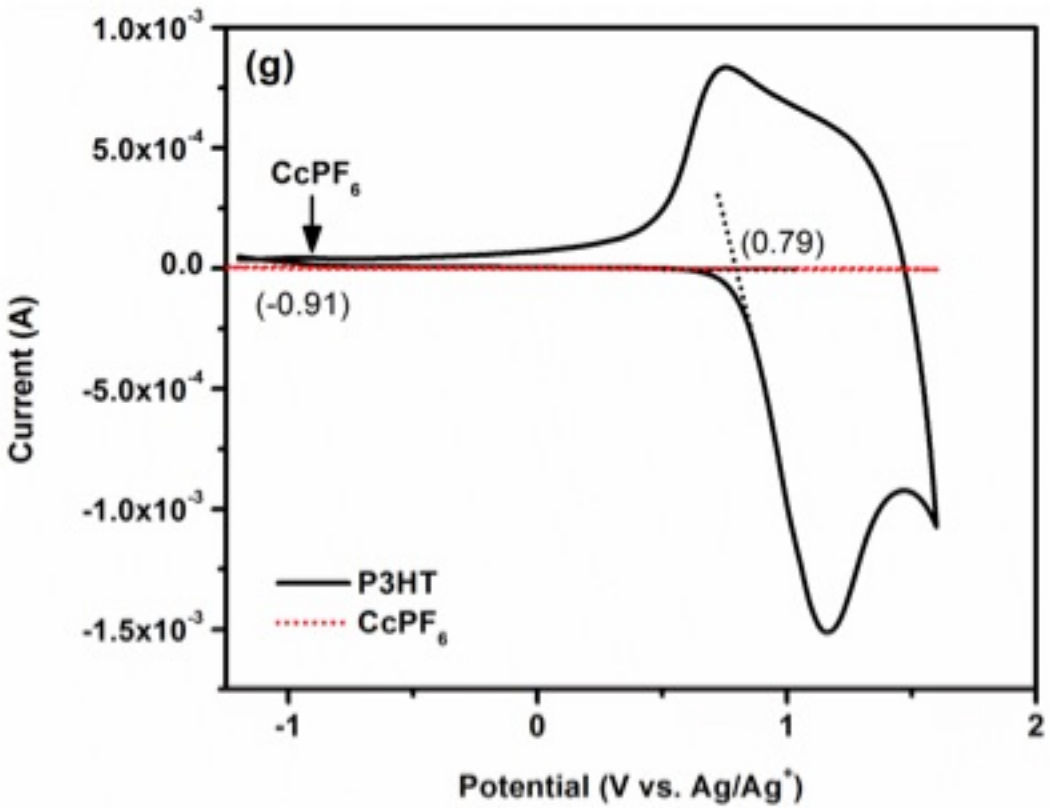

Figure S3.7g Cyclic voltammogram of **P3HT** with $CcPF_6$ as internal reference in a 0.1 M solution of $[n\text{-}Bu_4N]^+[PF_6]^-$ in acetonitrile.

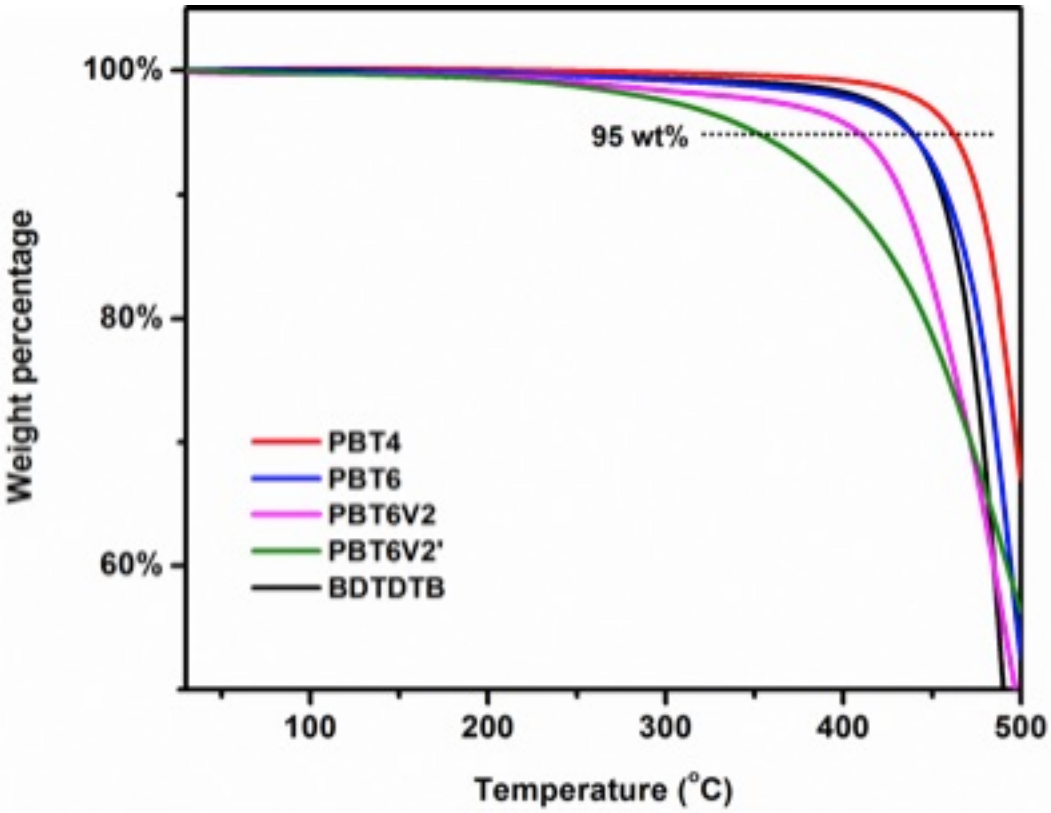

Figure S3.8. Thermo gravimetric analysis of polymers and oligomer (thermal decomposition temperature defined as the temperature of 5% weight-loss).

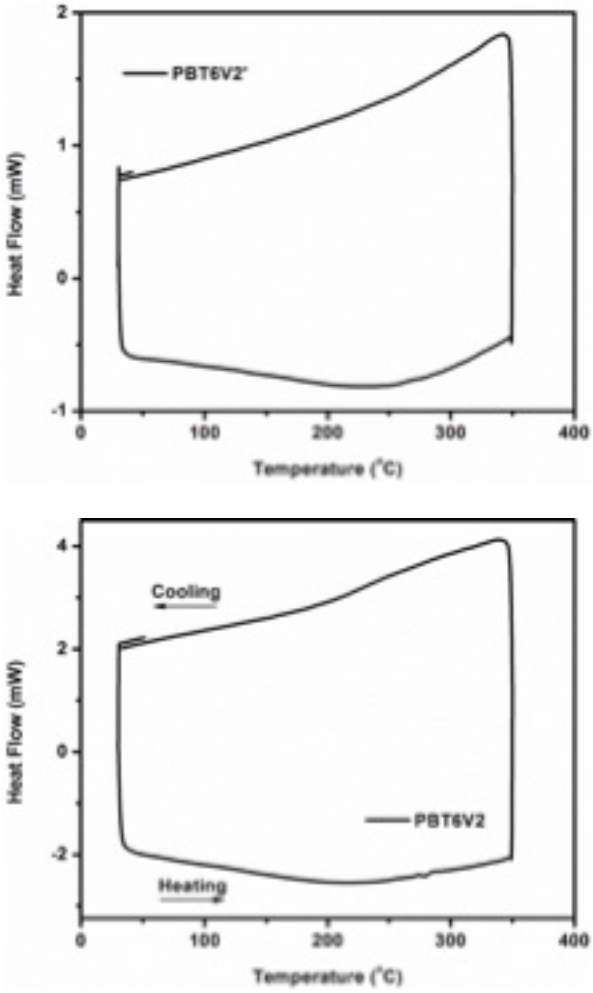

Figure S3.9. Differential scanning calorimetry diagrams of **PBT6V2** (left) and **PBT6V2'** (right) display no thermal transitions in the second heating / cooling scan at 10 °C / min.

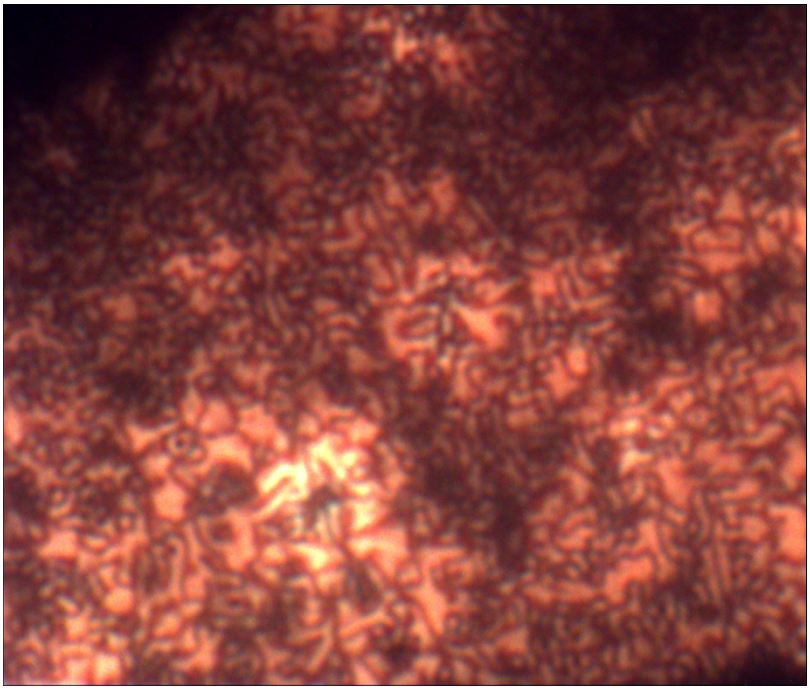

Figure S3.10. Thin film morphology of **PBT6(L)** under POM at room temperature (**PBT6(L)** film was prepared by spin-coating a 8 mg/ mL solution of **PBT6(L)** in DCB followed by annealing at 200 °C for 1 h)

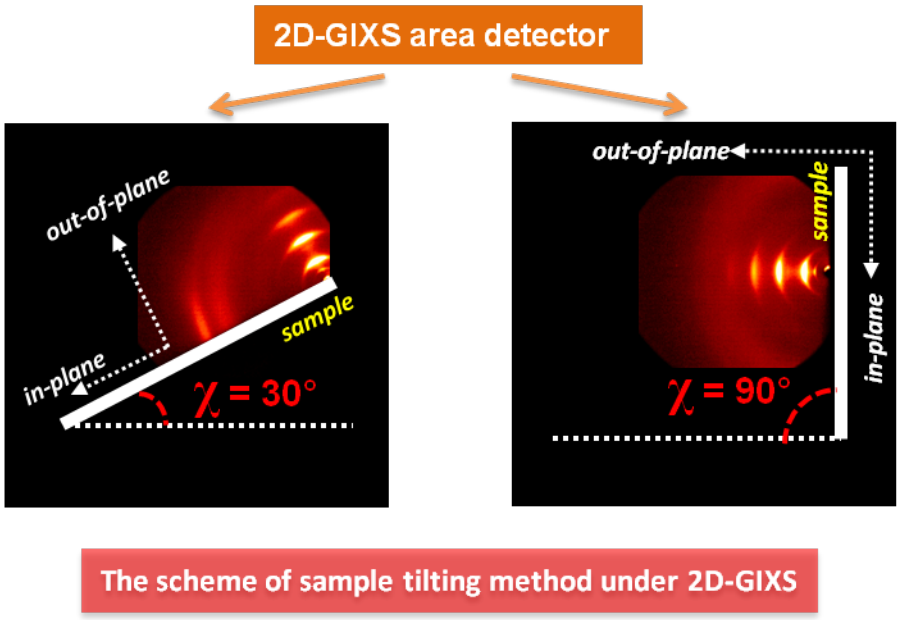

Figure S3.11a The scheme of sample tilting under 2D-GIXS measurement. The direction of X-ray incidence beam is perpendicular to the 2D_GIXS area detector.

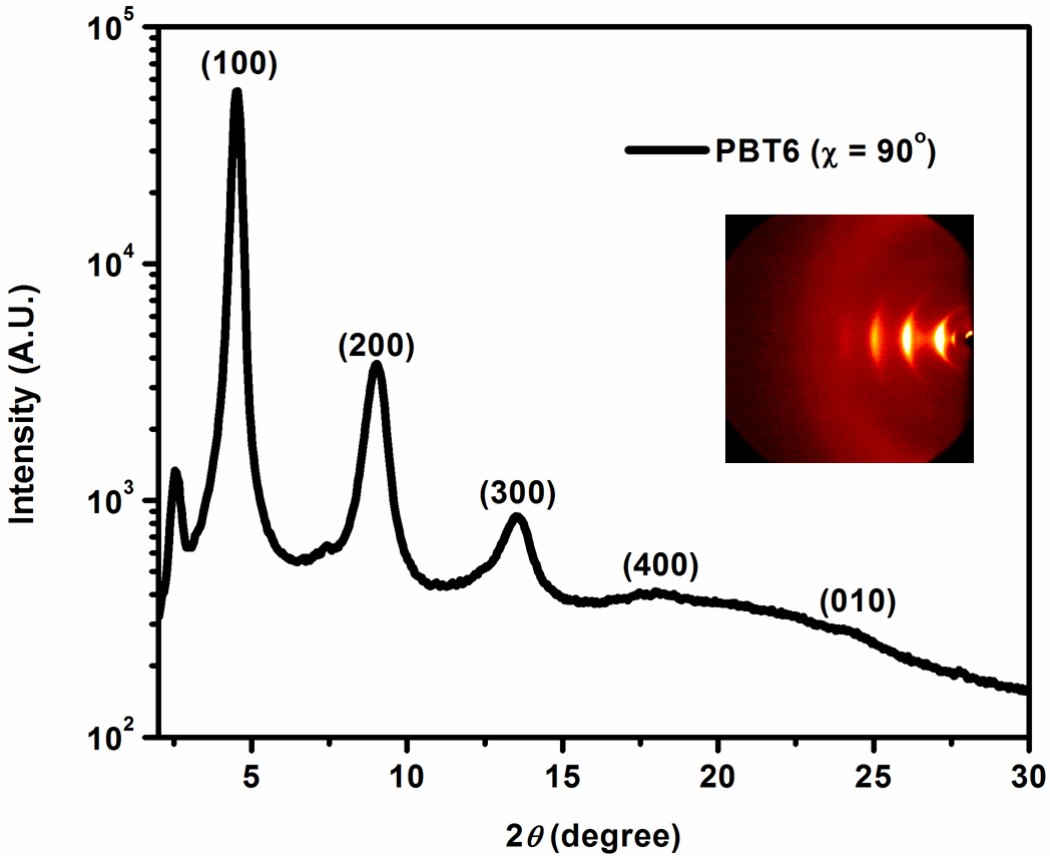

Figure S3.11b. 2D-GIXS area detector image of a **PBT6** drop-cast film tilted at χ = 90° (inset) and the corresponding integrated intensity diffraction pattern.

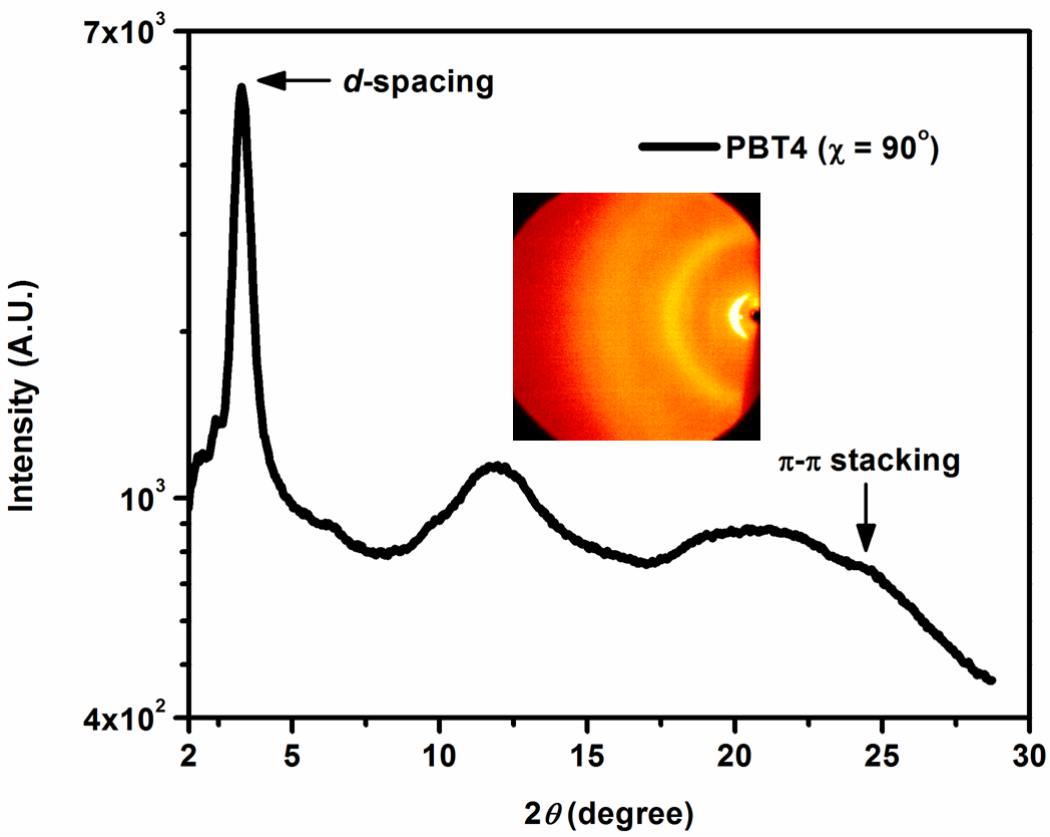

Figure S3.11c. 2D-GIXS area detector image of a **PBT4** drop-cast films tilted at $\chi = 90°$ (inset) and the corresponding integrated intensity diffraction pattern.

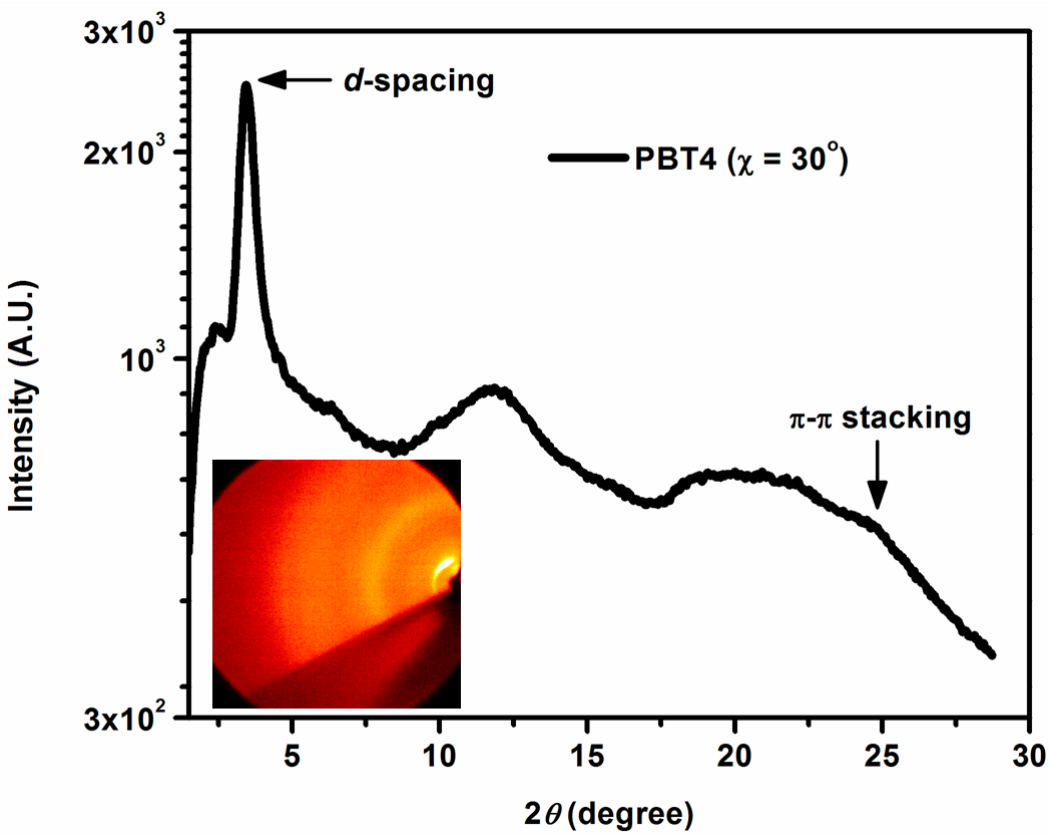

Figure S3.11d. 2D-GIXS area detector image of a **PBT4** drop-cast films tilted at $\chi = 30°$ (inset) and the corresponding integrated intensity diffraction pattern.

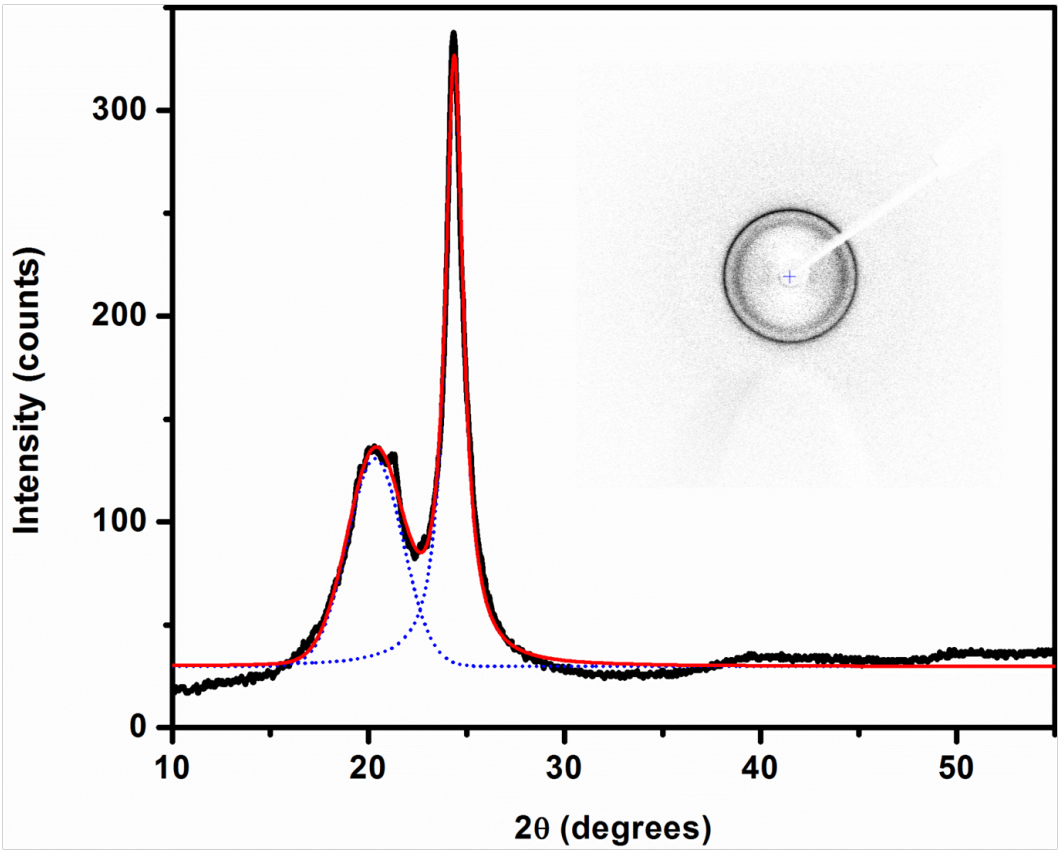

Figure S3.12. The integrated intensity diffraction patterns of **PBT6** drop-cast film measured by transmission 2D-WAXD. The inset is the corresponding area detector image.

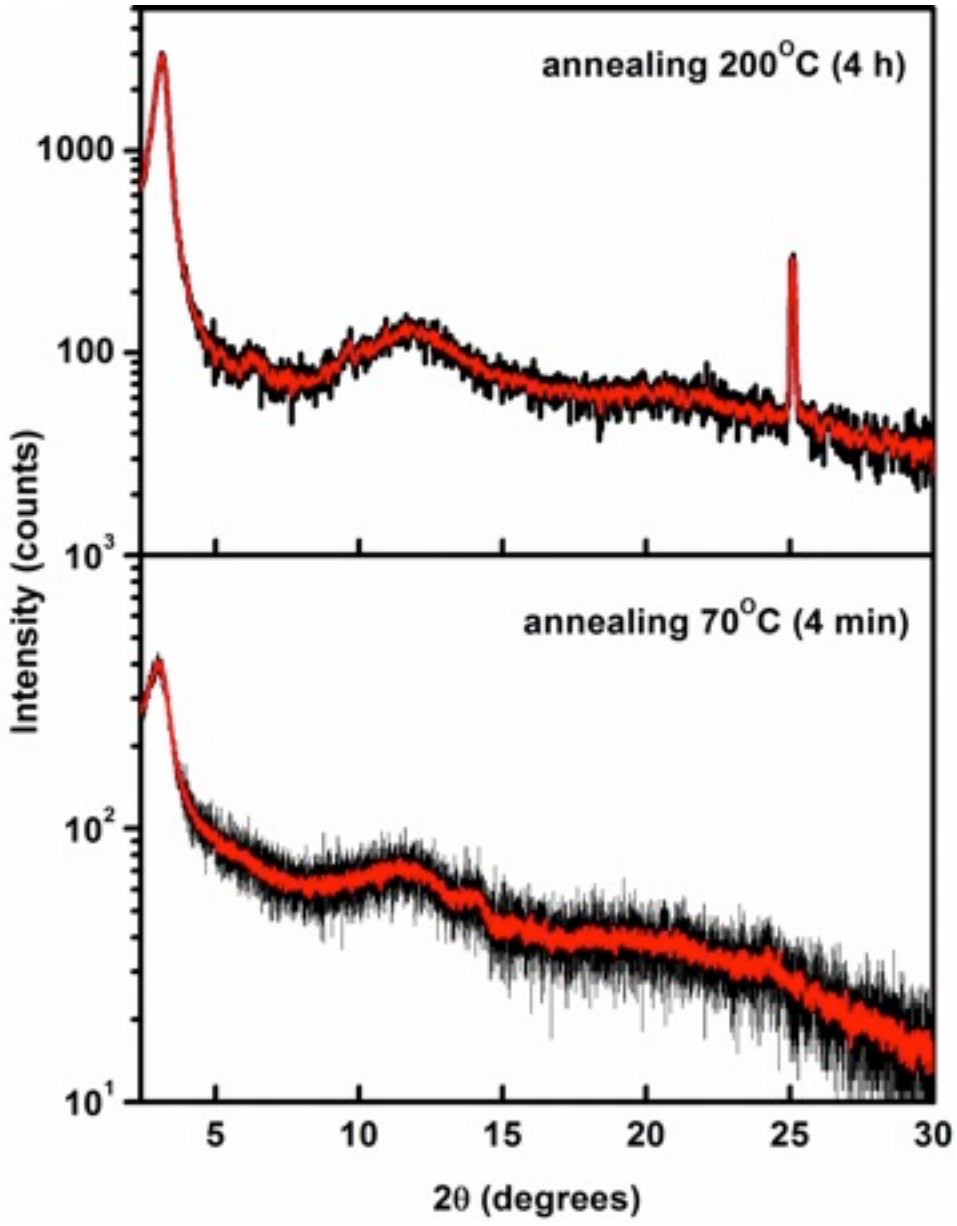

Figure S3.13. 1D-XRD (out-of-plane) diffraction patterns of **PBT4** drop-cast film at room temperature and after annealing at 200 °C for 4 h

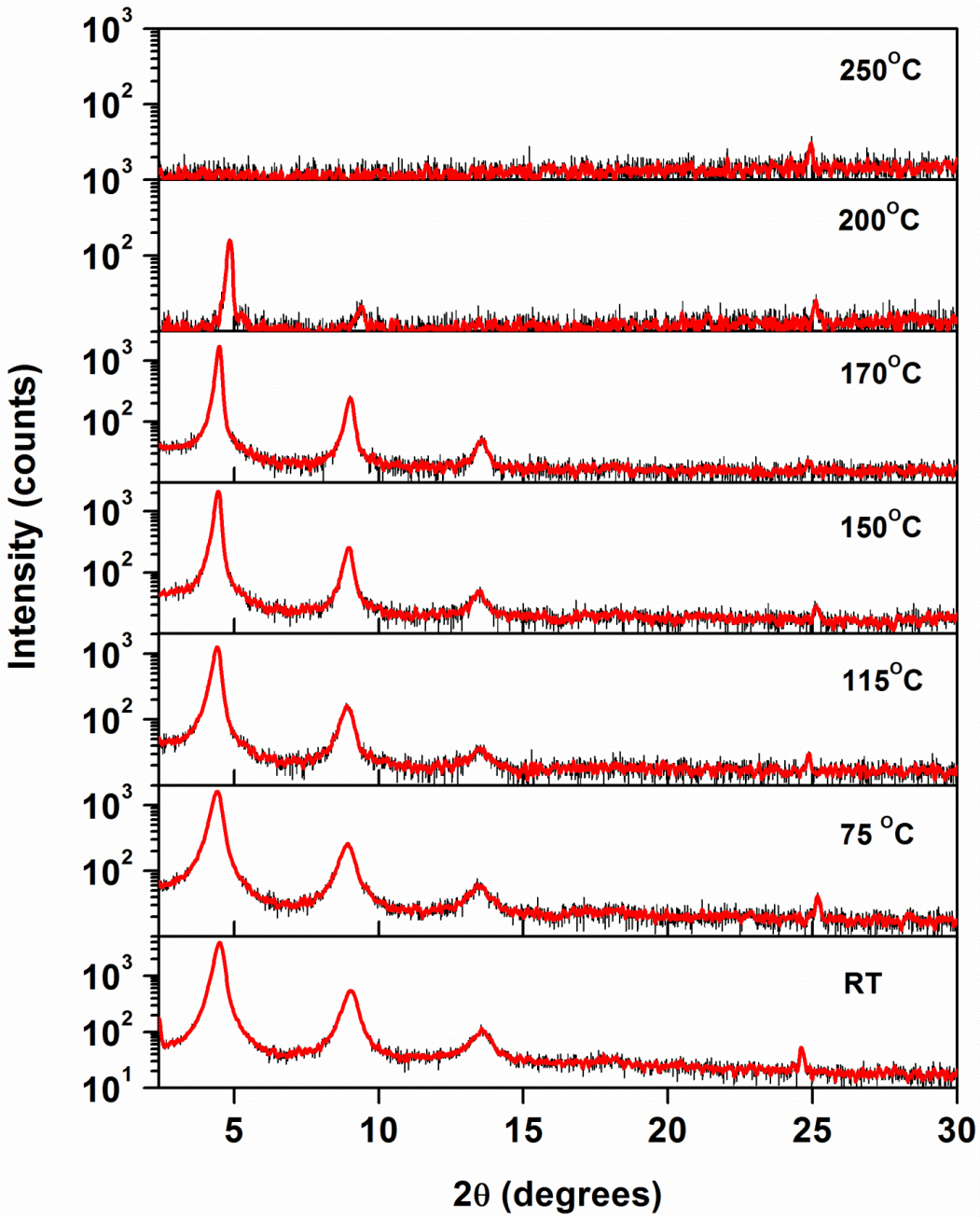

Figure S3.14. 1D-XRD (out-of-plane) patterns of **PBT6** drop-cast film at room temperature; after annealing at 75 °C for 1 h; after annealing at 115 °C for 1 h; after annealing at 150 °C for 1 h; after annealing at 170 °C for 1 h; after annealing at 200 °C for 1 h; after annealing at 250 °C for 1 h

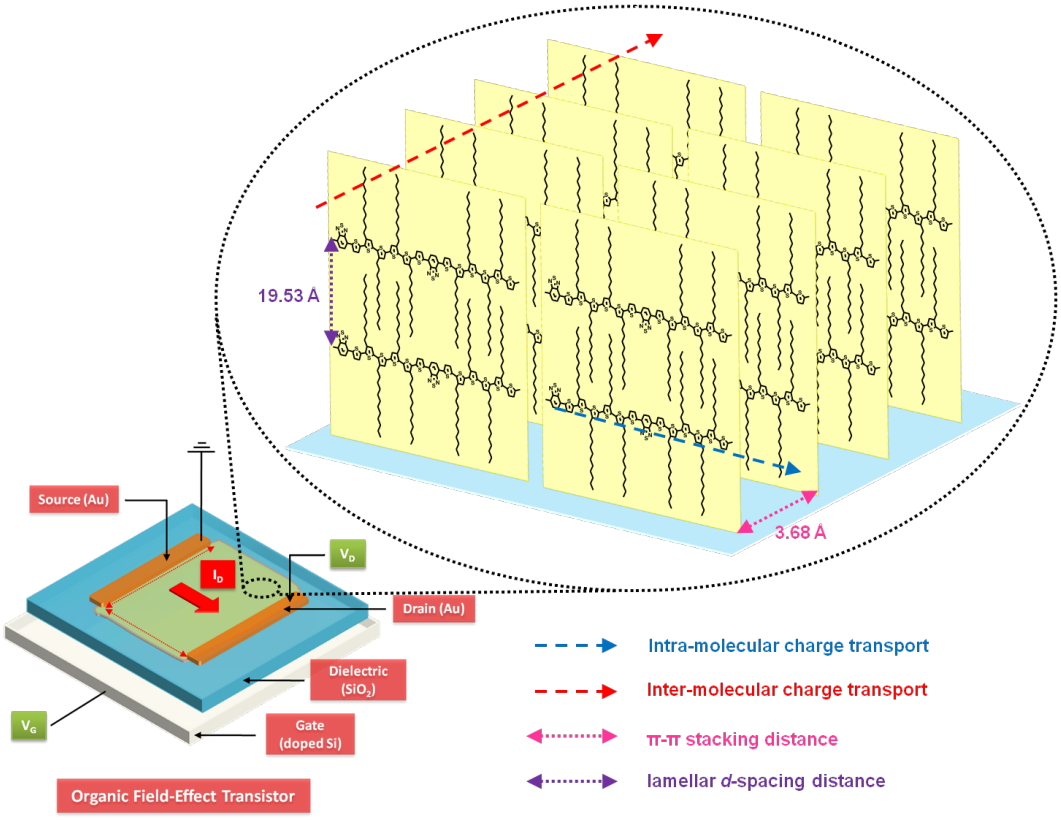

Figure S3.15. Idealized, lamellar π stacking edge-on orientation of **PBT6** thin film onto the bottom contact, bottom gate OFET substrate.

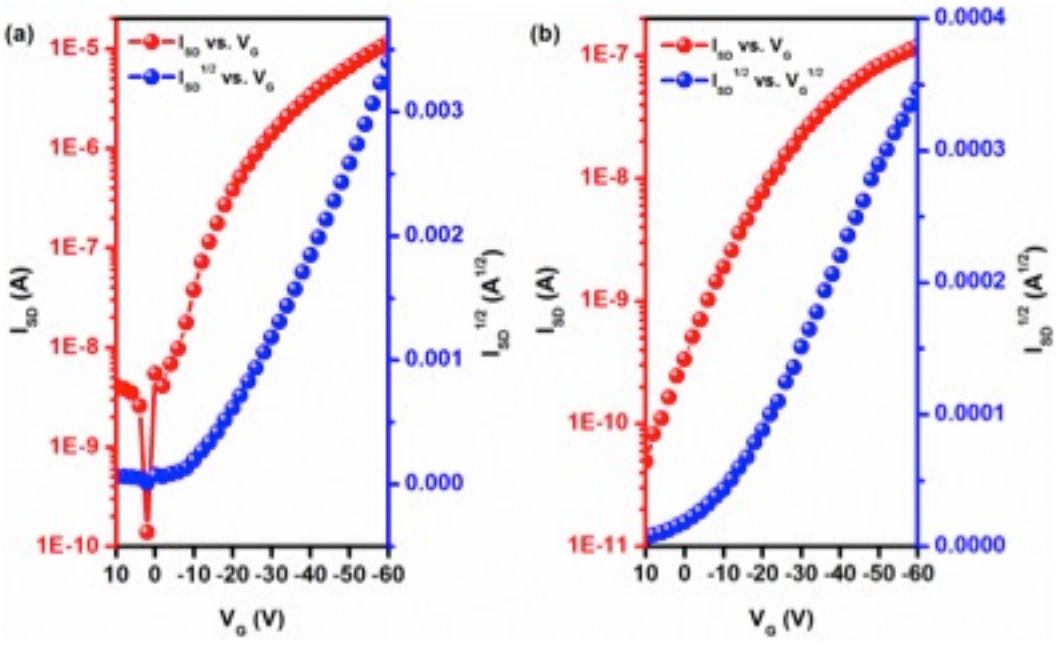

Figure S3.16. Transfer characterization of OFETs (V_{SD} = -80 V, channel size: 50 µm long x 2 mm wide): (a) spin-coated **PBT6(L)** film, and (b) spin-coated **PBT6V2** film.

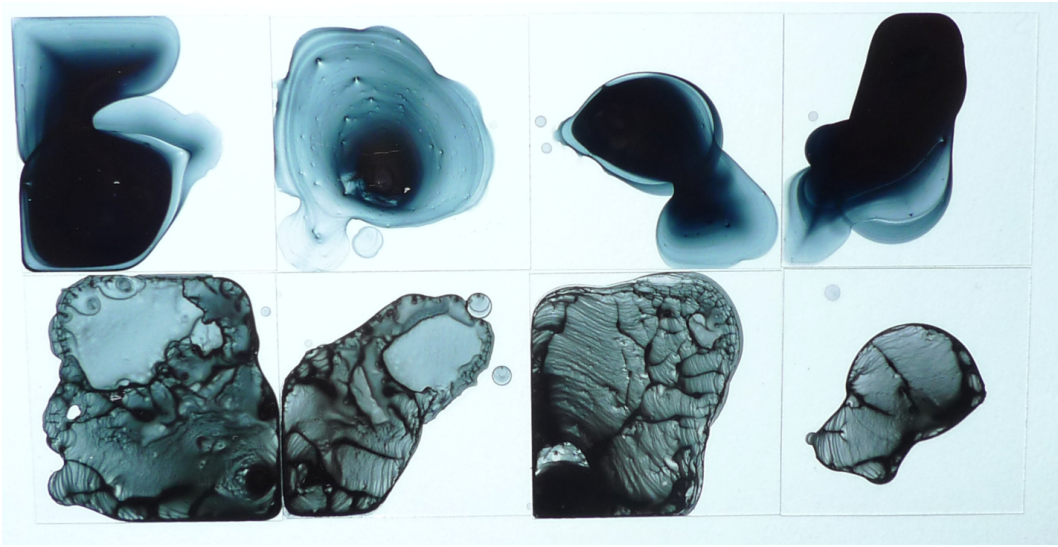

Figure S3.17. Photographs of drop cast films from 8 mg/ml of **PBT6** (upper row) and **PBT6(L)** in DCB on glass microcovers

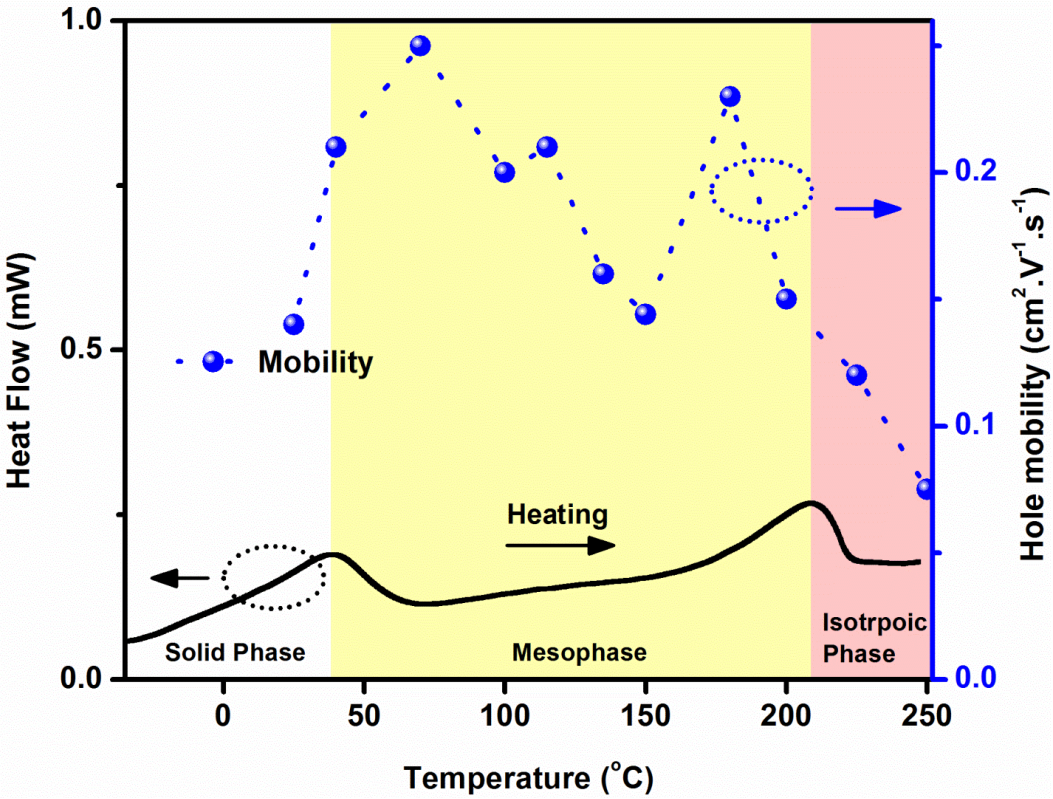

Figure S3.18. Hole mobility of **PBT6** from OFET measurements subjected to annealing in solid phase (room temperature), mesophase (40 °C, 70 °C, 100 °C, 115 °C, 135 °C, 150 °C and 180 °C) and isotropic phase (200 °C, 225 °C and 250 °C). The DSC trace at the bottom indicates the temperature of thermal transition.

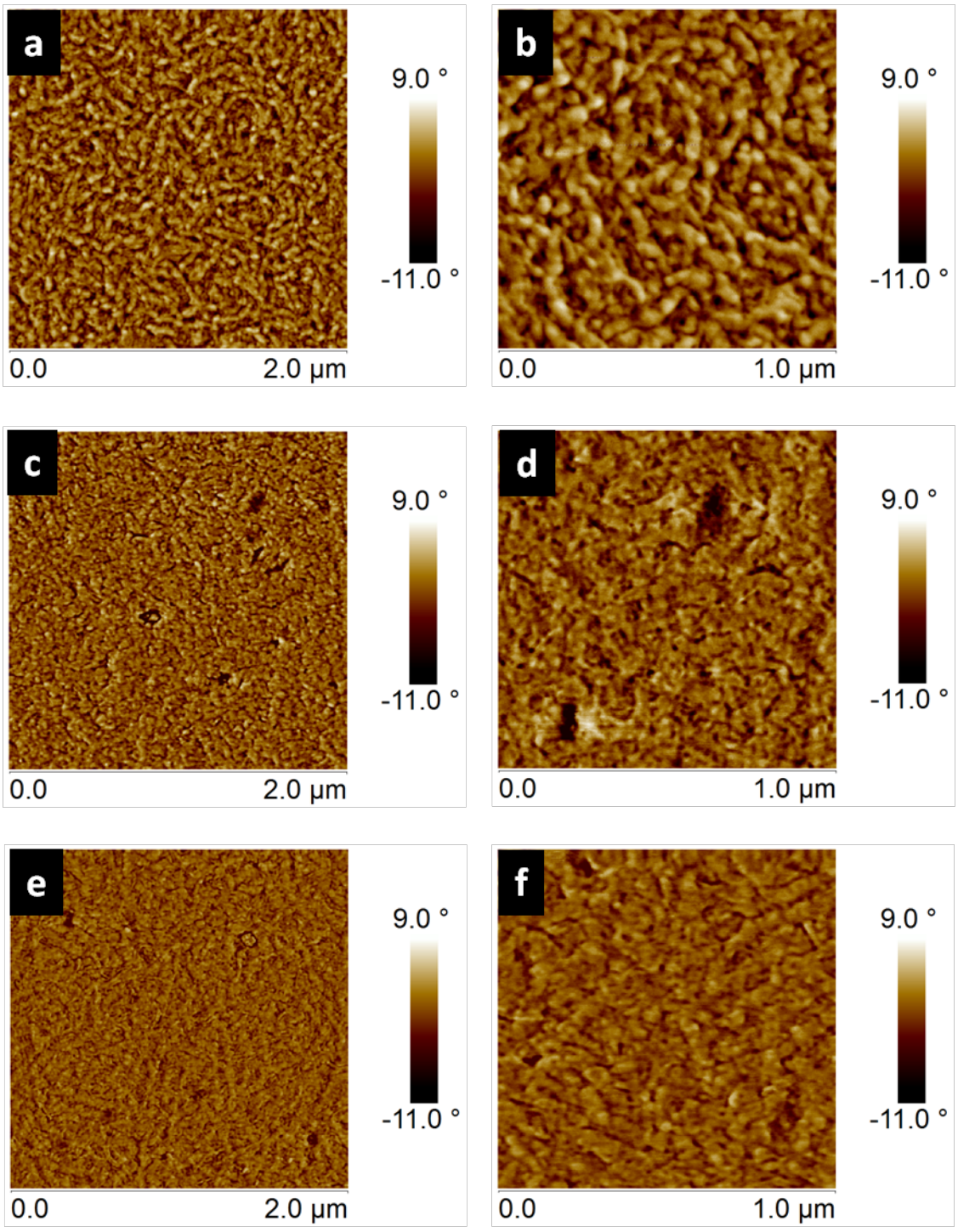
a
9.0 °
-11.0 °
0.0
2.0 µm
b
9.0 °
-11.0 °
0.0
1.0 µm
c
9.0 °
-11.0 °
0.0
2.0 µm
d
9.0 °
-11.0 °
0.0
1.0 µm
e
9.0 °
-11.0 °
0.0
2.0 µm
f
9.0 °
-11.0 °
0.0
1.0 µm

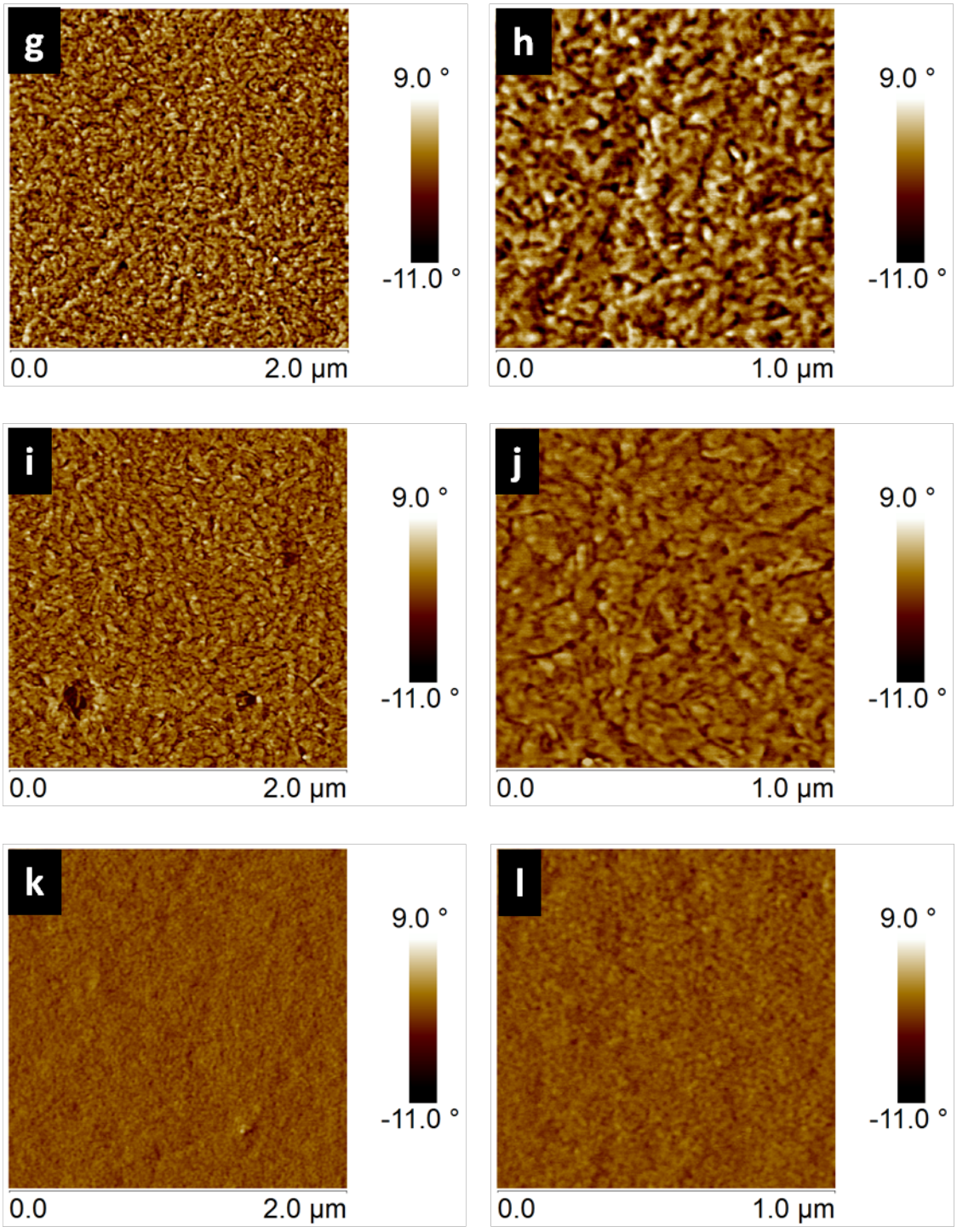

Figure S3.19. Tapping mode AFM phase images of **PBT6** films prepared by spin-coating 8 mg /mL polymer solutions in DCB onto OTS-18 pre-treated OFETs: (a, b) as spun, (c, d) after annealed at 39 °C for 2h, (e, f) annealed at 70 °C for 2h, (g, h) annealed at 100 °C for 2h, (i, j) annealed at 115 °C for 2h, and (k, l) annealed at 250 °C for 2h.

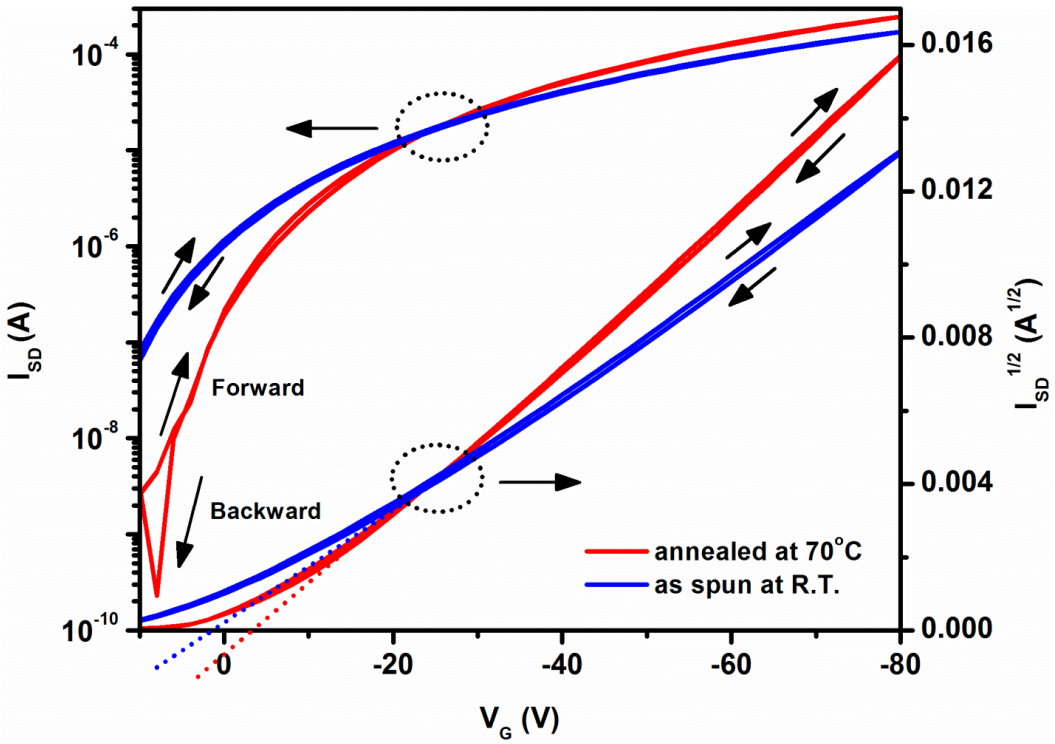

Figure S3.20. Transfer characterizations of OFETs at V_{SD} = -80 V (channel size: 50 μm long x 2 mm wide) based on a spin-coated **PBT6** film as spun at room temperature and annealed at 70 °C for 2 h, in sweeping mode. Arrows signify the sweeping directions (forward: 10 to -80 V; backward: -80 to 10 V) of gate voltage, V_G.

References

(1) Katritzky, A. R.; Fara, D. C.; Yang, H. F.; Tamm, K.; Tamm, T.; Karelson, M. *Chem. Rev.* **2004**, *104*, 175.

(2) (a) Kang, S. O.; Kim, J. J.; Choi, H.; Lee, J. W.; Kang, M. S.; Song, K.; Ko, J. *J. Mater. Chem.* **2008**, *18*, 5223. (b) Moule, A. J.; Tsami, A.; Buennagel, T. W.; Forster, M.; Kronenberg, N. M.; Scharber, M.; Koppe, M.; Morana, M.; Brabec, C. J.; Meerholz, K.; Scherf, U. *Chem. Mater.* **2008**, *20*, 4045.

(3) (a) Jung, H. T.; Jin, J. K.; Choi, J. K.; Kim, B. J.; Kang, H. B.; Yoon, S. C.; You, H. *Macromolecules* **2011**, *44*, 502. (b) Ong, K. H.; Lim, S. L.; Tan, H. S.; Wong, H. K.; Li, J.; Ma, Z.; Moh, L. C. H.; Lim, S. H.; De Mello, J. C.; Chen, Z. K. *Adv. Mater.* **2011**, *23*, 1409.

(4) (a) Biniek, L.; Chochos, C. L.; Hadziioannou, G.; Leclerc, N.; Leveque, P.; Heiser, T. *Macromol. Rapid Commun.* **2010**, *31*, 651. (b) Usta, H.; Facchetti, A.; Marks, T. J. *J. Am. Chem. Soc.* **2008**, *130*, 8580.

(5) Zagorska, M.; Krische, B. *Polymer* **1990**, *31*, 1379.

(6) Mcculloch, I.; Heeney, M.; Bailey, C.; Genevicius, K.; Macdonald, I.; Shkunov, M.; Sparrowe, D.; Tierney, S.; Wagner, R.; Zhang, W. M.; Chabinyc, M. L.; Kline, R. J.; Mcgehee, M. D.; Toney, M. F. *Nat. Mater.* **2006**, *5*, 328.

(7) Zhang, X. L.; Yamaguchi, R.; Moriyama, K.; Kadowaki, M.; Kobayashi, T.; Ishi-i, T.; Thiemann, T.; Mataka, S. *J. Mater. Chem.* **2006**, *16*, 736.

(8) Wang, J. L.; Tang, Z. M.; Xiao, Q.; Ma, Y. G.; Pei, J. *Org. Lett.* **2008**, *10*, 4271.

(9) Zoombelt, A. P.; Gilot, J.; Wienk, M. A.; Janssen, R. A. J. *Chem. Mater.* **2009**, *21*, 1663.

(10) (a) Mishra, S. P.; Palai, A. K.; Srivastava, R.; Kamalasanan, M. N.; Patri, M. *J. Polym. Sci. Pol. Chem.* **2009**, *47*, 6514. (b) Zhang, S. M.; Guo, Y. L.; Fan, H. J.; Liu, Y.; Chen, H. Y.; Yang, G. W.; Zhan, X. W.; Liu, Y. Q.; Li, Y. F.; Yang, Y. *J. Polym. Sci. Pol. Chem.* **2009**, *47*, 5498.

SUPPORT INOFRMATION-2

FOR CHAPTER 4

Materials and Methods

Chloroform, dichloromethane, toluene, isopropanol, THF, DMF, chlorobenzene and 1,2-dichorobenzene (ODCB) were purchased as anhydrous grade solvents from Sigma-Aldrich. THF was distilled from sodium benzophenone ketyl. Bis(triphenylphosphine)palladium(II) dichloride ($Pd(PPh_3)_2Cl_2$), 4,7-dibromobenzo[c]-1,2,5-thiadiazole, 2-(tributylstannyl)thiophene, tris(dibenzylideneacetone)dipalladium(0) ($Pd_2(dba)_3$), tri(o-tolyl)phosphine ($P(o\text{-tolyl})_3$), sodium diethyldithiocarbmate, and tetra-*n*-butylammonium hexafluorophosphate ($[n\text{-}Bu_4N]^+[PF_6]^-$) were purchased from Sigma-Aldrich. 3-Dodecylthiophene was purchased from Rieke Metals, *n*-octadecyltrichlorosilane (OTS-18) was purchased from Gelest, Inc. Silica gel was purchased from Sorbent Technologies (Premium Rf™, porosity: 60Å; particle size: 40-75 μm).

The microwave irridated polymerizations were conducted using a CEM Discover SP System. ^1H NMR and ^{13}C NMR spectra were recorded using a Varian Mercury Vx 400 (^1H, 400 MHz; ^{13}C, 100 MHz) nuclear magnetic resonance spectrometer.. Electron ionization mass spectra (EI-MS) were recorded using a Waters AutoSpec; matrix-assisted laser desorption/ionization mass spectral (MALDI-MS) mesurements were conducted on

a Bruker Autoflex III Smartbeam instrument. Molecular weights of **TBTD** polymers were measured using a PL-GPC 220 instrument (courtesy of the Prof. Richard F. Jordan Research Group in the Department of Chemistry at the University of Chicago) using 1,2,4-trichlorobenezene (TCB) as the mobile phase (stabilized with 125 ppm butylated hydroxytoluene) at 135 °C.

UV-vis absorption spectra was recorded on an Agilent 8453 UV-Visible Spectrophotometer. Polymer films for UV-vis absorption characterization were prepared by spin-coating polymer solutions (5 mg/mL in ODCB) onto OTS-18 pre-treated glass cover substrates. The details of OTS-18 pretreatment are depicted in the section of "OFET Device Fabrication and Characterization" (*vide infra*).

Cyclic voltammetry (CV) and differential pulse voltammetry (DPV) were performed using Princeton Applied Research Potentiostat/Galvanostat Model 273A with a three-electrode electrochemical cell consisting of a platinum disk working electrode, onto which polymers were drop casted from ODCB solution (1 mg/mL), a platinum flag counter electrode, and a Ag/Ag^+ reference electrode (10 mM of $AgNO_3$ and 0.5 M of Bu_4NPF_6 in acetonitrile).[1] The ferrocene/ferrocenium redox couple (Fc/Fc^+) was used as the internal standard (-4.80 eV versus vacuum). The CV was performed with a scan rate varying from 20 to 200 mV/s for five cycles. DPV parameters were set up as follows: step time 0.038 s, step size of 2 mV, and an amplitude of 100 mV.

Ultraviolet Photoemission Spectra (UPS) were measured on Kratos Axis UltraDLD XPS/UPS system, using He-I lamp radiation at 21.2 eV. All samples were in electronic equilibrium with the spectrometer via a metallic clip on the surface, and were run at a base pressure of 10^{-9} Torr. The Fermi level was calibrated using atomically clean silver. UPS were acquired at 5 eV pass energy and 0.05 eV step size with the aperture and iris set to 55 μm. From the secondary electron edge (SEE) of the UPS we calculated the work function (ϕ = 21.22-SEE) for each polymer, and from the emission close to the Fermi level we determine the position of valence band maximum. IP (= –HOMO) and ϕ were calculated by equations Eq. S3.1. and S3.2:

$$\mathrm{IP} = h\nu - (E_{\mathrm{cutoff}} - \varepsilon_{\mathrm{V}}^{\mathrm{F}}), \qquad \text{Eq. S3.1}$$

$$\phi = h\nu - E_{\mathrm{cutoff}} \qquad \text{Eq. S3.2}$$

where $h\nu$, E_{cutoff}, and $\varepsilon_{\mathrm{V}}^{\mathrm{F}}$ denote the incident photo energy (He I, 21.22 eV), the high binding energy cutoff, and the lowest binding energy point, respectively.

The thermal decomposition temperature of polymers were measured with a Perkin-Elmer Pyris 1 thermogravimetric analyzer (TGA) in a nitrogen atmosphere (25 mL/min) with a heating rate of 10 °C/min. Thermal transitions of polymers were measured with a TA Q200 Differential Scanning Calorimeter (DSC) in a nitrogen atmosphere (50 mL/min) with a heating/cooling rate of 10 °C/min. Each sample was scanned for five cycles.

1D-GIXS characterization was performed on a PANalytical X-ray diffractometer and reflectometer (operating voltage of 45 kV and current of 40 mA) equipped with a Cu K_α X-ray irradiation source (λ = 1.541 Å), and at a fixed incidence angle of 1°. 2D-GIWAXS characterization was carried out using a Bruker-AXS Microdiffractometer (operating voltage of 45 kV and current of 40 mA) with a 0.8 mm collimator, K_α monochromator, Hi-Star area detector, and Eulerian cradle sample holder, at a optimal incidence angle (0.8 - 2° for **TBTD** polymers), and a 90° or 30° out-plane tilt angle, γ.[2] Polymer films for 1D / 2D GIXS characterizations were prepared by drop casting ODCB solutions of the polymers (5 mg/mL) onto OTS-18 pre-treated SiO_2 dielectric (300 nm) / p^{++} doped Si substrates.

The surface morphology of polymer thin films were were characterized by AFM using a Bruker Dimension Icon Atomic Force Microscope System with ScanAsyst in tapping mode with a silicon etched probe tip. Polymer films for AFM characterization were prepared by spin-coating ODCB solutions of the polymers (5 mg/mL) onto OTS-18 pre-treated SiO_2 dielectric (300 nm) / p^{++} doped Si substrates. The thermal annealing treatments for **TBTD** polymer films under UV/vis absorption spectroscopy, UPS, 1D / 2D-GIXS, and AFM characterizations were conducted on a hotplate with temperature setting at 100, 150, 180, 200, 250, 300, 350, or 375 °C inside a glovebox filled with N_2.

Each thermal annealing treatment lasted for 30 min, followed by rapidly cooling to room temperature.

OFET Device Fabrication and Characterization

The bottom-contact-bottom-gate FET devices were fabricated on a heavily n doped silicon wafer <100> as the gate electrode with a 300 nm thick layer of thermally grown SiO_2 as the gate dielectric which has a capacitance of approximately 1.15 x 10^{-4} F/m^2. Au source and drain contacts (50 nm of Au contacts with 3 nm of Cr as the adhesion layer) with a fixed channel size (50 μm in length and 2 mm in width) were deposited via E-beam evaporator onto the SiO_2 layer using a photolithography lift-off process. Prior to deposition of polymer semiconductors, the devices were cleaned by sonication in acetone for 30 min and subsequently rinsed sequentially with acetone, methanol and isopropanol, followed by drying under a flow of nitrogen. The SiO_2 surface was pretreated by exposing the devices to UV/ozone for 30 min followed by immersion into a 2.54 x 10^{-3} M (1 μL / mL) solution of OTS-18 in anhydrous toluene overnight inside a nitrogen-filled glovebox. The devices were then cleaned by sonication in toluene for 10 min, followed by rinsing with acetone, methanol and isopropanol, and drying under a flow of nitrogen. The H_2O contact angle for SiO_2 surface after OTS-18 treatment is in the range of 95–105°. For spin-coated films, a hot polymer solution (5-6 mg/mL in ODCB) was spin-

coated onto OTS-18 pretreated FET substrates at 1500 rpm for 1 min inside glovebox. Drop-cast films on OTS-18 pretreated FET substrates were prepared using a hot solution (5-6 mg/mL in ODCB) inside glovebox. The resulting OFET devices were solvent-annealed in Petri dishes containing few drops of ODCB for 2 days inside glovebox. The thermal annealing treatments for **pTBTD** based OFETs were conducted on a hotplate with temperature setting at 100, 150, 200, 250, 300, and 350 °C inside a glovebox filled with N_2. Each thermal annealing treatment lasted for 30 min, followed by rapidly cooling to room temperature.

All OFET characterizations were performed using a probe station inside a nitrogen filled glovebox using an Agilent 4155C semiconductor parameter analyzer. The FET mobilities were calculated from the saturation regime (V_{SD} = –80 V) in the transfer plots of V_G versus I_{SD} by extracting the slope of the linear range of V_G vs. $I_{SD}^{1/2}$ plot and using the following equation:

$$\left.\frac{\partial I_{SD}^{1/2}}{\partial V_G}\right|_{V_{SD}} = \left(\mu_h C_{ox}(\frac{W}{2L})\right)^{1/2} \qquad \text{Eq. S3.3}$$

where I_{SD} and V_{SD} are the source-drain current (A) and source-drain voltage (V), respectively; V_G is the gate voltage (V) scanning from 35 to –10, –20 and –80 V in the transfer plot; C_{ox} is the capacitance per unit area of the gate dielectric layer, 1.15 x 10^{-4} F/m^2; W and L refer to the channel length (50 μm) and width (2 mm); μ_h represents the hole mobility in the saturation regime (cm^2/Vs).

In the following equation:

$$I_{SD} = \mu_h C_{ox} (\frac{W}{2L})(V_G - V_T)^2 \qquad \text{Eq. 3.4}$$

the threshold voltage, V_T, was calculated by extrapolating $V_T = V_G$ at $I_{SD} = 0$ in the V_G vs. $I_{SD}^{1/2}$ curve in the saturation regime (V_{SD} = –80 V). Current on and off ratio, $I_{ON/OFF}$, was determined through dividing maximum I_{SD} (I_{ON}) by the minimum I_{SD} at around V_G = 0 ~ 35 V (I_{OFF}).

Table S3.1. Hole-transport properties of **TBTD** polymers based OFET devices [a].

Samples	Annealing temp / °C	Film processing	Hole mobility ($cm^2V^{-1}s^{-1}$)		$I_{ON/OFF}$	$V_{TH,avg}$ / V
			Avg	Max		
pTBTD-5DH(H)	n/a	spin-coat	1.02	1.34	10^4-10^6	11.7
	100	spin-coat	0.86	1.1	10^5-10^7	23.4
	150	spin-coat	1.28	1.53	10^5-10^6	24.1
	200	spin-coat	1.63	1.98	10^6-10^8	21.3
	250	spin-coat	1.59	1.96	10^6-10^8	18.6
	300	spin-coat	2.32	2.95	10^5-10^6	12.8
pTBTD-5DH	n/a	spin-coat	0.62	0.68	10^5-10^7	-13.2
		drop-cast	0.43	0.62	10^5-10^6	-0.5
	100	spin-coat	0.76	1.01	10^5-10^6	7.7
		drop-cast	0.55	0.76	10^5-10^6	4.9
	150	spin-coat	0.99	1.5	10^4-10^6	13.1
		drop-cast	0.64	0.87	10^4-10^6	8.9
	200	spin-coat	0.84	1.08	10^4-10^6	11.3
		drop-cast	0.63	0.9	10^5-10^7	4.8

	250	spin-coat	0.87	1.24	10^6-10^6	9.4
		drop-cast	0.57	0.85	10^4-10^6	-5.5
	300	spin-coat	1.74	2	10^5-10^6	13.1
		drop-cast	1.06	1.21	10^5-10^7	5.4
pTBTD-2DT	n/a	spin-coat	0.49	0.77	10^6-10^6	8.8
		drop-cast	0.32	0.48	10^5-10^7	-21.4
	100	spin-coat	0.44	0.67	10^5-10^7	22.3
		drop-cast	0.29	0.33	10^5-10^6	0.2
	150	spin-coat	0.46	0.61	10^6-10^7	19.9
		drop-cast	0.27	0.36	10^5-10^7	2.4
	200	spin-coat	0.39	0.58	10^5-10^6	14.6
		drop-cast	0.24	0.32	10^4-10^7	9.2
	250	spin-coat	0.5	0.6	10^5-10^6	4.2
		drop-cast	0.26	0.32	10^5-10^7	-10.9
	300	spin-coat	0.4	0.54	10^6-10^7	-2.7
		drop-cast	0.4	0.81	10^5-10^7	-7
pTBTD-OD	n/a	spin-coat	0.05	0.07	10^4-10^5	7.3
		drop-cast	0.04	0.06	10^3-10^5	6.4
	100	spin-coat	0.08	0.1	10^5-10^5	18.9
		drop-cast	0.06	0.08	10^4-10^6	10.7
	150	spin-coat	0.08	0.1	10^4-10^5	11.3
		drop-cast	0.06	0.07	10^5-10^6	4.7
	200	spin-coat	0.11	0.15	10^3-10^5	-1
		drop-cast	0.08	0.12	10^5-10^6	1.8
	250	spin-coat	0.25	0.42	10^6-10^6	9.9
		drop-cast	0.11	0.19	10^4-10^7	2.5

300	spin-coat	0.3	0.34	10^6-10^7	7
	drop-cast	0.16	0.27	10^4-10^6	-4.6

[a] Characterization results were based on 5 – 8 of devices for each fabrication conduction.

Synthetic Details

All reactions were carried out under an argon atmosphere using a standard Schlenk line technique. The synthetic procedures for the preparation of 11-(4-bromobutyl)tricosane (**5**), 3,6-di(thiophen-2-yl)pyrrolo[3,4-c]pyrrole-1,4(2H,5H)-dione (**6**), 2,5-bis(2-decyltetradecyl)-3,6-di(thiophen-2-yl)pyrrolo[3,4-c]pyrrole-1,4(2H,5H)-dione (**7b**), 3,6-bis(5-bromothiophen-2-yl)-2,5-bis(2-decyltetradecyl)pyrrolo[3,4-c]pyrrole-1,4(2H,5H)-dione (**10**), and 4,7-bis(3'-dodecyl-[2,2'-bithiophen]-5-yl)benzo[c][1,2,5]thiadiazole (**BT4**), were modified from published literatures.[2-6]

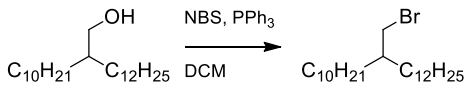

1 2

11-(bromomethyl)tricosane (2): Br_2 (6.39 mL, 0.125 mol, 1.05 eq.) was added to a solution of triphenylphosphine (32.7 g, 0.125 mol, 1.05 eq.) in anhydrous CH_2Cl_2 (110 mL) at 0 °C to form a pale yellow slurry. A solution of alcohol **1** (10 mL, 0.12 mol, 1.0 eq.) in CH_2Cl_2 was added dropwise at 0 °C via an addition funnel. The resulting mixture was stirred at room temperature overnight to give an orange solution. The organic solvent was evaporated under reduced pressure. The solid residue was extracted with hexane (3 x 50 mL). The organic solution was filtered, washed with brine (3 x 50 mL), dried over anhydrous $MgSO_4$, and concentrated under reduced pressure. The resulting orange oil

was purified by column chromatography (silica gel, hexane, TLC chromatography was stained with iodine), to afford **2** as a colorless oil (yield: 80%). ^{1}H NMR (400 MHz, $CDCl_3$) δ 3.45 (d, *J* = 4.8 Hz, 2H), 1.59 (s, 1H), 1.41–1.18 (m, 40H), 0.88 (t, *J* = 6.9 Hz, 6H). ^{13}C NMR (101 MHz, $CDCl_3$) δ 39.60, 39.50, 32.56, 31.91, 29.78, 29.68, 29.67, 29.65, 29.63, 29.59, 29.36, 29.34, 26.55, 22.68, 14.09. EI-MS (m/z): 337.3 [M^+–Br]; HRMS: [M^+–H] calcd for $C_{24}H_{48}Br$, 415.2939; found, 415.2950, Δ = 2.6 ppm.

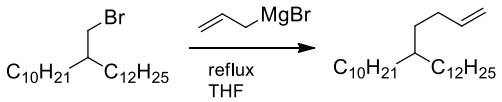

2 **3**

11-(but-3-en-1-yl)tricosane (3): Bromoalkane**2** (6.0 g, 14.4 mmol, 1.0 eq.) was dissolved in freshly distilled THF (14 mL). The resulting solution was purged by argon for 30 min, followed by the addition of additional THF (14 mL). Allylmagnesium bromide (7.55 mL of a 2.0 M solution in THF, 15.12 mmol, 1.05 eq.) was added and the resulting solution was heated at reflux for 24 h. D.I. water (15 mL) and sulfuric acid (30 mL of 10 wt%) were then added dropwise . The organic phase was extracted by Et_2O (3 x 30 mL). The organic extracts were washed with brine (3 x 50 mL). The resulting solution was dried over anhydrous $MgSO_4$, and concentrated under reduced pressure. The crude product was purified by column chromatography (silica gel, hexane, TLC chromatography was stained with iodine), to afford **2** colorless oil (yield: 75%). ^{1}H NMR

(400 MHz, $CDCl_3$) δ 5.81 (m, 1H), 5.04–4.87 (m, 2H), 2.07–1.95 (m, 2H), 1.37–1.13 (m, 43H), 0.88 (t, *J* = 6.9 Hz, 6H). ^{13}C NMR (101 MHz, $CDCl_3$) δ 139.60, 113.83, 36.91, 33.49, 32.95, 31.91, 31.06, 30.11, 29.69, 29.65, 29.35, 26.59, 22.68, 14.10. (Note: some peaks relating to carbon atoms on alkyl chains overlap in the ^{13}C NMR spectrum). EI-MS (m/z): 378.4 [M^+]; HRMS: [M^+] calcd for $C_{27}H_{54}$, 378.4226; found, 378.4221, Δ = -1.3 ppm.

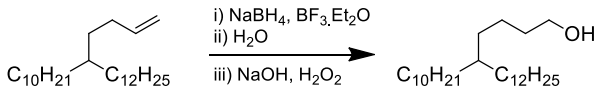

3 **4**

5-decylheptadecan-1-ol (4): $NaBH_4$ (0.65 g, 17.10 mmol, 0.46 eq.) was added to a solution of alkene **3** (14.00 g, 37.00 mmol, 1.00 eq.) in diglyme (34 mL). The mixture was stirred at room temperature until most of the $NaBH_4$ had dissolved (around 20 min). $BF_3.Et_2O$ (≥ 46.5%, BF_3 basis) was added dropwise through an addition funnel at 0 ˚C. The resulting mixture was stirred at room temperature for 2 h. D.I. water (2 mL) was added dropwise to quench $NaBH_4$ and BF_3. Aqueous NaOH (9.95 mL, of a 5 M solution, 49 mmol, 1.32 eq.) was added, followed by the dropwise addition of H_2O_2 (15.10 mL of a 30 wt% solution, 148.00 mmol, 4.00 eq.) through an addition funnel at 20 ºC. The resulting mixture was stirred at room temperature overnight, and poured to water (50 mL). The organic phase was extracted by Et_2O (3 x 30 mL). The organic extracts were

washed with saturated aqueous $NaHCO_3$ (4 x 50 mL) and brine (4 x 50 mL) to remove most of the diglyme. The resulting solution was dried over anhydrous $MgSO_4$, and concentrated under reduced pressure. The crude product was purified by column chromatography (silica gel, hexane/EtOAc, 8:1, v/v, TLC chromatography was stained with *p*-anisaldehyde.), to afford **4** as a colorless oil (yield: 75%). ^{1}H NMR (400 MHz, $CDCl_3$) δ 3.65 (t, J = 6.6 Hz, 2H), 1.60–1.49 (m, 4H), 1.37–1.14 (m, 43H), 0.88 (t, J = 6.8 Hz, 6H). ^{13}C NMR (101 MHz, $CDCl_3$) δ 63.10, 37.39, 33.60, 33.50, 33.28, 31.92, 30.13, 29.71, 29.71, 29.65, 29.35, 26.69, 22.87, 22.67, 14.09. (Note: some peaks relating to carbon atoms on alkyl chains overlap in ^{13}C NMR spectrum). EI-MS (m/z): 395.5 [M^+ - H]; HRMS: [M^+ - H] calcd for $C_{27}H_{55}O$, 395.4253; found, 395.4251, Δ = -0.5 ppm.

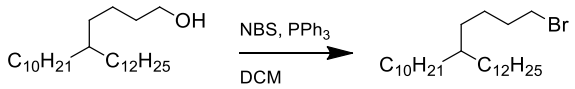

4 5

11-(4-bromobutyl)tricosane (5): PPh_3 (8.9 g, 34.5 mmol, 1.5 eq.) was added to a solution of alcohol **4** (9.0 g, 23.0 mmol, 1.0 eq.) in anhydrous CH_2Cl_2 (23 mL). The resulting solution was purged with argon for 30 min, followed by the addition of additional DCM (30 mL). NBS (7.27 g, 41.4 mmol, 1.8 eq.) was slowly added in the dark at 0 ˚C. The mixture was stirred at 0 °C for 30 min, allowed to warm to room temperature, and stirred at room temperature overnight. The resulting dark purple mixture

was extracted into CH_2Cl_2 (50 mL). The organic solvent was removed under reduced pressure. The solid residue was extracted with hexane (3 x 50 mL). The organic extracts were washed with brine (3 x 50 mL), dried over anhydrous $MgSO_4$, and concentrated under reduced pressure. The resulting brown oil was purified by column chromatography (silica gel, hexane), to afford colorless oil (yield: 80%). ^{1}H NMR (400 MHz, $CDCl_3$) δ 3.41 (t, J = 6.9 Hz, 2H), 1.88–1.79 (m, 2H), 1.44–1.34 (m, 2H), 1.34–1.17 (m, 43H), 0.88 (t, J = 6.9 Hz, 6H). ^{13}C NMR (101 MHz, $CDCl_3$) δ 37.24, 34.00, 33.55, 33.26, 32.74, 31.92, 30.10, 29.69, 29.65, 29.35, 26.64, 25.30, 22.68, 14.10. (Note: some peaks relating to carbon atoms on alkyl chains overlap in ^{13}C NMR spectrum). EI-MS (m/z): 459.3 [M^+]; HRMS: [M^+ - H] calcd for $C_{27}H_{54}Br$, 457.3409; found, 457.3423, Δ = 3.1 ppm.

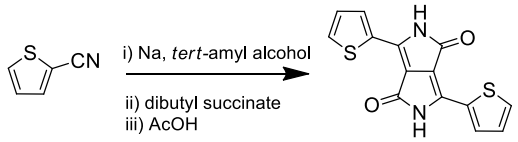

6

3,6-di(thiophen-2-yl)pyrrolo[3,4-c]pyrrole-1,4(2H,5H)-dione (6): Sodium (4.2 g, 185.0 mmol, 5.0 eq.) was cut into pieces and added into anhydrous *tert*-amyl alcohol (120 mL) under argon. The mixture was heated to 110 °C overnight, during which the sodium reacted. 2-Thiophenecarbonitrile (10.0 g, 92.0 mmol, 1.0 eq.) was added, followed by the dropwise addition of dibutyl succinate (8.4 g, 37.0 mmol, 1.0 eq.) at 110 °C. The resulting dark purple mixture was stirred at 110 °C for 7 h, before cooling down to 50 °C.

AcOH (11.6 mL, 203.5 mmol, 5.5 eq.) was then added. The mixture was heated at 100 °C for 30 min, before cooling down to room temperature. The resulting mixture was poured into MeOH (300 mL) and stirred for 1 h at room temperature. The precipitated dark red-purple residue was collected by filtration, and washed with MeOH (5 x 100 mL) and D.I. water (5 x 100 mL) to afford **6** as a dark red-purple solid. ^{1}H NMR (400 MHz, DMSO-d_6) δ 8.19 (dd, J = 3.8, 1.2 Hz, 2H), 7.94 (dd, J = 5.0, 1.1 Hz, 2H), 7.28 (dd, J = 5.0, 3.8 Hz, 2H). ^{13}C NMR (101 MHz, DMSO-d6) δ 162.07, 136.60, 133.11, 131.72, 131.24, 129.16, 109.00. EI-MS (m/z): 300.0 [M^+]; HRMS: [M^+] calcd for $C_{14}H_8N_2O_2S_2$, 300.0027; found, 300.0029, Δ = 0.7 ppm.

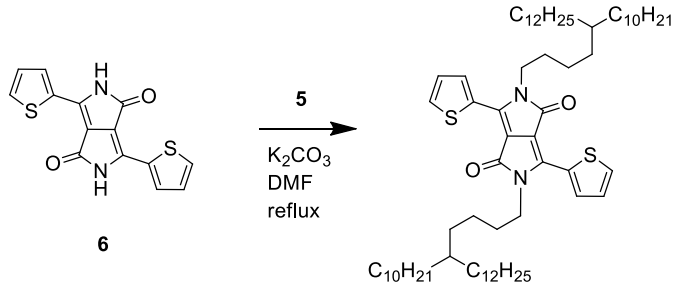

2,5-bis(5-decylheptadecyl)-3,6-di(thiophen-2-yl)pyrrolo[3,4-c]pyrrole-1,4(2H,5H)-dione (7a): 5 (3.60 g, 7.83 mmol, 2.35 eq.) was added into the mixture of **6** (1.00 g, 3.33 mmol, 1.00 eq.) and pre-dried K_2CO_3 (1.40 g, 5.00 mmol, 3.00 eq.) in DMF (55 mL) under argon. The mixture was heated at reflux for 24 h, before cooling to room temperature. D.I. H_2O (100 mL) was added and the mixture was extracted into $CHCl_3$ (50

mL). The organic solution was washed with brine (8 x 50 mL), dried over anhydrous $MgSO_4$, and concentrated under reduced pressure. The resulting dark residue was purified by column chromatography (silica gel, hexane/DCM, 1:1 v/v). The product was recrystallized from isopropanol to afford **7a** as a purple solid (yield: 83%). ^{1}H NMR (400 MHz, $CDCl_3$) δ 8.93 (dd, J = 3.9, 1.2 Hz, 2H), 7.63 (dd, J = 5.0, 1.2 Hz, 2H), 7.28 (dd, J = 5.0, 3.9 Hz, 2H), 4.07 (t, J = 8.0 Hz, 4H), 1.77–1.66 (m, 4H), 1.43–1.15 (m, 90H), 0.87 (t, J = 6.8 Hz, 12H). ^{13}C NMR (101 MHz, $CDCl_3$) δ 161.32, 139.98, 135.23, 130.58, 129.77, 128.57, 107.68, 42.26, 37.29, 33.55, 33.27, 30.35, 30.13, 29.71, 29.65, 29.35, 26.66, 24.04, 22.68, 14.10. (Note: some peaks relating to carbon atoms on alkyl chains overlap in ^{13}C NMR spectrum). EI-MS (m/z): 1057.9 [M^+]; HRMS: [M^+] calcd for $C_{68}H_{116}N_2O_2S_2$, 1056.8478; found, 1056.8555, Δ = 7.3 ppm.

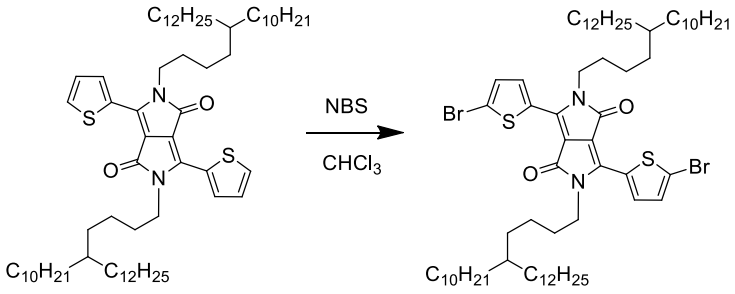

7a M1a

3,6-bis(5-bromothiophen-2-yl)-2,5-bis(5-decylheptadecyl)pyrrolo[3,4-c]pyrrole-1,4(2H,5H)-dione (M1a): NBS (280 mg, 1.60 mmol, 2.10 eq.) was added slowly into the solution of **7a** (800 mg, 0.76 mmol, 1.00 eq.) in $CHCl_3$ (38 mL) under argon. The

resulting mixture was stirred in the dark at 0 °C for 2 h, followed by stirring at room temperature overnight. The mixture was dissolved into $CHCl_3$ (30 mL), washed with brine (3 x 30 mL), dried over anhydrous $MgSO_4$, and concentrated under reduced pressure. The resulting dark residue was purified by column chromatography (silica gel, hexane/$CHCl_3$, 1:1, v/v), and further recrystallized from isopropanol to afford **M1a** as a purple solid (yield: 80%). ^{1}H NMR (400 MHz, $CDCl_3$) δ 8.69 (d, J = 4.2 Hz, 2H), 7.23 (d, *J* = 4.2 Hz, 2H), 3.98 (t, *J* = 8.0 Hz, 4H), 1.74–1.61 (m, 4H), 1.44–1.04 (m, 90H), 0.87 (t, *J* = 6.8 Hz, 12H). ^{13}C NMR (101 MHz, $CDCl_3$) δ 160.97, 138.95, 135.33, 131.61, 131.10, 119.10, 107.78, 42.30, 37.24, 33.54, 33.23, 31.92, 30.37, 30.14, 29.71, 29.70, 29.66, 29.35, 26.65, 24.00, 22.68, 14.11. (Note: some peaks relating to carbon atoms on alkyl chains overlap in ^{13}C NMR spectrum). EI-MS (m/z): 1215.7 [M^+]; HRMS: [M^+] calcd for $C_{68}H_{114}N_2O_2S_2Br_2$, 1212.6688; found, 1212.6723, Δ = 2.9 ppm.

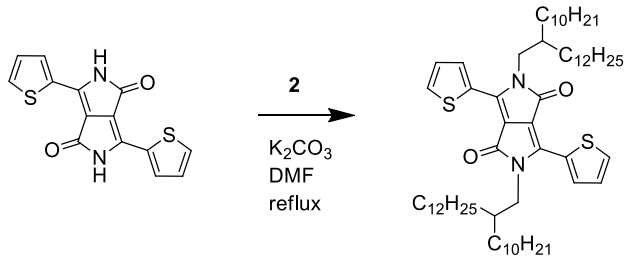

2,5-bis(2-decyltetradecyl)-3,6-di(thiophen-2-yl)pyrrolo[3,4-c]pyrrole-1,4(2H,5H)-dione (7b): 2 (3.9 g, 9.30 mmol, 2.80 eq.) was added into the mixture of **6** (1.00 g, 3.33

mmol, 1.00 eq.) and pre-dried K_2CO_3 (1.40 g, 5 mmol, 3.00 eq.) in DMF (47 mL) under argon. The mixture was heated at reflux for 24 h, before cooling to room temperature. D.I. H_2O (100 mL) was added and the mixture was extracted into $CHCl_3$ (50 mL). The organic solution was washed with brine (8 x 50 mL), dried over anhydrous $MgSO_4$, and concentrated under reduced pressure. The resulting dark residue was purified by column chromatography (silica gel, hexane/ethyl acetate, 100:5, v/v). The product was recrystallized from isopropanol, to afford **7b** as dark-red solid (yield: 30%). ^{1}H NMR (400 MHz, $CDCl_3$) δ 8.87 (dd, *J* = 3.9, 1.0 Hz, 2H), 7.62 (dd, *J* = 5.0, 1.1 Hz, 2H), 7.26 (dd, *J* = 3.9, 5.0 Hz, 2H), 4.02 (d, *J* = 7.7 Hz, 4H), 1.90 (m, 2H), 1.36–1.12 (m, 80H), 0.87 (t, *J* = 6.9 Hz, 6H), 0.87 (t, *J* = 6.9 Hz, 6H). ^{13}C NMR (101 MHz, $CDCl_3$) δ 161.72, 140.39, 135.17, 130.41, 129.82, 128.35, 107.92, 46.21, 37.72, 31.92, 31.91, 31.18, 30.00, 29.68, 29.66, 29.65, 29.63, 29.61, 29.54, 29.35, 29.34, 26.20, 22.68, 14.11. (Note: some peaks relating to carbon atoms on alkyl chains overlap in ^{13}C NMR spectrum). EI-MS (m/z): 973.7 [M^+]; HRMS: [M^+] calcd for $C_{62}H_{104}N_2O_2S_2$, 972.7539; found, 972.7523, Δ = -1.6 ppm.

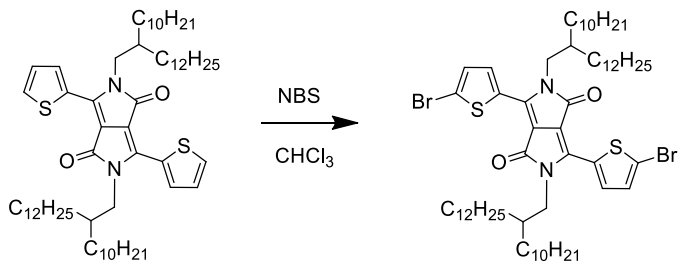

7b **M1b**

3,6-bis(5-bromothiophen-2-yl)-2,5-bis(2-decyltetradecyl)pyrrolo[3,4-c]pyrrole-1,4(2H,5H)-dione (M1b): NBS (160 mg, 0.90 mmol, 2.18 eq.) was added slowly into the solution of **7b** (400 mg, 0.41 mmol, 1.00 eq.) in $CHCl_3$ (16 mL) under argon. The resulting mixture was stirred in the dark overnight at room temperature. The mixture was dissolved into CH_2Cl_2 (20 mL), washed with brine (3 x 30 mL), dried over anhydrous $MgSO_4$, and concentrated under reduced pressure. The resulting dark residue was purified by column chromatography (silica gel, hexane/$CHCl_3$, 3:2, v/v), and further recrystallized from isopropanol, to afford **M1b** as a purple solid (yield: 75%). ^{1}H NMR (400 MHz, $CDCl_3$) δ 8.62 (d, J = 4.2 Hz, 2H), 7.21 (d, J = 4.2 Hz, 2H), 3.92 (d, J = 8.0 Hz, 4H), 1.87 (m, 2H), 1.34–1.13 (m, 80H), 0.87 (t, J = 6.8, 6H), 0.87 (t, J = 6.8, 6H). ^{13}C NMR (101 MHz, $CDCl_3$) δ 161.36, 139.36, 135.29, 131.40, 131.15, 118.92, 107.99, 46.33, 37.75, 31.92, 31.91, 31.17, 29.97, 29.70, 29.67, 29.65, 29.63, 29.54, 29.36, 29.34, 26.17, 22.68, 14.11. (Note: some peaks relating to carbon atoms on alkyl chains overlap in ^{13}C NMR spectrum). EI-MS (m/z): 1131.6 [M^+]; HRMS: [M^+] calcd for $C_{62}H_{102}N_2O_2S_2Br_2$, 1128.5749; found, 1128.5857, Δ = 9.6 ppm.

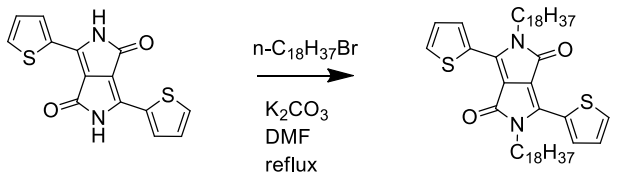

6 7c

2,5-dioctadecyl-3,6-di(thiophen-2-yl)pyrrolo[3,4-c]pyrrole-1,4(2H,5H)-dione (7c): 1-bromooctadecane (1.44 g, 4.30 mmol, 2.60 eq.) was added into the mixture of **6** (0.50 g, 1.66 mmol, 1.00 eq.) and pre-dried K_2CO_3 (1.40 g, 5.00 mmol, 3.00 eq.) in DMF (33 mL) under argon. The mixture was heated at reflux for 24 h, before cooling to room temperature. D.I. H_2O (100 mL) was added and the mixture was extracted into $CHCl_3$ (30 mL). The organic solution was washed with brine (8 x 50 mL), dried over anhydrous $MgSO_4$, and concentrated under reduced pressure. The resulting dark residue was purified by column chromatography (silica gel, hexane/$CHCl_3$, 1:3, v/v). The product was recrystallized from isopropanol, to afford **7c** as a purple solid (yield: 85%). ^{1}H NMR (400 MHz, $CDCl_3$) δ 8.92 (dd, J = 3.9, 1.2 Hz, 2H), 7.63 (dd, J = 5.0, 1.1 Hz, 2H), 7.28 (dd, J = 5.0, 3.9 Hz, 2H), 4.07 (t, J = 8.0 Hz, 4H), 1.79–1.68 (m, 4H), 1.35–1.15 (m, 60H), 0.88 (t, J = 6.8 Hz, 6H). ^{13}C NMR (101 MHz, $CDCl_3$) δ 161.35, 140.00, 135.22, 130.63, 129.77, 128.57, 107.68, 42.21, 31.91, 29.94, 29.68, 29.64, 29.62, 29.55, 29.51, 29.34, 29.23, 26.86, 22.67, 14.10. (Note: some peaks relating to carbon atoms on alkyl chains

overlap in ^{13}C NMR spectrum). EI-MS (m/z): 805.5 [M^+]; HRMS: [M^+ - H] calcd for $C_{50}H_{80}N_2O_2S_2$, 804.5661; found, 804.5676, Δ = 1.9 ppm.

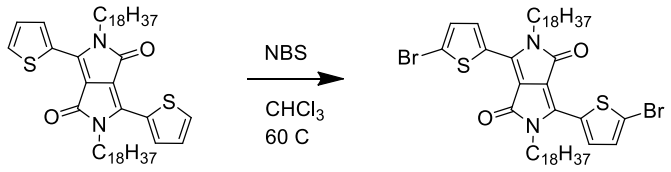

7c **M1c**

3,6-bis(5-bromothiophen-2-yl)-2,5-dioctadecylpyrrolo[3,4-c]pyrrole-1,4(2H,5H)-dione (M1c): NBS (75 mg, 0.42 mmol, 2.25 eq.) was added into the solution of **7c** (150 mg, 0.19 mmol, 1.00 eq.) in $CHCl_3$ (35 mL) under argon. The resulting mixture was stirred in the dark overnight at 60 °C. After cooling to room temperature, the mixture was poured to MeOH (200 mL) and stirred for 2 h. The precipitated dark powders were collected by filtration; and then purified by column chromatography (silica gel, hexane/$CHCl_3$, 1:2, v/v) (*note: hexane/$CHCl_3$ needs to be warmed to dissolve crude **M1c** before adding to column*), to afford **M1c** as a purple solid (yield: 90%). ^1H NMR (400 MHz, $CDCl_3$) δ 8.68 (d, *J* = 4.2 Hz, 2H), 7.23 (d, *J* = 4.2 Hz, 2H), 3.98 (t, *J* = 8.0 Hz, 4H), 1.70 (m, 4H), 1.36–1.20 (m, 60H), 0.87 (t, *J* = 6.9 Hz, 6H). EI-MS (m/z): 963.4 [M^+]; HRMS: [M^+] calcd for $C_{50}H_{78}N_2O_2S_2Br_2$, 960.3871; found, 960.3901, Δ = 3.1 ppm.

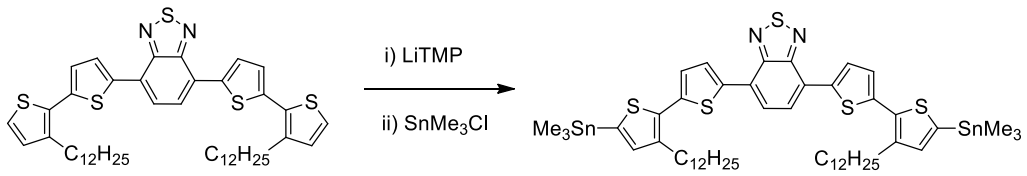

BT4 **M2**

4,7-bis(3'-dodecyl-5'-(trimethylstannyl)-[2,2'-bithiophen]-5yl)benzo[c][1,2,5]thiadiazole (M2): 2,2,6,6-tetramethylpiperidine (0.08 mL, 0.48 mmol, 3.84 eq.) in THF (0.5 mL) was cooled to -78 ˚C under argon, followed by the dropwise addition of *n*-butyllithium (0.16 mL of a 2.5 M solution in hexane, 0.40 mmol, 3.20 eq.). The resulting solution was stirred at -78 °C for 30 min, and was warmed to room temperature and stirred for 20 min, to afford lithium 2,2,6,6-tetramethylpiperidide (LTMP). It was subsequently cooled down to -78 ˚C. **BT4** (100 mg, 0.13 mmol, 1.00 eq.) in THF (1.8 mL) was added in a dropwise manner. After stirring at -78 ˚C for 1 h, $SnMe_3Cl$ (0.43 mL of a 1.0 M solution in THF, 0.44 mmol, 3.50 eq.) was added in a dropwise manner. The resulting solution was then warmed to room temperature and stirred for 12 h. After poured into D.I. H_2O (50 mL), the mixture was extracted into CH_2Cl_2 (3 x 15 mL), washed with brine (3 x 15 mL), dried over anhydrous $MgSO_4$, and concentrated under reduced pressure. The final product was washed with methanol (3 x 20 mL) and isolated **M2** as a purple gel. ^{1}H NMR (300 MHz, $CDCl_3$) δ 8.12 (d, J = 3.9 Hz, 2H), 7.85 (s, 2H), 7.20 (d, J = 3.9 Hz, 2H), 7.03 (s, 2H), 2.86 (t, J = 7.8 Hz, 4H), 1.70 (m, 4H), 1.46–1.15 (m, 36H), 0.86 (t, J = 6.7 Hz, 6H), 0.40 (s, 18H).

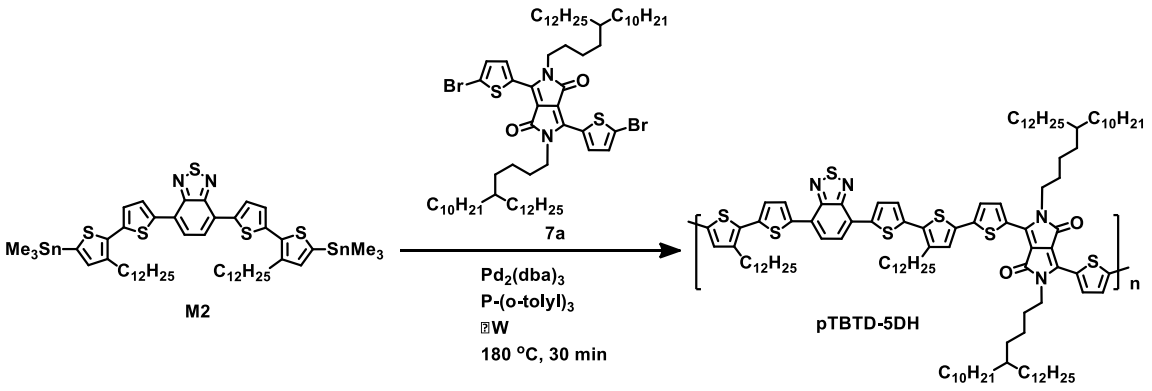

pTBTD-5DH: Monomers **M2** (118.2 mg, 0.11 mmol, 1.00 eq.) and **7a** (127 mg, 0.11 mmol, 1.00 eq.), and P(o-tolyl)$_3$ (12 mg, 0.04 mmol, 0.36 eq.), were placed in a microwave irradiation tube (10 mL). $Pd_2(dba)_3$ (3.9 mg, 4 μmol, 0.04 eq.) was added and the irradiation tube was then degassed and refilled with argon in sequence. PhCl (1.05 mL) was added, followed by a 3 cycles of freeze-pump-thaw. The resulting mixture was stirred at 180 °C under microwave irradiation for 30 min. The resulting dark slurry was dispersed in chloroform (20 mL) and the solution was poured into aqueous sodium diethyldithiocarbmate solution (100 mL of a solution containing 1g in 100 mL of D.I. water). The resulting mixture was stirred at 66 °C for 2 h to remove Pd. The organic solution was collected and concentrated under reduced pressure. The concentrated solution was added dropwise to methanol (300 mL). The precipitated solid was collected by filtration and purified by Soxhlet extraction sequentially using methanol (24 h), acetone (24 h), ethyl acetate (12 h), hexane (24 h), and $CHCl_3$ (2 h). The $CHCl_3$ solution was collected and then concentrated under reduced pressure. The concentrated solution was added in a dropwise manner to methanol (200 mL). The precipitate was collected by

filtration and dried under vacuum at room temperature for 12 h to afford **pTBTD-5DH** as a black solid (135 mg, yield: 70%). The residue left inside the Soxhlet extraction thimble was dissolved in ODCB, which was added dropwise to methanol (200 mL). The precipitate was collected by filtration and dried under vacuum at room temperature for 12 h to afford **pTBTD-5DH(H)** as a black solid (41 mg, yield: 20%). Elemental analysis. Calculated for $C_{114}H_{172}N_4O_2S_7$: C, 73.81 %; H, 9.35 %; N, 3.02 %; S, 12.10 %. Found: C, 72.45 %; H, 9.51 %; N, 2.91 %; S, 11.60 %.

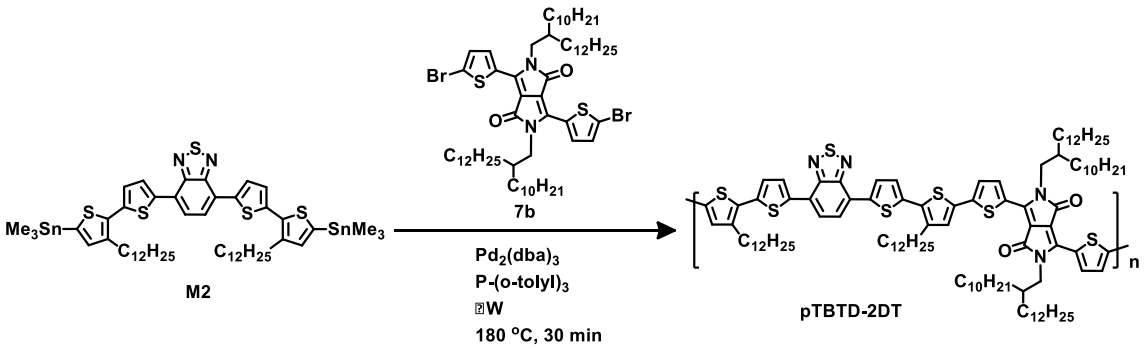

pTBTD-2DT: Monomer **M2** (129.1 mg, 0.12 mmol, 1.00 eq.) and **7b** (130 mg, 0.12 mmol, 1.00 eq.), and P(o-tolyl)$_3$ (13 mg, 0.04 mmol, 0.36 eq.) were placed in a microwave irradiation tube (10 mL). $Pd_2(dba)_3$ (4.2 mg, 4 μmol, 0.04 eq.) was added and the irradiation tube was then degassed and refilled with argon. PhCl (1.15 mL) was added, followed by a 3 cycles of freeze-pump-thaw. The resulting mixture was stirred at 180 °C under microwave irradiation for 30 min. The resulting dark slurry was dispersed in chloroform (20 mL) and the solution was poured into aqueous sodium

diethyldithiocarbmate solution (100 mL of a solution containing 1g in 100 mL of D.I. water). The resulting mixture was stirred at 66 °C for 2 h to remove Pd. The organic solution was collected and concentrated under reduced pressure. The concentrated solution was added dropwise to methanol (300 mL). The precipitated solid was collected by filtration and purified by Soxhlet extraction sequentially using methanol (24 h), acetone (24 h), ethyl acetate (12 h), hexane (24 h), and $CHCl_3$ (2 h). The $CHCl_3$ solution was collected and then concentrated under reduced pressure. The concentrated solution was added in a dropwise manner to methanol (200 mL). The precipitate was collected by filtration and dried under vacuum at room temperature for 12 h to afford **pTBTD-2DT** as a black solid (190 mg, yield: 90%). Elemental analysis. Calculated for $C_{108}H_{160}N_4O_2S_7$: C, 73.25 %; H, 9.11 %; N, 3.16 %; S, 12.67 %. Found: C, 72.45 %; H, 9.16 %; N, 3.05 %; S, 12.31 %.

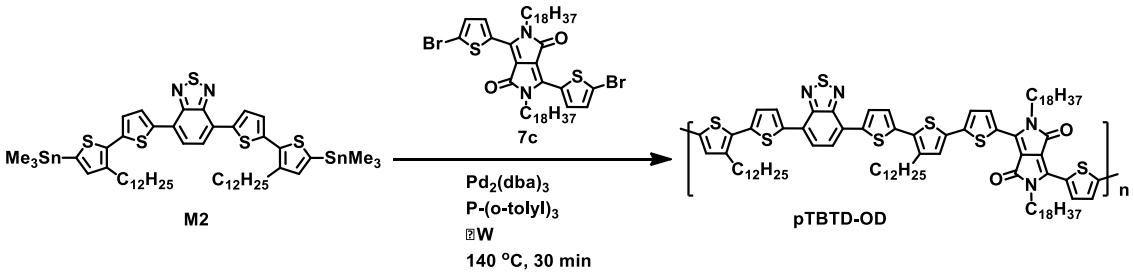

pTBTD-OD: Monomer **M2** (135 mg, 0.12 mmol, 1.00 eq.) and **7c** (115.4 mg, 0.12 mmol, 1.00 eq.), and P(o-tolyl)$_3$ (13.2 mg, 0.04 mmol, 0.36 eq.) were placed in a microwave irradiation tube (10 mL). $Pd_2(dba)_3$ (4.4 mg, 4 μmol, 0.04 eq.) was added and

the irradiation tube was then degassed and refilled with argon. PhCl (1.2 mL) was added, followed by a 3 cycles of freeze-pump-thaw. The resulting mixture was stirred under a 140 °C of microwave irradiation for 30 min. The resulting dark slurry was dispersed in chloroform (20 mL) and poured into aqueous sodium diethyldithiocarbmate solution (100 mL of a solution containing 1g in 100 mL of D.I. water). The resulting mixture was stirred at 66 °C for 2 h to remove Pd. The organic solution was collected and concentrated under reduced pressure. The concentrated solution was added dropwise to methanol (300 mL). The precipitated solid was collected by filtration and then washed by Soxhlet extraction sequentially using methanol (24 h), acetone (24 h), ethyl acetate (12 h), hexane (24 h), $CHCl_3$ (4 h), and PhCl (2 h). The PhCl solution was collected and then concentrated under reduced pressure. The concentrated solution was added in a dropwise manner to methanol (200 mL). The precipitate was collected by filtration and dried under vacuum at room temperature for 12 h to afford **pTBTD-OD** as a black solid (70 mg, yield: 36%). Elemental analysis. Calculated for $C_{96}H_{136}N_4O_2S_7$: C, 71.95 %; H, 8.55 %; N, 3.50 %; S, 14.01 %. Found: C, 69.89 %; H, 8.61%; N, 3.26 %; S, 13.19 %.

Schemes

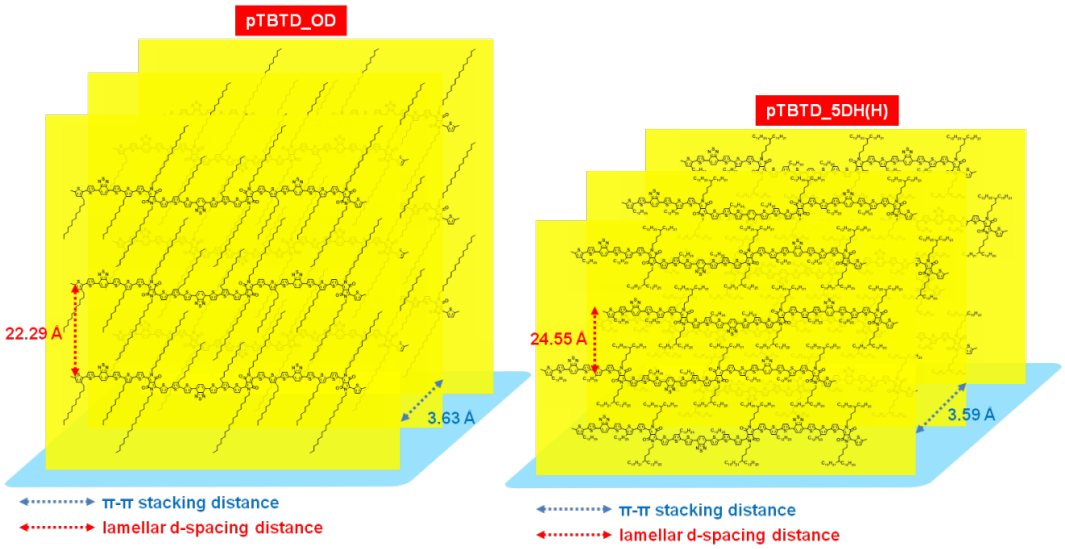

Scheme S4.1 The proposed lamellar structured edge-on orientation of **pTBTD-OD** and **pTBTD-5DH(H)** on SiO_2 substrate. **pTBTD-5DH** and **pTBTD-2DT** follow the same orientation with **pTBTD-5DH(H)**. The alkyl side chain packing of **pTBTD** polymers follows the interdigitated packing model.

Figures.

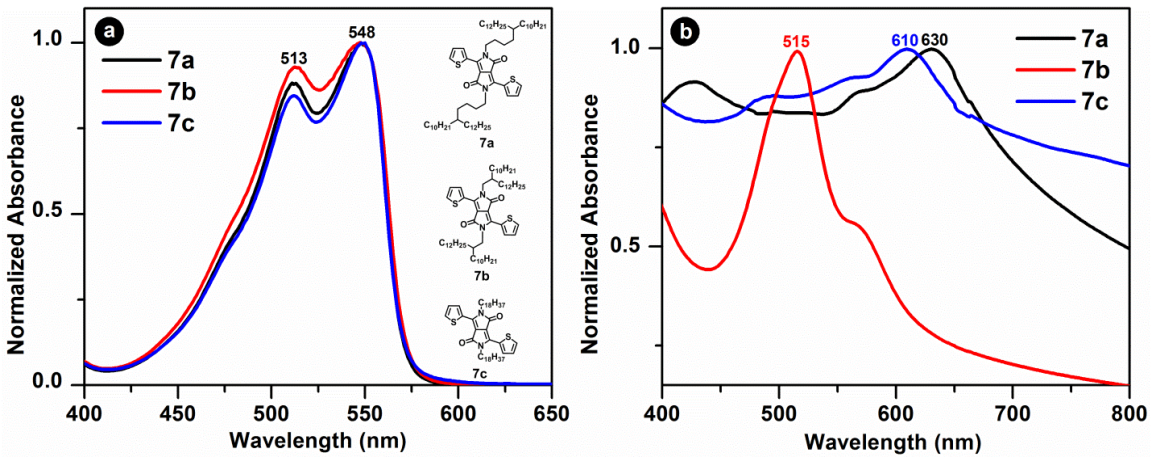

Figure S4.1. Absorption spectra of di(2-thienyl)diketopyrrolopyrrole compounds (**7a-c**): (a) in solution ($CHCl_3$), and (b) thin film.

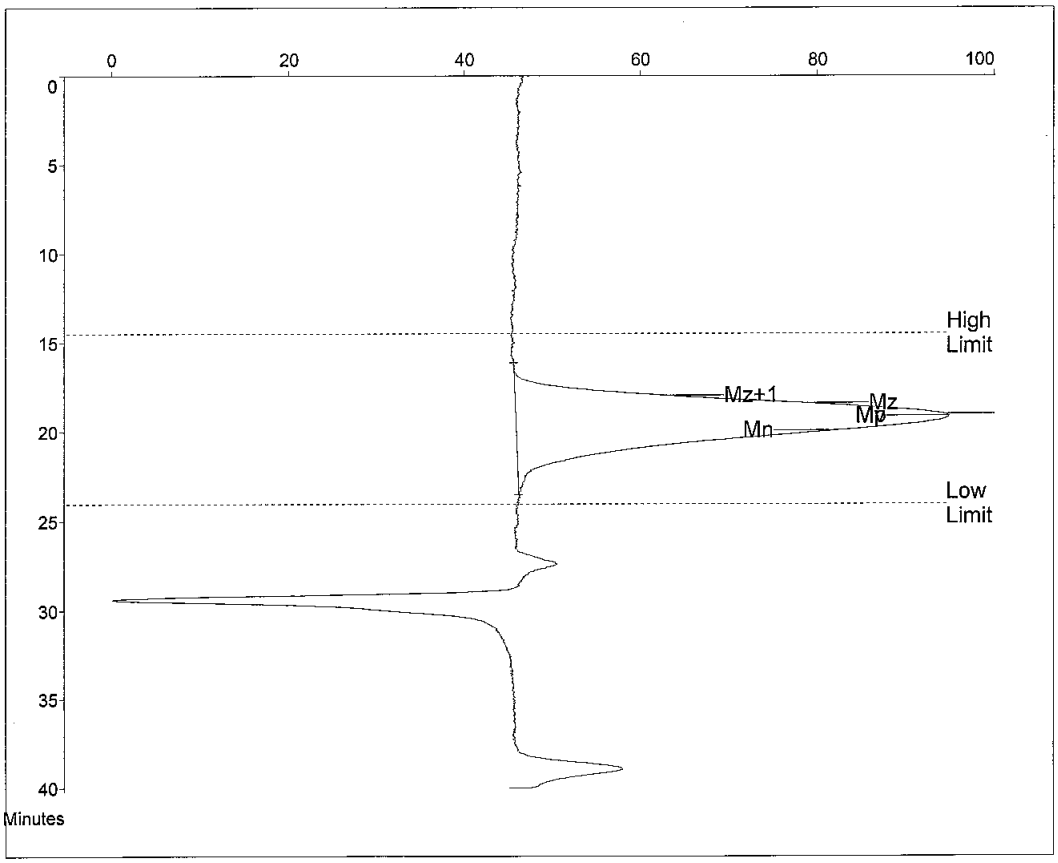

Molecular Weight Averages

Mp =	95501	Mz =	180890
Mn =	44414	Mz+1 =	274357
Mw =	103215	Mv =	92685
Polydispersity =	2.324	Peak Area =	1439735

Figure S4.2a. GPC characterization of **pTBTD-5DH** with TCB under 135 °C.

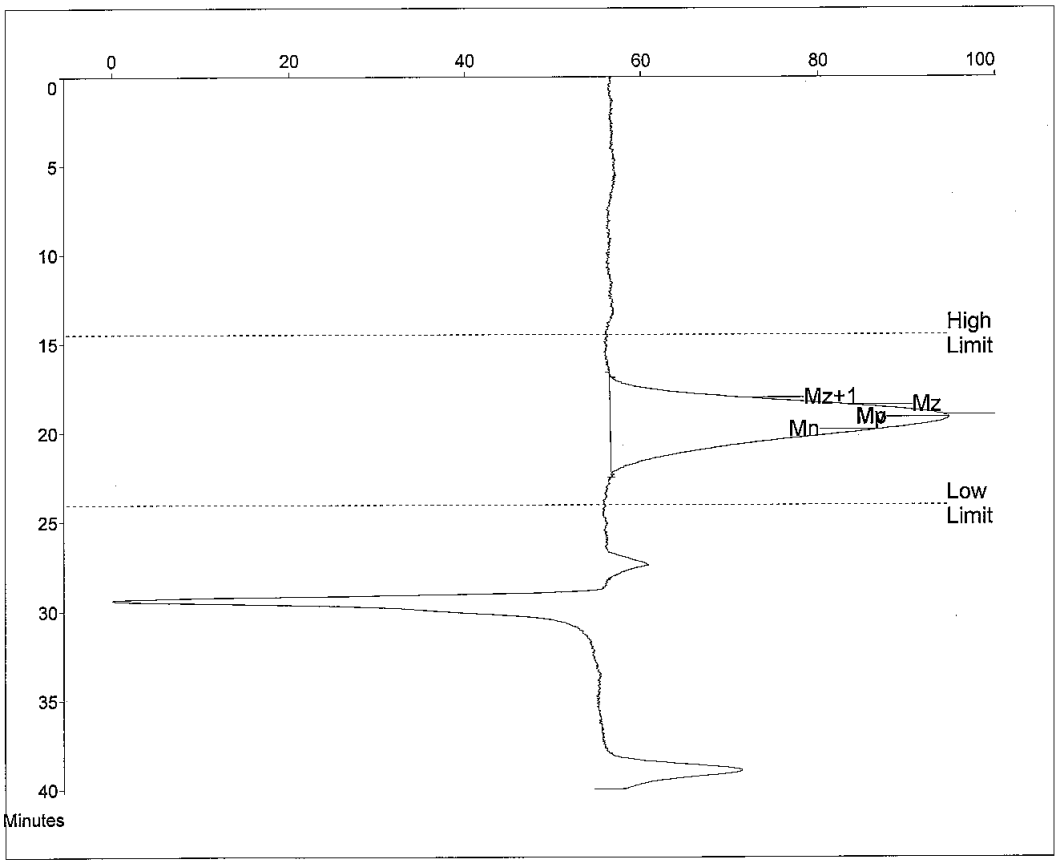

Molecular Weight Averages

Mp =	92624	Mz =	176811
Mn =	50156	Mz+1 =	257122
Mw =	104137	Mv =	94096
Polydispersity =	2.076	Peak Area =	1106836

Figure S4.2b. GPC characterization of **pTBTD-5DH(H)** with TCB at 135 °C.

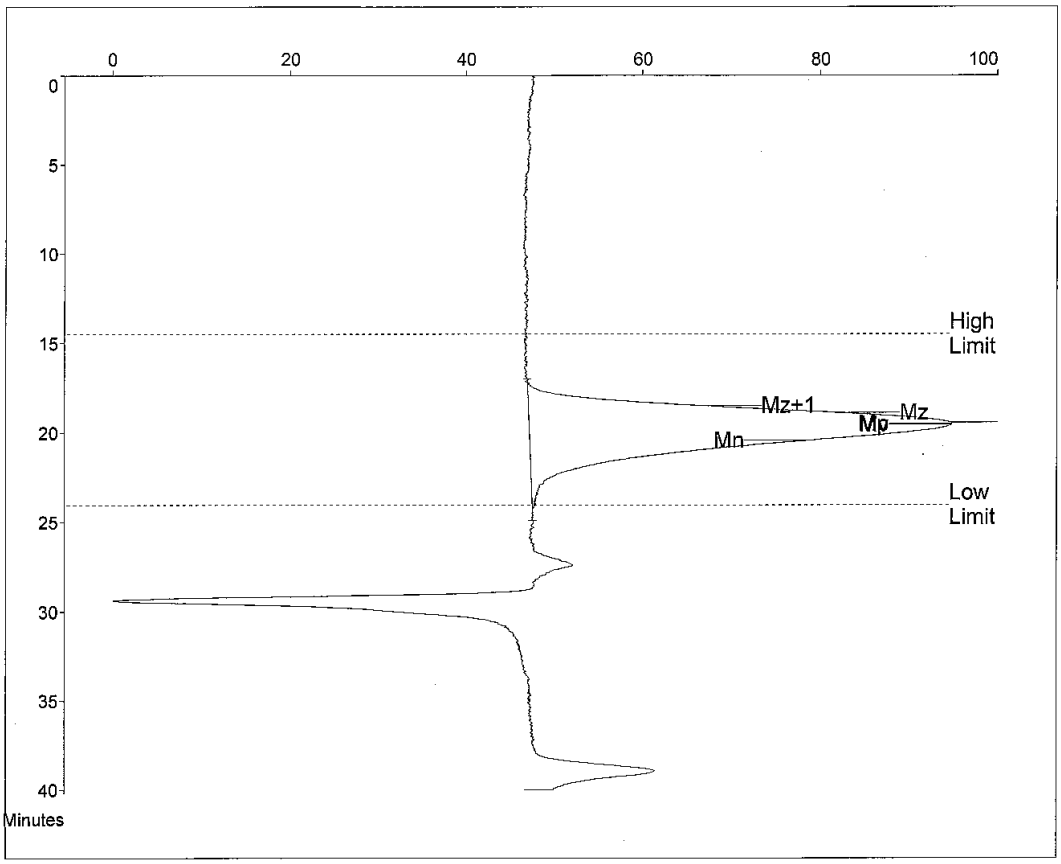

Molecular Weight Averages

Mp =	65074	Mz =	117070
Mn =	27682	Mz+1 =	169113
Mw =	69365	Mv =	62548
Polydispersity =	2.506	Peak Area =	1369241

Figure S4.2c. GPC characterization of **pTBTD-2DT** with TCB at 135 °C.

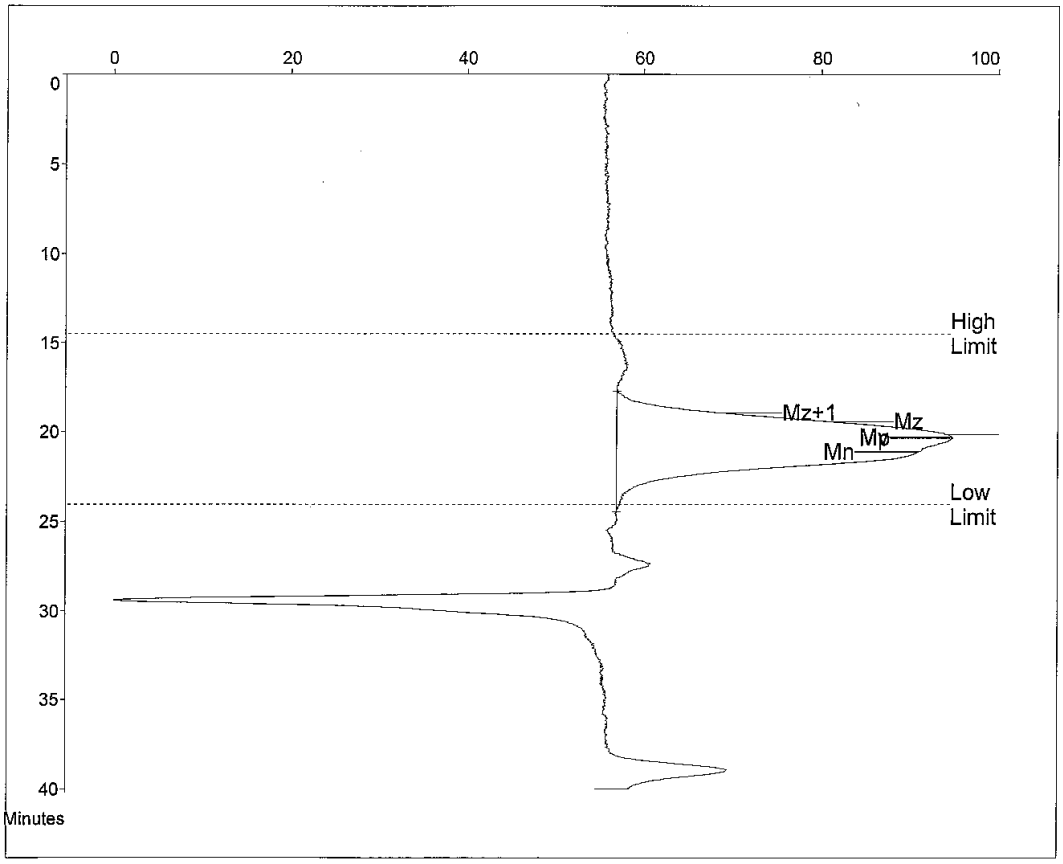

Molecular Weight Averages

Mp =	29857	Mz =	70818
Mn =	14199	Mz+1 =	110475
Mw =	36173	Mv =	31734
Polydispersity =	2.547	Peak Area =	1295146

Figure S4.2d. GPC characterization of **pTBTD-OD** with TCB at 135 °C.

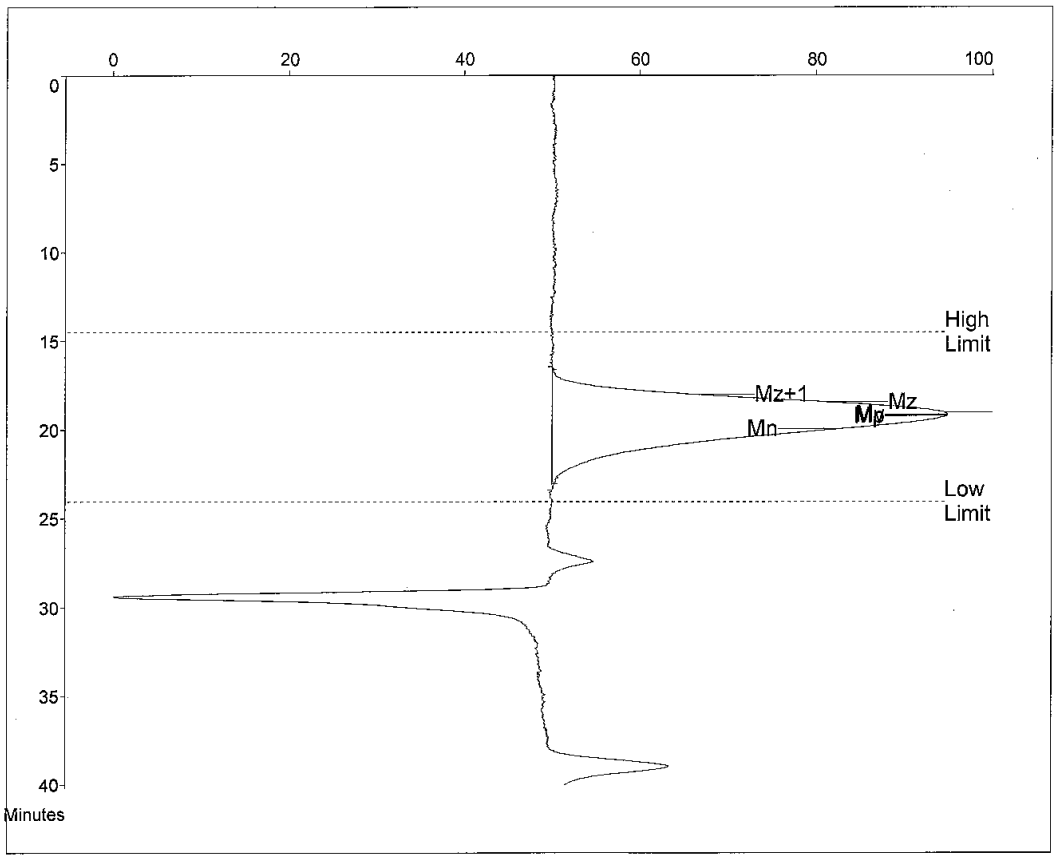

Molecular Weight Averages

Mp =	87123	Mz =	178116
Mn =	44034	Mz+1 =	266078
Mw =	102400	Mv =	91994
Polydispersity =	2.325	Peak Area =	1317757

Figure S4.2e. GPC characterization of **pTBTD-5DH** (polymerized at 160 °C for 30 min under microwave irradiation) with TCB at 135 °C.

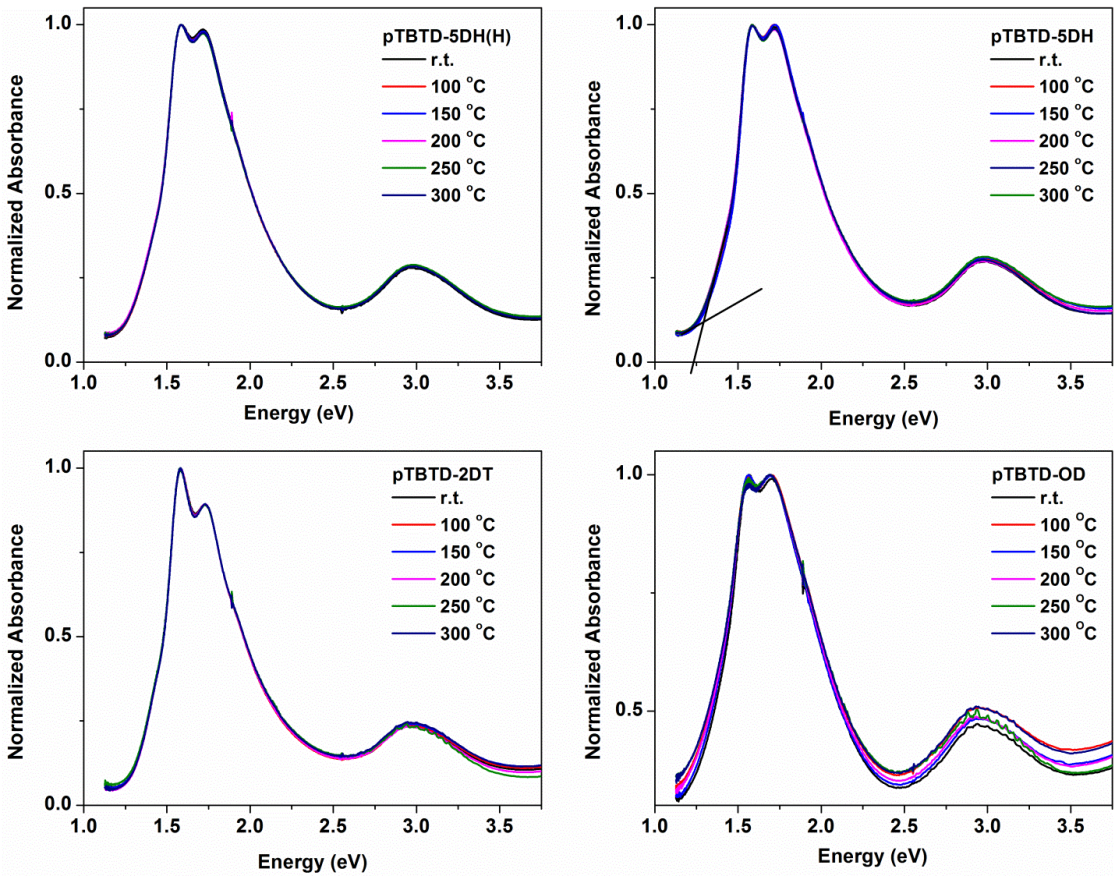

Figure S4.3. Absorption spectra of thin films of **TBTD** polymers at room temperature and after thermal annealing treatment under 100, 150, 200, 250, and 300 °C for 30 min followed by cooling down to room temperature.

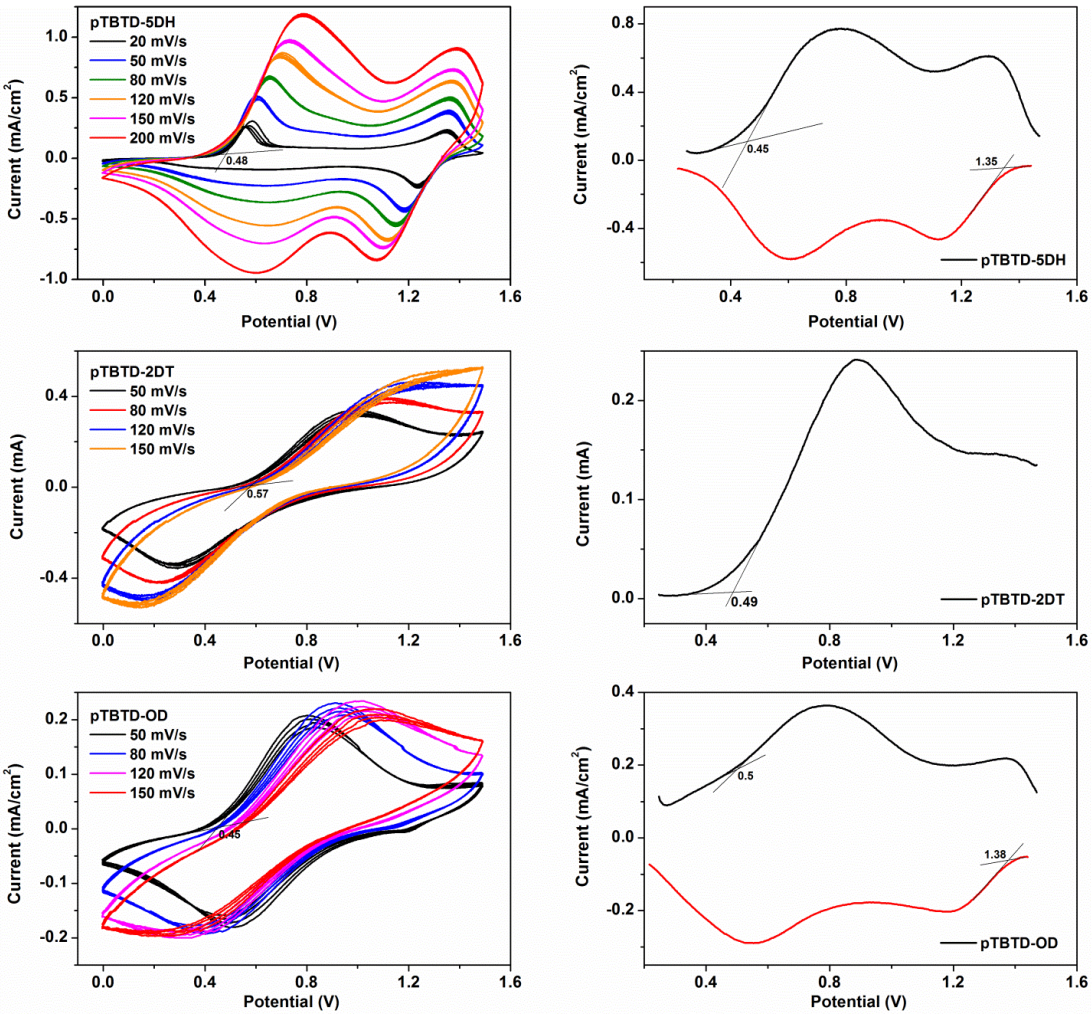

Figure S4.4. Electrochemical characterizations of **TBTD** polymer films under cyclic voltammetry (CV) model and differential pulse voltammetry (DPV) model.

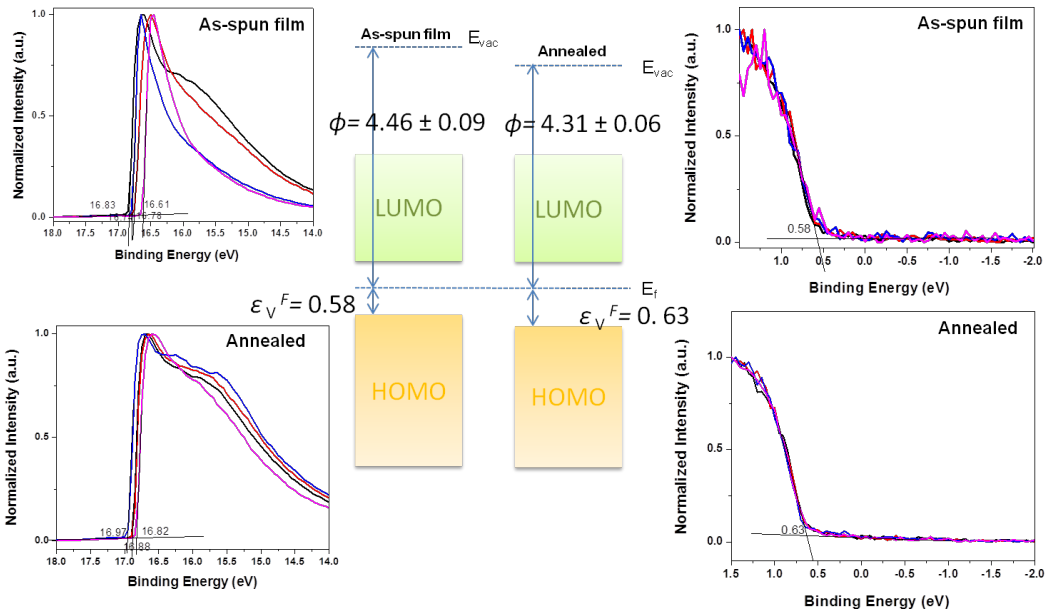

Figure S4.5a. UPS characterization of **pTBTD-5DH** before (as-spun film) and after thermal annealing treatment (200 °C for 30 min)

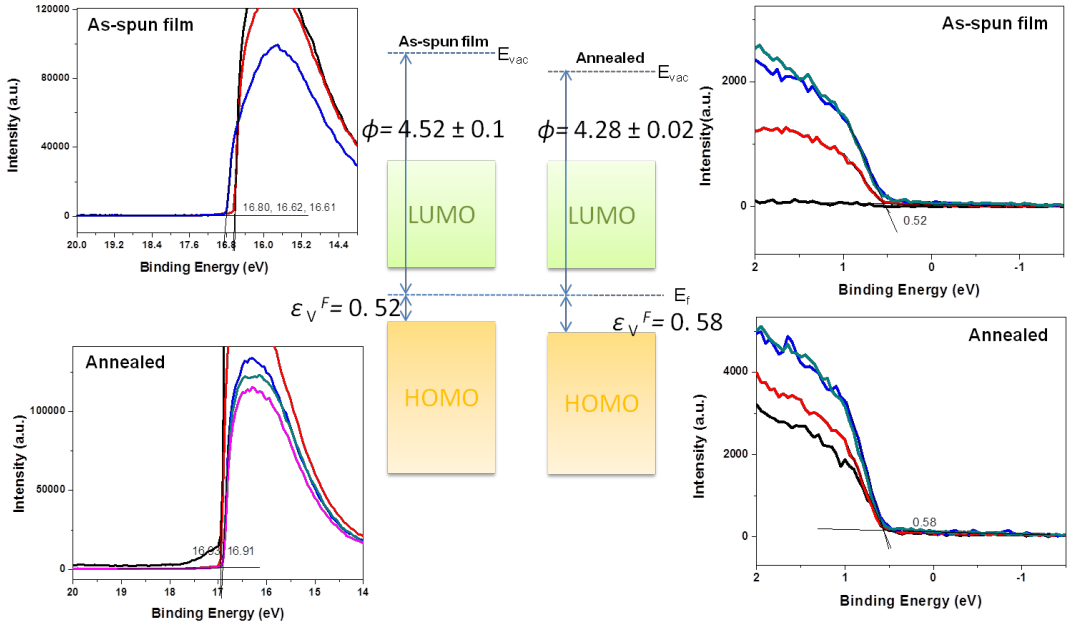

Figure S4.5b. UPS characterization of **pTBTD-2DT** before (as-spun film) and after thermal annealing treatment (200 °C for 30 min)

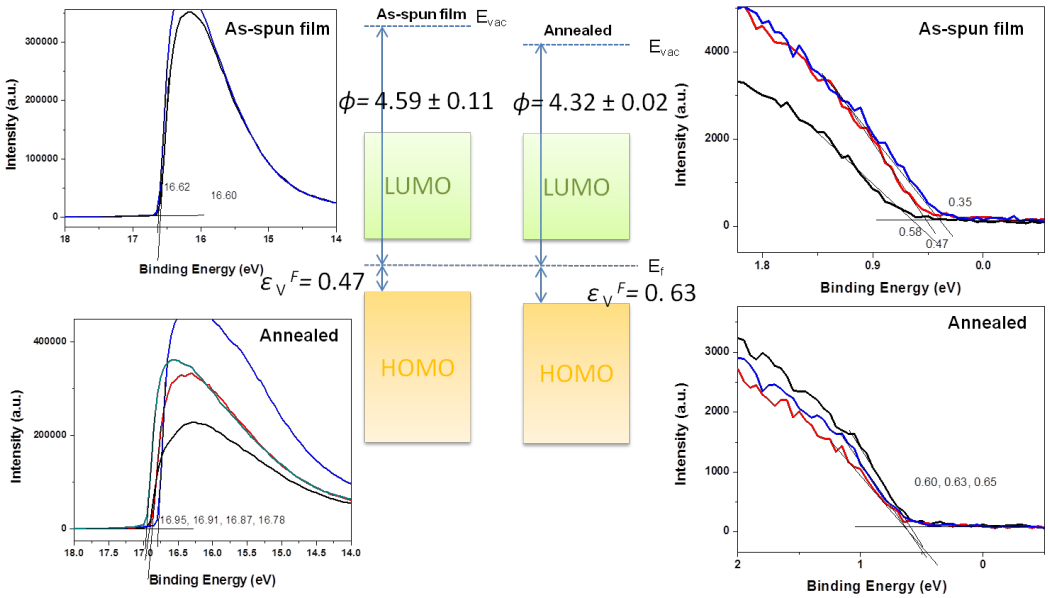

Figure S4.5c. UPS characterization of **pTBTD-OD** before (as-spun film) and after thermal annealing treatment (300 °C for 30 min)

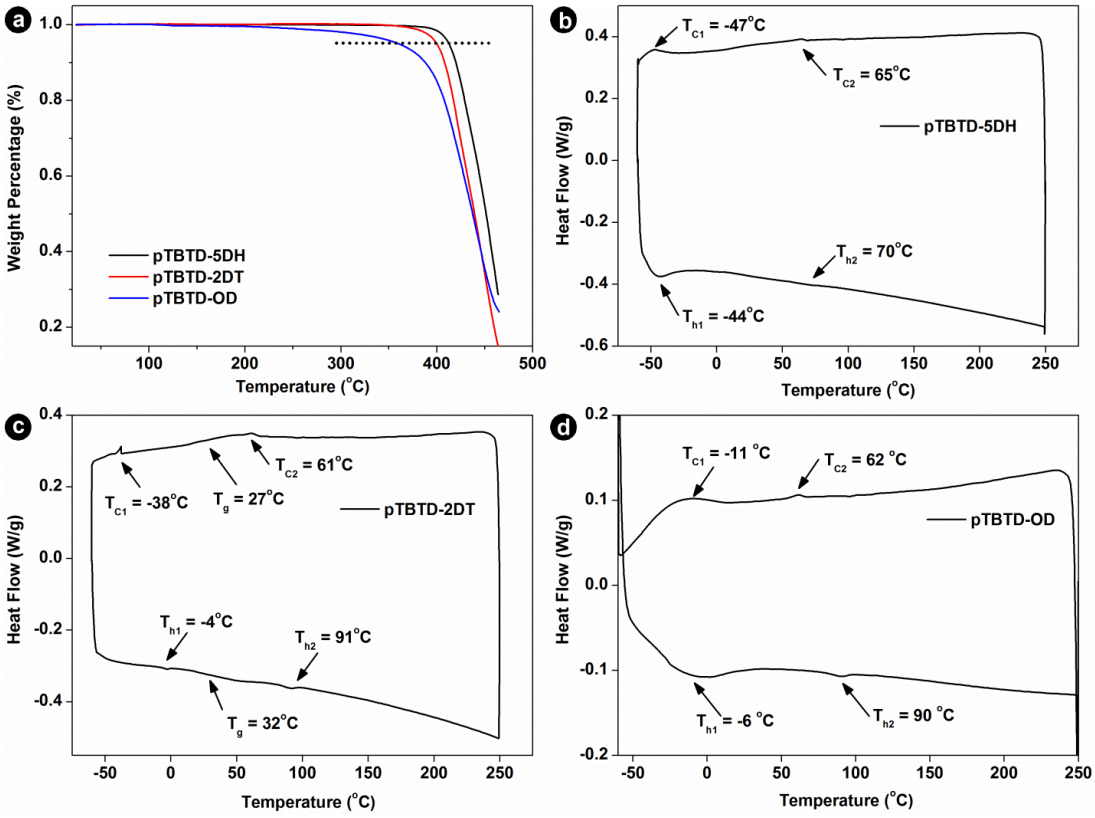

Figure S4.6. (a) TGA of **TBTD** polymers in a nitrogen atmosphere (25 mL/min) at a heating rate of 10 °C/min; thermal transition characterization of (b) **pTBTD-5DH**, (c) **pTBTD-2DT**, (d) **pTBTD-OD** under DSC. All DSC characterizations were based on the 2nd heating and cooling processes in a nitrogen atmosphere with a nitrogen flow rate of 50 mL/min and a heating/cooling rate of 10 °C/min.

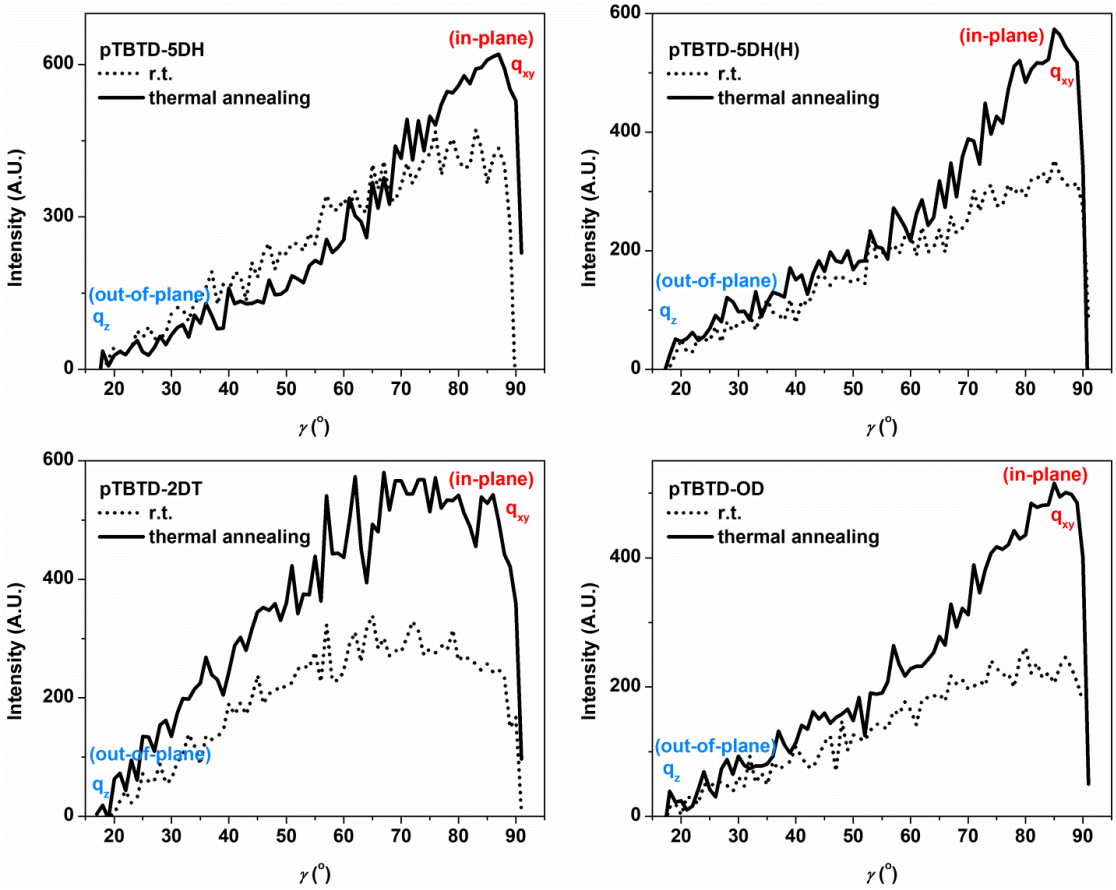

Figure S4.7. The intensity variation of the (010) peak (at 2θ = 24 - 25°) along the γ axis from q_z (out-of-plane) to q_{xy} (in-plane) before and after thermal annealing. **pTBTD-5DH**, **pTBTD-5DH(H)**, and **pTBTD-2DT** were annealed at 200 °C for 30 min; **pTBTD-OD** was annealed at 300 °C for 30 min.

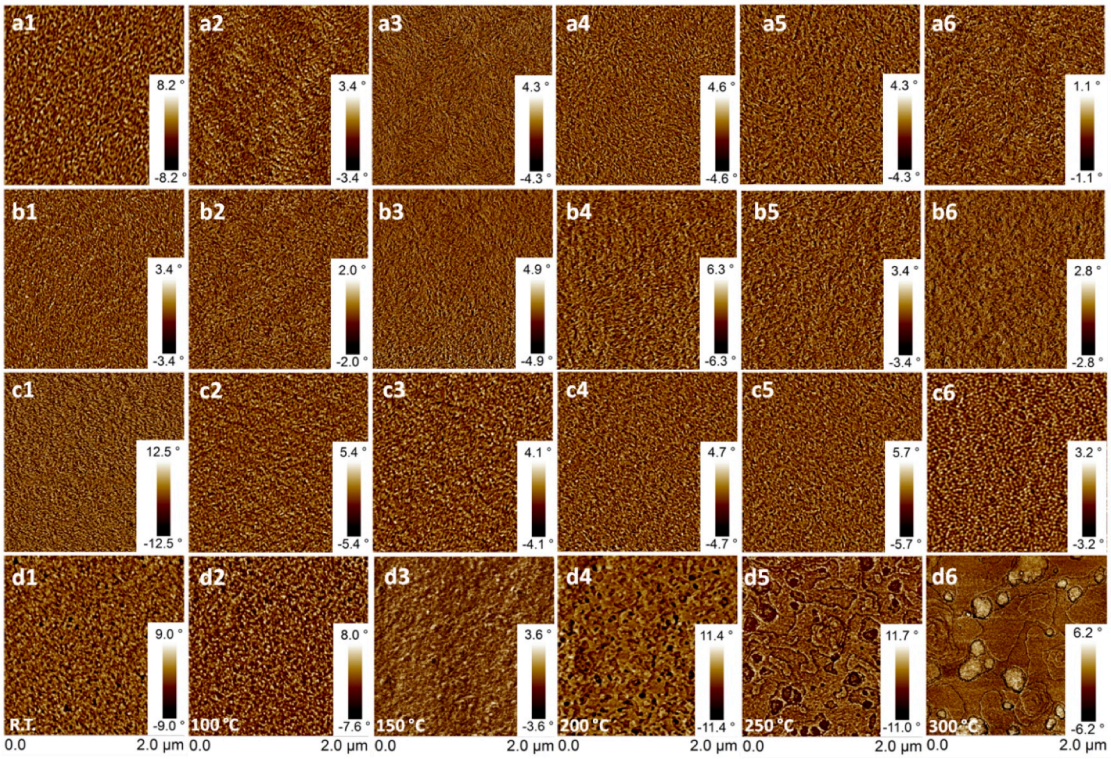

Figure S4.8a. Tapping mode AFM phase images of **TBTD** polymers ((a) **pTBTD-5DH**; (b) **pTBTD-5DH(H)**; (c) **pTBTD-2DT**; (d) **pTBTD-OD**) recorded at room temperature; and after annealing at 100 °C (a1–d1), 150 °C (a2–d2), 200 °C (a3–d3), 250 °C (a4–d4), and 300 °C (a5–d5) for 30 min at each temperature, followed by cooling down to room temperature.

It is noteworthy that **pTBTD-2DT** phase morphology varied from nano-fibrillar features with widths of *ca*. 20 nm and lengths of *ca*. 150 nm in as-spun film to unexpected features consisting of isotropic strings of nano-beads with diameters of *ca*. 58 nm and lengths of *ca*. 200-300 nm (**c6**). More interestingly, the fine granules on the **pTBTD-OD** film surface appeared to be agglomerated with an increase in annealing temperature; and eventually formed a terraced pattern with annealing at 300 °C (**d2**–**d6**).

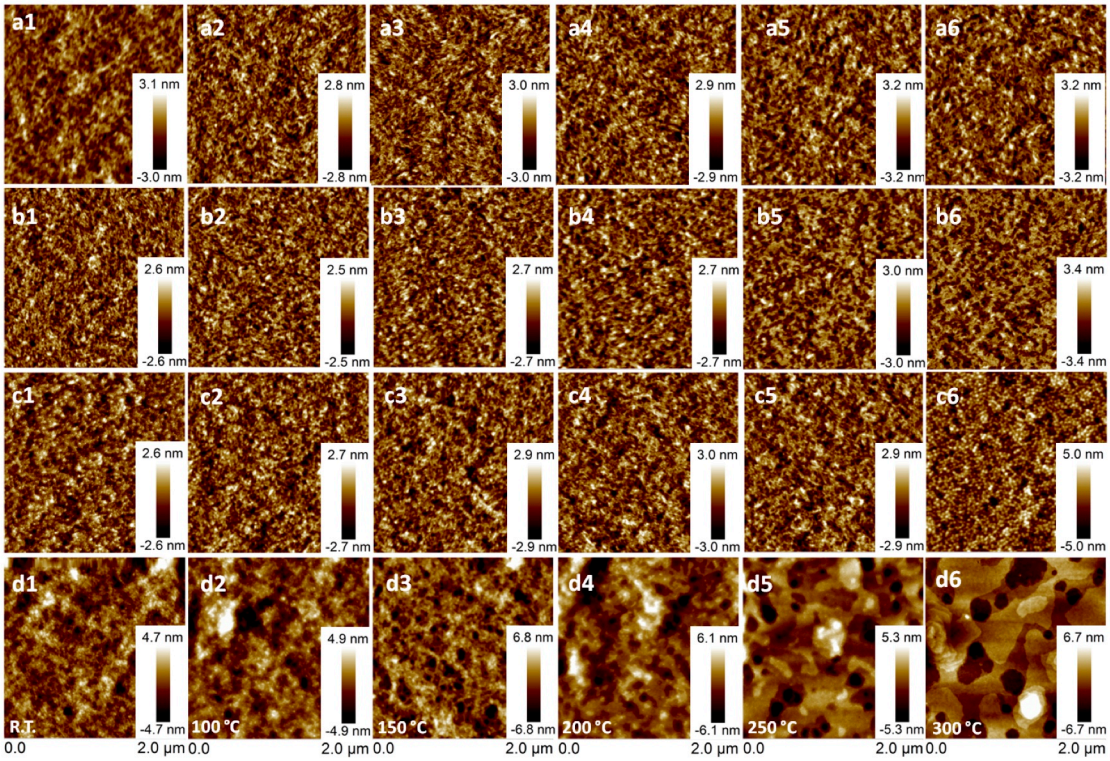

Figure S4.8b. Tapping mode AFM height images of **TBTD** polymers ((a) **pTBTD-5DH**; (b) **pTBTD-5DH(H)**; (c) **pTBTD-2DT**; (d) **pTBTD-OD**) recorded at room temperature; and after annealing at 100 °C (a1–d1), 150 °C (a2–d2), 200 °C (a3–d3), 250 °C (a4–d4), and 300 °C (a5–d5) for 30 min at each temperature, followed by cooling down to room temperature.

The fine granules on the **pTBTD-OD** film surface appeared to be agglomerated with an increase in annealing temperature; and eventually formed a terraced pattern with annealing at 300 °C (**d2-d6**).

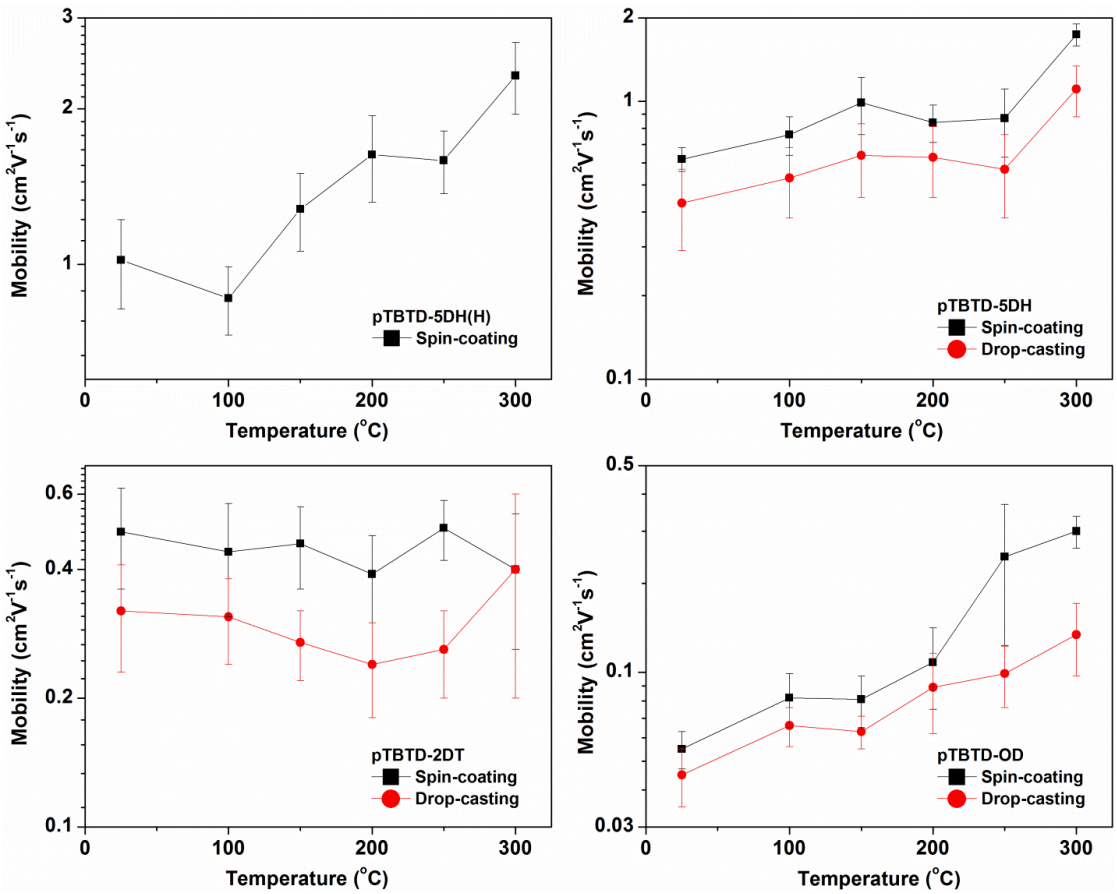

Figure S4.9. The variation of field effect hole mobility of **TBTD** polymers after thermal annealing treatment under the temperature of 100, 150, 200, 250, and 300 °C for 30 min. **TBTD** polymers were deposited onto OFET devices by spin-coating or drop-casting.

References:

[1] P. M. Beaujuge, H. N. Tsao, M. R. Hansen, C. M. Amb, C. Risko, J. Subbiah, K. R. Choudhury, A. Mavrinskiy, W. Pisula, J. L. Bredas, F. So, K. Mullen, J. R. Reynods, *J. Am. Chem. Soc.* **2012**, *134*, 8944.

[2] B. Y. Fu, J. Baltazar, Z. K. Hu, A. T. Chien, S. Kumar, C. L. Henderson, D. M. Collard, E. Reichmanis, *Chem. Mater.* **2012**, *24*, 4123.

[3] Y. H. Lee, A. Ohta, Y. Yamamoto, Y. Komatsu, K. Kato, T. Shimizu, H. Shinoda, S. Hayami, *Polyhedron* **2011**, *30*, 3001.

[4] C. H. Woo, P. M. Beaujuge, T. W. Holcombe, O. P. Lee, J. M. J. Frechet, *J. Am. Chem. Soc.* **2010**, *132*, 15547.

[5] L. J. Huo, J. H. Hou, H. Y. Chen, S. Q. Zhang, Y. Jiang, T. L. Chen, Y. Yang, *Macromolecules* **2009**, *42*, 6564.

[6] S. Cho, J. Lee, M. H. Tong, J. H. Seo, C. Yang, *Adv. Funct. Mater.* **2011**, *21*, 1910.

SUPPORTING INFORMATION-3

FOR CHAPTER 5

Materials and Methods

Chloroform, dichloromethane, toluene, isopropanol, THF, DMF, 2-methoxyethanol, chlorobenzene and 1,2-dichorobenzene (DCB) were purchased as anhydrous grade solvents from Sigma-Aldrich. Mesitylene was purchased from Acros Organics. THF was distilled from sodium benzophenone. 2-Bromothiazole was purchased from Scientific Matrix. Tetrabutylammonium bromide (n-Bu_4NBr), n,n-diisopropylethylamine (DIPEA), diisopropylamine (DIPA), palladium(II) acetate ($Pd(OAc)_2$), tris(dibenzylideneacetone)-dipalladium(0) ($Pd_2(dba)_3$), tri(o-tolyl)phosphine (P(*o*-tolyl)$_3$), sodium diethyldithiocarbmate, polyethylenimine (PEIE, 80% ethoxylated solution, 35 — 40 wt.% in H_2O with *ca*. 70 kDa of Mw), and tetra-*n*-butylammonium hexafluorophosphate ($[n\text{-}Bu_4N]^+[PF_6]^-$) were purchased from Sigma-Aldrich. BCB (XU.71918, Cyclotene™) was purchased from Dow Chemicals. CYTOP (CTL-809M) and its corresponding solvent (CT-solv.180) were purchased from Asahi Glass, Co. *N*-octadecyltrichlorosilane (OTS-18) was purchased from Gelest, Inc. Silica gel was purchased from Sorbent Technologies (Premium Rf™, porosity: 60Å; particle size: 40-75 μm).

The microwave irridated polymerizations were conducted using a CEM Discover SP System. ^{1}H and ^{13}C NMR spectra were recorded using a Varian Mercury Vx 400 (^{1}H, 400 MHz; ^{13}C, 100 MHz) and Vx 300 (^{1}H, 300 MHz; ^{13}C, 75 MHz) nuclear magnetic resonance spectrometer. Electron ionization mass spectra (EI-MS) were recorded using a Waters AutoSpec. Molecular weights of **PDBTz** were measured using a PL-GPC 220 instrument (courtesy of Ben Cherniawski and Prof. Alejandro L Briseno in the Department of Polymer Science and Engineering, University of Massachusetts Amherst) using 1,2,4-trichloro- benezene (TCB) as the mobile phase at 135 °C.

UV-vis absorption spectra was recorded on an Agilent 8453 UV-Visible Spectrophotometer. **PDBTz** films for UV-vis absorption characterization were prepared by spin-coating polymer solutions in DCB (5 mg/mL), *o*-xylene (5 mg/mL), *p*-xylene (4 mg/mL), and THN (5 mg/mL) onto OTS-18 pre-treated glass cover substrates. The details of OTS-18 pretreatment are depicted in the section of "OFET Device Fabrication and Characterization" (*vide infra*). Cyclic voltammetry (CV) and differential pulse voltammetry (DPV) were performed using Princeton Applied Research Potentiostat/Galvanostat Model 273A with a three-electrode electrochemical cell consisting of a platinum disk working electrode, onto which polymers were drop casted from DCB solution (1 mg/mL), a platinum flag counter electrode, and a Ag/Ag^{+} reference electrode (10 mM of $AgNO_3$ and 0.5 M of Bu_4NPF_6 in acetonitrile). The

ferrocene/ferrocenium redox couple (Fc/Fc^+) was used as the internal standard (-5.08 eV versus vacuum).[1] The CV was performed with a scan rate varying from 50 to 200 mV/s for five cycles. DPV parameters were set up as follows: step time 0.038 s, step size of 2 mV, and an amplitude of 100 mV.

Ultraviolet Photoemission Spectra (UPS) were measured on Kratos Axis UltraDLD XPS/UPS system, using He-I lamp radiation at 21.2 eV. All samples were in electronic equilibrium with the spectrometer via a metallic clip on the surface, and were run at a base pressure of 10^{-9} Torr. The Fermi level was calibrated using atomically clean silver. UPS were acquired at 5 eV pass energy and 0.05 eV step size with the aperture and iris set to 55 μm. From the secondary electron edge (SEE) of the UPS we calculated the work function (ϕ = 21.22-SEE) for each polymer, and from the emission close to the Fermi level we determine the position of valence band maximum. IP (= –HOMO) and ϕ were calculated by equations (1) and (2):

$$\mathrm{IP} = h\nu - (E_{\mathrm{cutoff}} - \varepsilon_V^{\mathrm{F}}) \qquad \text{Eq. S5.1}$$

$$\phi = h\nu - E_{\mathrm{cutoff}} \qquad \text{Eq. S5.2}$$

where $h\nu$, E_{cutoff}, and $\varepsilon_V^{\mathrm{F}}$ denote the incident photo energy (He I, 21.22 eV), the high binding energy cutoff, and the lowest binding energy point, respectively.

The thermal decomposition temperature of polymer was measured with a Perkin-Elmer Pyris 1 thermogravimetric analyzer (TGA) in a nitrogen atmosphere (25 mL min^{-1})

with a heating rate of 10 °C min^{-1}. Thermal transitions of polymer was measured with a TA Q200 Differential Scanning Calorimeter (DSC) in a nitrogen atmosphere (50 mL min^{-1}) with a heating/cooling rate of 10 °C min^{-1}. Each sample was scanned for three cycles.

2D-GIWAXS characterization was carried out using a Bruker-AXS Microdiffractometer (operating voltage of 45 kV and current of 40 mA) with a 0.8 mm collimator, K_α monochromator, Hi-Star area detector, and Eulerian cradle sample holder, at an optimal incidence angle (0.8 — 2° for **PDBTz**), and a 30° out-plane tilt angle. **PDBTz** films for 2D- GIWAXS characterizations were prepared by drop casting **PDBTz** solutions in DCB (5 mg mL^{-1}), *o*-xylene (5 mg mL^{-1}), *p*-xylene (4 mg mL^{-1}), and THN (5 mg mL^{-1}) onto BCB pre-treated SiO_2 dielectric (300 nm) / p^{++} doped Si substrates. The details of BCB pretreatment are depicted in the section of "OFET Device Fabrication and Characterization" (*vide infra*).

The coherence length (τ) of <100> and <010> peaks were calculated based on Scherrer equation:

$$\tau = \frac{K\lambda}{\beta Cos\theta} \qquad \text{Eq. S5.3}$$

where K is a dimensionless shape factor (0.9); λ refers to the incidence X-ray wavelength (1.54059 Å in this study); β represents the FWHM (radians) of <100> and <010> peaks along 2θ direction; and θ denotes to Bragg angle.

PDBTz film orientation distribution was investigated by Herman's orientation function (*S*), as shown in Equation (4) and (5):

$$f = \frac{\int_0^{\pi/2} I(\chi) Cos^2(\chi)\, Sin(\chi) d\chi}{\int_0^{\pi/2} I(\chi)\, Sin(\chi) d\chi} \quad \text{Eq. S5.4}$$

$$S = \tfrac{1}{2}(3f-1) \quad \text{Eq. S5.5}$$

For instance, **Figure S5.11** shows the <100> and <010> peak distributions along with χ, within a **PDBTz** film cast from *o*-xylene. To simplify the calculation, χ was defined as 0° at the q_z axis (out-of-plane), and as 90° at the q_{xy} axis (in-plane). The $I(\chi)$ term is the <100> or <010> intensity at each χ, and sin(χ) represents a geometric intensity correction factor. The molecular orientation parameter, *f*, refers to the average lattice plane orientation relative to χ_{max}, the azimuthal angle at which $I(\chi)$ approaches the maximum. According to Equation (4), S = 1, if on average, the lattice planes completely align parallel to χ_{max}; S = -1/2 if they completely orient perpendicular to χ_{max}; while S = 0 if the lattice planes orient randomly.

The surface morphology of **PDBTz** films were characterized by AFM using a Bruker Dimension Icon Atomic Force Microscope System with ScanAsyst in tapping mode with silicon etched probe tip. Polymer films for AFM characterizations were prepared by spin-coating **PDBTz** solutions in DCB (5 mg mL^{-1}), *o*-xylene (5 mg mL^{-1}), *p*-xylene (4 mg

mL^{-1}), and THN (5 mg mL^{-1}) onto BCB pre-treated SiO_2 dielectric (300 nm) / p^{++} doped Si substrates.

The thermal annealing treatments for **PDBTz** films under UV/vis absorption (**Figure S5.8**), 2D-GIWAXS, and AFM characterizations were implemented on a hotplate with temperature setting at 100 and 150 °C inside a glovebox filled with N_2. Each thermal annealing treatment lasted for 30 min, followed by rapidly cooling to room temperature.

OFET Device Fabrication and Characterization

The BGTC FET devices were fabricated on a heavily p doped silicon wafer <100> as the gate electrode with a 300 nm thick layer of thermally grown SiO_2 as one gate dielectric. BCB pre-diluted in mesitylene with a ratio of 1:20 (v/v) was spin coated onto SiO_2/Si substrates at 3,000 rpm for 1 min. The resulting substrates were annealed at 265 °C for 1.5 h inside a nitrogen-filled glovebox for cross-linking, followed by cooling down to room temperature for 30 min. The BCB/SiO_2 bilayer dielectric has a capacitance of *ca*. 1.04 x 10^{-4} Fm^{-2}. The hot **PDBTz** solutions (4-6 mg mL^{-1}) were subsequently spin-coated (at 1,800 rpm for 1 min) onto BCB/SiO_2 substrates inside glovebox. The spin-coated **PDBTz** based substrates were then annealed at 150 °C for 30 min, followed by rapidly cooling to room temperature. 100 nm of Ca and 150 nm of Al (as a barrier layer to avoid

Ca oxidation) were thermally deposited onto polymer layer in sequence via shadow masks as source and drain electrodes, with channel sizes fixing in width (2 mm) and varying in length (50, 100, 150, and 200 μm). The aluminum layer (150 nm) is attempting to enhance the oxidative stability of the electrodes.

The TGBC OFETs were fabricated based on glass substrates (Corning® 1737). 50 nm of Ag was deposited onto glass substrates as source and drain electrodes via E-beam evaporation, with channel sizes fixing in width (4.5 mm) and varying in length (80, 120, 160, and 200 μm), followed by spin coating (at 5,000 rpm for 1 min, with an acceleration of 1,000 rpm/s) 0.01 or 0.05 wt% of PEIE solution in 2-methoxyethanol. The resultant substrates were annealed at 100 °C for 10 min in a glovebox, affording an ultra-thin PEIE layer with a thickness < 1.5 nm (an exact thickness is not accurate due to the resolution limitation of ellipsometer under 1.5 nm). **PDBTz** solutions were thereafter spin-coated (at 1,800 rpm for 1 min) onto substrates inside glovebox. The spin-coated **PDBTz** based substrates were then annealed at 150 °C for 30 min, followed by rapidly cooling to room temperature. The 2 wt% of CYTOP solution prepared via diluting 9 wt% of CYTOP solution (CTL-809M) by CT-solv. 180 (1: 3.5, v/v) was subsequently spin coated (3,000 rpm for 1 min) onto the polymer layer, followed by a thermal annealing treatment at 100 °C for 20 min in glovebox, to afford a 40 nm of CYTOP layer. A Savannah 100 ALD system from Cambridge Nanotech Inc. was used to deposit 50 nm-thick Al_2O_3 dielectric

films[2] Films were grown at 110 °C using alternating exposures of trimethyl aluminum [$Al(CH_3)_3$] and H_2O vapor at a deposition rate of approximately 0.1 nm per cycle. Each deposition cycle (1 ML) lasted 24 s, yielding a total deposition time of around 4 h for 500 cycles. The resultant CYTOP/Al_2O_3 bilayer dielectric has a capacitance of *ca*. 3.18 x 10^{-4} Fm^{-2}. 100 nm of Al gate electrodes were deposited by thermal evaporation through a shadow mask.

The bottom-gate-bottom-contact (BGBC) FET devices encapsulated by CYTOP (**Scheme S2**) were employed to characterize the air stability of **PDBTz** under 20 °C and 55-65 RH%. BGBC OFETs were fabricated on a heavily p doped silicon wafer <100> as the gate electrode with a 300 nm thick layer of thermally grown SiO_2 as the gate dielectric. Au source and drain contacts (50 nm of Au contacts with 3 nm of Cr as the adhesion layer) with a fixed channel size (50 μm in length and 2 mm in width) were deposited via E-beam evaporator onto the SiO_2 layer using a photolithography lift-off process. Prior to deposition of polymer semiconductors, the devices were cleaned by sonication in acetone for 30 min and subsequently rinsed sequentially with acetone, methanol and isopropanol, followed by drying under a flow of nitrogen. The SiO_2 surface was pretreated by exposing the devices to UV/ozone for 30 min followed by immersion into a 2.54 x 10^{-3} M (1 μL mL^{-1}) solution of OTS-18 in anhydrous toluene overnight inside glovebox. The devices were then cleaned by sonication in toluene for 10 min,

followed by rinsing with acetone, methanol and isopropanol, and drying under a flow of nitrogen. The H_2O contact angle for SiO_2 surface after OTS-18 treatment is in the range of 95–105°; while OTS-18 modified SiO_2 dielectric has a capacitance of *ca*. 1.1 x 10^{-4} Fm^{-2}. **PDBTz** solutions were thereafter spin-coated (at 1,800 rpm for 1 min) onto substrates inside glovebox. The spin-coated **PDBTz** based substrates were then annealed at 150 °C for 30 min, followed by rapidly cooling to room temperature. The resultant OFET devices were encapsulated via spin coating 9 wt% of CYTOP solution (at 4,000 rpm for 1 min), followed by a thermal annealing treatment at 100 °C for 20 min in glovebox, to afford a *ca*. 900 nm of CYTOP encapsulation layer. The OFET devices were stored in the ambient condition (25 ^{o}C, 55-65 RH%) and measured periodically inside glovebox to assess the effect of air on **PDBTz** based device performance (air stability).

The capacitances of the dielectric layers were measured via Agilent 4284A Precision LCR Meter. For BCB/SiO_2 bilayer dielectric, a parallel-plate capacitor was fabricated on a heavily p doped silicon wafer <100> as one electrode with a 300 nm thick layer of thermally grown SiO_2. BCB layer was afforded using the identical method in BGTC OFET device fabrication (*vide supra*). 150 nm of Al were thermally deposited onto polymer layer in sequence via shadow masks as the 2nd electrode. For OTS-18/SiO_2 dielectric, the capacitor was fabricated on a heavily p doped silicon wafer <100> as one electrode with a 300 nm thick layer of thermally grown SiO_2. OTS-18 was grown onto

the SiO_2 substrate using the identical method in BGBC OFET device fabrication (*vide supra*). 150 nm of Al were thermally deposited onto polymer layer in sequence via shadow masks as the 2nd electrode.

All OFET characterizations were performed using a probe station inside a nitrogen filled glovebox using an Agilent 4155C (for BGTC and BGBC OFETs) or Agilent E5272A (for TGBC OFETs) semiconductor parameter analyzers. The FET mobilities were calculated from the saturation regime (V_{SD} = 80 V in BGTC and BGBC OFETs, and V_{SD} = 10 V in TGBC OFETs) in the transfer plots of V_G versus I_{SD} by extracting the slope of the linear range of V_G vs. $I_{SD}^{1/2}$ plot and using the following equation:

$$\left.\frac{\partial I_{SD}^{1/2}}{\partial V_G}\right|_{V_{SD}} = \left(\mu_h C_{ox}(\frac{W}{2L})\right)^{1/2} \qquad \text{Eq. S5.3}$$

where I_{SD} and V_{SD} are the source-drain current (A) and source-drain voltage (V), respectively; V_G is the gate voltage (V) scanning from -20 to 80 V (for BGTC and BGBC OFETs) or 0 to 16 V (for TGBC OFETs) in the transfer plot; C_{ox} is the capacitance per unit area of the gate dielectric layer. W and L refer to the channel length and width; μ_e represents the electron field-effect mobility in the saturation regime ($cm^2V^{-1}s^{-1}$).

In this study, the threshold voltage, V_{th}, was calculated by extrapolating $V_T = V_G$ at I_{SD} = 0 in the V_G vs. $I_{SD}^{1/2}$ curve. Current on and off ratio, $I_{ON/OFF}$, was determined through

dividing maximum I_{SD} (I_{ON}) by the minimum I_{SD} at around V_G in the range of -40 to 0 V (I_{OFF}).

Hansen Solubility Parameter Characterization

PDBTz (1.5 mg) was mixed with 0.3 and/or 1.5 mL of solvent as per the defined procedure for solubility parameter determination and heated at 60 °C for at least 1 h.[3] Solutions were cooled to ambient temperature where they remained for 12 h. The solubility parameters were determined from these solutions via visual examination. Solvents were categorized as poor if they were unable to dissolve more than 5 mg of **PDBTz**/mL of solvent and good if they were able to dissolve more than 5 mg of **PDBTz**/mL of solvent. For the purposes of Hansen solubility parameter (HSP) analysis using requisite software (Hansen Solubility Parameters in Practice 3rd edition), a poor solvent was assigned a value of "0" and good solvent was assigned a value of "1".

DFT Studies of PDBTz and PDQT Oligomers and Their Subunits

A DFT study of the building blocks for **PDBTz** and PDQT was performed, to explore the effect of bithiazole on polymer conformation and molecular orbitals. Popular DFT methods, such as B3LYP, suffer from delocalization error, *i.e.*, they tend to overly

delocalize the electron density. As a result, properties such as torsion barriers and molecular orbital distributions can be poorly described when studying highly conjugated systems. Therefore, we rely here on a long-range corrected hybrid functional, ωB97X, with the cc-pVDZ basis set.[4]

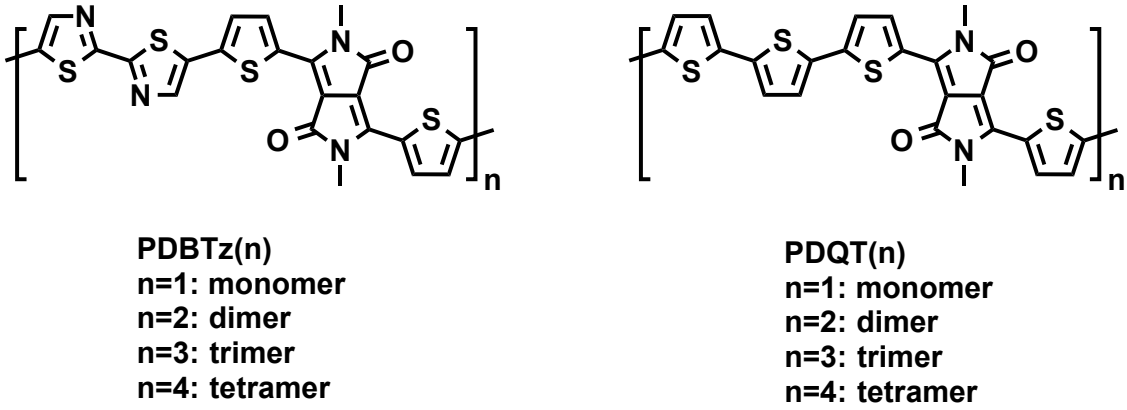

Figure S5.1. Monomer, dimer, trimer, and tetramer of PDBTz and PDQT investigated at the DFT level. Side chains were defined as methyl group to simplify the DFT calculation.

The standard ωB97X functional has been shown to accurately reproduce torsion potentials for bithiophene.[5] The range separation parameter ω ($bohr^{-1}$) determines where the electron exchange description changes from DFT (in the short range) to Hartree-Fock (in the long range), according to:

$$\frac{1}{r} = \frac{1-\mathrm{erf}\,(\omega r)}{r} + \frac{erf(\omega r)}{r} \qquad \text{Eq. S5.4}$$

where erf represents the error function.

The optimum ω-value has been shown to vary with the conjugation length of the system; thus, the use of the default ω-value would yield an improper description of the

(de)localization effects.[6] The range separation parameter ω was optimized for the system following the fundamental-gap tuning procedure:[7]

$$J_{IP}(\omega) = \left|\varepsilon^{\omega}_{HOMO}(N) + E^{\omega}_{gs}(N-1) - E^{\omega}_{gs}(N)\right| \quad \text{Eq. S5.5}$$

$$J_{EA}(\omega) = \left|\varepsilon^{\omega}_{HOMO}(N+1) + E^{\omega}_{gs}(N) - E^{\omega}_{gs}(N+1)\right| \quad \text{Eq. S5.6}$$

$$J_{gap}(\omega) = \sqrt{\left(J_{IP}(\omega)\right)^2 + \left(J_{EA}(\omega)\right)^2} \quad \text{Eq. S5.7}$$

In this procedure $\varepsilon^{\omega}_{HOMO}(N)$ and $\varepsilon^{\omega}_{HOMO}(N+1)$ are the HOMO energies for an N (neutral) and N+1 (anionic) electron system. $E^{\omega}_{gs}(N-1)$, $E^{\omega}_{gs}(N)$, and $E^{\omega}_{gs}(N+1)$ are the total energies for the N-1 (cationic), N (neutral) and N+1 (anionic) electron systems. The ω-value is varied until the minimum value of $J_{gap}(\omega)$ is found. Although the basis set used in the tuning process may be of initial concern, especially since the tuning procedure involves calculations of the anion with a basis set lacking diffuse functions, it has previously been established that the results from the ω tuning procedure change a trivial amount upon using basis sets larger than the one we are considering.[8] Nonetheless the basis set effects were explored for the model case of bithiophene where the tuned ω parameter using the larger aug-cc-pVTZ basis set was identical to that obtained with the smaller cc-pVDZ basis set. As has been consistently the case in earlier studies of highly conjugated systems using various functionals, the tuned ω-values are found to be smaller than the ωB97X default ω-value of 0.3 bohr^{-1}.[6] This holds true even in bithiophene that is the smallest conjugated building block considered (**Table S1**).

Table S5.1. Tuned ω for systems using tuned-ωB97X/cc-pVDZ// tuned-ωB97X/cc-pVDZ.

compound	ω (bohr^{-1})	ω (bohr^{-1}) using aug-cc-pVTZ
bithiophene	0.221	0.221
bithiazole	0.237	---
1	0.195	---
thiothiazole	0.226	---
PDBTz1	0.143	---
PDBTz2	0.115	---
PDBTz3	0.106	---
PDPPT41	0.142	---
PDPPT42	0.112	---
PDPPT43	0.103	---

The torsional potentials of the subunits were tested with the tuned-ωB97X functional, as the standard ωB97X functional was shown to give accurate torsional potentials when compared with benchmark calculations.[5] Tuned-ωB97X predicts bithiophene to have an optimized S-C-C-S dihedral angle of 152° in comparison to 148° measured by gas phase electron diffraction,[4d] 156° for MP2/aug-cc-pVTZ calculations,[5] which lends confidence that the methodology we use is appropriate for determining this torsion. The tuned-ωB97X energies were also compared to spin component scaled second order Møller–Plesset (SCS-MP2) results using the cc-pVTZ basis set, as this method is expected to produce reliable results to serve as a benchmark.[9] The torsional space of the

other interactions were explored to determine the preferred conformational orientations of the polymer building blocks (**Figure 5.2**). The torsions angle is determined by S-C-C-S for bithiophene and bithiazole while S-C-C-N determined the dihedral angle for **1** (**Figure 5.2**). Tuned-ωB97X predicts the torsional potential of bithiazole to be about 1.4 kcal/mol less at the *trans*-co-planar orientation relative to the approximately 150° dihedral angle found in bithiophene. In the case of **1**, tuned-ωB97X overestimated the rotational barrier height by about 2 kcal/mol with respect to SCS-MP2, but still yields the correct minimum energy dihedral angle.

The frontier molecular orbital distributions and energies of bithiophene and bithiazole were compared (Figure S5.3). Examination reveals a rather small difference in the HOMO and LUMO wavefunction characteristics between bithiazole and bithiophene. The HOMO-LUMO energy gaps are similar for both bithiazole (8.34 eV) and bithiophene (8.27 eV); as expected, the HOMO and LUMO energies are more stabilized in bithiazole, by about 0.65 eV.

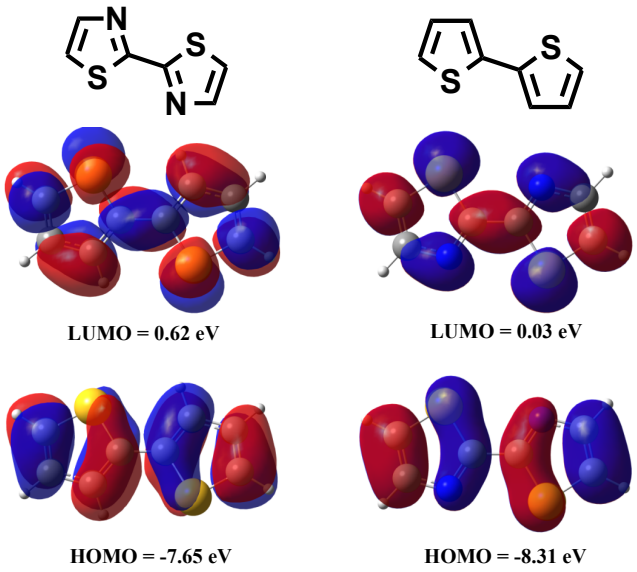

Figure S5.2. Plots of the frontier molecular orbitals for bithiophene (left) and bithiazole (right) using an isovalue of 0.02. Eigenvalues are shown below the respective orbital.

We considered oligomers up to the tetramer to represent the polymers. The HOMO-LUMO energy gap is predicted to be essentially identical for the monomer units, 4.76 eV for **PDBTz(1)** and 4.76 eV for PDQT(1). This trend continues for the other **PDBTz** and PDQT oligomers studied. The S-C-C-S dihedral angles for the bithiazole and bithiophene units are 180° and 155° for **PDBTz(1)** and PDQT(1) respectively, illustrating the increased planarity of the (isolated) **PDBTz(1)** monomer units. In the longer systems. the S-C-C-S dihedral angle for the bithiazole units in **PDBTz(4)** remains 180° while bithiophene in PDQT(4) varies from 155° to 168°.

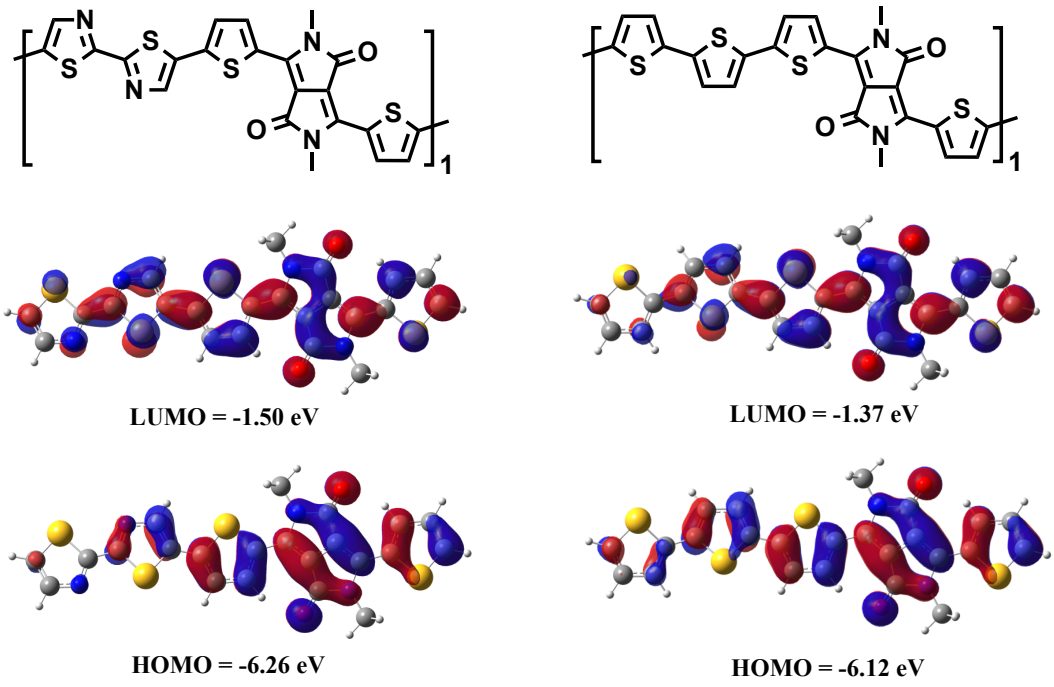

Figure S5.3. Plots of the frontier molecular orbitals for **PDBTz(1)** (left) and PDQT(1) (right) using an isovalue of 0.02. Eigenvalues are shown below the respective orbital.

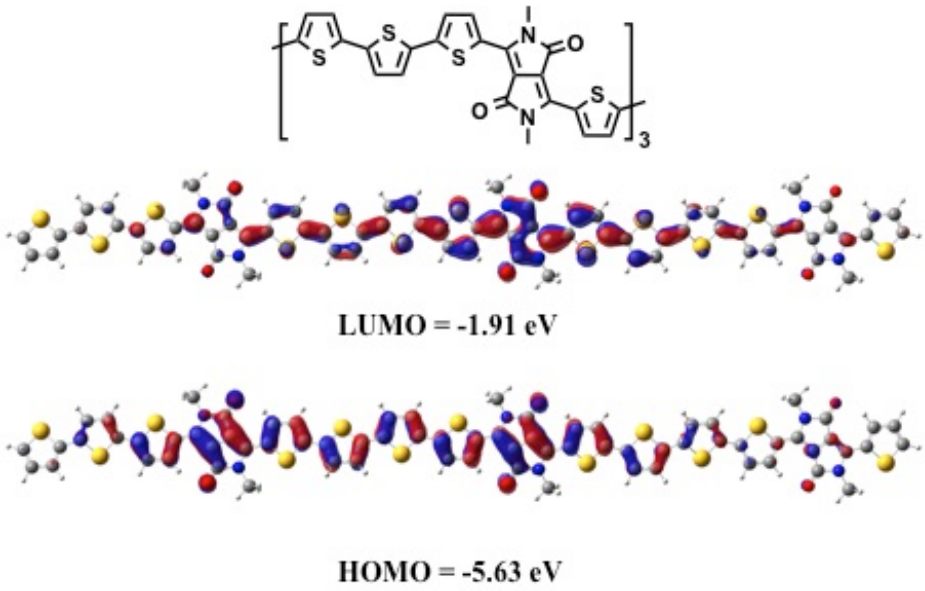

Figure S5.4a. Plots of the frontier molecular orbitals for PDQT(3) using an isovalue of 0.02. Eigenvalues are shown below the respective orbital.

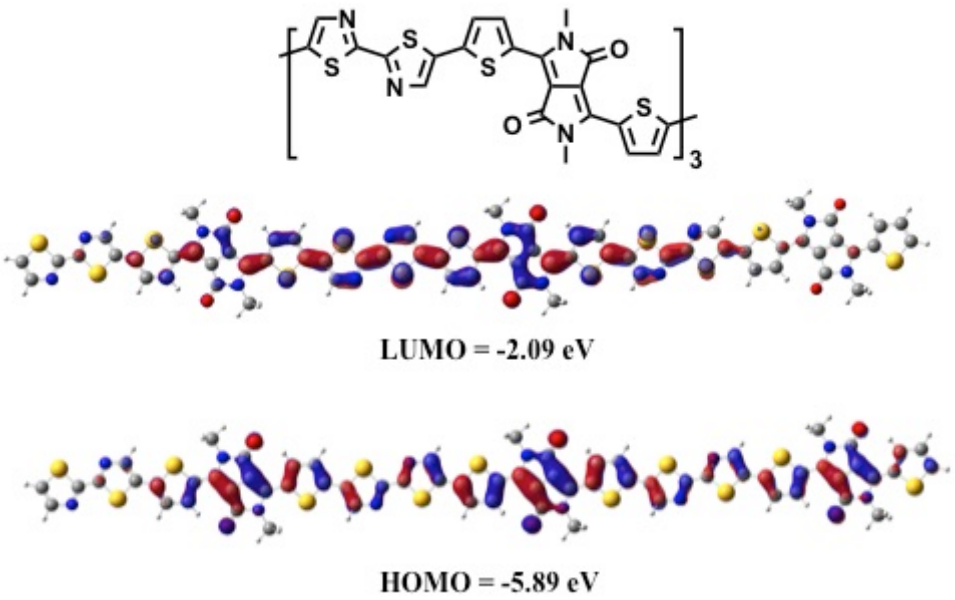

Figure S5.4b. Plots of the frontier molecular orbitals for **PDBTz(3)** using an isovalue of 0.02. Eigenvalues are shown below the respective orbital.

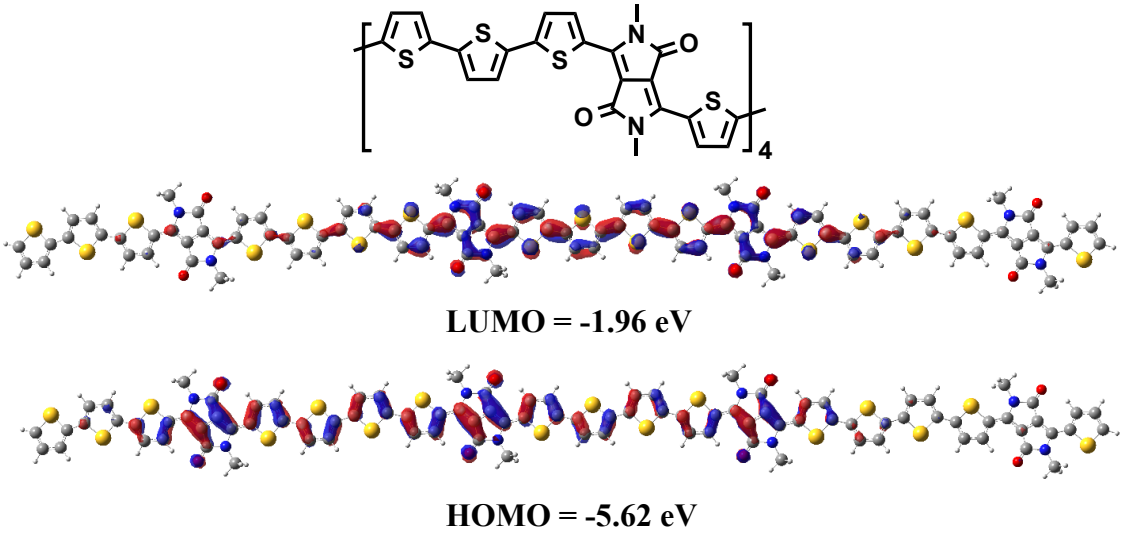

Figure S5.5a. Plots of the frontier molecular orbitals for PDQT(4) using an isovalue of 0.02. Eigenvalues are shown below the respective orbital.

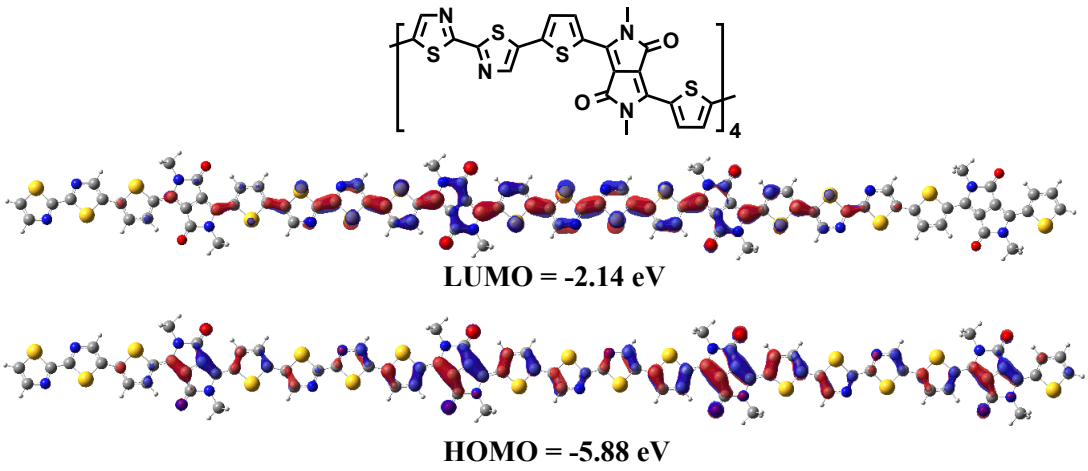

Figure S5.5b. Plots of the frontier molecular orbitals for **PDBTz(4)** using an isovalue of 0.02. Eigenvalues are shown below the respective orbital.

A reasonable starting geometry was generated using ωB97X/cc-pVDZ. Then the ω-value for this functional was tuned using the fundamental-gap tuning method (*vide supra*). The geometry was re-optimized using the newly tuned ω-value with the same method. The process of tuning the ω-value and re-optimizing the geometry was repeated until the change in the ω-value was less than 1×10^{-3} $bohr^{-1}$. In the case of calculating torsional potentials, the tuned ω-value for the optimized geometry was used for all dihedral angles. The dihedral angles were varied from 0° to 180° in increments of 5°.

Table S5.2. HOMO and LUMO energies and HOMO-LUMO energy gaps.

molecule	HOMO (eV)	LUMO (eV)	HOMO-LUMO Gap (eV)
bithiophene	-7.65	0.62	8.27
bithiazole	-8.31	0.03	8.34
$PDBTz_1$	-6.26	-1.50	4.76
$PDBTz_2$	-5.97	-1.96	4.01
$PDBTz_3$	-5.89	-2.09	3.79
$PDBTz_4$	-5.88	-2.14	3.73
$PDQT_1$	-6.12	-1.37	4.75
$PDQT_2$	-5.74	-1.77	3.97
$PDQT_3$	-5.63	-1.91	3.71
$PDQT_4$	-5.62	-1.96	3.66

Synthetic Details

The synthetic procedures for the preparation of 2,2'-bithizole (**1**), 5,5'-bis(trimethyl-stannyl)-2,2'-bithiazole (**2**), and 2,5-bis(5-decylheptadecyl)-3,6-di(thiophen-2-yl)pyrrolo[3,4- c]pyrrole-1,4(2H,5H)-dione (**M1**) were modified from published literatures.[10]

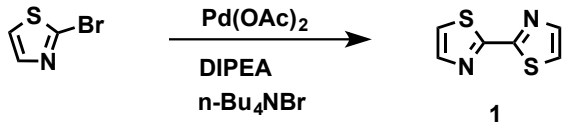

1

2,2'-bithiazole (1): 2-bromothiazole (2.00 g, 12.20 mmol, 1.00 eq.), n,n-diisopropylethyl- amine (DIPEA, 2.13 mL, 12.20 mmol, 1.00 eq.), n-Bu_4NBr (1.97 g, 6.10 mmol, 0.50 eq.), and $Pd(OAc)_2$ (0.14 g, 0.61 mmol, 0.05 eq.) were dissolved into toluene (33.3 mL) under argon. The mixture was heated at reflux overnight, before cooling to room temperature. D.I. H_2O (100 mL) was added and the mixture was extracted into dichloromethane (50 mL). The organic solution was washed with brine (4x50 mL), dried over anhydrous MgSO4, and concentrated under reduced pressure. The resultant dark residue was purified by column chromatography (silica gel, hexane/DCM, 1:8 v/v), followed by recrystallization from heptane to afford 2,2'-bithiazole as needle-like pale yellow crystals (yield: 60%). ^1H NMR (300 MHz, $CDCl_3$) δ 7.90 (d, J = 3.1, 2H), 7.44 (d, J = 3.1, 2H). ^{13}C NMR (75 MHz, $CDCl_3$) δ 161.32, 139.98, 135.23, 130.58,

129.77, 128.57, 107.68, 42.26, 37.29, 33.55, 33.27, 30.35, 30.13, 29.71, 29.65, 29.35, 26.66, 24.04, 22.68, 14.10. EI- MS (m/z): 168.0 [M].

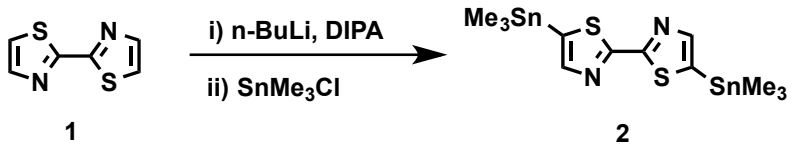

1 2

5,5'-bis(trimethylstannyl)-2,2'-bithiazole (2): DIPA (0.45 mL, 3.12 mmol, 3.50 eq.) in THF (2 mL) was cooled to -78 ˚C under argon, followed by the dropwise addition of n-butyllithium (1.00 mL of a 2.5 M solution in hexane, 2.50 mmol, 2.80 eq.). The resulting solution was stirred at 0 °C for 30 min to afford lithium diisopropylamide (LDA). It was subsequently cooled down to -78 ˚C. Compound **1** (150 mg, 0.9 mmol, 1.00 eq.) in THF (3.9 mL) was added in a dropwise manner generating an orange solution. After stirring at -78 ˚C for 2 h, $SnMe_3Cl$ (3.25 mL of a 1.0 M solution in THF, 3.25 mmol, 3.64 eq.) was added in a dropwise manner. The resulting solution was then warmed to room temperature and stirred for 12 h. After poured into D.I. H_2O (50 mL), the mixture was extracted into CH_2Cl_2 (3 x 15 mL), washed with brine (3 x 15 mL), dried over anhydrous $MgSO_4$, and concentrated under reduced pressure. The final product was washed with hexane at -78 ˚C and isolated compound **2** as a pale yellow solid. ^1H NMR (300 MHz, $CDCl_3$) δ 7.77 (s, 2 H), 0.41 (s, 18H).

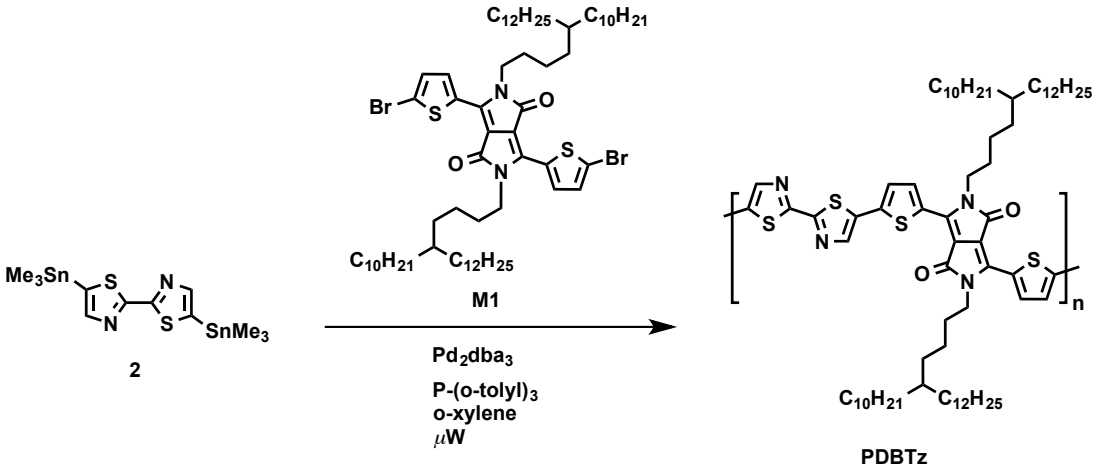

Poly(dithienyl-diketopyrrolopyrrole-dithiazole) (PDBTz): Monomers **2** (60 mg, 0.12 mmol, 1.00 eq.) and **M1** (148 mg, 0.12 mmol, 1.00 eq.), and P(o-tolyl)$_3$ (14.8 mg, 0.05 mmol, 0.40 eq.), were placed in a microwave irradiation tube (10 mL). $Pd_2(dba)_3$ (4.5 mg, 4 μmol, 0.04 eq.) was added and the irradiation tube was then degassed and refilled with argon in sequence. *o*-Xylene (1.05 mL) was added, followed by a 3 cycles of freeze-pump-thaw. The resulting mixture was stirred at 160 °C under microwave irradiation for 1.5 h. The resulting dark gel like crude product was dispersed in chloroform (20 mL) and the solution was poured into aqueous sodium diethyldithiocarbmate solution (100 mL of a solution containing 1g in 100 mL of D.I. water). The resulting mixture was stirred at 75 °C for 2 h to remove Pd. The organic solution was collected and concentrated under reduced pressure. The concentrated solution was added dropwise to methanol (300 mL). The precipitated solid was collected by filtration and purified by Soxhlet extraction sequentially using methanol (24 h), acetone (24 h), ethyl acetate (12 h), hexane (24 h), and $CHCl_3$ (2 h). The $CHCl_3$ solution

was collected and then concentrated under reduced pressure. The concentrated solution was added in a dropwise manner to methanol (200 mL). The precipitate was collected by filtration and dried under vacuum at room temperature for 12 h to afford **PDBTz** as a black solid (145 mg, yield: 90%). Elemental analysis. Calculated for $C_{74}H_{116}N_4O_2S_4$: C, 72.73 %; H, 9.57 %; N, 4.58 %; S, 10.50 %. Found: C, 72.54 %; H, 9.44 %; N, 4.53 %; S, 10.35 %.

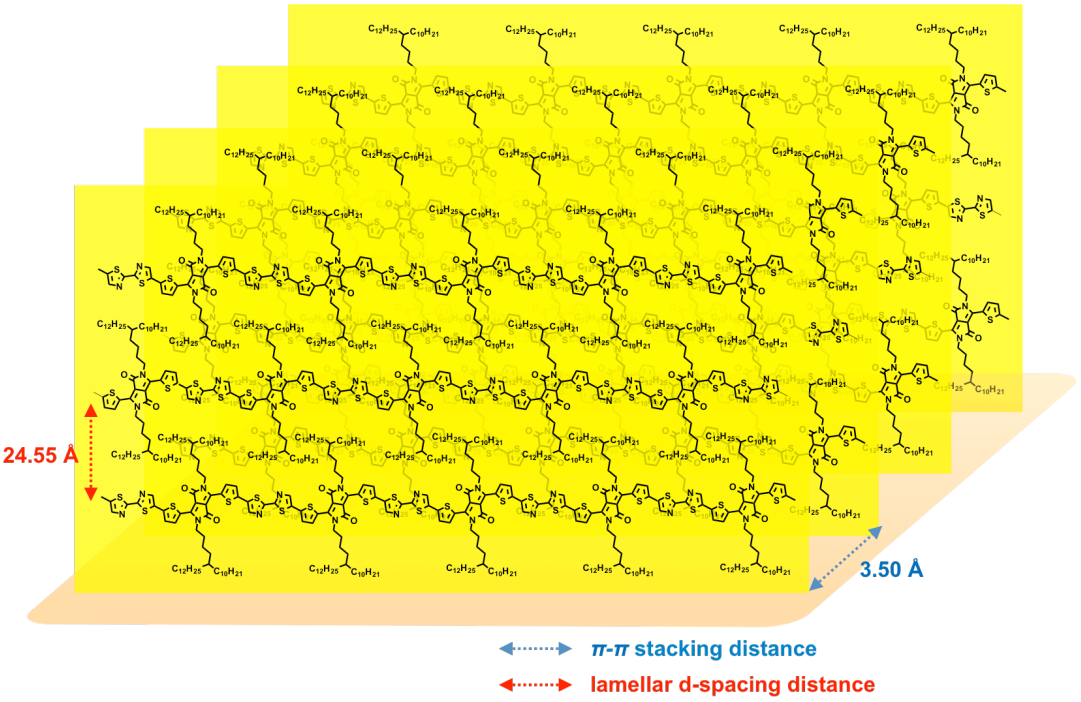

Scheme S5.1. The estimated lamellar structured edge-on orientation of **PDBTz** on substrate. The alkyl side chain packing of **PDBTz** follows the interdigitated packing model.

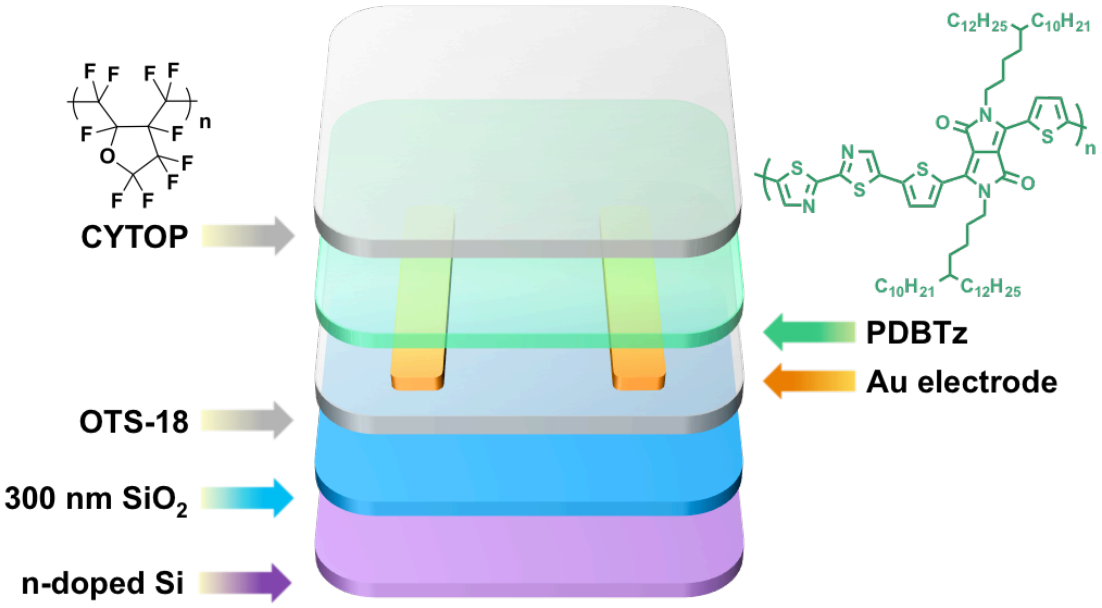

Scheme S5.2. The architecture of **PDBTz** based bottom-gate/bottom-contact OFET devices encapsulated via a *ca*. 900 nm of CYTOP layer.

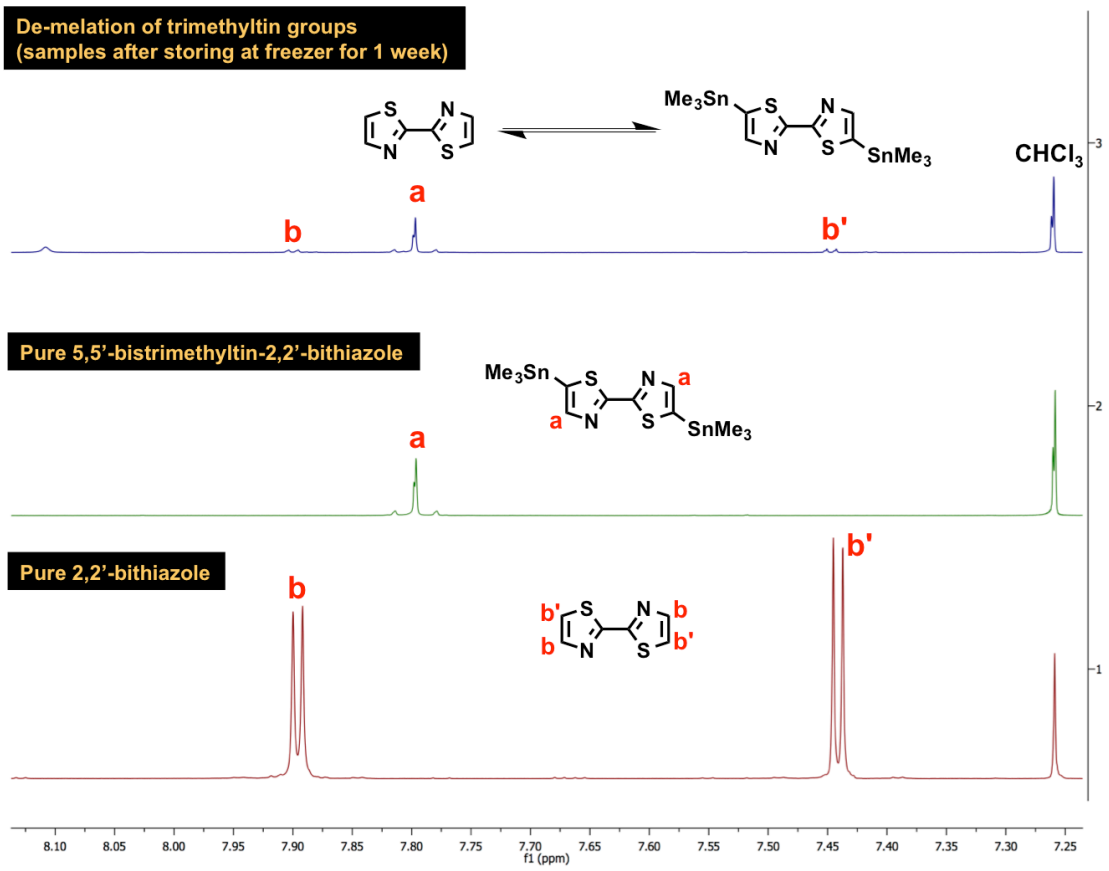

Figure S5.6 The ^{1}H-NMR results of pure 2,2'-thiazole, 5,5'-bistrimethyltin-2,2'-bithiazole, and de-metalation of 5,5'-bistrimethyltin-2,2'-bithiazole after samples stored at freezer for 1 week.

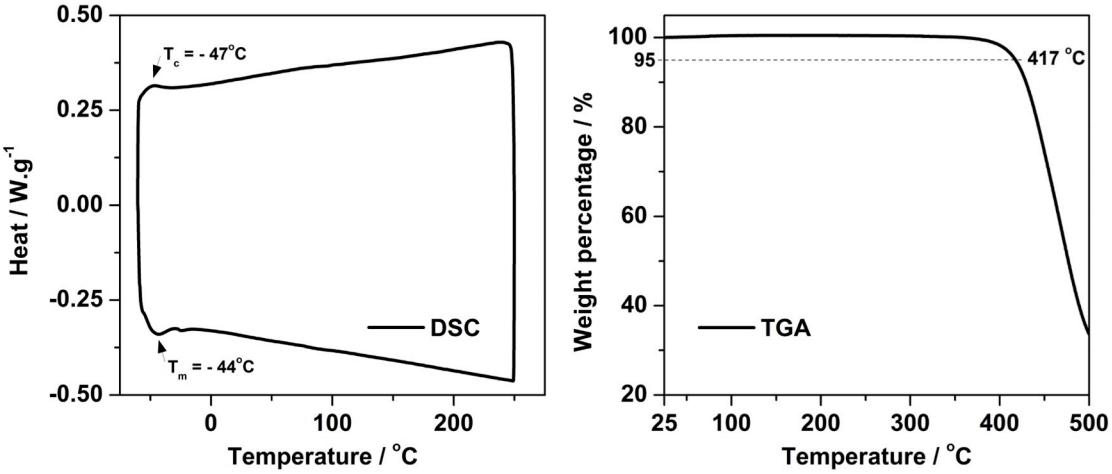

Figure S5.7. Left: thermal transition characterization of **PDBTz** under DSC. All DSC characterizations were based on the 2nd heating and cooling processes in a nitrogen atmosphere with a nitrogen flow rate of 50 mL/min and a heating/cooling rate of 10 °C/min. Right: TGA of **PDBTz** in a nitrogen atmosphere (25 mL min^{-1}) at a heating rate of 10 °C min^{-1}.

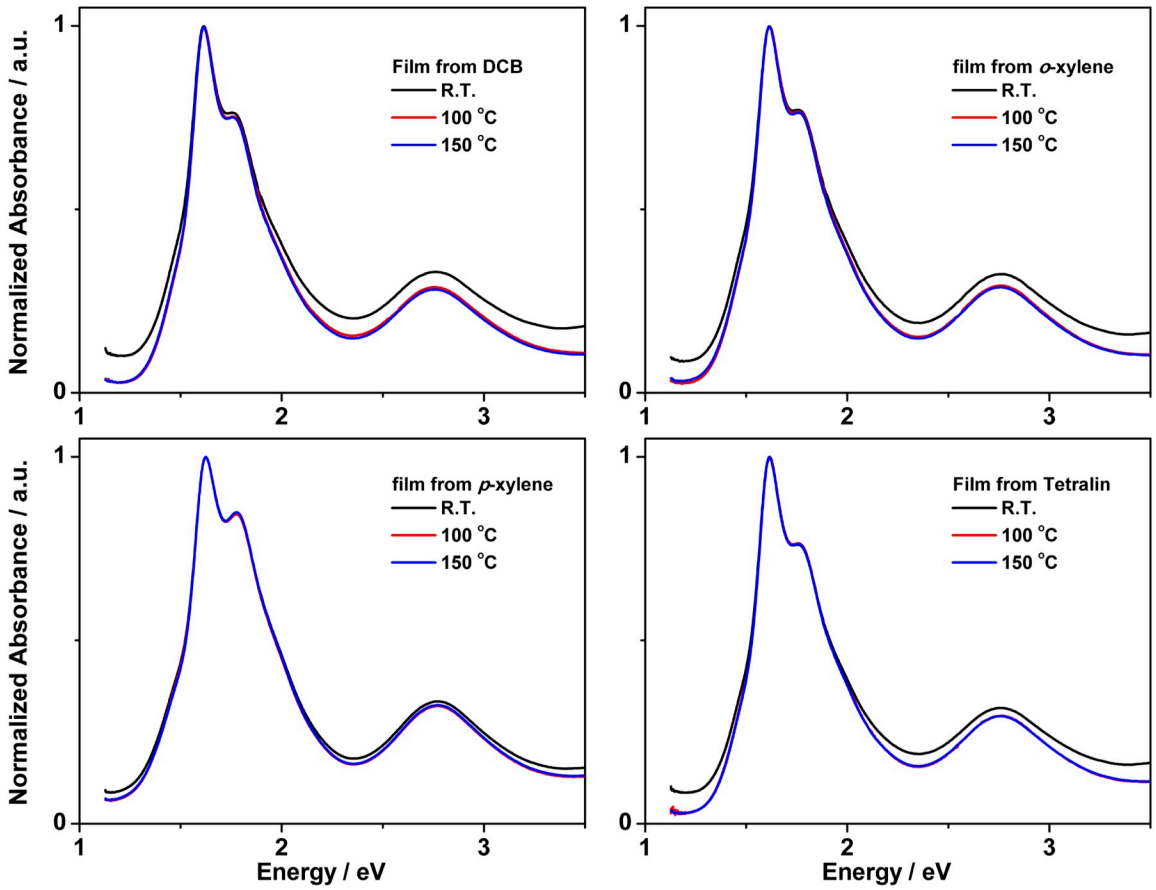

Figure S5.8. Absorption spectra of **PDBTz** thin films cast from DCB, *o*-xylene, *p*-xylene, and tetralin at room temperature and after thermal annealing treatment under 100 and 150 °C for 30 min followed by cooling down to room temperature.

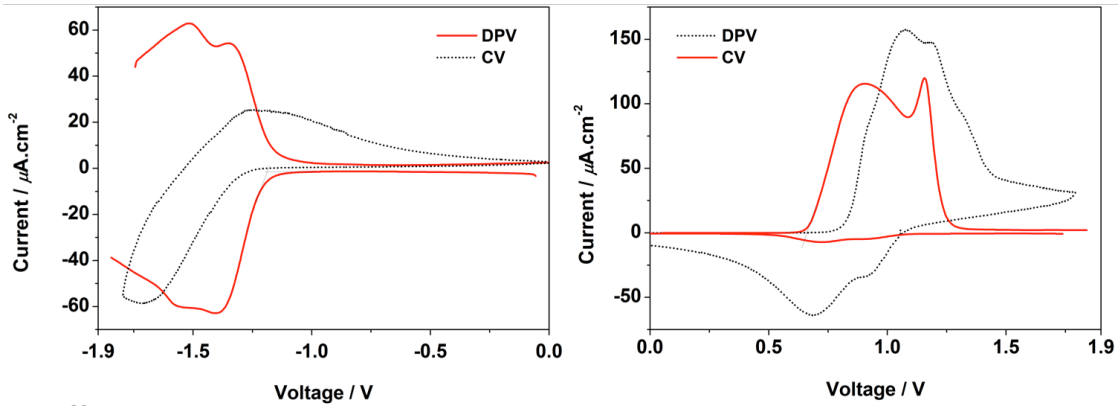

Figure S5.9. Electrochemical characterizations of **PDBTz** films under cyclic voltammetry (CV) and differential pulse voltammetry (DPV).

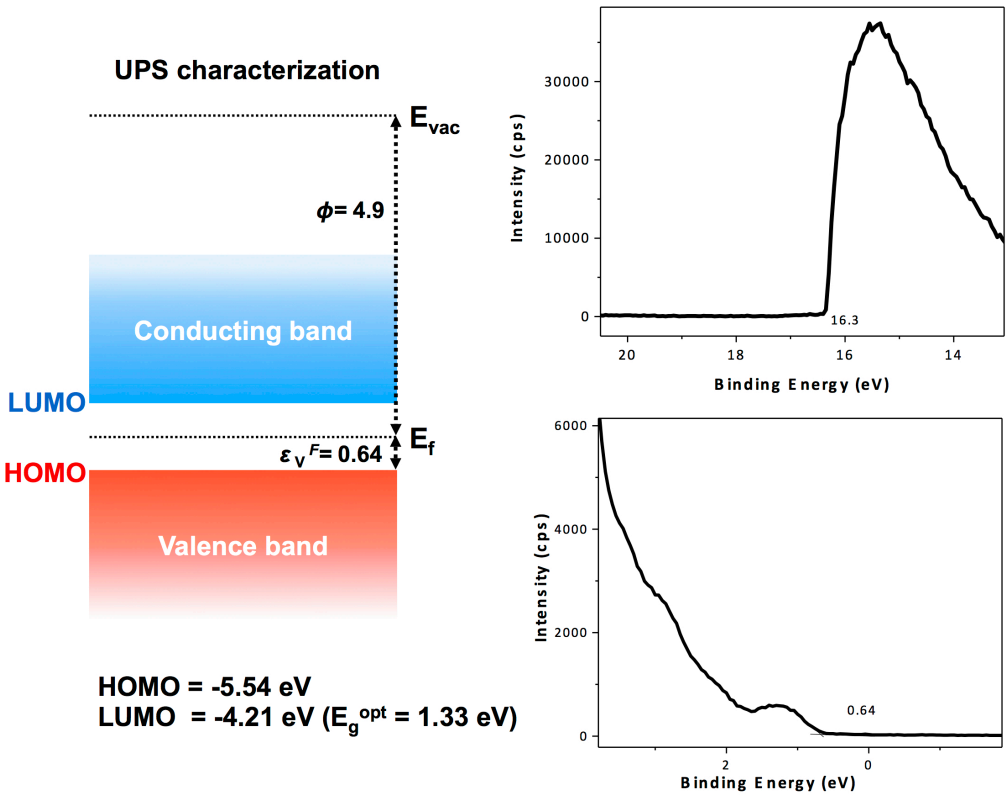

Figure S5.10. UPS characterization of **PDBTz** thin-films after thermal annealing treatment at 150 °C for 30 min.

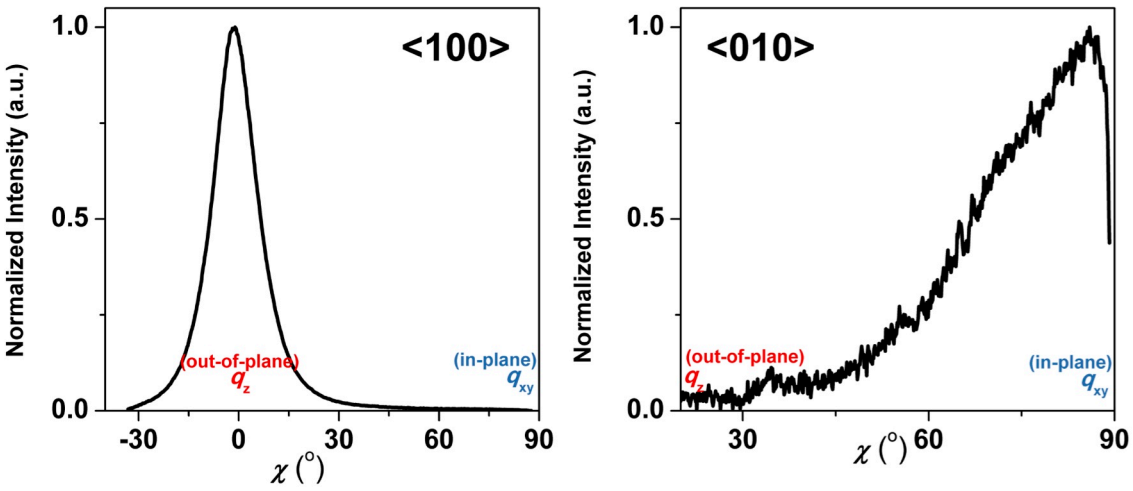

Figure S5.11. The intensity distribution of the <010> and <010> peaks of **PDBTz** films along the χ axis from q_z (out-of-plane, $\chi = 0°$) to q_{xy} (in-plane, $\chi = 90°$).

Reference

[1] a) C. M. Cardona, W. Li, A. E. Kaifer, D. Stockdale, G. C. Bazan, *Adv. Mater.* **2011**, *23*, 2367; b) R. Stalder, J. G. Mei, J. Subbiah, C. Grand, L. A. Estrada, F. So, J. R. Reynolds, *Macromolecules* **2011**, *44*, 6303.

[2] a) X. H. Zhang, B. Domercq, X. D. Wang, S. Yoo, T. Kondo, Z. L. Wang, B. Kippelen, *Org Electron* **2007**, *8*, 718; b) J. B. Kim, C. Fuentes-Hernandez, W. J. Potscavage, X. H. Zhang, B. Kippelen, *Appl Phys Lett* **2009**, *94*.

[3] M. Chang, D. Choi, B. Fu, E. Reichmanis, *ACS Nano* **2013**, *7*, 5402.

[4] a) J. D. Chai, M. Head-Gordon, *J. Chem. Phys.* **2008**, *128*; b) T. H. Dunning, *The Journal of Chemical Physics* **1989**, *90*, 1007; c) D. E. Woon, T. H. Dunning, *The Journal of Chemical Physics* **1993**, *98*, 1358; d) S. Samdal, E. J. Samuelsen, H. V. Volden, *Synth. Met.* **1993**, *59*, 259; e) C. Quattrocchi, R. Lazzaroni, J. L. Bredas, *Chem. Phys. Lett.* **1993**, *208*, 120; f) A. A. Mohamed, *Int. J. Quantum Chem.* **2000**, *79*, 367.

[5] J. W. G. Bloom, S. E. Wheeler, *J. Chem. Theory Comput.* **2014**, *10*, 3647.

[6] T. Körzdörfer, J.-L. Brédas, *Acc. Chem. Res.* **2014**, *47*, 3284.

[7] a) L. Kronik, T. Stein, S. Refaely-Abramson, R. Baer, *J. Chem. Theory Comput.* **2012**, *8*, 1515; b) N. Kuritz, T. Stein, R. Baer, L. Kronik, *J. Chem. Theory*

Comput. **2011**, *7*, 2408; c) R. Baer, E. Livshits, U. Salzner, *Annual Review of Physical Chemistry, Vol 61* **2010**, *61*, 85; d) I. T. Lima, C. Risko, S. G. Aziz, D. A. da Silva Filho, J.-L. Bredas, *J Mater Chem C* **2014**, *2*, 8873.

[8] a) C. Sutton, T. Korzdorfer, M. T. Gray, M. Brunsfeld, R. M. Parrish, C. D. Sherrill, J. S. Sears, J. L. Bredas, *J. Chem. Phys.* **2014**, *140*; b) H. T. Sun, J. Autschbach, *J. Chem. Theory Comput.* **2014**, *10*, 1035.

[9] K. E. Riley, J. A. Platts, J. Rezac, P. Hobza, J. G. Hill, *J. Phys. Chem. A* **2012**, *116*, 4159.

[10] a) M. Lemaire, J. Hassan, L. Lavenot, C. Gozzi, *Tetrahedron Lett.* **1999**, *40*, 857; b) M. O. Wolf, M. S. Wrighton, *Chem. Mater.* **1994**, *6*, 1526; c) B. Y. Fu, J. Baltazar, A. R. Sankar, P. H. Chu, S. Y. Zhang, D. M. Collard, E. Reichmanis, *Adv. Funct. Mater.* **2014**, *24*, 3734.

REFERENCES

[1] a) C. L. Wang, H. L. Dong, W. P. Hu, Y. Q. Liu, D. B. Zhu, *Chem. Rev.* **2012**, *112*, 2208; b) A. J. Heeger, *Chem. Soc. Rev.* **2010**, *39*, 2354; c) S. R. Forrest, *Nature* **2004**, *428*, 911.

[2] a) J. G. Mei, Y. Diao, A. L. Appleton, L. Fang, Z. N. Bao, *J. Am. Chem. Soc.* **2013**, *135*, 6724; b) P. M. Beaujuge, J. M. J. Frechet, *J. Am. Chem. Soc.* **2011**, *133*, 20009.

[3] a) J. Zaumseil, H. Sirringhaus, *Chem. Rev.* **2007**, *107*, 1296; b) C. R. Newman, C. D. Frisbie, D. A. da Silva, J. L. Bredas, P. C. Ewbank, K. R. Mann, *Chem. Mater.* **2004**, *16*, 4436.

[4] a) H. B. Wang, D. H. Yan, *Npg Asia Materials* **2010**, *2*, 69; b) H. Sirringhaus, *Adv. Mater.* **2014**, *26*, 1319.

[5] H. J. Chen, Y. L. Guo, G. Yu, Y. Zhao, J. Zhang, D. Gao, H. T. Liu, Y. Q. Liu, *Adv. Mater.* **2012**, *24*, 4618.

[6] K.-J. Baeg, M. Caironi, Y.-Y. Noh, *Adv. Mater.* **2013**, *25*, 4210.

[7] a) M. L. Hammock, A. Chortos, B. C. K. Tee, J. B. H. Tok, Z. A. Bao, *Adv. Mater.* **2013**, *25*, 5997; b) S. J. Benight, C. Wang, J. B. H. Tok, Z. A. Bao, *Prog. Polym. Sci.* **2013**, *38*, 1961.

[8] a) M. C. Gather, A. Kohnen, K. Meerholz, *Adv Mater* **2011**, *23*, 233; b) R. C. Evans, P. Douglas, C. J. Winscom, *Coordin Chem Rev* **2006**, *250*, 2093; c) B. Geffroy, P. Le Roy, C. Prat, *Polym Int* **2006**, *55*, 572; d) N. T. Kalyani, S. J. Dhoble, *Renew Sust Energ Rev* **2012**, *16*, 2696; e) T. Sekitani, H. Nakajima, H. Maeda, T. Fukushima, T. Aida, K. Hata, T. Someya, *Nat Mater* **2009**, *8*, 494.

[9] Wikipedia, http://en.wikipedia.org/wiki/OLED/ *(Accessed February 2015)*.

[10] OLED-Info.com, http://www.oled-info.com/ubi-flexible-oled-market-will-reach-176-billion-2020/ *(Accessed February 2015)*.

[11] a) T. Lei, J. H. Dou, Z. J. Ma, C. H. Yao, C. J. Liu, J. Y. Wang, J. Pei, *J. Am. Chem. Soc.* **2012**, *134*, 20025; b) H. L. Yip, A. K. Y. Jen, *Energy Environ. Sci.* **2012**, *5*, 5994; c) H. J. Son, B. Carsten, I. H. Jung, L. Yu, *Energy Environ. Sci.* **2012**, *5*, 8158; d) Y. Z. Lin, Y. F. Li, X. W. Zhan, *Chem. Soc. Rev.* **2012**, *41*, 4245; e) B. Kippelen, J. L. Bredas, *Energy Environ. Sci.* **2009**, *2*, 251.

[12] a) J. You, L. Dou, K. Yoshimura, T. Kato, K. Ohya, T. Moriarty, K. Emery, C.-C. Chen, J. Gao, G. Li, Y. Yang, *Nat Commun* **2013**, *4*, 1446; b) Y. S. Liu, C. C. Chen, Z. R. Hong, J. Gao, Y. Yang, H. P. Zhou, L. T. Dou, G. Li, Y. Yang, *Scientific Reports* **2013**, *3*; c) M. C. Scharber, D. Wuhlbacher, M. Koppe, P. Denk, C. Waldauf, A. J. Heeger, C. L. Brabec, *Adv. Mater.* **2006**, *18*, 789; d) S. Mathew, A. Yella, P. Gao, R. Humphry-Baker, B. F. E. Curchod, N. Ashari-Astani, I. Tavernelli, U. Rothlisberger, M. K. Nazeeruddin, M. Gratzel, *Nature Chem.* **2014**, *6*, 242.

[13] a) J. H. Yang, H. L. Yip, A. K. Y. Jen, *Adv. Energy Mater.* **2013**, *3*, 549; b) B. Russ, M. J. Robb, F. G. Brunetti, P. L. Miller, E. E. Perry, S. N. Patel, V. Ho, W. B. Chang, J. J. Urban, M. L. Chabinyc, C. J. Hawker, R. A. Segalman, *Adv Mater* **2014**, *26*, 3473; c) O. Bubnova, Z. U. Khan, A. Malti, S. Braun, M. Fahlman, M. Berggren, X. Crispin, *Nat Mater* **2011**, *10*, 429; d) G. J. Snyder, E. S. Toberer, *Nat Mater* **2008**, *7*, 105.

[14] a) M. A. Baldo, S. Lamansky, P. E. Burrows, M. E. Thompson, S. R. Forrest, *Appl Phys Lett* **1999**, *75*, 4; b) S. K. Park, T. N. Jackson, J. E. Anthony, D. A. Mourey, *Appl Phys Lett* **2007**, *91*; c) R. S. Loewe, S. M. Khersonsky, R. D. McCullough, *Adv. Mater.* **1999**, *11*, 250; d) H. Y. Chen, J. H. Hou, S. Q. Zhang, Y. Y. Liang, G. W. Yang, Y. Yang, L. P. Yu, Y. Wu, G. Li, *Nat. Photonics* **2009**, *3*, 649; e) X. K. Gao, C. A. Di, Y. B. Hu, X. D. Yang, H. Y. Fan, F. Zhang, Y. Q. Liu, H. X. Li, D. B. Zhu, *J. Am. Chem. Soc.* **2010**, *132*, 3697.

[15] A. J. Heeger, *Mrs Bulletin* **2001**, *26*, 900.

[16] a) Z. B. Henson, K. Mullen, G. C. Bazan, *Nature Chem.* **2012**, *4*, 699; b) F. Garnier, A. Yassar, R. Hajlaoui, G. Horowitz, F. Deloffre, B. Servet, S. Ries, P. Alnot, *J. Am. Chem. Soc.* **1993**, *115*, 8716; c) I. Mcculloch, M. Heeney, C. Bailey, K. Genevicius, I. Macdonald, M. Shkunov, D. Sparrowe, S. Tierney, R. Wagner, W. M. Zhang, M. L. Chabinyc, R. J. Kline, M. D. Mcgehee, M. F. Toney, *Nat. Mater.* **2006**, *5*, 328.

[17] a) B. A. Jones, A. Facchetti, M. R. Wasielewski, T. J. Marks, *J. Am. Chem. Soc.* **2007**, *129*, 15259; b) T. A. Chen, X. M. Wu, R. D. Rieke, *J. Am. Chem. Soc.* **1995**, *117*, 233; c) H. Yan, Z. H. Chen, Y. Zheng, C. Newman, J. R. Quinn, F. Dotz, M. Kastler, A. Facchetti, *Nature* **2009**, *457*, 679; d) A. Facchetti, Z. H. Chen, Y. Zheng, H. Yan, *J. Am. Chem. Soc.* **2009**, *131*, 8.

[18] a) H. Sirringhaus, N. Tessler, R. H. Friend, *Science* **1998**, *280*, 1741; b) G. Horowitz, *Adv. Mater.* **1998**, *10*, 365.

[19] a) J. L. Bredas, D. Beljonne, V. Coropceanu, J. Cornil, *Chem. Rev.* **2004**, *104*, 4971; b) W. Brütting, C. Adachi, R. J. Holmes, *Physics of Organic*

Semiconductors, Wiley, **2012**; c) Z. Bao, J. Locklin, *Organic Field-Effect Transistors*, CRC Press, **2007**.

[20] a) L. L. Chua, J. Zaumseil, J. F. Chang, E. C. W. Ou, P. K. H. Ho, H. Sirringhaus, R. H. Friend, *Nature* **2005**, *434*, 194; b) H. Sirringhaus, M. Bird, T. Richards, N. Zhao, *Advanced Materials (Weinheim, Germany)* **2010**, *22*, 3893; c) X. Y. Cheng, M. Caironi, Y. Y. Noh, J. P. Wang, C. Newman, H. Yan, A. Facchetti, H. Sirringhaus, *Chem. Mater.* **2010**, *22*, 1559; d) H. E. Katz, Z. N. Bao, S. L. Gilat, *Acc. Chem. Res.* **2001**, *34*, 359.

[21] X. Y. Cheng, Y. Y. Noh, J. P. Wang, M. Tello, J. Frisch, R. P. Blum, A. Vollmer, J. P. Rabe, N. Koch, H. Sirringhaus, *Adv. Funct. Mater.* **2009**, *19*, 2407.

[22] a) D. Braga, G. Horowitz, *Advanced Materials (Weinheim, Germany)* **2009**, *21*, 1473; b) D. Natali, M. Caironi, *Advanced Materials (Weinheim, Germany)* **2012**, *24*, 1357.

[23] J. Cornil, D. Beljonne, J. P. Calbert, J. L. Bredas, *Adv. Mater.* **2001**, *13*, 1053.

[24] a) M. Wu, K. Pangal, J. C. Sturm, S. Wagner, *Appl Phys Lett* **1999**, *75*, 2244; b) W. Li, S. Varlamov, J. Dore, M. Green, *Mater Lett* **2013**, *107*, 1.

[25] a) E. M. Kaidashev, M. Lorenz, H. von Wenckstern, A. Rahm, H. C. Semmelhack, K. H. Han, G. Benndorf, C. Bundesmann, H. Hochmuth, M. Grundmann, *Appl Phys Lett* **2003**, *82*, 3901; b) E. M. C. Fortunato, P. M. C. Barquinha, A. C. M. B. G. Pimentel, A. M. F. Goncalves, A. J. S. Marques, R. F. P. Martins, L. M. N. Pereira, *Appl Phys Lett* **2004**, *85*, 2541.

[26] a) J. H. Na, M. Kitamura, Y. Arakawa, *Appl Phys Lett* **2008**, *93*; b) H. Yabuta, M. Sano, K. Abe, T. Aiba, T. Den, H. Kumomi, K. Nomura, T. Kamiya, H. Hosono, *Appl Phys Lett* **2006**, *89*; c) M. Kim, J. H. Jeong, H. J. Lee, T. K. Ahn, H. S. Shin, J. S. Park, J. K. Jeong, Y. G. Mo, H. D. Kim, *Appl Phys Lett* **2007**, *90*.

[27] a) J. Li, Y. Zhao, H. S. Tan, Y. L. Guo, C. A. Di, G. Yu, Y. Q. Liu, M. Lin, S. H. Lim, Y. H. Zhou, H. B. Su, B. S. Ong, *Scientific Reports* **2012**, *2*, 754; b) Y. C. Wu, B. Su, L. Jiang, A. J. Heeger, *Adv. Mater.* **2013**, *25*, 6526; c) H. R. Tseng, H. Phan, C. Luo, M. Wang, L. A. Perez, S. N. Patel, L. Ying, E. J. Kramer, T. Q. Nguyen, G. C. Bazan, A. J. Heeger, *Adv. Mater.* **2014**, *26*, 2993; d) G. Kim, S. J. Kang, G. K. Dutta, Y. K. Han, T. J. Shin, Y. Y. Noh, C. Yang, *J. Am. Chem. Soc.* **2014**, *136*, 9477.

[28] a) S. P. Tiwari, X. H. Zhang, W. J. Potscavage, B. Kippelen, *J. Appl. Phys.* **2009**, *106*, 054504; b) A. Luzio, L. Criante, V. D'Innocenzo, M. Caironi, *Sci Rep-Uk* **2013**, *3*; c) T. Lei, J. H. Dou, X. Y. Cao, J. Y. Wang, J. Pei, *Adv Mater* **2013**, *25*, 6589; d) T. Lei, X. Xia, J.-Y. Wang, C.-J. Liu, J. Pei, *J Am Chem Soc* **2014**, *136*,

2135; e) H. Y. Li, F. S. Kim, G. Q. Ren, S. A. Jenekhe, *J Am Chem Soc* **2013**, *135*, 14920.

[29] a) Y. Zhao, Y. L. Guo, Y. Q. Liu, *Adv Mater* **2013**, *25*, 5372; b) X. Gao, Y. Hu, *J Mater Chem C* **2014**, *2*, 3099; c) M. Sommer, *J Mater Chem C* **2014**, *2*, 3088; d) H. Usta, A. Facchetti, T. J. Marks, *Acc. Chem. Res.* **2011**, *44*, 501.

[30] a) C. C. Chueh, K. Yao, H. L. Yip, C. Y. Chang, Y. X. Xu, K. S. Chen, C. Z. Li, P. Liu, F. Huang, Y. W. Chen, W. C. Chenb, A. K. Y. Jen, *Energy Environ. Sci.* **2013**, *6*, 3241; b) Y. Chen, S. Q. Zhang, Y. Wu, J. H. Hou, *Adv. Mater.* **2014**, *26*, 2744; c) H.-J. Yun, G. B. Lee, D. S. Chung, Y.-H. Kim, S.-K. Kwon, *Adv. Mater.* **2014**, *26*, 6612.

[31] a) A. C. Mayer, M. F. Toney, S. R. Scully, J. Rivnay, C. J. Brabec, M. Scharber, M. Koppe, M. Heeney, I. McCulloch, M. D. McGehee, *Adv. Funct. Mater.* **2009**, *19*, 1173; b) J. Lee, A. R. Han, H. Yu, T. J. Shin, C. Yang, J. H. Oh, *J. Am. Chem. Soc.* **2013**, *135*, 9540; c) M. S. Chen, O. P. Lee, J. R. Niskala, A. T. Yiu, C. J. Tassone, K. Schmidt, P. M. Beaujuge, S. S. Onishi, M. F. Toney, A. Zettl, J. M. J. Frechet, *J. Am. Chem. Soc.* **2013**, *135*, 19229; d) B. G. Kim, E. J. Jeong, J. W. Chung, S. Seo, B. Koo, J. S. Kim, *Nat. Mater.* **2013**, *12*, 659; e) L. Meager, R. S. Ashraf, S. Mollinger, B. C. Schroeder, H. Bronstein, D. Beatrup, M. S. Vezie, T. Kirchartz, A. Salleo, J. Nelson, L. McCulloch, *J. Am. Chem. Soc.* **2013**, *135*, 11537; f) T. Lei, J. H. Dou, J. Pei, *Adv. Mater.* **2012**, *24*, 6457.

[32] a) Y. F. Li, Y. Cao, J. Gao, D. L. Wang, G. Yu, A. J. Heeger, *Synth. Met.* **1999**, *99*, 243; b) V. Coropceanu, J. Cornil, D. A. da Silva, Y. Olivier, R. Silbey, J. L. Bredas, *Chem. Rev.* **2007**, *107*, 926.

[33] B. Y. Fu, J. Baltazar, Z. K. Hu, A. T. Chien, S. Kumar, C. L. Henderson, D. M. Collard, E. Reichmanis, *Chem. Mater.* **2012**, *24*, 4123.

[34] B. Y. Fu, J. Baltazar, A. R. Sankar, P. H. Chu, S. Y. Zhang, D. M. Collard, E. Reichmanis, *Adv. Funct. Mater.* **2014**, *24*, 3734.

[35] B. Fu, C. Y. Wang, B. D. Rose, Y. Jiang, M. Chang, P. H. Chu, Z. Yuan, C. Fuentes-Hernandez, B. Kippelen, J. Brédas, D. M. Collard, E. Reichmanis, (Ed.: Submitted), **2015**.

[36] V. C. Sundar, J. Zaumseil, V. Podzorov, E. Menard, R. L. Willett, T. Someya, M. E. Gershenson, J. A. Rogers, *Science* **2004**, *303*, 1644.

[37] a) D. Knipp, R. A. Street, A. Volkel, J. Ho, *J Appl Phys* **2003**, *93*, 347; b) S. E. Fritz, S. M. Martin, C. D. Frisbie, M. D. Ward, M. F. Toney, *J Am Chem Soc* **2004**, *126*, 4084.

[38] Z. X. Liang, Q. Tang, J. B. Xu, Q. A. Miao, *Adv. Mater.* **2011**, *23*, 1535.

[39] H. Minemawari, T. Yamada, H. Matsui, J. Tsutsumi, S. Haas, R. Chiba, R. Kumai, T. Hasegawa, *Nature* **2011**, *475*, 364.

[40] a) B. Kosata, V. Kozmik, J. Svoboda, V. Novotna, P. Vanek, M. Glogarova, *Liq Cryst* **2003**, *30*, 603; b) H. Ebata, T. Izawa, E. Miyazaki, K. Takimiya, M. Ikeda, H. Kuwabara, T. Yui, *J Am Chem Soc* **2007**, *129*, 15732; c) A. Y. Amin, A. Khassanov, K. Reuter, T. Meyer-Friedrichsen, M. Halik, *J Am Chem Soc* **2012**, *134*, 16548; d) T. Mori, T. Nishimura, T. Yamamoto, I. Doi, E. Miyazaki, I. Osaka, K. Takimiya, *J Am Chem Soc* **2013**, *135*, 13900; e) K. Niimi, S. Shinamura, I. Osaka, E. Miyazaki, K. Takimiya, *J. Am. Chem. Soc.* **2011**, *133*, 8732; f) A. N. Sokolov, S. Atahan-Evrenk, R. Mondal, H. B. Akkerman, R. S. Sanchez-Carrera, S. Granados-Focil, J. Schrier, S. C. B. Mannsfeld, A. P. Zoombelt, Z. N. Bao, A. Aspuru-Guzik, *Nature Communications* **2011**, *2*; g) X. H. Zhang, B. Domercq, X. D. Wang, S. Yoo, T. Kondo, Z. L. Wang, B. Kippelen, *Org Electron* **2007**, *8*, 718; h) F. J. Zhang, Y. B. Hu, T. Schuettfort, C. A. Di, X. K. Gao, C. R. McNeill, L. Thomsen, S. C. B. Mannsfeld, W. Yuan, H. Sirringhaus, D. B. Zhu, *J Am Chem Soc* **2013**, *135*, 2338; i) J. J. Chang, Q. Ye, K. W. Huang, J. Zhang, Z. K. Chen, J. S. Wu, C. Y. Chi, *Org Lett* **2012**, *14*, 2964; j) J. H. Oh, S. L. Suraru, W. Y. Lee, M. Konemann, H. W. Hoffken, C. Roger, R. Schmidt, Y. Chung, W. C. Chen, F. Wurthner, Z. N. Bao, *Adv. Funct. Mater.* **2010**, *20*, 2148; k) B. J. Jung, K. Lee, J. Sun, A. G. Andreou, H. E. Katz, *Adv. Funct. Mater.* **2010**, *20*, 2930; l) B. A. Jones, M. J. Ahrens, M. H. Yoon, A. Facchetti, T. J. Marks, M. R. Wasielewski, *Angew Chem Int Edit* **2004**, *43*, 6363; m) R. Schmidt, J. H. Oh, Y. S. Sun, M. Deppisch, A. M. Krause, K. Radacki, H. Braunschweig, M. Konemann, P. Erk, Z. A. Bao, F. Wurthner, *J Am Chem Soc* **2009**, *131*, 6215; n) J. Rivnay, L. H. Jimison, J. E. Northrup, M. F. Toney, R. Noriega, S. F. Lu, T. J. Marks, A. Facchetti, A. Salleo, *Nat. Mater.* **2009**, *8*, 952; o) C. D. Sheraw, T. N. Jackson, D. L. Eaton, J. E. Anthony, *Adv Mater* **2003**, *15*, 2009; p) S. Miao, A. L. Appleton, N. Berger, S. Barlow, S. R. Marder, K. I. Hardcastle, U. H. F. Bunz, *Chem-Eur J* **2009**, *15*, 4990; q) D. Q. Liu, X. M. Xu, Y. R. Su, Z. K. He, J. B. Xu, Q. Miao, *Angewandte Chemie-International Edition* **2013**, *52*, 6222; r) Y. L. Qiao, Y. L. Guo, C. M. Yu, F. J. Zhang, W. Xu, Y. Q. Liu, D. B. Zhu, *J Am Chem Soc* **2012**, *134*, 4084.

[41] a) M. Melucci, L. Favaretto, A. Zanelli, M. Cavallini, A. Bongini, P. Maccagnani, P. Ostojo, G. Derue, R. Lazzaroni, G. Barbarello, *Adv. Funct. Mater.* **2010**, *20*, 445; b) E. Da Como, M. A. Loi, M. Murgia, R. Zamboni, M. Muccini, *J Am Chem Soc* **2006**, *128*, 4277; c) Y. Zhang, C. Kim, J. Lin, T. Q. Nguyen, *Adv. Funct. Mater.* **2012**, *22*, 97; d) J. Youn, P. Y. Huang, Y. W. Huang, M. C. Chen, Y. J. Lin, H. Huang, R. P. Ortiz, C. Stern, M. C. Chung, C. Y. Feng, L. H. Chen, A. Facchetti, T. J. Marks, *Adv. Funct. Mater.* **2012**, *22*, 48; e) S. Ando, R.

Murakami, J. Nishida, H. Tada, Y. Inoue, S. Tokito, Y. Yamashita, *J Am Chem Soc* **2005**, *127*, 14996; f) D. K. Hwang, R. R. Dasari, M. Fenoll, V. Alain-Rizzo, A. Dindar, J. W. Shim, N. Deb, C. Fuentes-Hernandez, S. Barlow, D. G. Bucknall, P. Audebert, S. R. Marder, B. Kippelen, *Adv Mater* **2012**, *24*, 4445.

[42] K. Takimiya, S. Shinamura, I. Osaka, E. Miyazaki, *Adv Mater* **2011**, *23*, 4347.

[43] H. Y. Li, B. C. K. Tee, J. J. Cha, Y. Cui, J. W. Chung, S. Y. Lee, Z. N. Bao, *J Am Chem Soc* **2012**, *134*, 2760.

[44] a) A. L. Appleton, S. M. Brombosz, S. Barlow, J. S. Sears, J. L. Bredas, S. R. Marder, U. H. F. Bunz, *Nat. Commun.* **2010**, *1*; b) C. Reese, Z. N. Bao, *Materials Today* **2007**, *10*, 20.

[45] Y. Diao, B. C. K. Tee, G. Giri, J. Xu, D. H. Kim, H. A. Becerril, R. M. Stoltenberg, T. H. Lee, G. Xue, S. C. B. Mannsfeld, Z. N. Bao, *Nat. Mater.* **2013**, *12*, 665.

[46] Y. B. Yuan, G. Giri, A. L. Ayzner, A. P. Zoombelt, S. C. B. Mannsfeld, J. H. Chen, D. Nordlund, M. F. Toney, J. S. Huang, Z. N. Bao, *Nature Communications* **2014**, *5*.

[47] H. K. Tian, Y. F. Deng, F. Pan, L. Z. Huang, D. H. Yan, Y. H. Geng, F. S. Wang, *J. Mater. Chem.* **2010**, *20*, 7998.

[48] a) D. T. James, B. K. C. Kjellander, W. T. T. Smaal, G. H. Gelinck, C. Combe, I. McCulloch, R. Wilson, J. H. Burroughes, D. D. C. Bradley, J. S. Kim, *ACS Nano* **2011**, *5*, 9824; b) J. Smith, R. Hamilton, I. McCulloch, N. Stingelin-Stutzmann, M. Heeney, D. D. C. Bradley, T. D. Anthopoulos, *J. Mater. Chem.* **2010**, *20*, 2562; c) M. B. Madec, D. Crouch, G. R. Llorente, T. J. Whittle, M. Geoghegan, S. G. Yeates, *J. Mater. Chem.* **2008**, *18*, 3230.

[49] a) R. Hamilton, J. Smith, S. Ogier, M. Heeney, J. E. Anthony, I. McCulloch, J. Veres, D. D. C. Bradley, T. D. Anthopoulos, *Adv. Mater.* **2009**, *21*, 1166; b) J. Smith, W. M. Zhang, R. Sougrat, K. Zhao, R. P. Li, D. K. Cha, A. Amassian, M. Heeney, I. McCulloch, T. D. Anthopoulos, *Adv Mater* **2012**, *24*, 2441.

[50] a) T. A. Chen, R. D. Rieke, *J. Am. Chem. Soc.* **1992**, *114*, 10087; b) R. D. Mccullough, R. D. Lowe, M. Jayaraman, D. L. Anderson, *J. Org. Chem.* **1993**, *58*, 904.

[51] a) T. Yamamoto, D. Komarudin, M. Arai, B. L. Lee, H. Suganuma, N. Asakawa, Y. Inoue, K. Kubota, S. Sasaki, T. Fukuda, H. Matsuda, *J. Am. Chem. Soc.* **1998**, *120*, 2047; b) T. Yamamoto, S. Otsuka, K. Namekawa, H. Fukumoto, I. Yamaguchi, T. Fukuda, N. Asakawa, T. Yamanobe, T. Shiono, Z. G. Cai, *Polymer* **2006**, *47*, 6038.

[52] a) J. Lee, S. Cho, J. H. Seo, P. Anant, J. Jacob, C. Yang, *J. Mater. Chem.* **2012**, *22*, 1504; b) C. Kanimozhi, N. Yaacobi-Gross, K. W. Chou, A. Amassian, T. D. Anthopoulos, S. Patil, *J. Am. Chem. Soc.* **2012**, *134*, 16532.

[53] X. R. Zhang, L. J. Richter, D. M. DeLongchamp, R. J. Kline, M. R. Hammond, I. McCulloch, M. Heeney, R. S. Ashraf, J. N. Smith, T. D. Anthopoulos, B. Schroeder, Y. H. Geerts, D. A. Fischer, M. F. Toney, *J. Am. Chem. Soc.* **2011**, *133*, 15073.

[54] a) R. Stalder, J. G. Mei, J. Subbiah, C. Grand, L. A. Estrada, F. So, J. R. Reynolds, *Macromolecules* **2011**, *44*, 6303; b) B. S. Ong, Y. L. Wu, P. Liu, S. Gardner, *J. Am. Chem. Soc.* **2004**, *126*, 3378; c) M. Heeney, C. Bailey, K. Genevicius, M. Shkunov, D. Sparrowe, S. Tierney, I. McCulloch, *J. Am. Chem. Soc.* **2005**, *127*, 1078; d) I. Osaka, T. Abe, S. Shinamura, E. Miyazaki, K. Takimiya, *J. Am. Chem. Soc.* **2010**, *132*, 5000; e) I. Osaka, T. Abe, S. Shinamura, K. Takimiya, *J. Am. Chem. Soc.* **2011**, *133*, 6852.

[55] I. Osaka, M. Saito, H. Mori, T. Koganezawa, K. Takimiya, *Adv. Mater.* **2012**, *24*, 425.

[56] a) C. Piliego, T. W. Holcombe, J. D. Douglas, C. H. Woo, P. M. Beaujuge, J. M. J. Frechet, *J. Am. Chem. Soc.* **2010**, *132*, 7595; b) X. Guo, R. P. Ortiz, Y. Zheng, Y. Hu, Y.-Y. Noh, K.-J. Baeg, A. Facchetti, T. J. Marks, *J. Am. Chem. Soc.* **2011**, *133*, 1405.

[57] Z. H. Chen, Y. Zheng, H. Yan, A. Facchetti, *J Am Chem Soc* **2009**, *131*, 8.

[58] H. Y. Li, F. S. Kim, G. Q. Ren, E. C. Hollenbeck, S. Subramaniyan, S. A. Jenekhe, *Angew Chem Int Edit* **2013**, *52*, 5513.

[59] J. D. Yuen, R. Kumar, D. Zakhidov, J. Seifter, B. Lim, A. J. Heeger, F. Wudl, *Adv. Mater.* **2011**, *23*, 3780.

[60] X. Guo, F. S. Kim, M. J. Seger, S. A. Jenekhe, M. D. Watson, *Chemistry of Materials* **2012**, *24*, 1434.

[61] a) I. Kang, H. J. Yun, D. S. Chung, S. K. Kwon, Y. H. Kim, *J. Am. Chem. Soc.* **2013**, *135*, 14896; b) L. Ying, B. B. Y. Hsu, H. M. Zhan, G. C. Welch, P. Zalar, L. A. Perez, E. J. Kramer, T. Q. Nguyen, A. J. Heeger, W. Y. Wong, G. C. Bazan, *J. Am. Chem. Soc.* **2011**, *133*, 18538; c) Y. P. Zou, A. Najari, P. Berrouard, S. Beaupre, B. R. Aich, Y. Tao, M. Leclerc, *J. Am. Chem. Soc.* **2010**, *132*, 5330; d) R. Kim, P. S. K. Amegadze, I. Kang, H. J. Yun, Y. Y. Noh, S. K. Kwon, Y. H. Kim, *Adv. Funct. Mater.* **2013**, *23*, 5719; e) J. H. Park, E. H. Jung, J. W. Jung, W. H. Jo, *Adv. Mater.* **2013**, *25*, 2583; f) B. Sun, W. Hong, Z. Yan, H. Aziz, Y. Li, *Adv Mater* **2014**, n/a; g) S. G. Hahm, Y. Rho, J. Jung, S. H. Kim, T. Sajoto, F. S.

Kim, S. Barlow, C. E. Park, S. A. Jenekhe, S. R. Marder, M. Ree, *Adv. Funct. Mater.* **2013**, *23*, 2060.

[62] A. Facchetti, *Chem. Mater.* **2011**, *23*, 733.

[63] a) H. C. Yang, T. J. Shin, L. Yang, K. Cho, C. Y. Ryu, Z. N. Bao, *Adv. Funct. Mater.* **2005**, *15*, 671; b) G. Li, Y. Yao, H. Yang, V. Shrotriya, G. Yang, Y. Yang, *Adv. Funct. Mater.* **2007**, *17*, 1636; c) A. R. Aiyar, J. I. Hong, E. Reichmanis, *Chem. Mater.* **2012**, *24*, 2845.

[64] J. Mei, Z. Bao, *Chem. Mater.* **2014**, *26*, 604.

[65] a) M. Sato, S. Tanaka, K. Kaeriyama, *Synth. Met.* **1986**, *14*, 279; b) U. Salzner, J. B. Lagowski, P. G. Pickup, R. A. Poirier, *Synth. Met.* **1998**, *96*, 177.

[66] B. W. Boudouris, V. Ho, L. H. Jimison, M. F. Toney, A. Salleo, R. A. Segalman, *Macromolecules* **2011**, *44*, 6653.

[67] J. H. Liu, I. A. Mikhaylov, J. H. Zou, I. Osaka, A. E. Masunov, R. D. McCullough, L. Zhai, *Polymer* **2011**, *52*, 2302.

[68] G. Sauve, A. E. Javier, R. Zhang, J. Y. Liu, S. A. Sydlik, T. Kowalewski, R. D. McCullough, *J. Mater. Chem.* **2010**, *20*, 3195.

[69] R. A. J. Janssen, J. C. Bijleveld, A. P. Zoombelt, S. G. J. Mathijssen, M. M. Wienk, M. Turbiez, D. M. de Leeuw, *J. Am. Chem. Soc.* **2009**, *131*, 16616.

[70] M. D. Watson, X. G. Guo, *Org. Lett.* **2008**, *10*, 5333.

[71] K. H. Ong, S. L. Lim, H. S. Tan, H. K. Wong, J. Li, Z. Ma, L. C. H. Moh, S. H. Lim, J. C. De Mello, Z. K. Chen, *Adv. Mater.* **2011**, *23*, 1409.

[72] S. C. Price, A. C. Stuart, L. Q. Yang, H. X. Zhou, W. You, *J. Am. Chem. Soc.* **2011**, *133*, 4625.

[73] a) P. Sonar, S. P. Singh, Y. Li, M. S. Soh, A. Dodabalapur, *Adv. Mater.* **2010**, *22*, 5409; b) Y. N. Li, S. P. Singh, P. Sonar, *Adv. Mater.* **2010**, *22*, 4862.

[74] a) N. A. Brunelli, S. A. Didas, K. Venkatasubbaiah, C. W. Jones, *J. Am. Chem. Soc.* **2012**, *134*, 13950; b) T. Lei, Y. Cao, Y. L. Fan, C. J. Liu, S. C. Yuan, J. Pei, *J. Am. Chem. Soc.* **2011**, *133*, 6099.

[75] a) R. S. Ashraf, A. J. Kronemeijer, D. I. James, H. Sirringhaus, I. McCulloch, *Chem. Commun. (Cambridge, U. K.)* **2012**, *48*, 3939; b) G. W. P. Van Pruissen, F. Gholamrezaie, M. M. Wienk, R. A. J. Janssen, *J. Mater. Chem.* **2012**, *22*, 20387.

[76] H. J. Chen, Y. L. Guo, Z. P. Mao, G. Yu, J. Y. Huang, Y. Zhao, Y. Q. Liu, *Chemistry of Materials* **2013**, *25*, 3589.

[77] J. Lee, A. R. Han, J. Kim, Y. Kim, J. H. Oh, C. Yang, *J. Am. Chem. Soc.* **2012**, *134*, 20713.

[78] a) J. G. Mei, D. H. Kim, A. L. Ayzner, M. F. Toney, Z. A. Bao, *J. Am. Chem. Soc.* **2011**, *133*, 20130; b) J. H. Dou, Y. Q. Zheng, T. Lei, S. D. Zhang, Z. Wang, W. B. Zhang, J. Y. Wang, J. Pei, *Adv. Funct. Mater.* **2014**, *24*, 6270.

[79] a) P. Leriche, J. M. Raimundo, M. Turbiez, V. Monroche, M. Allain, F. X. Sauvage, J. Roncali, P. Frere, P. J. Skabara, *J. Mater. Chem.* **2003**, *13*, 1324; b) S. H. Jung, H. K. Kim, S. H. Kim, Y. H. Kim, S. C. Jeoung, D. Kim, *Macromolecules* **2000**, *33*, 9277.

[80] I. Osaka, G. Sauve, R. Zhang, T. Kowalewski, R. D. McCullough, *Adv. Mater.* **2007**, *19*, 4160.

[81] S. Q. Xiao, A. C. Stuart, S. B. Liu, H. X. Zhou, W. You, *Adv. Funct. Mater.* **2010**, *20*, 635.

[82] C. Winnewisser, L. Burgi, M. Turbiez, R. Pfeiffer, F. Bienewald, H. J. Kirner, *Adv. Mater.* **2008**, *20*, 2217.

[83] J. R. Reynolds, R. Stalder, J. G. Mei, *Macromolecules* **2010**, *43*, 8348.

[84] H. A. Saadeh, L. Lu, F. He, J. E. Bullock, W. Wang, B. Carsten, L. Yu, *Acs Macro Lett* **2012**, *1*, 361.

[85] Y. Takeda, T. L. Andrew, J. M. Lobez, A. J. Mork, T. M. Swager, *Angew Chem Int Edit* **2012**, *51*, 9042.

[86] J. F. Chang, B. Q. Sun, D. W. Breiby, M. M. Nielsen, T. I. Solling, M. Giles, I. McCulloch, H. Sirringhaus, *Chem. Mater.* **2004**, *16*, 4772.

[87] B. R. Aich, S. Beaupre, M. Leclerc, Y. Tao, *Organic Electronics* **2014**, *15*, 543.

[88] W.-Y. Lee, G. Giri, Y. Diao, C. J. Tassone, J. R. Matthews, M. L. Sorensen, S. C. B. Mannsfeld, W.-C. Chen, H. H. Fong, J. B. H. Tok, M. F. Toney, M. He, Z. Bao, *Adv. Funct. Mater.* **2014**, n/a.

[89] A. R. Aiyar, J. I. Hong, R. Nambiar, D. M. Collard, E. Reichmanis, *Adv. Funct. Mater.* **2011**, *21*, 2652.

[90] G. Giri, E. Verploegen, S. C. B. Mannsfeld, S. Atahan-Evrenk, D. H. Kim, S. Y. Lee, H. A. Becerril, A. Aspuru-Guzik, M. F. Toney, Z. A. Bao, *Nature* **2011**, *480*, 504.

[91] a) R. R. Sondergaard, M. Hosel, F. C. Krebs, *Journal of Polymer Science Part B-Polymer Physics* **2013**, *51*, 16; b) M. Brinkmann, L. Hartmann, L. Biniek, K. Tremel, N. Kayunkid, *Macromol. Rapid Commun.* **2014**, *35*, 9.

[92] a) P. Apilo, J. Hiltunen, M. Välimäki, S. Heinilehto, R. Sliz, J. Hast, *Progress in Photovoltaics: Research and Applications* **2014**, n/a; b) F. C. Krebs, *Sol. Energy Mater. Sol. Cells* **2009**, *93*, 394.

[93] a) C. Luo, A. K. K. Kyaw, L. A. Perez, S. Patel, M. Wang, B. Grimm, G. C. Bazan, E. J. Kramer, A. J. Heeger, *Nano Lett.* **2014**, *14*, 2764; b) H. R. Tseng, L. Ying, B. B. Y. Hsu, L. A. Perez, C. J. Takacs, G. C. Bazan, A. J. Heeger, *Nano Lett.* **2012**, *12*, 6353.

[94] a) M. Singh, H. M. Haverinen, P. Dhagat, G. E. Jabbour, *Adv. Mater.* **2010**, *22*, 673; b) B. Derby, *Annu. Rev. Mater. Res.* **2010**, *40*, 395; c) H. N. Tsao, K. Mullen, *Chem. Soc. Rev.* **2010**, *39*, 2372.

[95] K. Mathauer, P. van der Schaaf, J. Brill, in *Proc. SPIE, Vol. 8831*, **2013**, pp. 883102.

[96] a) R. Zhang, B. Li, M. C. Iovu, M. Jeffries-EL, G. Sauve, J. Cooper, S. J. Jia, S. Tristram-Nagle, D. M. Smilgies, D. N. Lambeth, R. D. McCullough, T. Kowalewski, *J. Am. Chem. Soc.* **2006**, *128*, 3480; b) R. J. Kline, M. D. McGehee, E. N. Kadnikova, J. S. Liu, J. M. J. Frechet, *Adv. Mater.* **2003**, *15*, 1519.

[97] a) A. Zen, J. Pflaum, S. Hirschmann, W. Zhuang, F. Jaiser, U. Asawapirom, J. P. Rabe, U. Scherf, D. Neher, *Adv. Funct. Mater.* **2004**, *14*, 757; b) A. M. Ballantyne, L. Chen, J. Dane, T. Hammant, F. M. Braun, M. Heeney, W. Duffy, I. McCulloch, D. D. C. Bradley, J. Nelson, *Adv. Funct. Mater.* **2008**, *18*, 2373.

[98] J. F. Chang, J. Clark, N. Zhao, H. Sirringhaus, D. W. Breiby, J. W. Andreasen, M. M. Nielsen, M. Giles, M. Heeney, I. McCulloch, *Physical Review B* **2006**, *74*.

[99] R. Noriega, J. Rivnay, K. Vandewal, F. P. V. Koch, N. Stingelin, P. Smith, M. F. Toney, A. Salleo, *Nat. Mater.* **2013**, *12*, 1037.

[100] a) R. C. Coffin, J. Peet, J. Rogers, G. C. Bazan, *Nature Chem.* **2009**, *1*, 657; b) K. Koynov, A. Bahtiar, T. Ahn, R. M. Cordeiro, H. H. Horhold, C. Bubeck, *Macromolecules* **2006**, *39*, 8692; c) H. N. Tsao, D. M. Cho, I. Park, M. R. Hansen, A. Mavrinskiy, D. Y. Yoon, R. Graf, W. Pisula, H. W. Spiess, K. Mullen, *J. Am. Chem. Soc.* **2011**, *133*, 2605; d) A. V. Tunc, B. Ecker, Z. Dogruyol, S. Juchter, A. L. Ugur, A. Erdogmus, S. E. San, J. Parisi, E. von Hauff, *Journal of Polymer Science Part B-Polymer Physics* **2012**, *50*, 117; e) T.-Y. Chu, J. Lu, S. Beaupré, Y. Zhang, J.-R. Pouliot, J. Zhou, A. Najari, M. Leclerc, Y. Tao, *Adv. Funct. Mater.* **2012**, *22*, 2345.

[101] T. Nakano, *pi-Stacked Polymers and Molecules: Theory, Synthesis, and Properties*, Springer Japan, **2013**.

[102] H. Klauk, *Organic Electronics II: More Materials and Applications*, Wiley, **2012**.

[103] a) J. L. Bredas, J. P. Calbert, D. A. da Silva, J. Cornil, *Proc. Natl. Acad. Sci. U. S. A.* **2002**, *99*, 5804; b) X. L. Feng, V. Marcon, W. Pisula, M. R. Hansen, J. Kirkpatrick, F. Grozema, D. Andrienko, K. Kremer, K. Mullen, *Nat. Mater.* **2009**, *8*, 421.

[104] R. E. i. E. Transfer.

[105] H. T. Yi, Y. Chen, K. Czelen, V. Podzorov, *Adv Mater* **2011**, *23*, 5807.

[106] H. T. Yi, M. M. Payne, J. E. Anthony, V. Podzorov, *Nature Communications* **2012**, *3*.

[107] B. Balan, C. Vijayakumar, A. Saeki, Y. Koizumi, S. Seki, *Macromolecules* **2012**, *45*, 2709.

[108] R. S. Loewe, P. C. Ewbank, J. S. Liu, L. Zhai, R. D. McCullough, *Macromolecules* **2001**, *34*, 4324.

[109] a) P. T. Henderson, D. M. Collard, *Chem. Mater.* **1995**, *7*, 1879; b) S. C. Rasmussen, J. C. Pickens, J. E. Hutchison, *Chem. Mater.* **1998**, *10*, 1990.

[110] a) J. K. Stille, *Angew. Chem. Int. Ed.* **1986**, *25*, 508; b) V. Farina, V. Krishnamurthy, W. J. Scott, in *Organic Reactions*, John Wiley & Sons, Inc., **2004**; c) C. Torborg, M. Beller, *Adv Synth Catal* **2009**, *351*, 3027.

[111] a) F. S. Han, *Chem Soc Rev* **2013**, *42*, 5270; b) N. Miyaura, A. Suzuki, *Chem Rev* **1995**, *95*, 2457.

[112] a) K. Sonogashira, *J Organomet Chem* **2002**, *653*, 46; b) R. Chinchilla, C. Najera, *Chem Rev* **2007**, *107*, 874; c) R. Chinchilla, C. Najera, *Chem Soc Rev* **2011**, *40*, 5084.

[113] a) J. A. Casares, P. Espinet, B. Fuentes, G. Salas, *J Am Chem Soc* **2007**, *129*, 3508; b) G. Lessene, *Aust J Chem* **2004**, *57*, 107.

[114] D. Mc Cartney, P. J. Guiry, *Chem Soc Rev* **2011**, *40*, 5122.

[115] F. So, C. M. Amb, S. Chen, K. R. Graham, J. Subbiah, C. E. Small, J. R. Reynolds, *J. Am. Chem. Soc.* **2011**, *133*, 10062.

[116] P. Berrouard, A. Najari, A. Pron, D. Gendron, P. O. Morin, J. R. Pouliot, J. Veilleux, M. Leclerc, *Angew Chem Int Edit* **2012**, *51*, 2068.

[117] a) Q. Guo, J. X. Dong, D. Y. Wan, D. Wu, J. S. You, *Macromol Rapid Comm* **2013**, *34*, 522; b) M. Wakioka, Y. Kitano, F. Ozawa, *Macromolecules* **2013**, *46*, 370; c) J. Kuwabara, T. Yasuda, S. J. Choi, W. Lu, K. Yamazaki, S. Kagaya, L. Han, T. Kanbara, *Adv. Funct. Mater.* **2014**, *24*, 3226; d) J. Jo, A. Pron, P.

Berrouard, W. L. Leong, J. D. Yuen, J. S. Moon, M. Leclerc, A. J. Heeger, *Advanced Energy Materials* **2012**, *2*, 1397.

[118] L. G. Mercier, M. Leclerc, *Accounts Chem Res* **2013**, *46*, 1597.

[119] A. E. Rudenko, B. C. Thompson, *J Polym Sci Pol Chem* **2015**, *53*, 135.

[120] X. F. Liu, W. Wen, G. C. Bazan, *Adv. Mater.* **2012**, *24*, 4505.

[121] a) V. Senkovskyy, R. Tkachov, H. Komber, M. Sommer, M. Heuken, B. Voit, W. T. S. Huck, V. Kataev, A. Petr, A. Kiriy, *J. Am. Chem. Soc.* **2011**, *133*, 19966; b) V. Senkovskyy, R. Tkachov, H. Komber, A. John, J. U. Sommer, A. Kiriy, *Macromolecules* **2012**, *45*, 7770.

[122] G. C. Schmidt, D. Hoft, K. Haase, A. C. Hubler, E. Karpov, R. Tkachov, M. Stamm, A. Kiriy, F. Haidu, D. R. T. Zahn, H. Yan, A. Facchetti, *Journal of Materials Chemistry C* **2014**, *2*, 5149.

[123] R. S. Ashraf, M. Shahid, E. Klemm, M. Al-Ibrahim, S. Sensfuss, *Macromol. Rapid Commun.* **2006**, *27*, 1454.

[124] S. Lee, D. C. Paine, K. K. Gleason, *Adv Funct Mater* **2014**, *24*, 7187.

[125] D. C. Borrelli, S. Lee, K. K. Gleason, *J Mater Chem C* **2014**, *2*, 7223.

[126] a) M. Saito, I. Osaka, E. Miyazaki, K. Takimiya, H. Kuwabara, M. Ikeda, *Tetrahedron Lett* **2011**, *52*, 285; b) S. Shinamura, I. Osaka, E. Miyazaki, A. Nakao, M. Yamagishi, J. Takeya, K. Takimiya, *J. Am. Chem. Soc.* **2011**, *133*, 5024; c) S. Subramanian, S. K. Park, S. R. Parkin, V. Podzorov, T. N. Jackson, J. E. Anthony, *J Am Chem Soc* **2008**, *130*, 2706.

[127] a) J. H. Hou, M. H. Park, S. Q. Zhang, Y. Yao, L. M. Chen, J. H. Li, Y. Yang, *Macromolecules* **2008**, *41*, 6012; b) Y. Y. Liang, D. Q. Feng, Y. Wu, S. T. Tsai, G. Li, C. Ray, L. P. Yu, *J. Am. Chem. Soc.* **2009**, *131*, 7792; c) L. J. Huo, J. H. Hou, S. Q. Zhang, H. Y. Chen, Y. Yang, *Angew. Chem. Int. Edit.* **2010**, *49*, 1500; d) G. L. Gibson, T. M. McCormick, D. S. Seferos, *J. Am. Chem. Soc.* **2012**, *134*, 539; e) J. C. Bijleveld, M. Shahid, J. Gilot, M. M. Wienk, R. A. J. Janssen, *Adv. Funct. Mater.* **2009**, *19*, 3262; f) J. Y. Liu, R. Zhang, G. Sauve, T. Kowalewski, R. D. McCullough, *J. Am. Chem. Soc.* **2008**, *130*, 13167; g) Z. Fei, M. Shahid, N. Yaacobi-Gross, S. Rossbauer, H. Zhong, S. E. Watkins, T. D. Anthopoulos, M. Heeney, *Chem. Commun. (Cambridge, U. K.)* **2012**, *48*, 11130; h) I. Mcculloch, R. S. Ashraf, L. Biniek, H. Bronstein, C. Combe, J. E. Donaghey, D. I. James, C. B. Nielsen, B. C. Schroeder, W. M. Zhang, *Accounts Chem Res* **2012**, *45*, 714; i) W. M. Zhang, J. Smith, S. E. Watkins, R. Gysel, M. McGehee, A. Salleo, J. Kirkpatrick, S. Ashraf, T. Anthopoulos, M. Heeney, I. McCulloch, *J Am Chem Soc* **2010**, *132*, 11437.

[128] M. Q. He, F. X. Zhang, *J. Org. Chem.* **2007**, *72*, 442.

[129] a) G. Lu, H. Usta, C. Risko, L. Wang, A. Facchetti, M. A. Ratner, T. J. Marks, *J. Am. Chem. Soc.* **2008**, *130*, 7670; b) B. C. Schroeder, Z. G. Huang, R. S. Ashraf, J. Smith, P. D'Angelo, S. E. Watkins, T. D. Anthopoulos, J. R. Durrant, I. McCulloch, *Adv. Funct. Mater.* **2012**, *22*, 1663.

[130] a) H. X. Zhou, L. Q. Yang, S. C. Price, K. J. Knight, W. You, *Angew. Chem. Int. Edit.* **2010**, *49*, 7992; b) N. Cho, K. Song, J. K. Lee, J. Ko, *Chem-Eur J* **2012**, *18*, 11433; c) X. G. Guo, R. P. Ortiz, Y. Zheng, M. G. Kim, S. M. Zhang, Y. Hu, G. Lu, A. Facchetti, T. J. Marks, *J. Am. Chem. Soc.* **2011**, *133*, 13685; d) A. J. Kronemeijer, E. Gili, M. Shahid, J. Rivnay, A. Salleo, M. Heeney, H. Sirringhaus, *Adv. Mater.* **2012**, *24*, 1558; e) G. K. Dutta, A. R. Han, J. Lee, Y. Kim, J. H. Oh, C. Yang, *Adv. Funct. Mater.* **2013**, *23*, 5317.

[131] M. Zhang, H. N. Tsao, W. Pisula, C. D. Yang, A. K. Mishra, K. Mullen, *J. Am. Chem. Soc.* **2007**, *129*, 3472.

[132] a) S. Cho, J. Lee, M. H. Tong, J. H. Seo, C. Yang, *Adv. Funct. Mater.* **2011**, *21*, 1910; b) J. D. Yuen, J. Fan, J. Seifter, B. Lim, R. Hufschmid, A. J. Heeger, F. Wudl, *J. Am. Chem. Soc.* **2011**, *133*, 20799; c) J. Fan, J. D. Yuen, M. F. Wang, J. Seifter, J. H. Seo, A. R. Mohebbi, D. Zakhidov, A. Heeger, F. Wudl, *Adv. Mater.* **2012**, *24*, 2186.

[133] H. Huang, Z. Chen, R. P. Ortiz, C. Newman, H. Usta, S. Lou, J. Youn, Y.-Y. Noh, K.-J. Baeg, L. X. Chen, A. Facchetti, T. Marks, *J. Am. Chem. Soc.* **2012**, *134*, 10966.

[134] J. E. Anthony, J. S. Brooks, D. L. Eaton, S. R. Parkin, *J Am Chem Soc* **2001**, *123*, 9482.

[135] N. Nijegorodov, V. Ramachandran, D. P. Winkoun, *Spectrochim Acta A* **1997**, *53*, 1813.

[136] F. H. Li, Y. Zhou, F. L. Zhang, X. J. Liu, Y. Q. Zhan, M. Fahlman, *Chem. Mater.* **2009**, *21*, 2798.

[137] a) K. Asadi, F. Gholamrezaie, E. C. P. Smits, P. W. M. Blom, B. de Boer, *J. Mater. Chem.* **2007**, *17*, 1947; b) D. M. Alloway, A. L. Graham, X. Yang, A. Mudalige, R. Colorado, V. H. Wysocki, J. E. Pemberton, T. R. Lee, R. J. Wysocki, N. R. Armstrong, *J. Phys. Chem. C* **2009**, *113*, 20328; c) H. B. Akkerman, B. de Boer, *Journal of Physics-Condensed Matter* **2008**, *20*; d) H. B. Akkerman, R. C. G. Naber, B. Jongbloed, P. A. van Hal, P. W. M. Blom, D. M. de Leeuw, B. de Boer, *Proc. Natl. Acad. Sci. U. S. A.* **2007**, *104*, 11161; e) E. C. P. Smits, S. G. J. Mathijssen, P. A. van Hal, S. Setayesh, T. C. T. Geuns, K. A. H.

A. Mutsaers, E. Cantatore, H. J. Wondergem, O. Werzer, R. Resel, M. Kemerink, S. Kirchmeyer, A. M. Muzafarov, S. A. Ponomarenko, B. de Boer, P. W. M. Blom, D. M. de Leeuw, *Nature* **2008**, *455*, 956.

[138] B. de Boer, A. Hadipour, M. M. Mandoc, T. van Woudenbergh, P. W. M. Blom, *Adv. Mater.* **2005**, *17*, 621.

[139] P. Stoliar, R. Kshirsagar, M. Massi, P. Annibale, C. Albonetti, D. M. de Leeuw, F. Biscarini, *J. Am. Chem. Soc.* **2007**, *129*, 6477.

[140] Q. J. Cai, M. B. Chan-Park, Z. S. Lu, C. M. Li, B. S. Ong, *Langmuir* **2008**, *24*, 11889.

[141] Y. H. Zhou, C. Fuentes-Hernandez, J. Shim, J. Meyer, A. J. Giordano, H. Li, P. Winget, T. Papadopoulos, H. Cheun, J. Kim, M. Fenoll, A. Dindar, W. Haske, E. Najafabadi, T. M. Khan, H. Sojoudi, S. Barlow, S. Graham, J. L. Bredas, S. R. Marder, A. Kahn, B. Kippelen, *Science* **2012**, *336*, 327.

[142] Z. Chen, M. J. Lee, R. Shahid Ashraf, Y. Gu, S. Albert-Seifried, M. Meedom Nielsen, B. Schroeder, T. D. Anthopoulos, M. Heeney, I. McCulloch, H. Sirringhaus, *Adv. Mater.* **2012**, *24*, 647.

[143] G. Horowitz, R. Hajlaoui, H. Bouchriha, R. Bourguiga, M. Hajlaoui, *Adv. Mater.* **1998**, *10*, 923.

[144] a) C. A. Di, Y. Q. Liu, G. Yu, D. B. Zhu, *Acc. Chem. Res.* **2009**, *42*, 1573; b) J. C. Love, L. A. Estroff, J. K. Kriebel, R. G. Nuzzo, G. M. Whitesides, *Chemical Reviews (Washington, DC, United States)* **2005**, *105*, 1103.

[145] a) D. H. Kim, B. L. Lee, H. Moon, H. M. Kang, E. J. Jeong, J. I. Park, K. M. Han, S. Lee, B. W. Yoo, B. W. Koo, J. Y. Kim, W. H. Lee, K. Cho, H. A. Becerril, Z. Bao, *J. Am. Chem. Soc.* **2009**, *131*, 6124; b) H. A. Um, J. Shin, T. W. Lee, M. J. Cho, D. H. Choi, *Synth. Met.* **2013**, *184*, 61.

[146] a) H. Sirringhaus, P. J. Brown, R. H. Friend, M. M. Nielsen, K. Bechgaard, B. M. W. Langeveld-Voss, A. J. H. Spiering, R. A. J. Janssen, E. W. Meijer, P. Herwig, D. M. de Leeuw, *Nature* **1999**, *401*, 685; b) R. J. Kline, M. D. Mcgehee, M. F. Toney, *Nat. Mater.* **2006**, *5*, 222.

[147] a) L. L. Chua, P. K. H. Ho, H. Sirringhaus, R. H. Friend, *Appl. Phys. Lett.* **2004**, *84*, 3400; b) M. E. Roberts, N. Queralto, S. C. B. Mannsfeld, B. N. Reinecke, W. Knoll, Z. N. Bao, *Chem. Mater.* **2009**, *21*, 2292; c) G. Schwartz, B. C. K. Tee, J. G. Mei, A. L. Appleton, D. H. Kim, H. L. Wang, Z. N. Bao, *Nature Communications* **2013**, *4*, 1859.

[148] a) T. Sakanoue, H. Sirringhaus, *Nat. Mater.* **2010**, *9*, 736; b) D. K. Hwang, C. Fuentes-Hernandez, J. Kim, W. J. Potscavage, S. J. Kim, B. Kippelen, *Advanced Materials (Weinheim, Germany)* **2011**, *23*, 1293.

[149] a) K. J. Baeg, D. Khim, S. W. Jung, M. Kang, I. K. You, D. Y. Kim, A. Facchetti, Y. Y. Noh, *Adv. Mater.* **2012**, *24*, 5433; b) J. H. Li, Z. H. Sun, F. Yan, *Adv. Mater.* **2012**, *24*, 88.

[150] a) G. H. Lu, J. Blakesley, S. Himmelberger, P. Pingel, J. Frisch, I. Lieberwirth, I. Salzmann, M. Oehzelt, R. Di Pietro, A. Salleo, N. Koch, D. Neher, *Nature Communications* **2013**, *4*; b) M. H. Yoon, C. Kim, A. Facchetti, T. J. Marks, *J. Am. Chem. Soc.* **2006**, *128*, 12851.

[151] C. Kim, Z. M. Wang, H. J. Choi, Y. G. Ha, A. Facchetti, T. J. Marks, *J. Am. Chem. Soc.* **2008**, *130*, 6867.

[152] M. E. Roberts, S. C. B. Mannsfeld, N. Queralto, C. Reese, J. Locklin, W. Knoll, Z. N. Bao, *Proc. Natl. Acad. Sci. U. S. A.* **2008**, *105*, 12134.

[153] a) J. Seo, S. Park, S. Nam, H. Kim, Y. Kim, *Scientific Reports* **2013**, *3*; b) J. Veres, S. D. Ogier, S. W. Leeming, D. C. Cupertino, S. M. Khaffaf, *Adv. Funct. Mater.* **2003**, *13*, 199.

[154] Y. L. Wu, P. Liu, B. S. Ong, *Appl. Phys. Lett.* **2006**, *89*.

[155] a) Y. Takahashi, T. Hasegawa, S. Horiuchi, R. Kumai, Y. Tokura, G. Saito, *Chem. Mater.* **2007**, *19*, 6382; b) K. Fukuda, Y. Takeda, Y. Yoshimura, R. Shiwaku, L. T. Tran, T. Sekine, M. Mizukami, D. Kumaki, S. Tokito, *Nature Communications* **2014**, *5*.

[156] a) R. P. Ortiz, A. Facchetti, T. J. Marks, *Chemical Reviews (Washington, DC, United States)* **2010**, *110*, 205; b) A. Facchetti, M. H. Yoon, T. J. Marks, *Adv. Mater.* **2005**, *17*, 1705.

[157] a) N. Kim, W. J. Potscavage, B. Domercq, B. Kippelen, S. Graham, *Appl. Phys. Lett.* **2009**, *94*, 163308; b) N. Kim, S. Graham, K. J. Hwang, *Mater. Res. Bull.* **2014**, *58*, 24; c) N. Kim, S. Graham, *Thin Solid Films* **2013**, *547*, 57.

[158] D. Y. Khim, H. Han, K. J. Baeg, J. W. Kim, S. W. Kwak, D. Y. Kim, Y. Y. Noh, *Adv. Mater.* **2013**, *25*, 4302.

[159] a) L. Biniek, N. Leclerc, T. Heiser, R. Bechara, M. Brinkmann, *Macromolecules* **2013**, *46*, 4014; b) K. Tremel, F. S. U. Fischer, N. Kayunkid, R. Di Pietro, R. Tkachov, A. Kiriy, D. Neher, S. Ludwigs, M. Brinkmann, *Adv. Energy Mater.* **2014**, *4*.

[160] G. Li, R. Zhu, Y. Yang, *Nat. Photonics* **2012**, *6*, 153.

[161] J.-L. Bredas, *Mater. Horiz.* **2014**, *1*, 17.

[162] a) R. Steyrleuthner, M. Schubert, I. Howard, B. Klaumunzer, K. Schilling, Z. H. Chen, P. Saalfrank, F. Laquai, A. Facchetti, D. Neher, *J. Am. Chem. Soc.* **2012**, *134*, 18303; b) R. Steyrleuthner, R. Di Pietro, B. A. Collins, F. Polzer, S. Himmelberger, M. Schubert, Z. Chen, S. Zhang, A. Salleo, H. Ade, A. Facchetti, D. Neher, *J Am Chem Soc* **2014**, *136*, 4245.

[163] V. Balzani, P. Ceroni, A. Juris, *Photochemistry and Photophysics: Concepts, Research, Applications*, Wiley, **2014**.

[164] a) J. Clark, C. Silva, R. H. Friend, F. C. Spano, *Phys. Rev. Lett.* **2007**, *98*; b) J. Clark, J. F. Chang, F. C. Spano, R. H. Friend, C. Silva, *Appl. Phys. Lett.* **2009**, *94*, 163306.

[165] J. S. Ha, K. H. Kim, D. H. Choi, *J. Am. Chem. Soc.* **2011**, *133*, 10364.

[166] a) F. C. Spano, C. Silva, *Annu. Rev. Phys. Chem.* **2014**, *65*, 477; b) C. Hellmann, F. Paquin, N. D. Treat, A. Bruno, L. X. Reynolds, S. A. Haque, P. N. Stavrinou, C. Silva, N. Stingelin, *Adv Mater* **2013**, *25*, 4906; c) Y. Z. Xu, J. G. Liu, H. Y. Wang, X. H. Yu, R. B. Xing, Y. C. Han, *Soft Matter* **2013**, *9*, 9849.

[167] C. M. Cardona, W. Li, A. E. Kaifer, D. Stockdale, G. C. Bazan, *Adv. Mater.* **2011**, *23*, 2367.

[168] B. Jancy, S. K. Asha, *Chemistry of Materials* **2008**, *20*, 169.

[169] E. Gann, X. Gao, C.-a. Di, C. R. McNeill, *Adv. Funct. Mater.* **2014**, *24*, 7211.

[170] M. S. Park, A. Aiyar, J. O. Park, E. Reichmanis, M. Srinivasarao, *J. Am. Chem. Soc.* **2011**, *133*, 7244.

[171] M. Watanabe, K. Tsuchiya, T. Shinnai, M. Kijima, *Macromolecules* **2012**, *45*, 1825.

[172] M. Heeney, C. Bailey, M. Giles, M. Shkunov, D. Sparrowe, S. Tierney, W. M. Zhang, I. McCulloch, *Macromolecules* **2004**, *37*, 5250.

[173] Z. J. Zheng, K. H. Yim, M. S. M. Saifullah, M. E. Welland, R. H. Friend, J. S. Kim, W. T. S. Huck, *Nano Lett.* **2007**, *7*, 987.

[174] D. H. Kim, J. Lee, J. I. Park, J. W. Chung, W. H. Lee, G. Giri, B. Yoo, B. Koo, J. Y. Kim, Y. W. Jin, K. Cho, B. L. Lee, S. Lee, *Adv. Funct. Mater.* **2011**, *21*, 4442.

[175] a) W. Pisula, M. Zorn, J. Y. Chang, K. Mullen, R. Zentel, *Macromol. Rapid Commun.* **2009**, *30*, 1179; b) L. Schmidt-Mende, A. Fechtenkotter, K. Mullen, E. Moons, R. H. Friend, J. D. MacKenzie, *Science* **2001**, *293*, 1119; c) M. O'Neill, S. M. Kelly, *Adv. Mater.* **2011**, *23*, 566.

[176] a) K. C. Park, K. Levon, *Macromolecules* **1997**, *30*, 3175; b) V. Ho, B. W. Boudouris, R. A. Segalman, *Macromolecules* **2010**, *43*, 7895; c) V. Causin, C. Marega, A. Marigo, L. Valentini, J. M. Kenny, *Macromolecules* **2005**, *38*, 409.

[177] a) S. H. Wang, M. Kappl, I. Liebewirth, M. Muller, K. Kirchhoff, W. Pisula, K. Mullen, *Adv. Mater.* **2012**, *24*, 417; b) Y. Liu, H. L. Dong, S. D. Jiang, G. Y. Zhao, Q. Q. Shi, J. H. Tan, L. Jiang, W. P. Hu, X. W. Zhan, *Chem. Mater.* **2013**, *25*, 2649; c) S. Y. Min, T. S. Kim, B. J. Kim, H. Cho, Y. Y. Noh, H. Yang, J. H. Cho, T. W. Lee, *Nature Communications* **2013**, *4*; d) K. Rahimi, I. Botiz, N. Stingelin, N. Kayunkid, M. Sommer, F. P. V. Koch, H. Nguyen, O. Coulembier, P. Dubois, M. Brinkmann, G. Reiter, *Angewandte Chemie-International Edition* **2012**, *51*, 11131; e) J. H. Kim, D. H. Lee, D. S. Yang, D. U. Heo, K. H. Kim, J. Shin, H.-J. Kim, K.-Y. Baek, K. Lee, H. Baik, M. J. Cho, D. H. Choi, *Adv. Mater.* **2013**, *25*, 4102.

[178] a) L. H. Jimison, M. F. Toney, I. McCulloch, M. Heeney, A. Salleo, *Adv. Mater.* **2009**, *21*, 1568; b) C. R. McNeill, H. Ade, *J Mater Chem C* **2013**, *1*, 187; c) J. Rivnay, S. C. B. Mannsfeld, C. E. Miller, A. Salleo, M. F. Toney, *Chemical Reviews* **2012**, *112*, 5488.

[179] J. Rivnay, R. Steyrleuthner, L. H. Jimison, A. Casadei, Z. H. Chen, M. F. Toney, A. Facchetti, D. Neher, A. Salleo, *Macromolecules* **2011**, *44*, 5246.

[180] G. H. Lu, J. Y. Chen, W. T. Xu, S. J. Li, X. N. Yang, *Adv Funct Mater* **2014**, *24*, 4959.

[181] T. R. Andersen, T. T. Larsen-Olsen, B. Andreasen, A. P. L. Bottiger, J. E. Carle, M. Helgesen, E. Bundgaard, K. Norrman, J. W. Andreasen, M. Jorgensen, F. C. Krebs, *Acs Nano* **2011**, *5*, 4188.

[182] a) M. Chang, D. Choi, B. Y. Fu, E. Reichmanis, *ACS Nano* **2013**, *7*, 5402; b) S. Ferdous, F. Liu, D. Wang, T. P. Russell, *Adv. Energy Mater.* **2014**, *4*; c) D. T. Duong, B. Walker, J. Lin, C. Kim, J. Love, B. Purushothaman, J. E. Anthony, T. Q. Nguyen, *Journal of Polymer Science Part B-Polymer Physics* **2012**, *50*, 1405; d) K. R. Graham, P. M. Wieruszewski, R. Stalder, M. J. Hartel, J. G. Mei, F. So, J. R. Reynolds, *Adv. Funct. Mater.* **2012**, *22*, 4801.

[183] a) S. Hugger, R. Thomann, T. Heinzel, T. Thurn-Albrecht, *Colloid Polym. Sci.* **2004**, *282*, 932; b) W. L. Ma, C. Y. Yang, X. Gong, K. Lee, A. J. Heeger, *Adv. Funct. Mater.* **2005**, *15*, 1617.

[184] a) H. Fuchigami, A. Tsumura, H. Koezuka, *Appl. Phys. Lett.* **1993**, *63*, 1372; b) C. Zhang, J. Y. Sun, R. Li, S. S. Sun, E. Lafalce, X. M. Jiang, *Macromolecules* **2011**, *44*, 6389.

[185] a) B. C. Thompson, Y. G. Kim, T. D. McCarley, J. R. Reynolds, *J. Am. Chem. Soc.* **2006**, *128*, 12714; b) S. C. Price, A. C. Stuart, W. You, *Macromolecules* **2010**, *43*, 4609; c) I. McCulloch, M. Heeney, M. L. Chabinyc, D. DeLongchamp, R. J. Kline, M. Coelle, W. Duffy, D. Fischer, D. Gundlach, B. Hamadani, R. Hamilton, L. Richter, A. Salleo, M. Shkunov, D. Sporrowe, S. Tierney, W. Zhong, *Adv. Mater.* **2009**, *21*, 1091.

[186] a) P. Sonar, S. P. Singh, S. Sudhakar, A. Dodabalapur, A. Sellinger, *Chemistry of Materials* **2008**, *20*, 3184; b) W. Yue, Y. Zhao, H. K. Tian, D. Song, Z. Y. Xie, D. H. Yan, Y. H. Geng, F. S. Wang, *Macromolecules* **2009**, *42*, 6510.

[187] a) H. A. M. van Mullekom, J. A. J. M. Vekemans, E. E. Havinga, E. W. Meijer, *Materials Science & Engineering R-Reports* **2001**, *32*, 1; b) S. H. Park, A. Roy, S. Beaupre, S. Cho, N. Coates, J. S. Moon, D. Moses, M. Leclerc, K. Lee, A. J. Heeger, *Nat. Photonics* **2009**, *3*, 297; c) N. Blouin, A. Michaud, D. Gendron, S. Wakim, E. Blair, R. Neagu-Plesu, M. Belletete, G. Durocher, Y. Tao, M. Leclerc, *J. Am. Chem. Soc.* **2008**, *130*, 732; d) H. X. Zhou, L. Q. Yang, S. Q. Xiao, S. B. Liu, W. You, *Macromolecules* **2010**, *43*, 811.

[188] P. T. Wu, F. S. Kim, S. A. Jenekhe, *Chem. Mater.* **2011**, *23*, 4618.

[189] a) N. Leclerc, A. Michaud, K. Sirois, J. F. Morin, M. Leclerc, *Adv. Funct. Mater.* **2006**, *16*, 1694; b) S. P. Wen, J. N. Pei, Y. H. Zhou, P. F. Li, L. L. Xue, Y. W. Li, B. Xu, W. J. Tian, *Macromolecules* **2009**, *42*, 4977; c) Z. M. Tang, T. Lei, K. J. Jiang, Y. L. Song, J. A. Pei, *Chem. Asian J.* **2010**, *5*, 1911.

[190] a) A. A. Jahnke, G. W. Howe, D. S. Seferos, *Angew Chem Int Edit* **2010**, *49*, 10140; b) T. Yamamoto, T. Yasuda, Y. Sakai, S. Aramaki, *Chem. Mater.* **2005**, *17*, 6060.

[191] a) F. S. Liang, J. P. Lu, J. F. Ding, R. Movileanu, Y. Tao, *Macromolecules* **2009**, *42*, 6107; b) G. Zotti, B. Vercelli, A. Berlin, S. Destri, M. Pasini, V. Hernandez, J. T. L. Navarrete, *Chem. Mater.* **2008**, *20*, 6847; c) J. Casado, L. L. Miller, K. R. Mann, T. M. Pappenfus, Y. Kanemitsu, E. Orti, P. M. Viruela, R. Pou-Amerigo, V. Hernandez, J. T. L. Navarrete, *J. Phys. Chem. B* **2002**, *106*, 3872.

[192] a) J. M. Tour, R. L. Wu, *Macromolecules* **1992**, *25*, 1901; b) P. Bauerle, T. Fischer, B. Bidlingmeier, A. Stabel, J. P. Rabe, *Angewandte Chemie-International Edition in English* **1995**, *34*, 303; c) R. S. Becker, J. S. deMelo, A. L. Macanita, F. Elisei, *J Phys Chem-Us* **1996**, *100*, 18683.

[193] a) V. Shrotriya, J. Ouyang, R. J. Tseng, G. Li, Y. Yang, *Chem. Phys. Lett.* **2005**, *411*, 138; b) J. M. J. Frechet, C. H. Woo, B. C. Thompson, B. J. Kim, M. F. Toney, *J. Am. Chem. Soc.* **2008**, *130*, 16324.

[194] Y. Qin, M. A. Hillmyer, *Macromolecules* **2009**, *42*, 6429.

[195] R. Rieger, D. Beckmann, W. Pisula, M. Kastler, K. Mullen, *Macromolecules* **2010**, *43*, 6264.

[196] a) J. F. Chang, J. Clark, N. Zhao, H. Sirringhaus, D. W. Breiby, J. W. Andreasen, M. M. Nielsen, M. Giles, M. Heeney, I. McCulloch, *Physical Review B* **2006**, *74*, 115318; b) J. Kim, B. Lim, K. J. Baeg, Y. Y. Noh, D. Khim, H. G. Jeong, J. M. Yun, D. Y. Kim, *Chem. Mater.* **2011**, *23*, 4663.

[197] S. Song, Y. Jin, S. H. Kim, J. Moon, K. Kim, J. Y. Kim, S. H. Park, K. Lee, H. Suh, *Macromolecules* **2008**, *41*, 7296.

[198] B. S. Ong, Y. L. Wu, P. Liu, S. Gardner, *Adv. Mater.* **2005**, *17*, 1141.

[199] B. Lim, K. J. Baeg, H. G. Jeong, J. Jo, H. Kim, J. W. Park, Y. Y. Noh, D. Vak, J. H. Park, J. W. Park, D. Y. Kim, *Adv. Mater.* **2009**, *21*, 2808.

[200] L. Biniek, C. L. Chochos, G. Hadziioannou, N. Leclerc, P. Leveque, T. Heiser, *Macromol. Rapid Commun.* **2010**, *31*, 651.

[201] a) W. P. Hsu, K. Levon, K. S. Ho, A. S. Myerson, T. K. Kwei, *Macromolecules* **1993**, *26*, 1318; b) S. L. Liu, T. S. Chung, *Polymer* **2000**, *41*, 2781.

[202] Y. Kim, S. Cook, S. M. Tuladhar, S. A. Choulis, J. Nelson, J. R. Durrant, D. D. C. Bradley, M. Giles, I. Mcculloch, C. S. Ha, M. Ree, *Nat. Mater.* **2006**, *5*, 197.

[203] a) M. L. Chabinyc, M. F. Toney, R. J. Kline, I. McCulloch, M. Heeney, *J. Am. Chem. Soc.* **2007**, *129*, 3226; b) H. L. Pan, Y. N. Li, Y. L. Wu, P. Liu, B. S. Ong, S. P. Zhu, G. Xu, *J. Am. Chem. Soc.* **2007**, *129*, 4112; c) I. Osaka, M. Shimawaki, H. Mori, I. Doi, E. Miyazaki, T. Koganezawa, K. Takimiya, *J. Am. Chem. Soc.* **2012**, *134*, 3498; d) Y. N. Li, P. Sonar, S. P. Singh, M. S. Soh, M. van Meurs, J. Tan, *J. Am. Chem. Soc.* **2011**, *133*, 2198.

[204] a) C. B. Nielsen, M. Turbiez, I. McCulloch, *Adv. Mater.* **2013**, *25*, 1859; b) X. Guo, S. R. Puniredd, M. Baumgarten, W. Pisula, K. Mullen, *Adv. Mater.* **2013**, *25*, 5467.

[205] a) Y. N. Li, P. Sonar, L. Murphy, W. Hong, *Energy Environ. Sci.* **2013**, *6*, 1684; b) L. T. Dou, J. B. You, J. Yang, C. C. Chen, Y. J. He, S. Murase, T. Moriarty, K. Emery, G. Li, Y. Yang, *Nat. Photonics* **2012**, *6*, 180; c) L. J. Huo, J. H. Hou, H. Y. Chen, S. Q. Zhang, Y. Jiang, T. L. Chen, Y. Yang, *Macromolecules* **2009**, *42*, 6564; d) S. Loser, C. J. Bruns, H. Miyauchi, R. P. Ortiz, A. Facchetti, S. I. Stupp, T. J. Marks, *J. Am. Chem. Soc.* **2011**, *133*, 8142.

[206] a) M. S. Chen, O. P. Lee, J. R. Niskala, A. T. Yiu, C. J. Tassone, K. Schmidt, P. M. Beaujuge, S. S. Onishi, M. F. Toney, A. Zettl, J. M. J. Fréchet, *J. Am. Chem.*

Soc., 10.1021/ja4088665; b) N. Blouin, A. Michaud, M. Leclerc, *Adv. Mater.* **2007**, *19*, 2295.

[207] a) J. R. Matthews, W. J. Niu, A. Tandia, A. L. Wallace, J. Y. Hu, W. Y. Lee, G. Giri, S. C. B. Mannsfeld, Y. T. Xie, S. C. Cai, H. H. Fong, Z. N. Bao, M. Q. He, *Chem. Mater.* **2013**, *25*, 782; b) A. T. Yiu, P. M. Beaujuge, O. P. Lee, C. H. Woo, M. F. Toney, J. M. J. Frechet, *J. Am. Chem. Soc.* **2012**, *134*, 2180; c) Z. Li, Y. G. Zhang, S. W. Tsang, X. M. Du, J. Y. Zhou, Y. Tao, J. F. Ding, *J. Phys. Chem. C* **2011**, *115*, 18002.

[208] Y. H. Lee, A. Ohta, Y. Yamamoto, Y. Komatsu, K. Kato, T. Shimizu, H. Shinoda, S. Hayami, *Polyhedron* **2011**, *30*, 3001.

[209] a) H. Bronstein, Z. Y. Chen, R. S. Ashraf, W. M. Zhang, J. P. Du, J. R. Durrant, P. S. Tuladhar, K. Song, S. E. Watkins, Y. Geerts, M. M. Wienk, R. A. J. Janssen, T. Anthopoulos, H. Sirringhaus, M. Heeney, I. McCulloch, *J. Am. Chem. Soc.* **2011**, *133*, 3272; b) M. Shahid, T. McCarthy-Ward, J. Labram, S. Rossbauer, E. B. Domingo, S. E. Watkins, N. Stingelin, T. D. Anthopoulos, M. Heeney, *Chem. Sci.* **2012**, *3*, 181.

[210] A. L. Dyer, E. J. Thompson, J. R. Reynolds, *Acs Appl Mater Inter* **2011**, *3*, 1787.

[211] J. L. Bredas, J. E. Norton, J. Cornil, V. Coropceanu, *Acc. Chem. Res.* **2009**, *42*, 1691.

[212] Y. D. Park, J. K. Park, J. H. Seo, J. D. Yuen, W. H. Lee, K. Cho, G. C. Bazan, *Adv. Energy Mater.* **2011**, *1*, 63.

[213] a) E. J. Zhou, J. Z. Cong, Q. S. Wei, K. Tajima, C. H. Yang, K. Hashimoto, *Angew Chem Int Edit* **2011**, *50*, 2799; b) M. Schubert, D. Dolfen, J. Frisch, S. Roland, R. Steyrleuthner, B. Stiller, Z. H. Chen, U. Scherf, N. Koch, A. Facchetti, D. Neher, *Adv. Energy Mater.* **2012**, *2*, 369.

[214] a) J. E. Anthony, A. Facchetti, M. Heeney, S. R. Marder, X. W. Zhan, *Adv. Mater.* **2010**, *22*, 3876; b) S. B. Heidenhain, Y. Sakamoto, T. Suzuki, A. Miura, H. Fujikawa, T. Mori, S. Tokito, Y. Taga, *J Am Chem Soc* **2000**, *122*, 10240.

[215] a) Y. Z. Lin, H. J. Fan, Y. F. Li, X. W. Zhan, *Advanced Materials (Weinheim, Germany)* **2012**, *24*, 3087; b) M. Mamada, J. I. Nishida, D. Kumaki, S. Tokito, Y. Yamashita, *Chem. Mater.* **2007**, *19*, 5404; c) M. O. Wolf, M. S. Wrighton, *Chem. Mater.* **1994**, *6*, 1526; d) T. Yamamoto, H. Suganuma, T. Maruyama, T. Inoue, Y. Muramatsu, M. Arai, D. Komarudin, N. Ooba, S. Tomaru, S. Sasaki, K. Kubota, *Chem. Mater.* **1997**, *9*, 1217.

[216] a) I. H. Jung, Y. K. Jung, J. Lee, J. H. Park, H. Y. Woo, J. I. Lee, H. Y. Chu, H. K. Shim, *J. Polym. Sci. Pol. Chem.* **2008**, *46*, 7148; b) T. Tao, Y. X. Peng, W.

Huang, X. Z. You, *J. Org. Chem.* **2013**, *78*, 2472; c) M. P. Johansson, J. Olsen, *J. Chem. Theory Comput.* **2008**, *4*, 1460.

[217] a) E. M. Breitung, C. F. Shu, R. J. McMahon, *J. Am. Chem. Soc.* **2000**, *122*, 1154; b) B. Bak, D. Christensen, L. Hansen-Nygaard, J. Rastrup-Andersen, *J. Mol. Spectrosc.* **1962**, *9*, 222.

[218] H. Usta, W. C. Sheets, M. Denti, G. Generali, R. Capelli, S. Lu, X. Yu, M. Muccini, A. Facchetti, *Chem. Mater.* **2014**, *26*, 6542.

[219] S. Ando, J. I. Nishida, H. Tada, Y. Inoue, S. Tokito, Y. Yamashita, *J. Am. Chem. Soc.* **2005**, *127*, 5336.

[220] F. Liu, C. Wang, J. K. Baral, L. Zhang, J. J. Watkins, A. L. Briseno, T. P. Russell, *J. Am. Chem. Soc.* **2013**, *135*, 19248.

[221] W. Y. Lee, G. Giri, Y. Diao, C. J. Tassone, J. R. Matthews, M. L. Sorensen, S. C. B. Mannsfeld, W. C. Chen, H. H. Fong, J. B. H. Tok, M. F. Toney, M. Q. He, Z. A. Bao, *Adv. Funct. Mater.* **2014**, *24*, 3524.

[222] M. Lemaire, J. Hassan, L. Lavenot, C. Gozzi, *Tetrahedron Lett.* **1999**, *40*, 857.

[223] L. A. Perez, P. Zalar, L. Ying, K. Schmidt, M. F. Toney, T. Q. Nguyen, G. C. Bazan, E. J. Kramer, *Macromolecules* **2014**, *47*, 1403.

[224] a) T. H. Dunning, *The Journal of Chemical Physics* **1989**, *90*, 1007; b) D. E. Woon, T. H. Dunning, *The Journal of Chemical Physics* **1993**, *98*, 1358; c) J. D. Chai, M. Head-Gordon, *J. Chem. Phys.* **2008**, *128*, 084106.

[225] a) W. Li, W. S. C. Roelofs, M. Turbiez, M. M. Wienk, R. A. J. Janssen, *Adv. Mater.* **2014**, *26*, 3304; b) B. Sun, W. Hong, Z. Q. Yan, H. Aziz, Y. N. Li, *Adv. Mater.* **2014**, *26*, 2636.

[226] a) P. Wei, J. H. Oh, G. F. Dong, Z. N. Bao, *J. Am. Chem. Soc.* **2010**, *132*, 8852; b) P. Wei, T. Menke, B. D. Naab, K. Leo, M. Riede, Z. Bao, *J. Am. Chem. Soc.* **2012**, *134*, 3999.

[227] a) B. D. Naab, S. Himmelberger, Y. Diao, K. Vandewal, P. Wei, B. Lussem, A. Salleo, Z. N. Bao, *Adv. Mater.* **2013**, *25*, 4663; b) B. D. Naab, S. Guo, S. Olthof, E. G. B. Evans, P. Wei, G. L. Millhauser, A. Kahn, S. Barlow, S. R. Marder, Z. A. Bao, *J. Am. Chem. Soc.* **2013**, *135*, 15018; c) B. D. Naab, S. Y. Zhang, K. Vandewal, A. Salleo, S. Barlow, S. R. Marder, Z. A. Bao, *Adv. Mater.* **2014**, *26*, 4268.

[228] H. Tanaka, M. Hirate, S. Watanabe, S.-i. Kuroda, *Adv. Mater.* **2014**, *26*, 2376.

[229] Y. B. Qi, S. K. Mohapatra, S. B. Kim, S. Barlow, S. R. Marder, A. Kahn, *Appl. Phys. Lett.* **2012**, *100*.

[230] a) R. A. Schlitz, F. G. Brunetti, A. M. Glaudell, P. L. Miller, M. A. Brady, C. J. Takacs, C. J. Hawker, M. L. Chabinyc, *Adv Mater* **2014**, *26*, 2825; b) Y. M. Sun, P. Sheng, C. A. Di, F. Jiao, W. Xu, D. Qiu, D. B. Zhu, *Adv Mater* **2012**, *24*, 932.